MEASUREMENTS AND THEORETICAL MODELING OF RADON DRIVING FORCES AND INDOOR RADON CONCENTRATIONS AND THE DEVELOPMENT OF RADON REDUCTION AND MITIGATION TECHNOLOGY

By

KAISS KAMAL Al-AHMADY

A DISSERTATION PRESENTED TO THE GRADUATE SCHOOL
OF THE UNIVERSITY OF FLORIDA IN PARTIAL FULFILLMENT
OF THE REQUIREMENTS FOR THE DEGREE OF
DOCTOR OF PHILOSOPHY

UNIVERSITY OF FLORIDA

1995

Copyright © 1995 Kaiss K. Al-Ahmady
All Rights Reserved

This Work is Dedicated to,

My Parents Dr. Kamal D. Al-Ahmady & Mrs. Zohor A. Rashied

My Wife Zahrah S. Al-Noory

My Children Ahmed & Farrah

&

My Brothers; Kossay, Saad, & Senan

ACKNOWLEDGMENTS

The author would like to express his appreciation and sincere thanks to the chairman of the supervisory committee, Dr. David E. Hintenlang, for his guidance, discussions and support during the course of this research.

Special thanks are extended to the committee members, Dr. William G. Vernetson and Dr. George R. Dalton from the Department of Nuclear Engineering Sciences, Dr. Paul Oppenheim from the School of Building Construction, and Dr. Fazil T. Najafi from the Department of Civil Engineering for their suggestions and help throughout the work in this research.

Support for this research has been provided by the U.S. Environmental Protection Agency and the Florida Department of Community Affairs. This support is gratefully acknowledged.

The author would like to express his deepest appreciation to his wife, Zahrah, whose understanding and patience provided the motivation needed to accomplish this research. A special word of thanks is devoted to the author's parents and brothers for their continuous moral support and encouragement.

TABLE OF CONTENTS

page

ACKNOWLEDGMENTS.................................... iv

ABSTRACT... vii

CHAPTERS

1 INTRODUCTION AND LITERATURE SURVEY................. 1

Nature of the Problem.............................. 1
Objective of the Research.......................... 5
    Main Goals..................................... 5
    Research Tasks................................. 5
Review of General Properties of Radon.............. 7
Radon Health Hazard................................ 8
Radon Availability and Migration in the Soil....... 17
The Indoor Radon Problem........................... 25
Radon-Rich Soil-Gas Transport Into Structures...... 28
Radon Mitigation Methods and Systems............... 35

2 MATHEMATICAL CONSIDERATIONS........................ 38

Gaseous-Phase Radon Transport in Soils............. 38
Multi-Phase Radon Transport in Soils............... 51
Pressure Distribution in Soil System............... 54

3 EXPERIMENTAL DESIGN AND METHODOLOGY................ 58

Outlines for the Experimental Design and Methodology.............................. 58
Selection Criterion for A Research Site............ 62
The University of Florida Radon Research House (UFRRH)........................... 63
Non-Radiological Measurements...................... 66
    Pressure Measurements.......................... 66
    Temperature and Humidity Measurements......... 73
    Flow Measurements.............................. 78
    Leakage and Ventilation Measurements.......... 83
    Weather Measurements........................... 91
Radiological Measurements.......................... 95

Collection and Classification of the Experimental Raw Data............................ 105
Processing of the Final Output Data Files......... 110
Experimental Error Assessment and Quality Control of the Measurements.................... 114
    Assessment of Experimental Error............. 114
    Quality Control of Non-Radiological Measurements............................ 117
    Quality Control of Radiological Measurements............................ 124

4 RESULTS AND DISCUSSION............................ 139

Observations of Physical Parameters Related to Indoor Radon................................ 139
    Initial Characterization of the Research Site........................... 139
    Time and Spatial Dependence of Pressure Differentials.................. 149
    Time and Spatial Dependence of Radon Concentrations.................... 176

Modeling of Physical Parameters Related to Indoor Radon................................ 202

    Barometric Pressure-Induced Pressure Differentials........................... 202
    Wind-Induced Pressure Differentials........................... 253
    Temperature-Induced Pressure Differentials........................... 259
    Structure Ventilation........................ 316
    Indoor Radon Concentrations.................. 328

Applications for Predicting and Controlling Long-Term Indoor Radon Concentrations........... 370

    Long-Term Indoor Radon Concentrations........ 370
    A System Design for Controlling Indoor Radon Concentrations............................ 383

5 CONCLUSIONS.. 403

Recommendations for Future Work.................. 412

REFERENCES.. 415

BIOGRAPHICAL SKETCH................................... 423

Abstract of Dissertation Presented to the Graduate School
of the University of Florida in Partial Fulfillment of the
Requirements for the Degree of Doctor of Philosophy

MEASUREMENTS AND THEORETICAL MODELING OF RADON DRIVING FORCES AND INDOOR RADON CONCENTRATIONS AND THE DEVELOPMENT OF RADON REDUCTION AND MITIGATION TECHNOLOGY

By

KAISS KAMAL Al-AHMADY

MAY 1995

Chairman: Dr. David E. Hintenlang
Major Department: Nuclear Engineering Sciences

A carefully selected, heavily instrumented, and fully controlled experimental facility was used to investigate and model indoor radon driving forces and concentrations. A semi-diurnal natural pumping of radon-rich soil gas model was based on an exponentially damped response of the sub-slab air volume pressure to changes in atmospheric pressure. A wind-induced pressure differentials model was based on the conservation of energy of the wind acting on the structure. A temperature-induced pressure differentials model was based on the linear approximation of the weakly exponentially-dependent pressures between two temperature zones under hydrostatic equilibrium.

A semi-empirical model to predict the time-dependent and time-averaged indoor radon concentrations was based on the mass balance principle of the radon gas in the indoor environment. An integrated model was developed that incorporated radon driving forces and concentrations models. This model was used to develop applications for predicting short-term to long term-indoor radon concentration ratios and designing indoor radon prevention systems.

The highest indoor radon concentrations for slab-on-grade structures has been found to occur when the structure experience neutral pressure conditions. Significant pulses of radon entry are predicted when wind blows on the leeward wall of a structure. It has been found that pressure differences induced by temperature differences are proportional to both the magnitude of the temperature differences and the average temperature between the indoors and outdoors. Under extreme weather conditions, they can generate pressure differences of several pascals that profoundly contribute to the entry and removal of indoor radon.

It has been demonstrated that increasing house ventilation rates by increasing the effective leakage area of the house shell does not reduce indoor radon concentrations as effectively as increasing house ventilation rates by controlled duct ventilation associated with the utilization of heating, ventilating, and air-conditioning (HVAC) systems. These results form the basis for strategies to minimize indoor radon concentrations while providing positive control over the quality of infiltration air through the HVAC unbalanced pressurization controller (HUPC) systems.

It has been shown that predictions of the annual indoor radon levels can be performed by applying the integrated model for each level utilizing a common reference time. This technique provides a significant tool to approach the conflict between short and long term indoor radon concentrations. It has been shown that significant reductions in indoor radon concentration may be achieved by the utilization of the HUPC concept. An application of this system reduced indoor radon concentrations from approximately 2000 Bq/m^3 to less than 120 Bq/m^3 in the indoor environment of the utilized facility.

CHAPTER 1
INTRODUCTION AND LITERATURE SURVEY

Nature of the Problem

Natural radioactive isotopes of radon gas have been present in nature for millions of years, probably since the down of creation. The dominant part of the natural radiation dose that a person is naturally exposed to during lifetime comes from inhaled radon and its decay products. Although the radon concentration in the atmosphere is negligible, concern over indoor radon concentrations began to become significant in the 1980s.

In the development of living facilities and structures there has been increasing control of building interiors. They are being made more and more isolated from the outdoors for various reasons such as reduced energy consumption. Unfortunately, one price of these developments is the indoor radon problem. These structures start to act as collectors and accumulators for the radon gas which is transported from the sub-structure area and other sources and enters the indoor living area. When ventilation in these structures is limited, elevated indoor radon concentrations could accumulate and, consequently, health problems could result.

Radon gas can enter the building interior from the soil system surrounding the structure, the potable water, building materials, and the outdoors. The gas can be transported by molecular diffusion and convection processes. Driving forces responsible for transporting radon into and from the indoor are associated with many environmental and indoor occupancy factors that are variable and inter-related in nature. Representing these driving forces and influencing factors that support predictions of indoor radon concentration is a difficult and complicated task. Models of radon driving forces and indoor radon concentrations are needed to from the physical and mathematical basis necessary to establish a quantitative description that can be employed in solving the indoor radon problem.

At least three fundamental areas must be addressed to develop effective technologies that provide engineering solutions to the indoor radon problem. The first area consists of studying, analyzing, and modeling the major driving forces responsible for radon entry into the indoor environment. The second area consists of studying, analyzing, and modeling the radon gas mass balance in the indoor environment. Models and analyses of driving forces affecting radon removal from the indoor volume need to be established at this stage of the overall approach to solve the indoor radon problem.

The third area consists of the establishment of mathematical and physical frameworks to facilitate solutions for two major objectives: the first is the design and development of indoor radon prevention technology and the second is the modeling of annual indoor radon concentrations as a function of the influencing factors.

In this work, the rest of this chapter is devoted to the introductory issues of the indoor radon problem. The next section of the chapter establishes the scope of the objectives of this research. Background necessary for supporting the subject of this work is then introduced including a survey reflecting existing knowledge of the subject.

Mathematical considerations concerning radon transport in the soil system and radon-rich soil-gas entry from the sub-structure area into the indoor are discussed in Chapter 2. These considerations are being employed to justify assumptions to be made in latter sections of this work.

Chapter 3 is devoted to experimental design and methodology. Since extensive experimentation was performed during this research, the chapter starts with an introductory part outlining the overall experimental design and methodology, followed by two detailed parts. The first delivers detailed descriptions of the experiments classified by the type of the measured parameter. The second part provides descriptions of the quality control and quality assurance of the measurements, as well as an assessment of the possible experimental errors associated with the testing performed in this research, following the same sequence of the section subject utilized in the first part of the chapter.

Chapter 4 represents the core of this work and is devoted to the results and discussion. This chapter is divided into three major parts corresponding to the logical sequence of the developments during this research. The first part of the chapter deals with the results collected from many experiments at the University of Florida Radon Research House (UFRRH), and the associated physical interpretations of these results. This part is written with a section's structure following the same sequence utilized in the preceding chapter of the experimental design and methodology (Chapter 3).

The second part of Chapter 4 shows the modeling efforts of this research, including the development of five mechanistic and empirical models. The first four models cover the major indoor radon driving forces affecting indoor radon entry and removal from the indoor environment. The fifth model deals with the mass balance of indoor radon gas where the four previous models are integrated to develop an overall mathematical framework governing indoor radon concentration.

The third part of Chapter 4 describes two major applications derived from the experimental data and models development discussed in the first and second part of the chapter. The two applications are represented by the development of a mathematical model and a procedure to predict long-term indoor radon concentrations from short-term testing results and corresponding environmental parameters, and a system design for an innovative radon reduction and control system, respectively. Finally, the conclusions drawn from this research, as well as recommendations for future work are provided in Chapter 5.

Objective of the Research

Main Goals

(1) to develop and integrate models for the prediction of major radon driving forces and the subsequent indoor radon concentrations, and

(2) to establish an innovative indoor radon prevention, reduction, and mitigation technology.

Research Tasks

(1) to model the time-dependent sub-structure soil-gas radon entry into a component in an indoor radon prediction model;

(2) to develop a mechanistic model to predict wind-induced pressure differentials that may be generated from wind blowing on the structure;

(3) to develop a model to predict the temperature-driven pressure differentials affecting indoor radon concentrations;

(4) to develop a model to predict time-averaged indoor radon concentration;

(5) to characterize the temperature effects on the sub-structure radon concentrations, indoor radon concentration, natural and mechanically driven structure leakage and ventilation rates;

(6) to integrate the sub-structure semi-diurnal barometric pressure-driven pressure differentials model, temperature-driven pressure differentials model, time-averaged indoor radon concentration model, and structure air change rate pressure differentials empirical model into the time rate of change of indoor radon concentration mass conservation equation;

(7) to characterize the effects of the structure heating, ventilating and air-conditioning (HVAC) system on the radon driving forces and indoor radon concentrations;

(8) to develop mathematical frameworks to translate the resulting modeling into design equations for an innovative indoor radon reduction system; and

(9) to develop an approach for predicting long-term indoor radon concentrations from short-term radon testing results.

Review of General Properties of Radon

Radon (Rn) is an odorless, colorless, almost inert, and radioactive gas. Radon is the heaviest element in the inert gases column in the periodic table. It has the highest boiling point, melting point, and critical temperature and pressure of the inert gases. Although it is an inert gas, radon can form some compounds such as complex fluorides and clathrate. Table 1-1 shows some properties of radon.

Radon is formed directly from the radioactive decay of radium. The latter is a part of the naturally occurring radioactive decay series of uranium (U-238 and U-235) and thorium (Th-232). Three isotopes of radon are produced from these decays: ^{222}Rn, ^{220}Rn, and ^{219}Rn; with half-lives of 3.825 days, 55.6 seconds and 3.92 seconds, respectively. The radon isotopes are usually in secular equilibrium with their parents in the environment.

The isotope ^{222}Rn, from the decay of ^{226}Ra, is the most important radon isotope, because it has the longest half-life, and the abundance of its parent (uranium series) in geological materials. However, in certain areas, where thorium-rich materials can be widely found, ^{220}Rn may also have a considerable effect on health (Schery 1985).

^{222}Rn decays to ^{218}Po by releasing an alpha particle of 5.49 million electron-volt (MeV) as follows:

$$^{222}\text{Rn} \longrightarrow {}^{218}\text{Po} + {}^{4}\text{He} + 5.49 \quad (\text{MeV})$$

Polonium-218, Lead-214, Bismuth-214, and Polonium-214 are the "immediate" daughters, or progeny of radon-222. All four radionuclides are chemically active and have relatively short half-lives. As shown in Tables 1-2 and 1-3, these progeny have half-lives of less than 30 minutes, which is comparable to the time required to complete one breathing cycle by the normal lung removal mechanism. As a result, radon progeny are likely to decay to ^{210}Pb, which has a half-life of 22.3 years. These deposits may reach significant levels upon continuing accumulation of exposure, which can cause potential health problems. The decay of the short-lived daughter ^{220}Rn also contributes to the total dose delivered by inhaling radon gas.

Radon Health Hazard

The accumulated dose of radon and its decay products is generated mainly from alpha particle decay which has the highest quality factor for depositing its energy into living tissues, compared to other radiations. Radon's radiological significance arises from two factors: (1) radon gas itself is chemically inactive (inert) and has a half-life that is long enough to easily reach and decay in the lung during inhalation; and (2) once radon has decayed in the lung, its decay products (radon progeny) are chemically very active and have short half-lives that make them easily attached in the

TABLE 1-1: Some physical properties of Radon.

Property[a]	Value
Boiling Point (°C)	-61.8
Critical Temperature (°C)	104.0
Critical Pressure (atmosphere)	62.0
Density (at normal pressure and temperature) (kg/m^3)	9.96
Melting Point (°C)	-71.0
Vapor Pressure (at 99.0 °C) (KPa)	13.0
Vapor Pressure (at 61.8 °C) (KPa)	100.0
Solubility Coefficient in Water (atmospheric pressure , 100 °C)	0.106
Solubility Coefficient in Water (atmospheric pressure, 0 °C)	0.507

[a] modified from (UNSC 1982).

TABLE 1-2: Major characteristics of ^{222}Rn and its decay products (part of ^{238}U decay chain).

Radionuclide	Half-Life	Alpha (MeV)	Beta (MeV)
Ra-226	1600y	4.06, 4.78	
Rn-222	3.825d	5.49	
Po-218	3.11m	6.00	
Pb-214	26.8m		0.67, 0.72, 1.02
Bi-214	19.9m		3.27, 1.54, 1.5
Po-214	164μs	7.69	
Pb-210	22.3y		0.02, 0.06
Bi-210	5.01d		1.16
Po-210	138d	5.03	
Pb-206	stable		

lung to deposit most of their decay energy into tissues.

The major radiological risk of inhaled radon and its decay products is the development of lung cancer. Lung cancer of the respiratory tract has emerged as the most common form of lethal cancer. It is estimated that lung cancer accounts for approximately one-fifth of all cancer yearly deaths in the United States (James 1984). The U.S. Environmental Protection Agency (EPA) estimated that radon is responsible for about 14,000 deaths per year (possible range from 7,000 to 30,000) and it is the second leading cause of lung cancer in the United States. Therefore indoor radon is considered to be one of the most serious environmental threats to public health.

TABLE 1-3: Major characteristics of ^{220}Rn and its decay products (part of ^{232}Th decay chain).

Radionuclide	Half-Life	Alpha (MeV)	Beta (MeV)
Ra-244	3.66d	5.69, 5.45	
Rn-220	55.6s	6.29	
Po-216	150ms	6.78	
Pb-212	10.6h		0.33, 0.57
Bi-212 (64%)	1.01h		2.25, 0.55
Po-212	298ns	8.78	
Pb-208	stable		
Bi-212 (36%)	1.01h	6.05	
Tl-208	3.05m		1.79, 1.28, 1.52
Pb-208	stable		

Figure 1-1 illustrates the position of radon as a cause of death with respect to other causes collected from data reported by the 1990 National Safety Council reports (EPA 1992). Table 1-4 shows estimations for the possible number of deaths in a sample of 100 persons versus exposure to different levels of radon concentration. The expectations are based on the independent effects of radon compared to other risk factors, such as smoking. Smoking will significantly enhance the radon risk factor by several times. The sample is for adult persons; children may be at higher risk.

TABLE 1-4: The risk of exposure to annual radon levels.

Annual[a] Radon Level Bq/m^3	Sample of 100 People (possible deaths %)	Radon Risk (lung cancer) Compares to:
3700 (100 pCi/l)	(27-63)%	Having 2000 chest x-rays each year.
1480 (40 pCi/l)	(12-38)%	Smoking 2 packs of cigarettes each day.
740 (20 pCi/l)	(6-21)%	Smoking 1 pack of cigarettes each day.
370 (10 pCi/l)	(3-12)%	Having 500 chest x-rays each year.
148 (4 pCi/l)	(1.3-5)%	Smoking half a pack of cigarettes each year.
74 (2 pCi/l)	(0.7-3)%	Having 100 chest x-rays each year.

[a] modified from (EPA 1986)

Tables 1-5 and 1-6 show the risk of radon exposure for smoking and non-smoking populations and equivalent risks in terms of the possible fatality risks illustrated in Figure 1-1. Quantitative estimation of radon gas concentration is conventionally specified in terms of activity rather than mass. The activity concentration of radon gas in a specific volume is used to measure the amount of radon. Representation of the quantities of radon progeny in the indoor environment, however, is more complicated. The collective concentration of a mixture of short-lived radon daughters in air normalized to the mixture alpha decay energy is used to estimate the concentration of radon short-lived decay products. This quantity is called the "equilibrium-equivalent" decay product concentration (EEDC). It is customary to give the EEDC in terms of the individual decay product concentration utilizing measured half-lives and alpha decay energies. Based on ^{238}U decay chain data given by Browne and Firestone (1986), the EEDC can be written as,

$$EEDC_{222} = 0.106 x A(^{218}Po) + 0.513 x A(^{214}Pb) + 0.381 x A(^{214}Bi)$$

$$EEDC_{220} = 0.913 x A(^{212}Pb) + 0.087 x A(^{212}Bi)$$

where A is the activity concentration (Bq/m^3) of each decay product. Progeny with very short half-lives, such as ^{214}Pb in the ^{222}Rn EEDC and (^{216}Pb, ^{212}Po) in the ^{220}Rn EEDC, do not significantly contribute to the EEDC because of their very

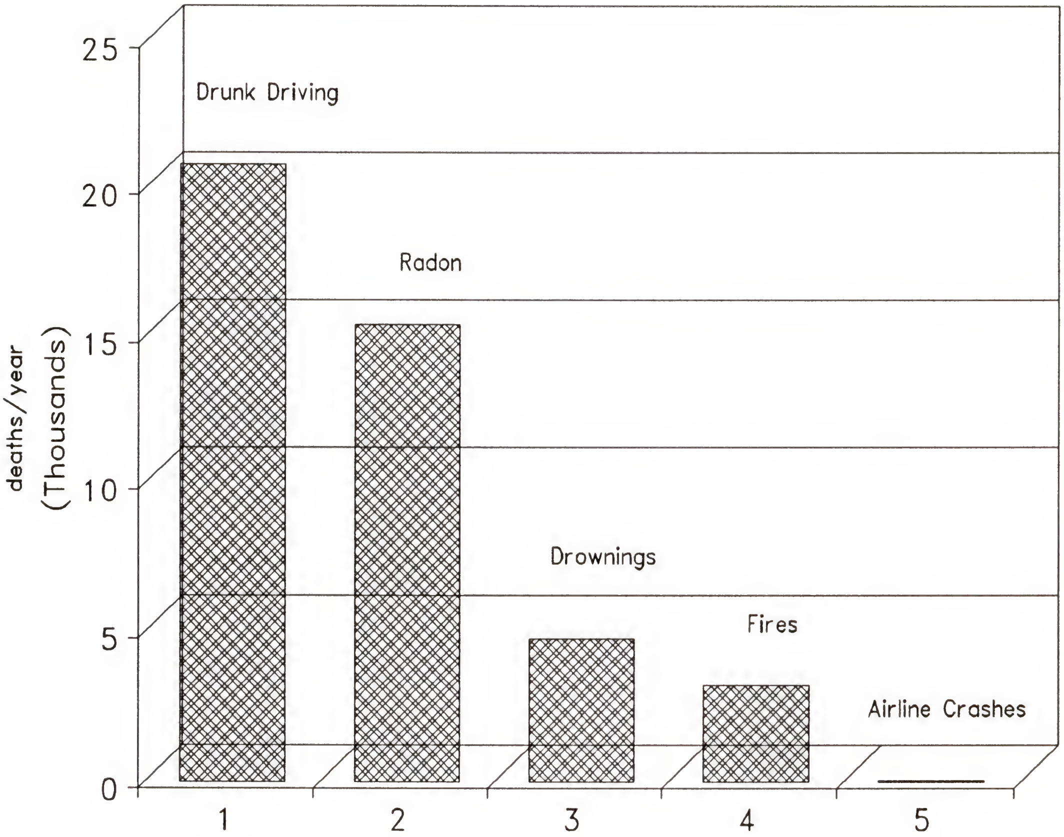

FIGURE 1-1: Estimation of fatalities per year attributed to indoor radon exposure and its relative position with respect to fatality causes. Modified From EPA 1992.

short life-time in the indoor air (Nero 1988).

The amount of each radon decay product that is required to produce the same potential alpha energy concentration (PAEC) has historically been used to describe the decay product concentration. The standard unit for this measure is the working level. The working level corresponds to the energy deposition for a specific volume and it relates the PAEC to the EEDC in SI units as,

$$\mathrm{PAEC}_{222}\ (\mathrm{J/Bq}) = 5.57 \times 10^{-9} \times \mathrm{EEDC}_{222}\ (\mathrm{J/m^{-3}})$$

$$\mathrm{EEDC}_{220}\ (\mathrm{J/Bq}) = 7.56 \times 10^{-8} \times \mathrm{EEDC}_{220}\ (\mathrm{J/m^{-3}})$$

When the time factor is introduced to the EEDC, the exposure from radon and its decay products can be estimated. Table 1-7 lists different parameters related to quantitative estimation of radon and its decay products in both SI and traditional units.

Usually, as the concentration of ^{222}Rn is significantly higher than that of ^{220}Rn, and within the scope of limited available data, some researchers have reported values of PAEC$_{220}$ decay product in buildings with average or below average ^{222}Rn concentrations which can be a significant fraction of the total PAEC. Further, the ratio of PAEC$_{220}$ to PAEC$_{222}$ can be in the range of 0.3 to 0.8 (Schery 1985, Toth 1984, Gumming and Scott 1982).

TABLE 1-5: Possible number of lung cancers and comparison of the risk of radon exposure for smokers.

Radon Level (Bq/m^3)	Possible Number of Lung Cancers per 1000 people (lifetime exposure)	Radon Exposure Risk of Cancer Compares to ...
740 20 (pCi/l)	135	100 times the risk of drowning
370 10 (pCi/l)	71	100 times the risk of dying in a home fire
296 8 (pCi/l)	57	80 times the risk of dying in a home fire
148 4 (pCi/l)	29	100 times the risk of dying in an airplane crash
74 2 (pCi/l)	15	2 times the risk of dying in a car crash
48.1 1.3 (pCi/l)	9	(average indoor radon level)
14.8 0.4 (pCi/l)	3	(average outdoor radon level)

If radon and all its daughters have the same activity, i.e., if they are in radioactive equilibrium, then the ratio of EEDC to radon concentration could be expressed as an equilibrium factor of one. However, it is believed that ^{222}Rn transport is dominated by pressure driven flow while ^{220}Rn transport is dominated by diffusion (Nero 1988). Expectations for the balance between purely diffusion and purely flow entry mechanisms, as well as other factors such as half life and abundance, generate an average ratio of ^{220}Rn to ^{222}Rn of several tenths to one (Toth 1984). These figures suggest that, in the indoor atmosphere, the total PAEC in indoor radon concentration is composed principally of ^{222}Rn and its decay products.

TABLE 1-6: Possible number of lung cancers and comparison of the risk of radon exposure for non-smokers.

Radon Level (Bq/m^3)	Possible Number of Lung Cancers per 1000 people (lifetime exposure)	Radon Exposure Risk of Cancer Compares to ...
740 20 (pCi/l)	8	the risk of being killed in a violent crime
370 10 (pCi/l)	4	half the risk of being killed in a violent crime
296 8 (pCi/l)	3	10 times the risk of dying in an airplane crash
148 4 (pCi/l)	2	the risk of drowning
74 2 (pCi/l)	1	the risk of dying in a home fire
48.1 1.3 (pCi/l)	<1	(average indoor radon level)
14.8 0.4 (pCi/l)	<1	(average outdoor radon level)

More evidence can be found in recent studies supporting the belief that ^{222}Rn is the major contributor to the radon health concern (NAS 1988). For this reason and other considerations such as the entry mechanisms, radon in this work shall refer to ^{222}Rn.

Radon Availability and Migration in the Soil

The ultimate source of radon is the uranium in geological materials. All rocks contain some uranium, with quantities estimated as (1-3) parts per million (ppm). The rocks break down due to environmental mechanical and chemical weathering factors to form soils at the earth's surface. The uranium content of the generated soils is about the same as in the forming rocks, i.e., about 1-3 ppm on the average. Building materials, for the same reason, contain some percentage of radium that is derived from predecessor radioisotopes in the earth materials. Earth materials such as light-colored volcanic rocks, granite, dark shales, phosphate bearing sedimentary rocks, and metamorphic rocks contain higher than average uranium percentages. These rocks and their soils contain as much as 100 ppm uranium (USDOI 1992).

Radon in soils can be classified into two fundamental categories relative to its conditions in the soil. Those categories are the availability of radon gas in the soil and the migration of the gas in the soil system. Each category consists of two states of radon in terms of its potential to the indoor environment. The availability of radon in soil consists of the radon generation state and the radon in soil pores state. The other category of radon migration in the soil system consists of the migration in the soil state and the entry into structure state. The conditions of which radon

TABLE 1-7: The mathematical equivalence of radon and its decay product parameters in SI and traditional units.

Parameter	SI Unit	Traditional Unit	Conversion (traditional to SI)
Activity	Bq	Ci	3.7×10^{10}
Concentration	Bq/m^3	pCi/l	37
PAEC	J/m^3	WL	2.08×10^{-5}
$EEDC_{222}$	Bq/m^3	WL(PAEC)	3740
$EEDC_{220}$	Bq/m^3	WL(PAEC)	276
Exposure	$J.s/m^3$	WLM	12.97
Exposure	$Bq.y/m^3$	WLM	73.9
Exposure	J/m^3	WLM/y	4.11×10^{-7}
Exposure	Bq/m^3	WLM/y	73.9

may be classified in soil are complicated and affected by many parameters. Radon can move from one state to another by transition processes that operate between two states. These processes are affected by many parameters, most of which are inter-related. Figure 1-2 A and B illustrates the radon state in the soil, the transition processes, and the factors affecting these transitions.

Radon is generated in the solid grains of the soil since it is formed from the radioactive decay of ^{226}Ra and the latter is a solid material. It must subsequently be transferred to the outside of the solid soil grain to have the potential to migrate. The transition process controlling this transfer is called radon emanation, and it is characterized by the radon

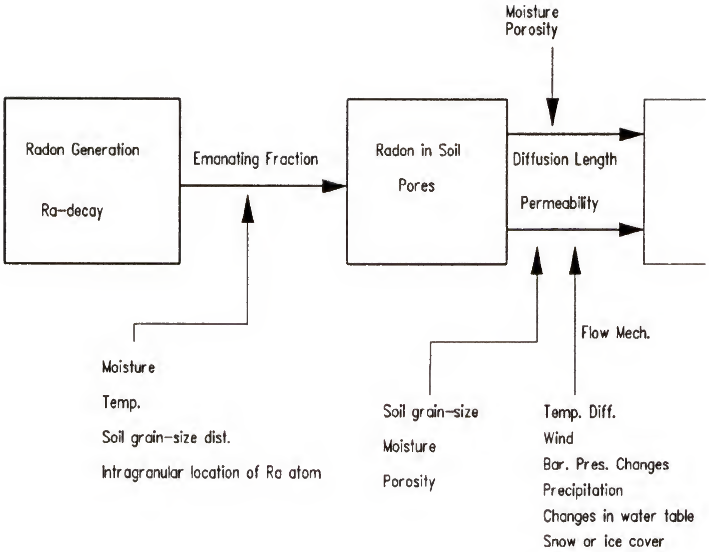
Moisture
Porosity
Radon Generation
Ra–decay
Emanating Fraction
Radon in Soil
Pores
Diffusion Length
Permeability
Moisture
Temp.
Soil grain–size dist.
Intragranular location of Ra atom
Flow Mech.
Soil grain–size
Moisture
Porosity
Temp. Diff.
Wind
Bar. Pres. Changes
Precipitation
Changes in water table
Snow or ice cover

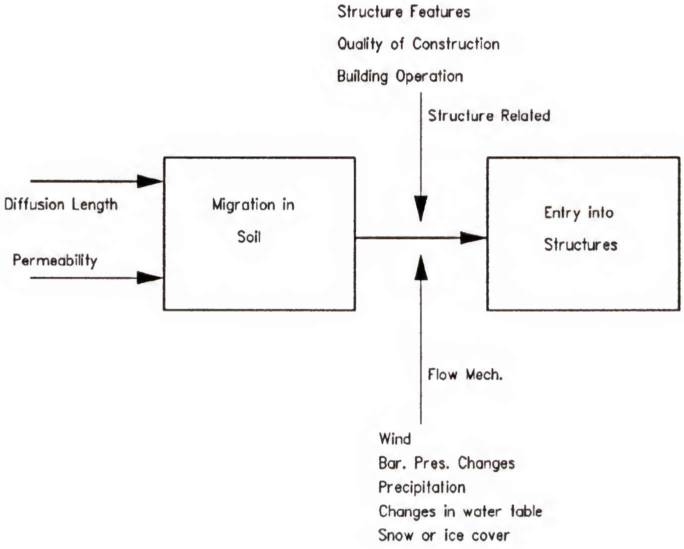
Structure Features
Quality of Construction
Building Operation
Structure Related
Diffusion Length
Permeability
Migration in
Soil
Entry into
Structures
Flow Mech.
Wind
Bar. Pres. Changes
Precipitation
Changes in water table
Snow or ice cover

FIGURE 1-2: (A) Illustration of the first two states of radon in the soil representing radon availability (above), (B) Illustration of the third and fourth states of radon in the soil representing radon migration (bottom).

emanation coefficient (it may also be called emanating fraction or power). After radon is emanated from the solid grain into the soil pore space, it enters the second state, radon in soil pores. Once radon enters the soil pores, it can be transferred into the third state, migration in soil, by transition processes controlled by its diffusion length and soil permeability. At the last stage radon becomes migratory and enters the fourth state, entry into structures, by diffusion and flow mechanisms.

For most soils, only 10-50 percent of the radon produced in the first state actually emanates from the mineral grain and enters the pore volume of the soil (USDOI 1992). Upon disintegration of ^{226}Ra, calculations based on the conservation of linear momentum, show that the radon atom recoils with an average kinetic energy of 86 keV (Bossus 1984). Depending on the relative position of formation and the direction of the recoil, the newly formed radon atom travels from its generation site in the solid grain until it loses its energy to the host materials. The host materials could be the solid grain of the formation, another solid grain, or materials confined in the soil pore, primarily water and air. The distance that the radon atom travel depends on the density and composition of the host materials. The range of radon atom transport in air is 63 μm and 0.1 μm in water (Tanner 1980). The transport range in water is approximately 600 times less than the range in air, and this fact will prove to be significant when the effect of soil water content on radon migration in the soil is considered.

The transition processes controlling the radon emanating fraction in the soil are affected by soil moisture, soil temperature, soil grain-size distribution, and the intragranular location of Ra atoms (Figure 1-2 A). Three components can be distinguished in describing the emanation of the radon atom from the solid soil grain into the surroundings. Those are direct recoil, indirect recoil, and diffusion components of the radon emanation coefficient. The direct component refers to the percentage of the recoiled radon atoms that terminate their paths in the soil pore spaces. The indirect component refers to the percentage of generated radon atoms that traverse through the soil pore space, penetrate another grain, and end their paths in that grain. The diffusion component refers to the recoil radon atoms that terminate their paths in the same solid grain where they formed and migrate into the pore space through molecular diffusion.

Among the factors that influence radon emanation, soil moisture content has been demonstrated to have a significant impact (Strong & Levins 1982). This effect can be easily seen through the significant reduction in radon atom recoil range from air to water. Fluid-filled soil pores contain most of the soil moisture. When the content of water in the pore space increases, the direct emanation coefficient component is increased since a greater fraction of the recoil radon atoms are trapped in the pore.

Soil moisture content consists of three components: gyroscopic, capillary, and gravitational. The last component represents the bulk of the water in the soil system that is affected by gravitational forces. The capillary component represents films of water around the solid soil grains that develop from the capillary properties of liquids with narrow channelling and surfaces. The gyroscopic component of soil moisture is derived from the electrostatic attraction between electrical charges on water and the solid soil grain. It consists only of a very small amount of the water in the soil and often is embedded within the solid soil grain. Most of the soil moisture effect is developed by the capillary component of soil moisture water. This component is responsible for generating water films around solid grain that act as a trap for recoiled radon atoms. The existence of water in excess of the capillary water will have a small effect on the radon emanation since most of the atoms are being stopped by the capillary water films. The gyroscopic component has only a minimal effect on emanation since it represents a very small percentage of soil moisture.

Once the radon enters the soil pore space, it becomes migratory. Soil permeability and diffusion length are the two factors affecting the transition of radon in soil pores state to the next state of migration in the soil. Soil permeability is the most important soil characteristic that affects indoor radon concentrations. This soil parameter measures how readily the soil gas, or generally a fluid, may flow through the soil. It is traditionally represented in units of area. The permeability of soils change significantly over the range of 10^{-7} m^2 for highly permeable soils, such as clean gravel, to values on the order of 10^{-16} m^2 for very low permeability soils such as homogenous clays.

Since soil permeability regulates fluid flow in porous soil media, it relates the flow with the pressure gradient. Customarily, intrinsic soil gas velocity is used as an indicator of the quantity of soil gas with regard to indoor radon concentration. The broad range of soil permeabilities make this parameter important to the transport of radon-rich soil gas from the sub-structure area into the indoor and consequently to the indoor radon concentration. Furthermore, because soil permeability is highly inhomogeneous, this parameter is difficult to model. At high permeability values, convective soil-gas transport becomes the dominant transport mechanism permitting increased radon entry and, generally, increased indoor radon concentrations. At low permeability values, convective flow is minimal and molecular diffusion transport of soil gas is dominant.

The second parameter regulating soil gas transport in the porous soil media is the diffusion length. Radon diffusion length in soil depends on both soil water content and soil porosity. Diffusion length is a characteristic parameter of radon diffusivity in the soil which is driven by concentration gradients and facilitated by molecular diffusion. It relates the radon diffusive flux to the radon concentration gradient. This relationship is governed by Fick's Law. When the latter relation is utilized, the mathematical representation of radon diffusion length is usually replaced by the radon diffusion coefficient.

In a porous medium, there are four formats of radon diffusion coefficient that can be used depending on the type of physical soil quantities utilized. A descriptive quantity of bulk versus pore volumes to determine concentration and bulk versus pore volumes to determine density results in a bulk and effective, or intrinsic, diffusion coefficient. The effective diffusion coefficient relates the gradient of the interstitial radon concentration to the radon flux density calculated across the pore soil area. The radon bulk diffusion coefficient relates radon flux density to the gradient of interstitial radon concentration calculated across a geometric or superficial area. When soil moisture increases, a high percentage of pore space is blocked, reducing the radon diffusion in the soil. Researchers have concluded that increasing soil moisture reduces the radon diffusion coefficient, while increasing the soil porosity increases the radon diffusion coefficient (Rogers et al. 1984).

The Indoor Radon Problem

The term "indoor radon" describes the existence of naturally radioactive radon (Rn) gas isotopes within a structure where humans usually live, work, or sleep. The indoor radon problem exists when elevated indoor radon concentrations are diagnosed in a residential, commercial, industrial, or recreational structure (Al-Ahmady et al. 1994). Although radon has always been present in nature, concern over indoor radon concentrations only began to arise in the 1980s. The highest indoor radon concentrations are associated with the development of living facilities and structures in which there has been increasing control of building interiors. Buildings are being made more and more isolated from the outdoors for various reasons, such as reduced energy consumption. However, these structures start to act as collectors and accumulators for radon gas that is drawn from the sub-structure soil area into the interior. When the interior ventilation is relatively restricted, the radon accumulation can become great enough to result in potential health problems.

The dominant part of natural radiation exposure during a person lifetime comes from inhaled radon and its decay products. Some researchers have indicated that about 55% of the average natural background radiation exposure may come from radon. Most of the remaining exposure derived from natural sources such as sun, air, water, soil and food (DOE 1986).

The accumulated dose from exposure to indoor radon is generated mainly from alpha particle decay, which has the highest quality factor for depositing its energy into living tissues. The collective concentration of a mixture of short-lived radon daughters in air normalized to the mixture alpha decay energy is used to quantitatively estimate the concentration of radon short-lived decay products.

The amount of each radon decay product that is required to produce the same potential alpha energy concentration may be used to describe the decay product concentration (Nero 1988). If radon and all its daughters have the same radioactivity, i.e., if they are in radioactive equilibrium, then the ratio of EEDC to radon concentration could be expressed as an equilibrium factor of one.

Sources of radon entry into structures are divided into three categories: sub-structure soil-gas, groundwater and structural materials. The contribution of structural materials to the indoor radon concentration is very small in residential structures such as single-family houses. It depends on the amount and type of building materials, and method of construction. Although the absolute contribution of building materials to an increased concentration of indoor radon may be significantly greater in large buildings than in small residential dwellings, the absolute contribution of this radon entry source is still considered small relative to the contribution of sub-structure soil-gas (Stranden 1988).

Groundwater can contribute to the indoor radon concentration when large amounts of radium are dissolved in potable water from radium-bearing geological materials, such as rocks. The groundwater contribution to the overall radon dose can be delivered by the inhalation of radon that is outgassed and becomes airborne during normal indoor water usage, or by the ingestion of radon-rich water into the stomach upon drinking of that water (Prichard & Gesell 1981, Suomela & Kahlos 1972).

Sub-structure soil-gas is the main source of radon entering structures and the major contributor to elevated indoor radon concentrations (Crameri et. al. 1989, Nazaroff et. al. 1988b, Nero & Nazaroff 1984). It is dependent on the radium content of the soil (usually one Bq/kg of radium yields radon at the rate of one atom/kg per second), and physical characteristics of the soil such as permeability, porosity, grain-size distribution and moisture content. Chemical properties and the possibilities of chemical reactions in the soil are not important here, because radon is an almost chemically inert gas and radioactive decay is not affected by chemical reactions.

The radon concentration in the ambient atmosphere (< 0.5 pCi/l) is so low that it is usually considered to be negligible. The indoor atmosphere is different, since the radon concentration can reach much higher levels when buildings act as collectors for the radon gas. At present, as with other radiations, there is no well-defined point at which to consider certain radon concentration levels to be dangerous. However, the U.S. Environmental Protection Agency (EPA) and several other national and international agencies recommend that action be taken if the radon concentration exceeds 148 Bq/m^3 (4 pCi/l).

Radon-Rich Soil-Gas Transport Into Structures

Radon is transported into structures such as residential houses from the surrounding materials. Radon can be transported into indoor atmosphere through cracks, holes, openings, and all other possible accesses into a structure. In fact, compared to the other radon entry sources (building materials and ground water), soil gas and its transport mechanisms comprise the most significant source and routes responsible for elevated indoor radon concentrations. In this research, the radon source term and the transport mechanism shall refer to the soil gas and its entry route.

Radon-rich soil gas can be transported and enter into structures through diffusion and convection processes. The molecular diffusion is driven by the radon concentration gradient between the sub-structure area and the interior. The most significant convective component of radon transport into the interior is due to the pressure-driven air-flow processes. Mechanisms which generate pressure gradients depend on environmental and indoor operational factors. The environmental factors that induce pressure differences include temperature differences, wind, meteorological conditions , and atmospheric pressure changes. The indoor operational factors can be divided into two parts: the human- and nonhuman-induced indoor operational factors. The nonhuman factors result from mechanically induced pressurization or depressurization of the indoor environment by household appliances, as well as heating, ventilation, and air conditioning (HVAC) systems. Other cases can be represented by the human-induced indoor operational factors, which are characterized by effects such as opening windows and doors.

Wind blowing directly toward a side of a structure may cause an increase in pressure at the structure's wall in order to conserve the change in the momentum initiated by the change of the wind velocity from the free stream to almost zero at the wall, neglecting the effect of the ground. However, wind-induced pressure differentials usually fluctuate rapidly and the determination of the fluctuation frequency has been considered an important parameter (Nazaroff et. al. 1988a). Van der Hoven (1957) utilized fourier transform analysis to obtain the frequency distribution of wind speed for a 100 m range. Fukuda (1955) had developed a theoretical treatment to obtain the wind-induced pressure frequency when such pressures are much smaller than atmospheric pressure.

The general scheme of characterizing the wind-induced pressures on radon entry can be connected to the soil permeability, the frequency of the developed pressure, and the magnitude of the developed pressure differential. More effects are expected to be observed when the frequency of the wind-induced pressure wave is long enough to propagate in the soil and large enough to produce a differential pressure across the structure slab and envelope.

Temperature differences between the indoor and the outdoors can cause air volume movements corresponding to the temperature gradient and, consequently, pressure differences. Further, temperature differences across walls separating air masses can cause pressure differences. The pressure differences also vary with the wall height. This phenomenon is known as the stack effect. Nazaroff et. al. (1987) performed experiments by inducing depressurization in two residential structures with basements to simulate the depressurization that can be generated by wind and temperature differences. They concluded that nearby soil pressure field and air movements are influenced by the temperature induced depressurization of the structures. They also reported the possibility that these effects may account for the higher than average indoor radon concentrations observed in these two houses with basements.

The stack effect results when air masses of different temperatures are separated by a wall, and can provide a pressure driven force to the convective component of radon transport into structures. This effect should exist principally at the wall-slab interfaces, causing a buoyant effect that draws air from the soil into the lower part of the structure and pushes it out through the upper part. It is believed that this mechanism increases outdoor-indoor pressure differences and increases indoor radon concentrations (Nero 1988, Nazaroff et. al. 1988).

Furrer et. al. (1991) reported a significant diurnal dependence between radon concentrations and meteorological conditions. They studied the dynamics of Rn transport from the cellar to the living area in an unheated house and found that strong, long term correlations between temperature differences and pressure differences exist between the indoors and outdoors. Experimental verification for this diurnal dependence is however in most cases profoundly affected by uncontrolled pressure changes across the structure shell due to natural and mechanical ventilation caused by the occupants activities and/or the utilization of the HVAC system.

Al-Ahmady and Hintenlang (1993a) have been utilizing an unoccupied full scale research house to characterize the temperature-driven pressure differentials. They utilized theoretical considerations of pressure differences induced between two zones of different temperature and noted a weakly exponential dependence to develop a mathematical treatment based on a linear approximation to the weakly exponentially dependent pressure difference between temperature zones under hydrostatic equilibrium. They demonstrated that the pressure differences induced by temperature differences between the indoor and outdoors are proportional to both the magnitude of the temperature differences and the average temperature between the indoor and outdoors.

The atmospheric pressure variation driven pressure differences are probably the most influential environmental parameter driving radon entry. Researchers have attributed the significant diurnal dependence of the radon concentration to meteorological conditions (Garzon et. al. 1986). Others have proposed that the transient atmospheric pressure changes associated with meteorological conditions can contribute to the radon transport terms (Tsang & Narasimhan 1991, Owczarski et. al. 1990, Clements & Wilkening 1974).

Al-Ahmady (1992a) presented the first experimental observations of the semi-diurnal atmospheric tidal barometric pressure variation as a continuous radon driving force, the natural pumping of radon, for slab-on-grade structures that were built on low permeability soil and fill materials. Hintenlang and Al-Ahmady (1992a) demonstrated that these naturally induced pressure differentials could continue to provide major contributions to radon entry when other sources of house depressurization or pressurization, and consequently outdoor air infiltration rates, are small.

The indoor operational factor pressure generating mechanisms have been investigated by researchers using both experimental and mathematical models. These factors are more difficult to address since they include the effects of the occupants. The irregular opening of windows causes a decrease in the pressure difference, as well as an increase in the infiltration air. Kozik et. al. (1993) studied the effect of interior door position on differential pressure in a slab-on-grade residential structure. These effects were characterized by replacing the structure HVAC central return with a ducted return so that the relative pressurization/ depressurization in the house may be observed. They concluded that by utilizing a ducted return air system the pressure differentials across the slab of the house can be equalized in the event that interior doors are closed.

Hubbard et. al. (1989) had studied radon gas dynamics in a house heated alternatively by an electric resistance heater and by forced air. The study concluded that heating and air-conditioning (HAC) systems have a significant impact on the pressure-driven radon rich soil-gas entry into houses. Hintenlang and Al-Ahmady (1993) studied the HVAC system effects on radon transport in Florida houses utilizing the same dedicated research structure mentioned earlier. They provided experimental evidence of reducing the natural pumping radon driving forces throughout the HVAC operation. Dyess et. al. (1993) applied previous observations to modify the air handling unit (AHU) design of a house HAC to reduce radon entry. The design method is simply executed by continuous operation of the AHU on low speed then switching to a higher speed in response to the heating/cooling. Continuous radon monitoring in the structure showed an average basement-to-outdoor differential pressure of 4 Pa, which is comparable to the semi-diurnal pressure differentials associated with the slabs of residential structures observed by other researchers.

Al-Ahmady et. al. (1993) developed the concept of the HVAC Unbalanced Pressurization Controller (HUPC) system for minimizing indoor radon concentration. The HUPC design was based on the experimental results obtained from continuous monitoring of indoor radon concentrations and house dynamics for a slab-on-grade structure. The concept satisfies both dependent functions of reducing radon entry and mitigating indoor radon concentration by providing slight pressurization to the house interior and maintaining specific indoor volumetric air changes by positive control of the system duct ventilation. Further investigations of the same structure have resulted in the development of a semi-empirical model that can be used to characterize the HVAC and other structure dynamics in modeling indoor radon concentrations (Hintenlang and Al-Ahmady 1994). A parametric study has demonstrated that increasing house ventilation rates created by increasing the effective leakage area of the house shell does not reduce indoor radon concentration as effectively as increasing house ventilation rates by controlled duct ventilation associated with the HVAC system.

Radon Mitigation Methods and Systems

Most practical techniques for reducing elevated indoor radon concentrations depend on the utilization of Active Soil Ventilation and Depressurization (ASV&D) systems. Although other methods have been developed to reduce and control elevated indoor radon concentrations, ASV&D systems are by far the most widely used and commercially available systems. The principle concept behind the operation of ASV&D systems is simple, as it depends on creating a low pressure area underneath the building structure. Radon-rich soil gas, the principle source of elevated indoor radon concentrations, may then be forced into the low pressure area and exhausted outdoors instead of sweeping into the building through openings between the sub-structure area and the building interior.

Four system designs (Drain Tile Ventilation, Block-Wall Ventilation, Isolation and Venting of Area Sources, and Sub-Slab Depressurization) can be distinguished based on the features of building structure (EPA 1988). Sub-Slab Depressurization (SSD) systems are the most effective and widely used ASV&D system. Due to their widespread use, simulation of their operation, incorporating different structural features, represents an important and useful tool serving radon education, control, and mitigation purposes. Simulation capabilities are particularly critical in analyzing the Pressure Field Extension (PFE) developed by the SSD system operation in different structures and for many design options. In addition, it is very useful for understanding the interaction between the PFE developed by an SSD system and the pressure differences across the structure slab which is the major radon driving force from the sub-structure area into the interior (Al-Ahmady & Hintenlang 1994c).

During SSD system operation, depressurization is developed under the foundation by drawing a suction on pipes installed into the soil/fill/aggregate area. The primary depressurization point is usually extended to cover larger volumes under the slab using highly permeable materials such as pit or a matting media. These media are connected to the end of the suction tube to provide better pressure field distribution and prevent blocking of the suction tube. The success of the SSD system is dependent on the extent to which negative pressure can be maintained under the slab area. This parameter is directly dependent on the pressure field extension developed by the system.

Modeling of the SSD system operation for residential structures has been developed. Simulation approaches for SSD operation in residential structures have been started from introductory considerations (Hintenlang & Barber 1991, Hintenlang & Furman 1990) and extended to more sophisticated modeling utilizing three dimensional spatial solutions for equations governing the generation of PFE in a soil system developed by SSD system operation (Hintenlang 1993).

Although simulation approaches for SSD modeling and system design in large structures such as hospitals, schools, and commercial buildings are the same in principle, applications for such activities are significantly more complicated due to the complexity of large structure foundations compared to residential ones. A mathematical modeling and a simulation approach for SSD systems dealing with radon mitigation applications in large buildings has been developed by Al-Ahmady and Hintenlang (1994c). Mitigation practices and documentation regarding reduction of indoor radon concentrations using SSD systems or any other radon mitigation systems in large structures are profoundly limited when compared with residential structures. Furthermore, the cost of installing radon mitigation systems in large structures is much more expensive, which suggests a strong need to use a simulation approach that helps to understand driving forces, analyze system performance, and produce a suitable system design prior to installation.

CHAPTER 2
MATHEMATICAL CONSIDERATIONS

Gaseous-Phase Radon Transport in Soils

The transport of radon from soil into structures can be described by convective and molecular diffusion components. The random molecular motion of a substance due to its concentration gradient is best represented by Fick's law as a diffusional flux density. The convective components of radon transport, which primarily result from pressure differentials, can be represented by Darcy's law.

In this chapter, the mathematical formulation describing radon concentration in the soil system is developed. As indicated in the previous chapter, radon may became a contributor to the indoor radon problem when it reaches the third state of its conditions in the soil and becomes migratory. Therefore, a differential volume in the pore air of the soil is considered for the following derivation. The derivation utilizes the differential volume approach to construct a radon concentration model and then integrate over the soil volume. The derivation also provides evidence to justify neglecting the radon diffusion transport component in some areas of this research. The mathematical formulation governing pressure generation in the soil system in response to forced convection is introduced. The latter treatment can be employed as the mathematical basis for designing some radon mitigation systems, particularly the Active Sub-Slab Depressurization Systems.

If a coordinate system is chosen at a certain position in the soil and remains stationary, then the molar flux density of gas species 1 in a mixture of two gases can be given relative to this coordinate as the following,

$$N_1 = f_1 \ (N_1+N_2) \ - C \ D_b \ \nabla f_1 \qquad (2\text{-}1)$$

where,

N_1 is the molar flux of gas 1 (moles/m^2s),

N_2 is the molar flux of gas 2 (moles/m^2s),

f_1 is the molar fraction of gas 1 in the mixture,

C is the molar concentration of the gas (moles/m^3),

D_b is the binary diffusion coefficient (m^2/s), and

∇ is the three-dimensional gradient operator.

In the above equation, the first term represents the convective transport component while the second term represents the molecular diffusion component relative to the mean convective velocity. It should be noticed that the diffusion component in the gas phase may be considered relative to other physical conditions such as mean temperature, mean pressure, and existence of other driving forces such as an electric field.

The mean pressure and temperature conditions correspond to pressure differences and temperature differences as the case of concentration differences is considered. The concentration difference is usually dominant in gaseous diffusion processes and the diffusion processes resulting from temperature and pressure differences are negligible relative to the concentration for applications encountered in this research. Therefore, the second term in the right-hand-side of Equation 2-1 is constructed based on Fick's first law, governing the relation between the concentration gradient and the diffusional flux density.

If the gas labeled as 2 is the soil gas and 1 is radon, then N_1 represents the molar flux density of radon. It is important to notice here that radon will be considered as a binary mixture in the soil gas. This neglects the effect of the transport of radon which may result from the diffusion of one or several other species in the soil gas. However, the effects of this multi-component diffusion in radon transport are minimal for soil-structure configurations dominated by the convective transport of soil gas (Nazaroff et. al. 1988).

For the purpose of this research, the assumption of a binary flow allows modeling using a suitable diffusion coefficient (D_e) instead of the binary diffusion coefficient (D_b). This coefficient covers the effects of the soil and near structure conditions. These conditions reduce the area through which radon may diffuse, as well as increase the average path length between points that radon may be transported. A consideration of an effective diffusion coefficient (D_e) will be sufficient here. Further discussion about multi-component diffusion may be found in references dealing with transport phenomena (Bird. et al. 1960).

The mole fraction of radon isotopes in the soil gas is nearly equivalent to the mole fraction of ^{222}Rn ($7.6x10^{-16}$ at 20 °C) which is small compared to the soil gas (Nazaroff et. al. 1988). Therefore, if the molecular diffusion of radon in the soil as a source of convection in the mixture is neglected, then N_1 can be neglected compared to the soil gas flux density N_2. Consequently, Equation 2-1 is reduced to,

$$N_1 = f_1 N_2 - C D_e \nabla f_1 \tag{2-2}$$

If the molar concentration of air (soil gas) remains constant in time and space then,

$$N_1 = f_1 N_2 - D_e \nabla C f_1 \tag{2-3}$$

or,

$$N_{Rn} = f_{Rn} N - D_e \nabla (C f_{Rn}) \tag{2-4}$$

where N is the molar flux density of the soil gas (air) in the soil pore space. It is customary to treat radon quantities in terms of activity since this is ultimately the major concern with regard to the radon health hazard. Terms in Equation 2-4 need to be multiplied by Avogadro's number (A_v) and the decay constant of radon (λ_{Rn}) to convert the molar flux density and molar concentration density into activity flux density and activity concentration density, respectively. Then,

$$A_v \lambda_{Rn} N_{Rn} = [f_{Rn} N - D_e \nabla f_{Rn} C] A_v \lambda_{Rn} \tag{2-5}$$

Dividing Equation 2-5 by the molar fraction of Rn in the soil gas yields,

$$\mathbf{A_f}(Rn) = A_m(Rn) \frac{N}{C} - D_e \nabla A_m(Rn) \tag{2-6}$$

where,

A_f(Rn) is the radon activity flux density (Bq/m^2s), and

A_m(Rn) is the radon activity concentration density (Bq/m^3).

Notice that N/C in the first term of the right-hand-side has units of velocity (m/s) and it is equivalent to the net soil gas velocity, so it can be replace by the symbol V,

$$\mathbf{A_f}(Rn) = A_m(Rn) \mathbf{V} - D_e \nabla A_m(Rn) \tag{2-7}$$

Equation 2-7 contains two transport terms, the first term (A_m(Rn)V) is the convective flux and the second term ($-D_e \nabla A_m$(Rn)) is the diffusive flux.

In order to apply Equation 2-7 in a complex soil system, assumptions have to be made. In fact, to account for the effect of the soil fill materials and near-structure conditions, an effective diffusion coefficient, has already been assumed. Further, these conditions increase the radon mean free path. This increase is not helpful for the soil porosity considerations which were assumed in developing the above equations, since radon atoms are assumed to be interacting with soil gas molecules (gaseous state). Fortunately, in the diffusion process inside the soil system, the pores are relatively larger than the applicable average radon mean free path which assures that the assumption is reasonable.

The dimensions of the pores are similar in size to the grain size. Since the required size should be comparable to the soil gas (compared to the air of 0.065 micrometer at 25 °C), the diffusion term in the equations can be applied to the soils of grain size on the order of approximately 0.065 micrometer or larger, which in fact, covers all soils larger than clays.

The porosity of the soil is affected by the soil water content. The diffusion term described above does not account for soil moisture and assumes dry soils and gaseous diffusion for radon only. In fact, only single phase diffusion was considered in the above treatment. In addition to the gaseous phase transport of radon in the soil, two other transport phases, liquid and solid may exist. Multi-phase radon transport might affect both diffusive and convective radon flux densities when parameters such as soil water moisture are considered. Since radon is an almost chemically inert gas and the average environmental temperatures are much higher than its condensing temperature, the diffusion process in the soil is dominated by the gaseous radon diffusion as a gas.

Radon transport by diffusion in liquid and solid phases therefore can be neglected for most practical applications. Support for this assumption can be found in experimental results, which show insufficient evidence to consider these effects important (Tanner 1980). However, treatments of the radon liquid and solid phase transport processes is a worthy effort in a uniform theoretical framework that would consider these processes simultaneously. Such a treatment shall be considered later in this chapter.

The dominant driving force for the convective radon transport component is the pressure differential. H. Darcy's experiments, which led to Darcy's law, describe the volume of interstitial fluid flowing per unit time per unit geometrical area as a result of an applied pressure differential, or the velocity vector. If the geometrical area in the soil, where the flow is defined, is small compared to the overall dimension of the soil and large compared to the individual pores, then the net superficial velocity vector can be given as,

$$\boldsymbol{V} = -\frac{[K]}{\mu}\nabla P \tag{2-8}$$

where,

[K] is the three-dimensional permeability matrix,

μ is the viscosity of the fluid, and

P is the pressure.

If the soil permeability is constant and isotropic, the three-dimension permeability matrix becomes the permeability coefficient, K. Further adjustments can be made by dividing V by the soil porosity ϵ, which is a dimensionless fraction representing the ratio of the air and water porosity to the bulk volume. Substituting V in the convective component of Equation 2-7, the superficial air velocity through the soil expressed in term of Darcy's law per unit pore area yields,

$$\boldsymbol{A_f}(Rn) = A_m(Rn)\frac{\boldsymbol{V}}{\epsilon} - D_e\,\nabla A_m(Rn) \tag{2-9}$$

Substituting Equation 2-8,

$$\boldsymbol{A_f}(Rn) = -A_m(Rn)\frac{K}{\mu\epsilon}\,\nabla P - D_e\,\nabla Am(Rn) \tag{2-10}$$

divided into two terms,

$$A_f^c(Rn) = -A_m(Rn)\;\frac{K}{\mu\epsilon}\;\nabla P \tag{2-11}$$

$$A_f^d(Rn) = -D_e\,\nabla A_m(Rn) \tag{2-12}$$

then,

$$\boldsymbol{A_f}(Rn) = A_f^c(Rn) + A_f^d(Rn) \tag{2-13}$$

where,

A_f^c(Rn) is the radon activity flux density per unit pore area due to convection, and

A_f^d(Rn) is the radon flux density due to molecular diffusion.

The nature of radon flux density removal mechanisms by both molecular diffusion and convection can be characterized by radon transport from a differential volume in a direction perpendicular to a volume surface area. The total radon diffusion from the differential volume can be calculated by integrating both fluxes over the total differential surface area. This integration is equivalent to integrating the divergence of these fluxes over the total differential volume, according to the divergence theorem,

$$\begin{aligned} \int_s A_f^d(Rn)\ ds &= \int_v \nabla A_f^d(Rn)\ dv \\ \int_s A_f^c(Rn)\ ds &= \int_v \nabla A_f^c(Rn)\ dv \end{aligned} \tag{2-14}$$

The limitation on $A_f^c(Rn)$ is determined by the dependence of Darcy's law on the Reynolds number. Usually Darcy's law starts to give incorrect results for high values of the Reynolds number. Scheidegger has given experimental evidence showing that applications of Darcy's law for Reynolds numbers smaller than 76 are acceptable (Scheidegger 1960). The typical pressure gradients in the soil due to airflow into structures results in Reynolds numbers much smaller than 76. Therefore, Darcy's law is approximately correct for radon transport applications.

A general transport equation that describes radon transport in the soil can be developed by considering the rate of change in the quantities of production, convective flow, molecular diffusion and decay. Under the limitations that arise from the application of Fick's law for molecular diffusion and Darcy's law for convective transport, the time rate of change in the radon activity concentration in the pore, for soils of low moisture content, can be written as

$$\int_{v} \frac{\partial A_m(Rn)}{\partial t}\, dv = -\int_{s} A_f^c(Rn)\, ds - \int_{s} A_f^d(Rn)\, ds - \int_{v} \lambda_{Rn} Am(Rn)\, dv + \int_{v} S\, dv \qquad (2\text{-}15)$$

where,

S is the volumetric radon source term in (Bq/m^3), and

λ_{Rn} is the radon decay constant (2.1x10^{-6} disintegration/s for ^{222}Rn).

The radon source term is the production of radon which occurs in the interstitial space of the soil and has free transport through the pore spaces. The production rate can be written as the following,

$$S = \left(\frac{1-\epsilon}{\epsilon}\right) A(Ra)\ \lambda_{Rn}\ f_e\ \rho_s \qquad (2\text{-}16)$$

where,

A(Ra) is the mass activity of radium concentration in the soil in (Bq/kg),

f_e is the emanation factor, the fraction of the radon that is generated in the soil and enters the pore volume,

ρ_s is the soil grain density in (kg/m^3), and

ϵ is the soil porosity. Substituting equations 2-11, 2-12 and 2-16 into 2-15 yields,

$$\int_v \frac{\partial A_m(Rn)}{\partial t}\, dv = \int_s A_m(Rn)\ \frac{K}{\mu\epsilon}\ \nabla P\, ds + \int_s D_e\, \nabla A_m(Rn)\, ds - \int_v \lambda_{Rn}\, A_m(Rn)\, dv + \int_v \left(\frac{1-\epsilon}{\epsilon}\right) A(Ra)\ \lambda_{Rn}\ f_e\, \rho_s\, dv \qquad (2\text{-}17)$$

Using Equation 2-14 for the total diffusion and convective integral terms results in,

$$\int_v \frac{\partial A_m(Rn)}{\partial t}\, dv = \int_v \nabla A_m(Rn)\ \frac{K}{\mu\epsilon}\ \nabla P\, dv + \int_v D_e\, \nabla^2 A_m(Rn)\, dv - \int_v \lambda_{Rn} A_m(Rn)\, dv + \int_v \frac{1-\epsilon}{\epsilon}\ A(Rn)\ \lambda_{Rn}\ f_e\, \rho_s\, dv \qquad (2\text{-}18)$$

or,

$$\frac{\partial A_m(Rn)}{\partial t} = A_m(Rn)\ \frac{K}{\mu\epsilon}\ \nabla^2 P + D_e\, \nabla^2\, A_m(Rn) - \lambda_{Rn}\, A_m(Rn) + \left(\frac{1-\epsilon}{\epsilon}\right) A(Ra)\ \lambda_{Rn}\ f_e\, \rho_s \qquad (2\text{-}19)$$

Equation 2-19 is the differential form of the general transport equation for radon transport in soil.

The equation can cover a certain area by integrating all terms over that specific area. Notice that the equation has time and space partial derivatives which make the analytical solution complicated. Equation 2-19 can be solved analytically for only simple geometries, requiring many assumptions. For realistic conditions numerical methods must be used.

Several assumptions can be made to simplify Equation 2-19; for example, the steady state solution is based on eliminating the time rate of change of the activity of radon concentration, i.e, the left hand side of Equation 2-19 becoming zero.

To examine the effect of each term in Equation 2-19, for particular applications, the molecular diffusion term can be simplified. An example would considers one dimensional (z axis) radon diffusion in soil without the effects of the structure, i.e., uncovered soil and low moisture content. If the radon activity concentration is assumed to be zero at the surface of the soil and the radon source is located at an infinite depth in the soil, then the radon activity concentration at depth z can be given by,

$$A_m^z(Rn) = A_m^\circ(Rn)\ (1-e^{-\frac{z}{l_{Rn}}}) \qquad (2\text{-}20)$$

where

$A_m^z(Rn)$ is the radon activity concentration at z,

A_m° (Rn) is the initial activity concentration, and

l_{Rn} is the radon diffusion length.

The radon diffusion length and the initial concentration can be given as,

$$l_{Rn} = \sqrt{\frac{D_e}{\lambda_{Rn}}} \qquad (2\text{-}21)$$

and,

$$A_m^\circ(Rn) = \frac{S}{\lambda_{Rn}} \qquad (2\text{-}22)$$

using Equation 2-16 results in,

$$A_m^\circ(Rn) = \left(\frac{1-\epsilon}{\epsilon}\right) f_e \, \rho_s \, A(Ra) \qquad (2\text{-}23)$$

Substituting Equations 2-20 and 2-23 into 2-12 yields,

$$A_f^d(Rn) = -D_e \, \frac{1-\epsilon}{\epsilon} \, f_e \, \rho_s \, A(Ra) \, \nabla(1-e^{-\frac{z}{l_{Rn}}}) \qquad (2\text{-}24)$$

and substituting Equation 2-21 into 2-24, for the one dimensional case, yields

$$A_f^d(Rn) = \frac{1-\epsilon}{\epsilon} \, f_e \, \rho_s \, A(Ra) \, \sqrt{D_e \lambda_{Rn}} \qquad (2\text{-}25)$$

The diffusive radon activity flux density per unit of geometric area is given by multiplying Equation 2-25 by the soil porosity ϵ,

$$A_f^d(Rn) = (1-\epsilon) \, \rho_s \, f_e \, A(Ra) \, \sqrt{D_e \lambda_{Rn}} \qquad (2\text{-}26)$$

The radon activity flux density is related to the radon activity concentration by Fick's law through the effective diffusion coefficient, as shown in Equation 2-12. The differential radon activity flux density from the molecular diffusion in Equation 2-26 is in fact, the application of Equation 2-12 on a solution, for $A_m(Rn)$, in the following partial differential equation. Describing the radon transport in soil by diffusion only,

$$\frac{\partial A_m(Rn)}{\partial t} = S - \lambda_{Rn} \, A_m(Rn) + D_e \, \nabla^2 A_m(Rn) \qquad (2\text{-}27)$$

Substituting Equation 2-16 into 2-27 yields,

$$\frac{\partial A_m(Rn)}{\partial t} = \left(\frac{1-\epsilon}{\epsilon}\right) A(Ra)\, \lambda_{Rn}\, f_e\, \rho_s - \lambda_{Rn}\, A_m(Rn) + D_e\, \nabla^2 A_m(Rn) \qquad (2\text{-}28)$$

Notice that Equation 2-28 is identical to Equation 2-19 except for the convective transport term being absent.

Applying typical values for ^{222}Rn in Equation 2-26 results in radon activity flux densities on the order of (10-20)x 10^{-3} (Bq/m^2s). Wilkening et al. estimated values of the mean ^{222}Rn activity flux density of approximately 0.015 Bq/m^2s, from data collected on widely spread regions (Wilkening et. al. 1972). Nazaroff et al. provided the radon activity flux, using typical values such as ρ_s=2.65x10^3 kg/m^3, f=0.2, ϵ=0.5, D_e= 2x10^{-6} m^2/s and radium mass activity of 30 Bq/kg, as 0.016 Bq/m^2s (Nazaroff et. al. 1988).

Multi-Phase Radon Transport in Soils

Multi-phase radon processes are involved in the generation of Rn atoms in the solid soil grains, soil liquid (water), and in the soil pore space. This generation particularly affects the radon emanation fraction between the first and second states of radon in the soil discussed in Chapter 1. However, all these factors could be included in the treatment by using a suitable radon emanation coefficient. Multi-phase radon transport in the soil also includes liquid and solid phases. Since this chapter is particularly concerned with the mathematical formulation supporting radon migration in the soil, the latter multi-phase effects are considered. A parametric approach can be utilized in treating transport phases separately and then relating their terms with coupled phase transfer functions (Rogers & Nielson 1991). Multi-phase transport considerations give rise to some physical phenomena related to radon that were not considered in gas phase radon transport treatment such as adsorption and absorption processes.

Radon can be adsorbed on the solid surface of soil grain where it can be transferred from the soil pore space. Neglecting the surface diffusion of adsorbed radon atoms, the time rate of change of the adsorbed radon activity concentration can be written as,

$$\frac{\delta A_m{}^s}{\delta t} = \frac{P\ (1-m)}{\rho}\ T_1 - \lambda_{Rn}\ A_m{}^s \qquad (2\text{-}29)$$

where,

$A_m{}^s$ is the adsorbed radon concentration in (Bq/kg),

m is the fraction of water saturation of soil pores,

P is the pore air gas pressure (Pa), and

T_1 is the transfer factor of radon from soil pore air (soil gas) into the soil solid surface (Bq/m^{2}s). Equation 2-29 represents the balance of radon activity concentration on the surface that is adsorbed by the soil grain in the pore space by the source and removal rates represented by the first and second terms in the right-hand-side, respectively.

The time rate of radon activity concentration density, A_{mw}, in the water-filled soil pore space can be written as,

$$\delta A_m{}^w = \nabla(D_w \nabla A_m{}^w) - \lambda_{Rn} A_m{}^w + \frac{R\rho\lambda E_w}{Pm} - \frac{R\lambda(1-P)}{K_{Ra}} + T_2 \qquad (2\text{-}30)$$

where,

D_w is the radon diffusion coefficient in a water-filled pore space (m^2/s),

R is radon concentration in the soil grain (Bq/kg),

E_w is the coefficient of radon emanation into the water-filled pores,

K_{Ra} is the radium equilibrium distribution coefficient in the solid-to-pore liquid (m^3/kg), and

T_2 is the radon transfer factor from pore air to pore liquid (Bq/m^3s).

Results from different researchers that characterize the transport of radon into structures through concrete slabs, show that the radon activity flux densities, which arrive to the indoor atmosphere, are 95% lower than expected values for uncovered soils under typical conditions (Nero & Nazaroff 1984, Landman 1982). In particular cases, accesses to the indoor atmosphere exist through cracks, holes and openings.

The radon activity flux density that penetrates into the indoor atmosphere would increase by a factor of several times. Typical factors of 4-8 times would be the case for (20-40)% of the uncovered radon activity flux. Even if 50% of the uncovered flux is transported to the indoors, the indoor radon flux would be in the range of approximately (5-10)x10^{-3} Bq/m^2 s. This figure, a greatly exaggerated entry rate, is still lower than what such entry could results in indoor radon concentrations found in many indoor atmospheres. This shows that the molecular diffusion of radon into the structure is insufficient to account for observed elevated indoor radon concentrations.

It is important to note that soil moisture may significantly affect the emanation coefficients and the effective diffusion coefficients. Furthermore, changes in the diffusion coefficients may occur for other reasons, such as the effects of the slab and foundation, as well as the change in radon concentration gradients between the sub-slab areas and the interiors. However, the overall effects, in most cases, tend to reduce the percentage of the uncovered soil diffusive radon flux that enters into the indoor atmosphere.

Pressure Distribution in Soil System

As pressure-driven transport has emerged as the most dominant contributor in driving sub-slab radon-rich soil-gas from the sub-structure area into the indoors, this section provides a mathematical treatment for the pressure field distribution that can be generated in response to forced pressure point(s) applied under the building slab. This framework also provides the mathematical basis to model the application of the Active Soil (or Sub-Slab) Depressurization (ASD) radon mitigation systems.

The time rate of change in position of a fluid particle in a porous medium can be expressed by the change in its velocity. If a differential volume, dV, in the soil is considered, the mass conservation equation of the soil gas in this volume can be established. In Cartesian coordinates, the net mass flow rate leaving the differential volume in a specific direction can be expressed by the change of the fluid velocity in the same direction. Neglecting the effect of gravity,

$$q_i = \rho \left(\frac{\delta v_i}{\delta_i}\right) dV \qquad (2\text{-}31)$$

where,

i defines the x, y, or z direction,

ρ is the density of soil gas (kg/m^3) and is assumed to be independent of gas position; i.e., constant,

q_i is the soil gas net mass flow rate (kg/s) in the i direction, and

dV is the differential volume (dx.dy.dz) in m^3.

A simple differential volume in Cartesian coordinates is a cube of six equal faces. Equation 2-31 expresses the net flow rate of the gas in the differential volume, that is, it compensates for the gas mass flow rate into the volume and the mass flow rate out of the volume. The net flow across of the six faces of dV can then be expressed as,

$$q_v = -\rho\left(\frac{\delta v_x}{\delta x} + \frac{\delta v_y}{\delta y} + \frac{\delta v_z}{\delta z}\right) dx\, dy\, dz \qquad (2\text{-}32)$$

The negative sign indicates that this mass flow rate algebraically contradicts the accumulation of the gas mass in the differential volume. Applying the mass conservation principle, the time rate of change of the soil gas mass in dV, the accumulation rate, must equal the net mass flow rate out of the volume. The mass of the soil gas in the differential volume can be expressed as,

$$dm = \rho\, \epsilon\, dV \qquad (2\text{-}33)$$

where dm is the soil gas mass (kg) and ϵ is the porosity. The time rate of change of m is then,

$$q_A = \frac{\delta m}{\delta t} = \frac{\delta \rho}{\delta t}\, \epsilon\, dx\, dy\, dz \qquad (2\text{-}34)$$

where q_A is the accumulated mass flow rate (kg/s) in the differential volume. To satisfy the mass conservation principle, the quantities q_A and q_V must be the same,

$$-\rho\left(\frac{\delta v_x}{\delta x} + \frac{\delta v_y}{\delta y} + \frac{\delta v_z}{\delta z}\right) dx\, dy\, dz = \frac{\delta \rho}{\delta t}\, \epsilon\, dx\, dy\, dz \qquad (2\text{-}35)$$

Considering the steady state situation, Equation 2-35 reduces to,

$$\frac{\delta v_x}{\delta x} + \frac{\delta v_y}{\delta y} + \frac{\delta v_z}{\delta z} = 0 \qquad (2\text{-}36)$$

This equation governs the spatial change in the soil gas velocity components. To represent the pressure under the slab for the purpose of estimating the PFE, Equation 2-31 can be employed to transform soil gas velocity into pressure. For an isotropic soil permeability, the expression for the velocity in Equation 2-31 is substituted into Equation 2-36, to yield,

$$\left(\frac{\delta^2}{\delta x^2} + \frac{\delta^2}{\delta y^2} + \frac{\delta^2}{\delta z^2}\right) . \ P = \nabla^2 P = 0 \qquad (2\text{-}37)$$

Equation 2-37 governs the steady state pressure condition in porous medium.

CHAPTER 3
EXPERIMENTAL DESIGN AND METHODOLOGY

Outlines for the Experimental Design and Methodology

There have been many previous experiments performed with regard to indoor radon in residential structures. Most of these experiments utilized experimental design and methodology to monitor and analyze a number of key parameters affecting the dynamics of indoor radon concentrations in occupied houses. However, a significant portion of the data collected from testing in occupied residential structures have shown unexplained fluctuations and large uncertainties. It was believed after years of experience that despite good cooperation of the house occupants with the experiments conductors to help insure appropriate measurements, the occupants' activities may have caused significant distortion in the monitoring conditions and systems.

Many experiments dealing with simultaneous measurement of indoor radon concentration, weather parameters, and other indoor environment occupancy parameters. There have been difficulties in tracking possible door and window opening, utilization of household appliances, and irregularities in using the structure heating, ventilating, and air-conditioning (HVAC) systems. Furthermore, detailed characterization of the structure and control over the range of experiment conditions and configurations were not possible most of the time. In summary, there was a significant need to utilize a controllable, unoccupied, and representative sample residential structure. Such a structure would facilitate flexibility in designing experiments and would provide the capability to fully control the indoor environment.

Once a selection criteria for a testing facility (next section) was determined, the overall measurement strategy required to facilitate the types of testing needed for this research is outlined in this section. Detailed descriptions of the type of measurement, measurement system, experimental procedure, calibration activities, and experimental error assessment are delivered in the following sections. Key parameters to be measured in this research can be divided into two major categories: non-radiological and radiological. The non-radiological parameters include pressure, temperature, humidity, air flow, wind speed, wind direction, and rainfall.

A type of measured parameter may conveys several measurements of the same parameter performed in different areas, different times, and/or different phonomania. Areas of testing consisted of the indoors (various locations), outdoors, attic, and sub-slab (sub-structure). For example, gage pressure measurements simultaneously collected between a location in the indoor area and a location in the sub-slab area can represent the time-dependent pressure variations at the location points, and the time-dependent differential pressure behavior between the indoor and the sub-slab at these testing locations. The radiological measurements include measuring radon concentrations in the areas mentioned above. Various systems are used to provide time-integrated and time-dependent radon measurements throughout this research.

The general measurement strategy is to perform experiments to measure simultaneously and continuously all radiological and non-radiological parameters of interest for this research using calibrated devices and systems. The data were collected by an industrial scale data acquisition and control system and controlled by a computer system.

Although continuous testing for all the parameter of interest was possible, the length of each test is limited by data storage (file size at the data acquisition system) and the memory size for the radon testing equipment. Although the data acquisition system used may collect and allocate large data files, the limit on size is established by a maximum of 1.44 M byte of the media disk to which the files were to be transferred for processing and analysis.

A typical testing period of 96-hour was utilized for most of the testing unless a specific need was established for longer or shorter time periods. This period was determined from the memory limit of the portable time-dependent measurement system (Pylon AB-5) used in this research for a sampling time interval of 10 minutes. Two approaches were utilized when testing periods greater than 96 hours were needed: adjusting the sampling time interval to larger than 10 minutes, or resetting the system between two testing minutes (during an 8-minute period) and re-run the experiment again. The data were then recombined using the common reference time. Equipment, devices, and systems were checked at the conclusion of each experimental period and calibrated as needed. If no mention of a specific testing period is made, the testing period utilized is 96 hours with a 10 minutes sampling time interval.

The next two sections of this chapter deal with the selection criterion that was utilized to select the UFRRH, and with the characteristics of the UFRRH. The rest of the chapter is divided into two parts; the first deals with the experimental design of the measurement, the measurement system, the conversion equation of the measured parameter, and the measurement procedure; the second part describes the data collection, data processing, calibration procedures, and assessment of experimental errors associated with the measurements.

Selection Criterion for A Research Site

Once it was decided to utilize unoccupied residential structure, a house selection criterion was developed for use in the selection process in the Gainesville (Florida) area and to insure reasonable representation of an average single-family residential structure. Implementation of the house selection criterion resulted in selecting the University of Florida Radon Research House (UFRRH).

The basic elements of the selection criterion applied in this work evaluated the house according to the following points:

(1) the living space floor area was specified to be between 140-233 square meters (1500-2500 square feet), to have sufficient slab structure to provide enough soil coverage for analyzing the interaction between the structure's sub-slab area and the building interior, to observe the effects on radon transport from the sub-structure area into the interior, and to simulate the average Florida single family house;

(2) the shape of the structure floor area was desired to be a simple rectangle or square to avoid the effects that may be developed as a result of irregular slab shapes;

(3) the structure foundation was required to be concrete slab-on-grade since this type represents most of the current construction practices in residential structures in Florida, as well as in large structures;

(4) the age of the structure was specified to be between 5 and 20 years since such age insures full development of slab cracks which may be a major path for air flow from the sub-structure area into the building interior;

(5) the surrounding area of the house was specified to provide reasonable isolation from disturbing conditions, particularly winds, with regard to indoor radon monitoring experiments. The house was selected in a highly wooded area which helped to significantly eliminate the effect of winds;

(6) the number of stories of the selected residential structure was specified to be one. The selection of a one-story house was designed to minimize the well characterized driving forces in multi-story residential structures such as the stack effect;

(7) the soil gas radon concentration was specified to be as high as possible, greater than 5000 pCi/l (185000 Bq/m^3), to provide a strong radon source term for the experiments and to facilitate a wide range of testing possibilities for both sub-slab and indoor radon concentrations.

The University of Florida Radon Research House (UFRRH)

Figure 3-1 shows the selected University of Florida Radon Research House floor plan. The UFRRH is a single-story residential structure and has a living floor area of approximately 163 m^2. It utilizes a floating concrete slab-on-grade type of construction contained by a concrete block stem wall and having a 10.1 m x 16.2 m footprint. It was built with a wood frame structure and concrete block walls that incorporates a family room, a living room, a kitchen, three bedrooms, two bathrooms, six closets, and a two car garage. Table 3-1 summarizes the basic characteristics of the UFRRH.

The house air handling system consists of a 12310 watts (3.5 ton) capacity air-conditioner with condensing unit located outside the house and a central forced air gas furnace unit lactated in the garage. The attic area of the house is vented and equipped with R-19 insulation. Both supply and return ducts are installed in the vented attic area. The return air is collected by a central register located in a central hall closet. The closet and the hallway act as the return plenum. A single 0.03 meter thick fiberglass rectangular trunk line of duct-board feeds the supply air into individual room.

FIGURE (3-1): The plan view of the University of Florida Radon Research House (UFRRH). Points 1-16 represent the locations of sub-slab tubes.

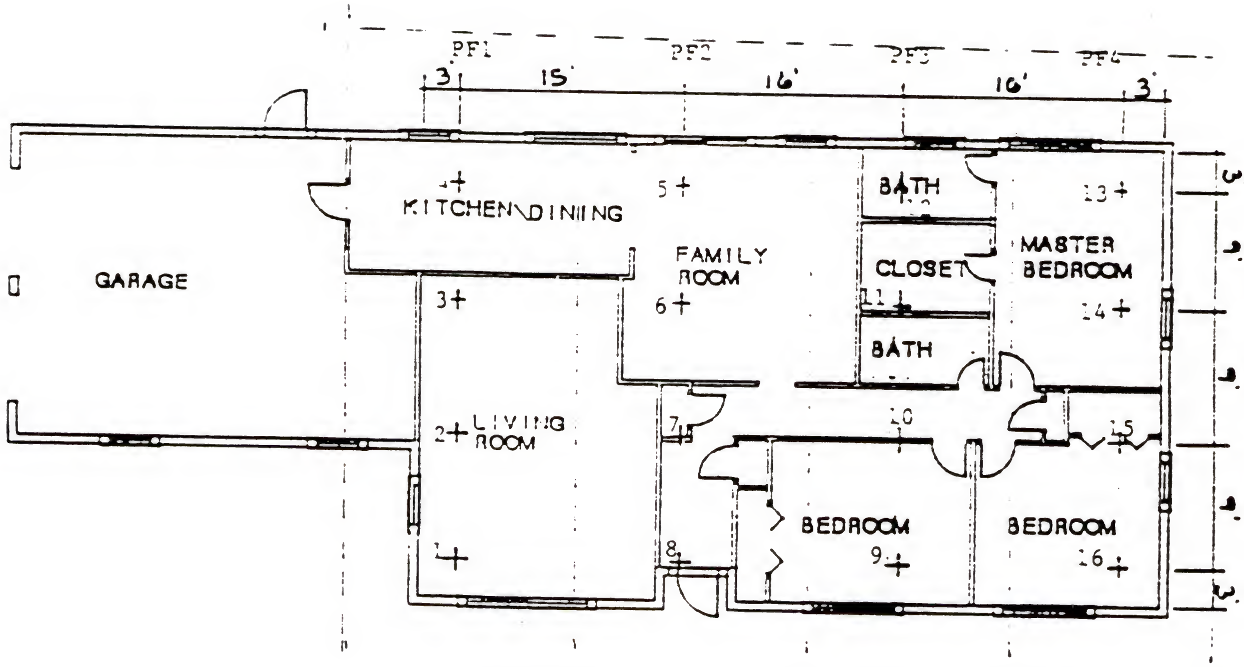
PF1
PF2
PF3
PF4
3
15
16'
16'
3
GARAGE
KITCHEN\DINING
FAMILY ROOM
LIVING ROOM
BATH
CLOSET
BATH
MASTER BEDROOM
BEDROOM
BEDROOM
1
2
3
4
5
6
7
8
9
10
11
12
13
14
15
16

FIGURE 3-1: The plan view of the University of Florida Radon Research House (UFRRH). Points 1-16 represent the locations of sub-slab tubes.

Non-Radiological Measurements

Pressure Measurements

Continuous time based measurements were designed to measure the time and spatial dependent responses of pressure, temperature, humidity, air flow, power consumption, and weather parameters. The house slab was divided into four pressure fields. Each field has four sub-slab access holes (parallel to the slab width) drilled through the approximately 9 cm. thick concrete slab. The holes have durable 4.76 mm (standard 3/16 inches I.D.) brass tubes which provide access to various points in the sub-slab area. These holes permit the measure of the differential pressure across the slab and the generation of sub-slab differential pressure maps. In addition, individual hole permits simulation for a point in sub-slab area for the purpose of providing access to perform temperature, pressure, air flow, and immediate sub-slab radon concentration measurements.

To provide pressure differential maps with reasonable resolution, 16 holes were made across the house slab in a uniform 4.87x2.74 meter grid pattern. The brass tubes penetrating the slab were connected to very sensitive current output differential pressure transmitters (Setra C264) via flexible nylon tubes. The transmitters operate with a full scale range of ∓25 Pa and have a minimum sensitivity of less than 1% (±0.25 Pa).

TABLE 3-1: The characteristics of the University of Florida Radon Research House (UFRRH).

Item	Value
Location	2418 NW 64th Terrace Gainesville, Florida
Slab Type	float Concrete slab-on-grade, no edge insulation
Foundation Type	concrete block
Frame Structure	wood (lined with concrete block walls on the outside)
Indoor Air Volume	approximately 400 m^3
Living Floor Area	approximately 163 m^2
Exterior Walls	0.2 m thick concrete block
Exterior Wall Insulation	R-5
Adjacent Walls	wood frame 0.48 m span
Adjacent Wall Insulation	R-11
Windows construction	single pane with metal frame
Interior Doors	solid core wood
Sliding door	metal frame and glass door in the family room
Air Change Rate per Hour @ 50 Pa	7.8
Air Conditioner	General Electric, 12310 watts condensing unit
Blower	direct drive 372 watt
Gas Furnace	GE, input capacity 1.6×10^8 J/hr, bonnet capacity 8.44×10^8 J/hr
Natural Ventilation (HVAC operational)	7.09×10^{-3} m^3/s
Radon Entry Rate (all systems off)	approximately 6.8 Bq/s
Average Indoor Radon Concentration	approximately 41 pCi/l (1517 Bq/m^3)

These pressure transmitters provide a standard output current of 4-20 mA. All transmitters are installed in parallel circuits where each unit regulates a current flow reflecting the value of the pressure difference that existing between the transmitter high and low pressure ports. The low pressure ports were left open to the house interior. Therefore, the indoor pressure was used as the reference pressure. Since the transmitter operates in differential mode, its calibrated operating point is located at 12 mA. The transmitter then decreases the current flow if the pressure on the low port is higher than the pressure on the high port and vice-versa. Figure 3-2 illustrates the operating range of the pressure transmitters and the linear equation used during data processing and calibration.

Transmitter outputs are collected by analog voltage input channel boards (MAI-16) installed within a Keithly Metrabyte micro-channel industrial scale data acquisition and control system. The transmitter current output was converted into voltage across the board input channel port by using high precision <1% shunt resistors. The interface between the Metrabyte system and the computer is provided through a driver board (μCMDB-64) responsible for generating and addressing the control data and pointer signals of the system. The Metrabyte system is interfaced and fully controlled by an IBM PS/2 computer system. A multi-connector ribbon cable type bus provides all required control signals, power signals, and data

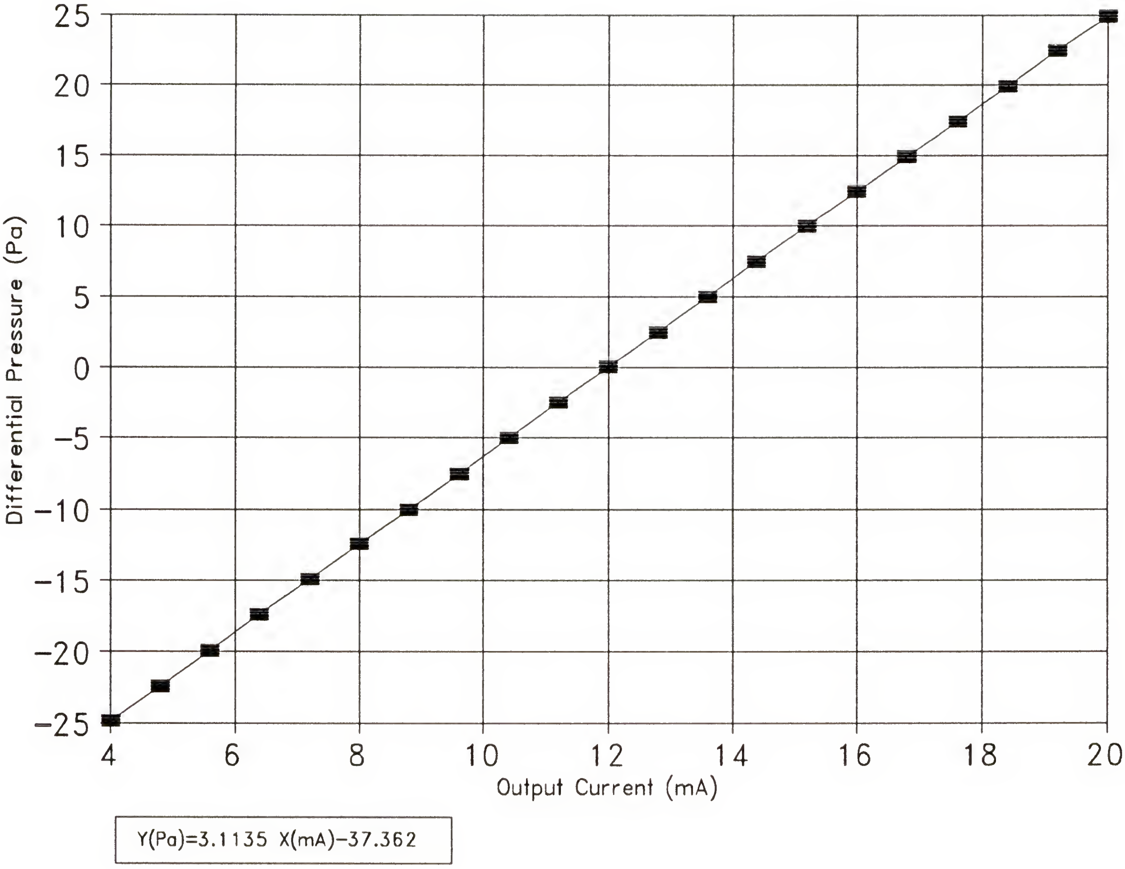

FIGURE 3-2: The correlation between the pressure transmitter (C264) signal output and differential pressure.

transfer between the system driver board and the input/output boards of the system.

The differential pressure measurements across the house shell were performed by measuring the differential pressure across the walls (outdoor to indoor differential pressure) of the house. Three sides (north, west, and east) of the UFRRH were covered for these measurements. The fourth side was not monitored because it is adjacent to the garage and the measurement would not have represented the indoor/outdoor pressure difference across that wall. The same low sensitivity pressure transmitters were utilized in these measurements and their circuits were integrated into the Metrabyte system in a manner similar to the transmitters monitoring pressure differentials across the house slab.

Pressure differential measurements across the UFRRH shell could also detect the effect of temperature difference driven pressures that might exist between the indoor and outdoor. The measurements are also sensitive to pressure differences that might be generated from winds blowing on the house shell as a result of the change in the wind air flow velocity at the exterior surface of the house walls.

The two sets of possible pressure differentials that might be generated, from temperature and wind effects, and monitored by the system can be distinguished by examining the phase shift in the reported values across two opposite walls of the house and the values of wind speed and direction reported by a weather station installed at the site. Measured pressure differentials that provided by wind may pick up a dynamic component developed by the wind gusts in addition to the static component developed by the hydrostatic pressure. The effect of wind gusts was dampened by using a hollow, spherical perforated ball to cover the outside end of the brass tube which penetrates across the house wall.

The inside end of these tubes was connected to a T-type plastic section via flexible nylon tubing. This arrangement allowed a triple pressure difference to be monitored by the system. Three pressure transmitters were utilized at these locations. Pressure differences were monitored between the indoor and outdoor, the indoor and sub-slab, and the outdoor and sub-slab. Figure 3-3 illustrates the three pressure differential connections near the three sides of the UFRRH walls.

Figure 3-4 shows the electrical block diagram for the pressure transmitters. The transmitters were connected to the system using an Omega switch board to provide flexibility during calibrations or to collect the measurements at specific slab test point. All pressure transmitters were zero-checked at the beginning of each experimental period and calibrated monthly according to the procedure described in a later section.

The indoor pressure was reasonably uniform throughout the house interior when all the doors were opened; therefore, the differential pressure map across the slab represents the spatial variation of the air pressure immediately below the slab.

Barometric pressure was measured at the UFRRH site and also obtained from the National Climate Data Center (U.S Department of Commerce). The latter source of weather data for the Gainesville area are collected from measurements at the Gainesville Florida Flight Service Station (FSS) located at the Gainesville Airport.

Barometric pressure measurements at the UFRRH was performed by installing a high accuracy symmetrical ceramic deformable capsule Setra (model 276) barometric pressure transducer system. The range of the transducer spans barometric pressure values from 600 to 1100 mbar. It operates on single mode voltage circuity that generates an industrial standard output voltage of 0-5 VDC.

The electrical circuit of the barometric pressure transducer is equivalent to a 4-terminal network which can be grounded at only one point, either at the negative excitation or the negative signal output lead. The circuit was integrated into an analog voltage input channel I/O board within the Metrabyte data acquisition and control system. All barometric pressure measurements were collected simultaneously with other differential pressure, temperature, humidity, and air flow measurements. Single mode circuitry was utilized with a floating operating point corresponding to the barometric pressure value at the time of the system operation. Figure 3-5 illustrates the range of the barometric pressure transducer and the linear equation utilized to convert the voltage readings into the equivalent engineering unit (bar).

Barometric pressure data from the National Climate Data Center for the Gainesville area was collected from the FSS station which is located 12.5 km from the UFRRH site. The spatial variation of barometric pressure (typical gradients are on the order of 1 Pa/km) (Blair & Fite 1965) produces a difference of less than 0.1% at the research house site compared to the typical values of the barometric pressure (on the order of 0.1 MPa) measured at the FSS station. This fact justifies the use of FSS data during the early stages of this research.

Temperature and Humidity Measurements

Temperature was regularly measured in each room, room register, supply and return ducts, HVAC thermostat location, attic and outdoors in most of the measurements. On a smaller scale, some experiments were designed to utilize temperature measurements collected at particular points, such as at one of the sub-slab tubes. All temperature measurements were performed by using T-type (copper vs. copper-nickel) thermocouple wires. This type of thermocouple wire was selected because of its resistance to humidity (bare wire) and the linearity between the signal output and the temperature

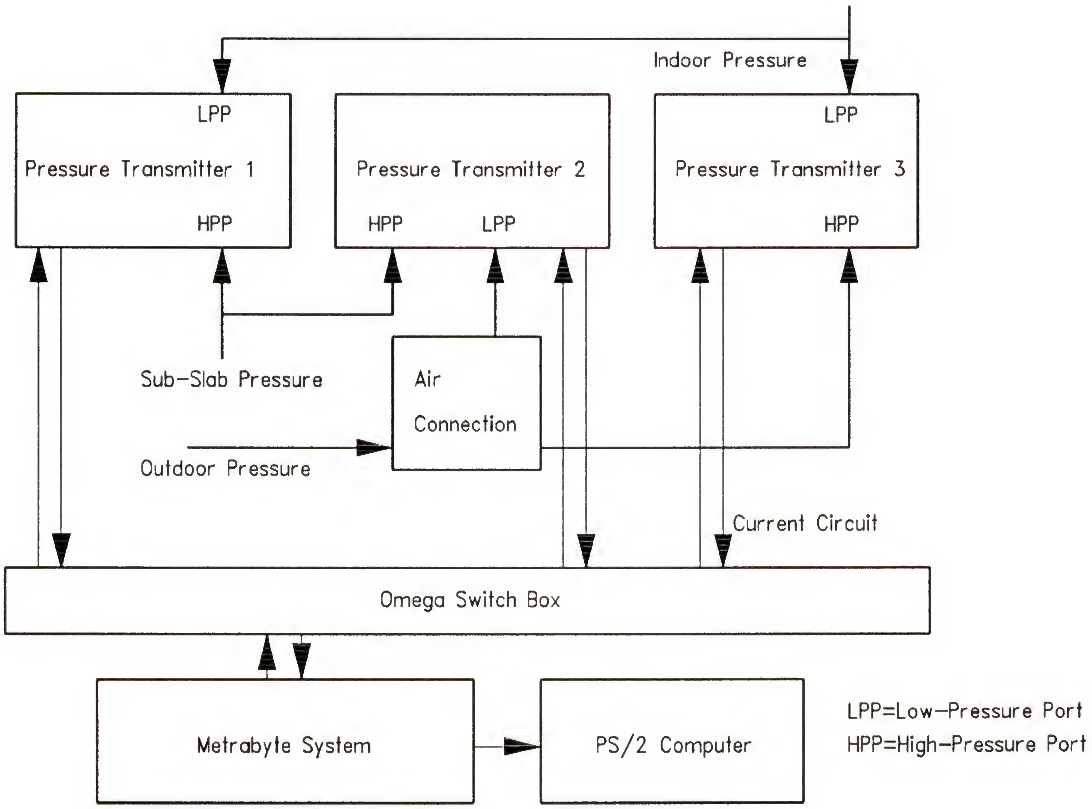
Indoor Pressure
LPP
Pressure Transmitter 1
HPP
Pressure Transmitter 2
HPP
LPP
LPP
Pressure Transmitter 3
HPP
Sub-Slab Pressure
Air
Connection
Outdoor Pressure
Current Circuit
Omega Switch Box
Metrabyte System
PS/2 Computer
LPP=Low-Pressure Port
HPP=High-Pressure Port

FIGURE 3-3: An illustration to the triple-junction connection for pressure difference measurements at the UFRRH.

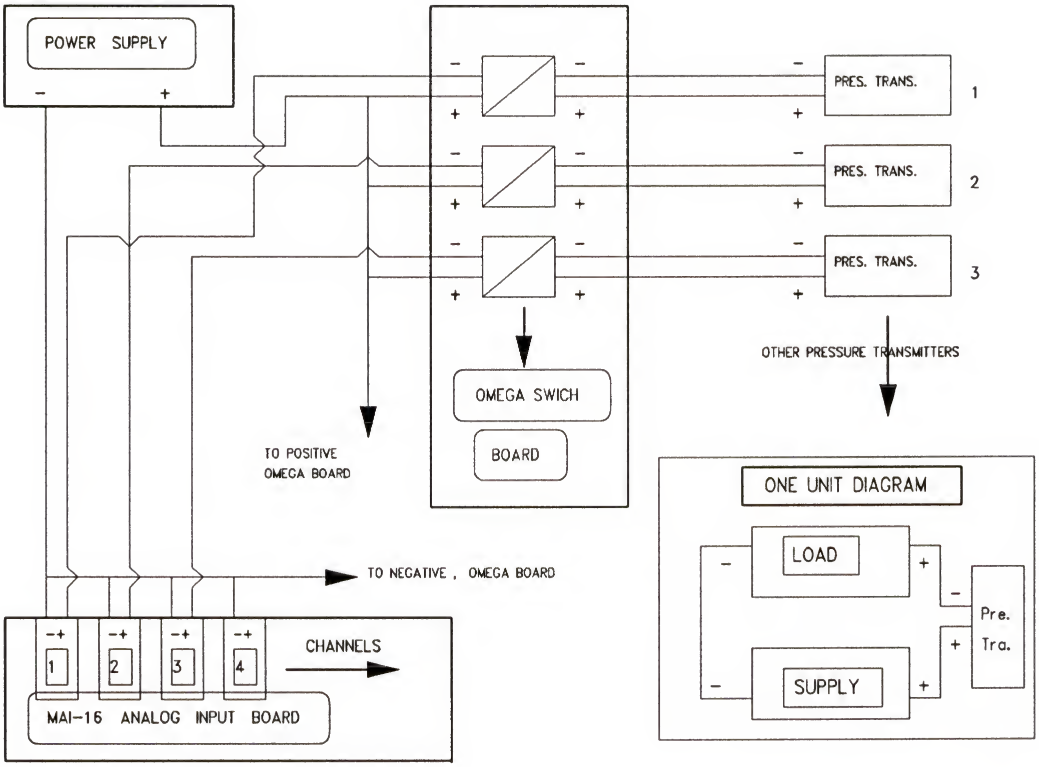
POWER SUPPLY
–
+
–
+
PRES. TRANS.
1
PRES. TRANS.
2
PRES. TRANS.
3
OTHER PRESSURE TRANSMITTERS
OMEGA SWICH
BOARD
TO POSITIVE OMEGA BOARD
TO NEGATIVE , OMEGA BOARD
CHANNELS
1
2
3
4
MAI–16 ANALOG INPUT BOARD
ONE UNIT DIAGRAM
LOAD
SUPPLY
Pre. Tra.

FIGURE 3-4: An illustration of the electrical block diagram of the differential pressure measurements at the UFRRH.

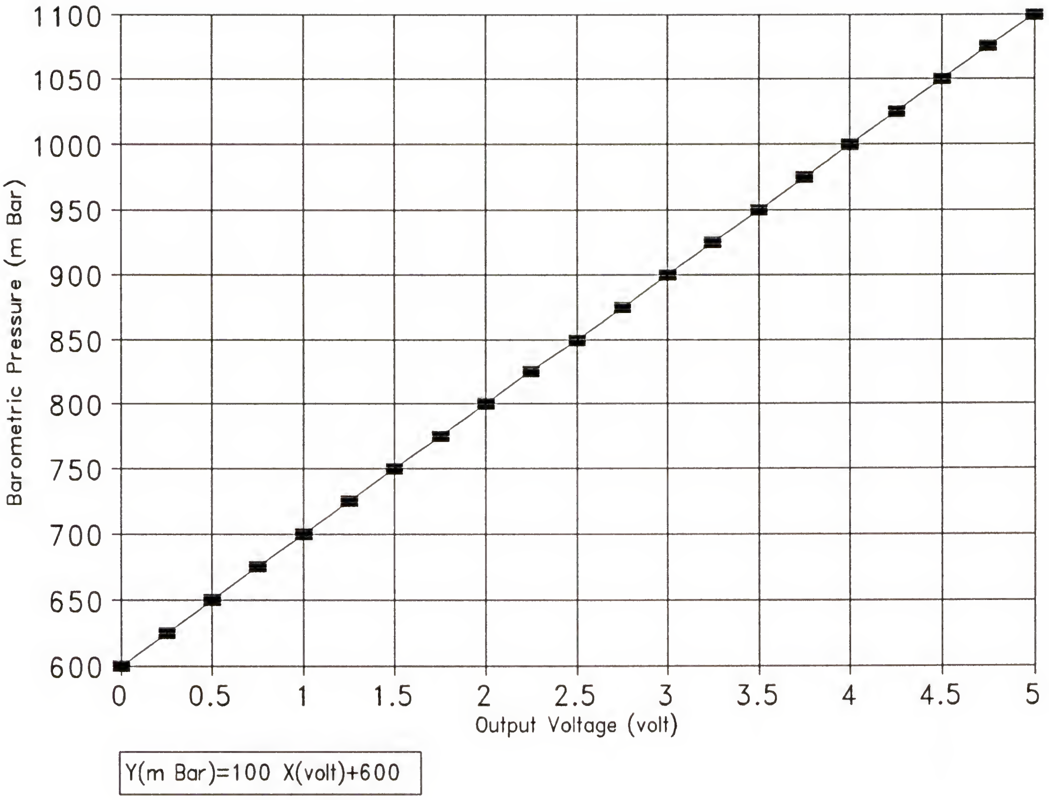

FIGURE 3-5: The linear correlation used for calculating the barometric pressure value at the UFRRH from the setra 270 barometric pressure transducer.

degree for low temperature ranges such as those encountered in residential structures.

T-type thermocouple wire can be used to measure temperature ranges from -200 to 350 °C (-328 to 662 °F) on thermocouple grade and from -60 to 100 °C (-76 to 212 °F) on extension grade. Therefore, it is suitable to the temperature measurements at the UFRRH. Unlike current signals collected from the pressure transmitters (which were connected to the Metrabyte system) through the switch box, all thermocouple wires were directly connected to analog input boards on the Metrabyte system.

The boards utilized for temperature measurement (Keithly MTHERM20) thermocouple input boards were specifically manufactured for temperature measurements. The thermocouple current signals were automatically converted into temperature degrees by the system boards. The cold junction temperature was regularly calibrated at the beginning of each measurement period.

Temperature was also monitored in the supply and return ducts and on two walls, in the living room and in the hallway near the HVAC thermostat location. Measurements at both walls were performed by the utilization of transmitters which continuously monitor two parameters. Each of these transmitters has two channels providing simultaneous measurement of the humidity as well as temperature. Two models, duct mounted (HMD 30 UB/YB) and wall mounted (HMW 30

UB/YB), Vaisala relative humidity and temperature transmitters were used.

These transmitters achieve high accuracy in humidity measurement by sensing a capacitance change in a micron thin polymer layer as it absorbs water vapor. This polymer is also unaffected by most dust and chemicals that might exist in the duct system or in the indoor environment. Both duct and wall mounted transmitters supply a standard output current of 4-20 mA. The output signals were connected an analog input board on the Metrabyte system through high accuracy shunt resistors. Figures 3-6 A and B illustrate the operating range of relative humidity and temperature transmitters and show the linear equations used to calculate the equivalent engineering quantities from the reported output converted signals. Figure 3-7 illustrates the block diagram of the temperature and relative humidity measurements at the UFRRH.

Flow Measurements

Two types of air flow measurements were performed. The first type of measurement covered the simultaneous monitoring of air flow in the duct system. These measurements utilized air flow transducers that were integrated with the Metrabyte data acquisition and control system. The second type of measurements consisted of individual tests of air flow in each register, and other areas in the house, during characterization of the structure leakage and ventilation.

For the continuous type of measurement, Kurz linear air velocity transducers (model 435DC) were used. A stand-alone module was utilized to produce minimal disturbance to the air flow in the duct.

These air flow transducers provide high accuracy measurement through two reference-grade platinum windings on an epoxy coated ceramic material, one acting as a mass velocity sensor winding and the other acting as a temperature-compensation winding. The latter winding senses the ambient temperature of the flowing gas and corrects the mass velocity sensor winding so that it is maintained at a constant 70-degree overheat.

The amount of current needed to maintain the overheat regulates the mass flow signal output. The unit supplies industrial standard analog output voltage of 0-5 VDC. All signals are inherently corrected to standard conditions of 25 °C and 760 mm Hg. All output signals were connected to analog input channels on the MAI-16 Input board controlled by the Metrabyte System. Figure 3-8 shows the linearized output voltage curve utilized during calibration and to calculate the corresponding flow reported by transducers output voltage signals.

The non-continuous air flow measurements were performed by using air balancing instruments such as Alnor Balometer. This device provides direct readings of the average air flow rate for either supply or return diffusers, with flexibility

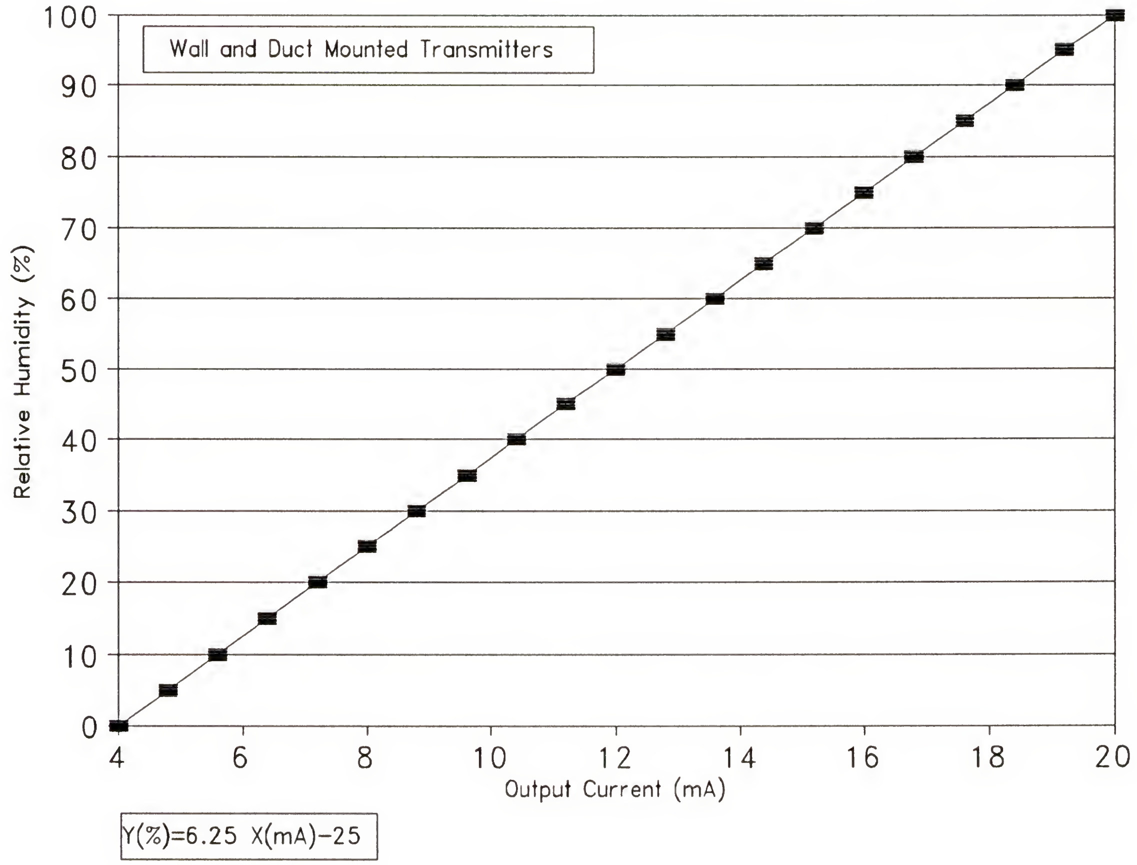

FIGURE 3-6 A: The operating range and linear correlation for relative humidity measurement at the UFRRH.

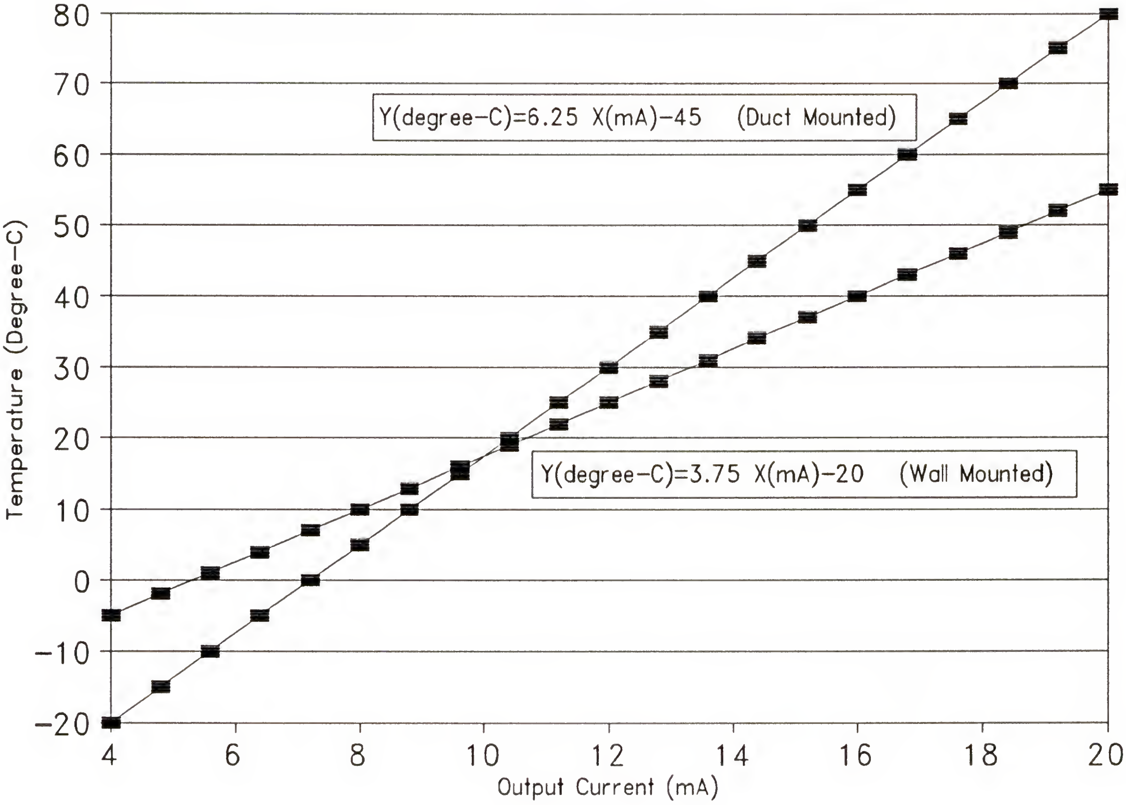

FIGURE 3-6 B: The operating range and linear correlation for duct and wall temperature measurements at the UFRRH.

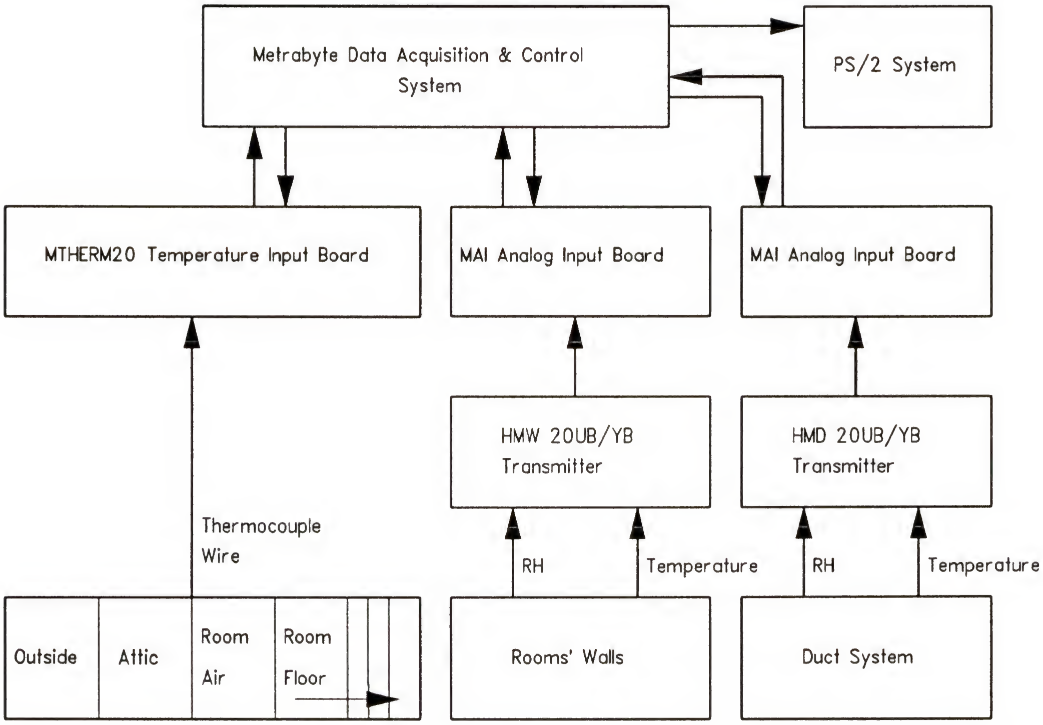
Metrabyte Data Acquisition & Control System
PS/2 System
MTHERM20 Temperature Input Board
MAI Analog Input Board
MAI Analog Input Board
HMW 20UB/YB Transmitter
HMD 20UB/YB Transmitter
Thermocouple Wire
RH
Temperature
RH
Temperature
Outside
Attic
Room Air
Room Floor
Rooms' Walls
Duct System

FIGURE (3-7): The block diagram of temperature and relative humidity measurements at the UFRRH.

for use on the ceiling, wall, or floor. The system eliminated the need for using multi-point velocity measurements to determine the averaging and area calculations. Such system forces the air into a manifold which senses flow (on two sides depending on the supply or return) at 16 points through the hood assembly. The system also provides meter readings in three ranges that cover flow rates from 0 to 1400 CFM. This system was utilized to characterize the HVAC system operation and to follow-up with changes in air flows due to modifications and control on the HVAC configuration.

Leakage and Ventilation Measurements

Mechanically induced indoor pressure conditions are produced by using a blower door. A blower door (Minneapolis) with a calibrated fan was installed on the sliding door located in the family room at the back center of the house. The blower door provides the required mechanical induced pressurization or depressurization of the indoors relative to the outdoors. Furthermore, the blower door and a flow hood were used to characterize the house shell and the HVAC duct leakage area.

Since the blower has a calibrated fan, standard calibration curves can be utilized to relate the flow rate to the pressure differences developed across the house shell (from the fan pressure) in response to the forced injection or removal of indoor air. Six operating conditions could be

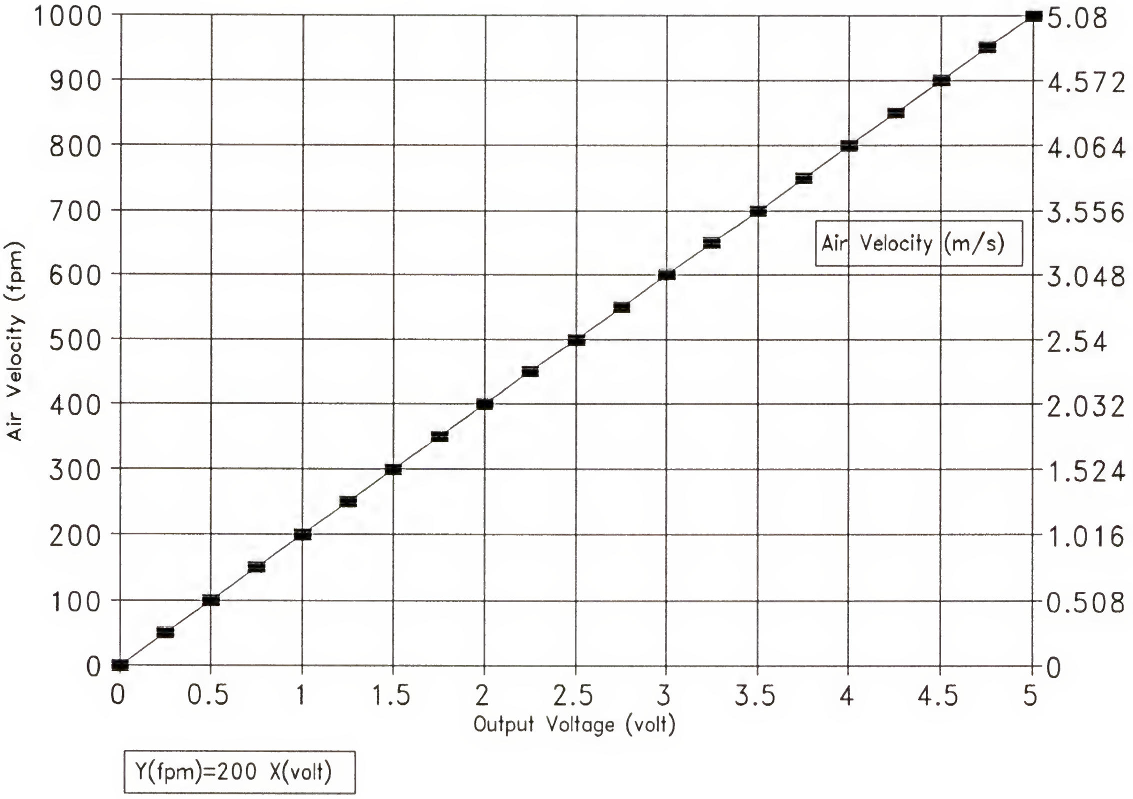

FIGURE 3-8: The linear correlation between air velocity and output voltage signal for flow measurement at the UFRRH.

utilized depending on the level of air blocking provided by holes in a blower door plate. The first blocking level is generated when no plate was used and the sixth air blocking level is generated when eight holes in the plate were blocked. Figure 3-9 illustrates the curves corresponding to the six configurations and shows the relation between the fan pressure difference and the air flow rate.

Blower door experiments were performed following ASTM blower door testing protocols (ASTM 1987) for pressure differential values ranging from 2 to 50 Pa between the indoor and the outdoors. However, when smaller pressure differences were needed, the blower door usually failed to provide stable flow rate. Instead, tracer gas techniques were utilized to characterize the UFRRH infiltration and natural ventilation rates. Within the scope of this research only single-zone tracer gas strategies were needed. The mass of the tracer gas must follow the conservation law (as expressed by the continuity equation) during the experiment; therefore, by monitoring the injection and concentration of the tracer, the rates of air exchange can be determined.

Two methods of tracer injection were utilized. Continuous injection was performed using the perfluorocarbon (PFT) measurements to determine average air exchange rates. A constant rate of the PFT is supplied by miniaturized diffusion-based sources that can be deployed in specific locations in the indoor environment, the outdoors and the sub-

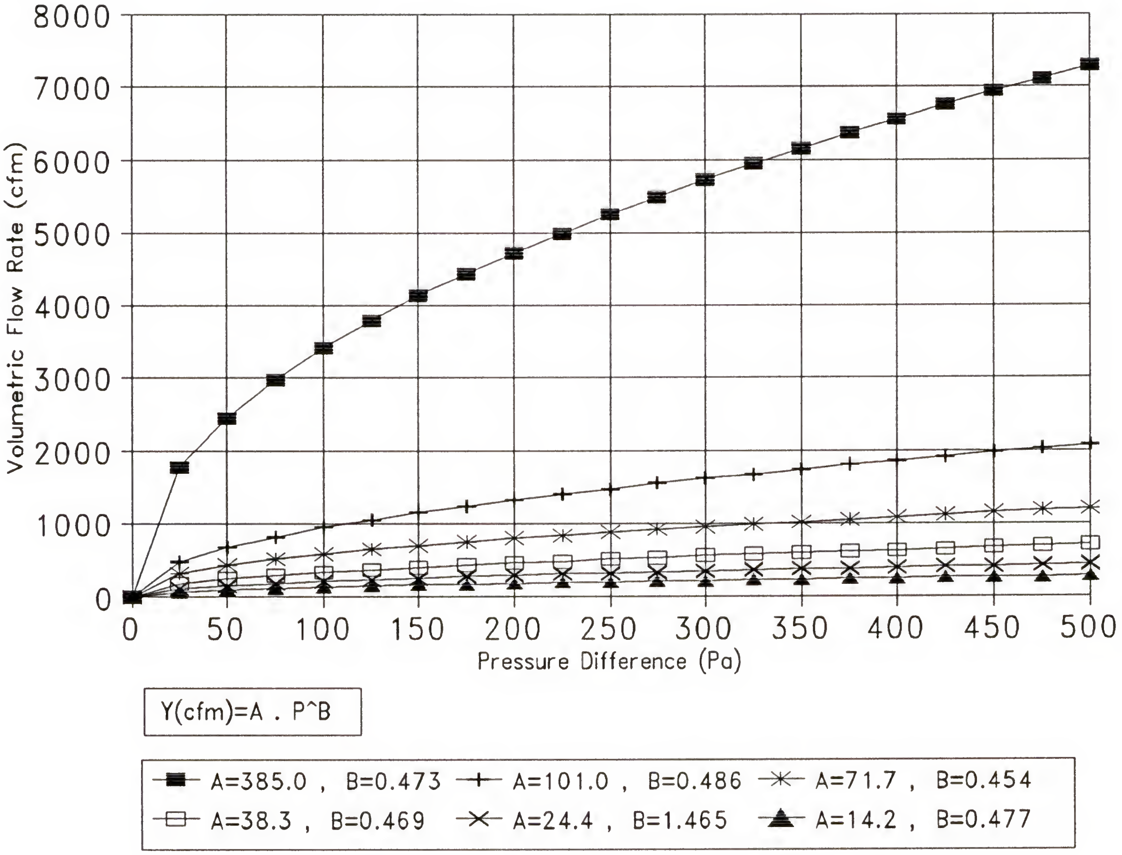

FIGURE 3-9: The relationship between the blower door fan pressure and air flow rate for six operating configurations. top to bottom: with cover, without cover, 4-hole plugged, 6-hole plugged, 7-hole plugged, & 8-hole plugged.

slab area. Capillary adsorption tube (CAT) samplers are then used to collect the PFT through air diffusion.

When continuous temperature measurements are taken at the CAT locations, the measurement results and the CAT are sent to Brookhaven National Laboratory for gas chromatography analysis that detects electron capture processes in the sample. The air exchange rate is calculated from the PFT release rate, the indoor volume, and the measured tracer concentration in the CAT. The resultant air exchange rate is directly proportional to the PFT release rate and indirectly to the tracer concentration and the indoor volume.

The pulsed injection method was also utilized at the UFRRH. However, it was exclusively used for characterizing the ventilation rate for a set of new houses that were employed to test passive and active radon reduction practices, methods, and systems. In this methodology, the tracer gas is injected for a specific period of time and mixed to ensure distribution in the indoor environment and detectable concentration. The concentration of the injected gas is then continuously monitored and analyzed. These concentrations decay with time and the experimental fit to the collected data determines the decay exponent. A linear fit could also be utilized if the gas concentration is plotted on a log scale, or on a linear scale with log values.

Two systems were selected for monitoring the pulsed injection tracer gas experiments depending on the tracer material. A carbon dioxide (CO_2) Gaztech (Telaire-model 1050) continuous monitor was utilized to record the CO_2 concentrations in ppm after pulsed release of the gas in the indoor environment. The system operate on a non-dispersive infrared sensor detecting CO_2 on the diffusion mode. The range of particle concentration detection is from zero to 1,999 ppm. The system output signal is analog linear 0-2 VDC and it can operate in non-condensing 5-95 % relative humidity environment. Figure 3-10 illustrates the linear relationship between the ppm and the system output signal that was utilized to calculate CO_2 concentration corresponding to the voltage input range of 0-2 VDC.

The other system utilized in the pulsed injection tracer gas experiments was used in both the UFRRH and the new houses. A Miran (model 203) specific vapor analyzer continuous monitor was used to monitor the release and decay of sulfur hexafluoride (SF_6) tracer gas in the indoor environment. The system operates by utilizing an infrared single beam spectrophotometer designed to measure a wide range of gas concentrations in air. The air is drawn into a 2.5-liter sampling cell by an integral air pump when it absorbs the infrared beam energy. The change in the beam energy is measured and converted into the equivalent absorber concentration in ppm. Detection ranges from 0-2000 ppm and the output signal is an analog voltage ranging from 0-1 VDC. The calibration curve between the system voltage output and the corresponding gas concentration in ppm is shown in Figure 3-10.

Pulsed injection tracer gas release for both systems was performed by an automatic assembly that controlled the tracer gas release every six hours. The assembly consisted of the gas tank fixed on wheels to facilitate moving and an electrically-controlled magnetic actuation valve. The actuation signal is supplied to the valve from a portable power source (battery) and controlled by an electrical timer.

Two experimental assemblies were built to perform the ventilation experiments and to facilitate data collection. Each assembly integrates a tracer gas detection system and two Setra low sensitivity differential pressure transmitters into a data logging and storing system. For data logging purposes, the Campbell Scientific programmable micrologger (model 21X) was utilized. Two differential mode analog voltage channels were used to log the pressure differential measurements, and one single mode analog voltage input channel was used for the tracer gas detection system output.

The logging and control system is equipped with standard Programmable Read Only Memory (PROM) that is used for the system's operational programs. The system supports eight analog input channels, four pulse input channels, four excitation output channels, two continuous analog output channels, and six digital control ports. It can be remotely operated and it supports standard serial input/output

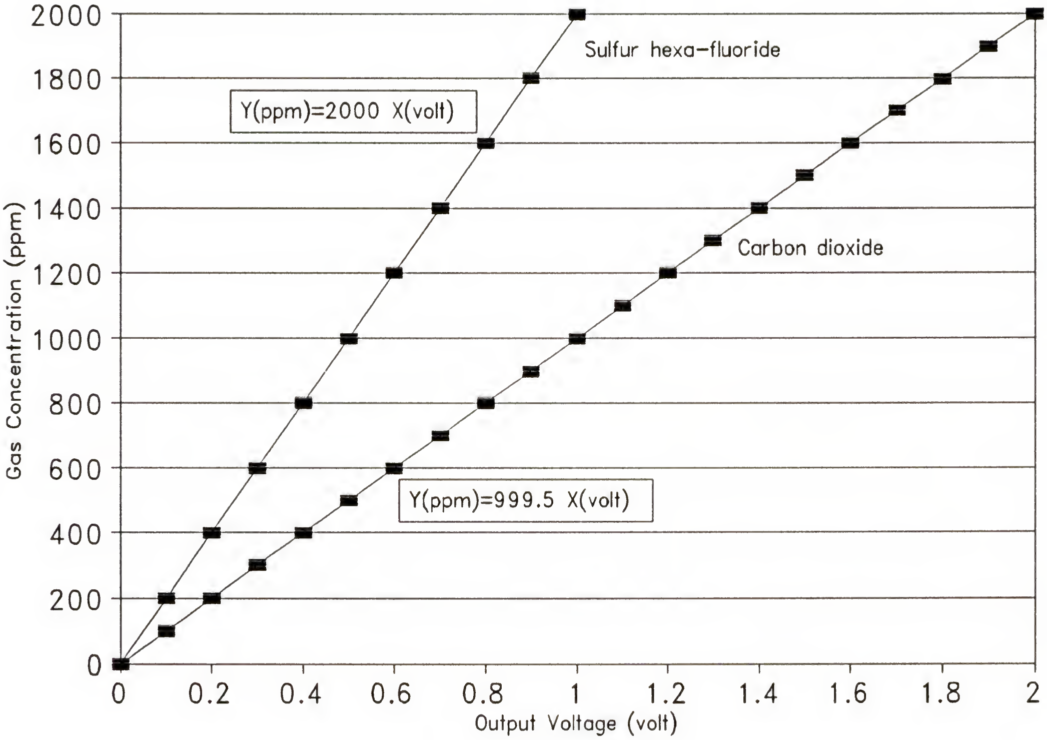

FIGURE 3-10: The linear correlation between gas concentration and system output voltages for ventilation measurements.

communications. Each system is programmed with a group of command instructions entered into a program table which can be executed according to a pre-specified execution interval. The latter interval determined the minimum time that measurements controlled by the system and data collection could be performed. Figure 3-11 illustrates the block diagram of the pulsed injection tracer gas experiments.

Weather Measurements

Weather parameters including wind speed, wind direction, and rainfall were measured by using a meteorological station installed at the top (above attic) of the UFRRH site. All output signals from the three transducers were conditioned and collected by a 21X micro-logging system. The data in the system were periodically retrieved through telecommunication to a computer at the University of Florida campus.

Wind speed measurement was performed by using a R.M. Young (model 03101-5) wind sentry anemometer that outputs a low level alternative current signal which can be read by the pulse count instruction of the 21X control program. The number of pulses collected by the system during the execution interval is recorded in the program output memory and then converted to its equivalent wind speed. Figure 3-12 shows the linear relation utilized to calculate the wind speed at the UFRRH from the pulses collected from the anemometer.

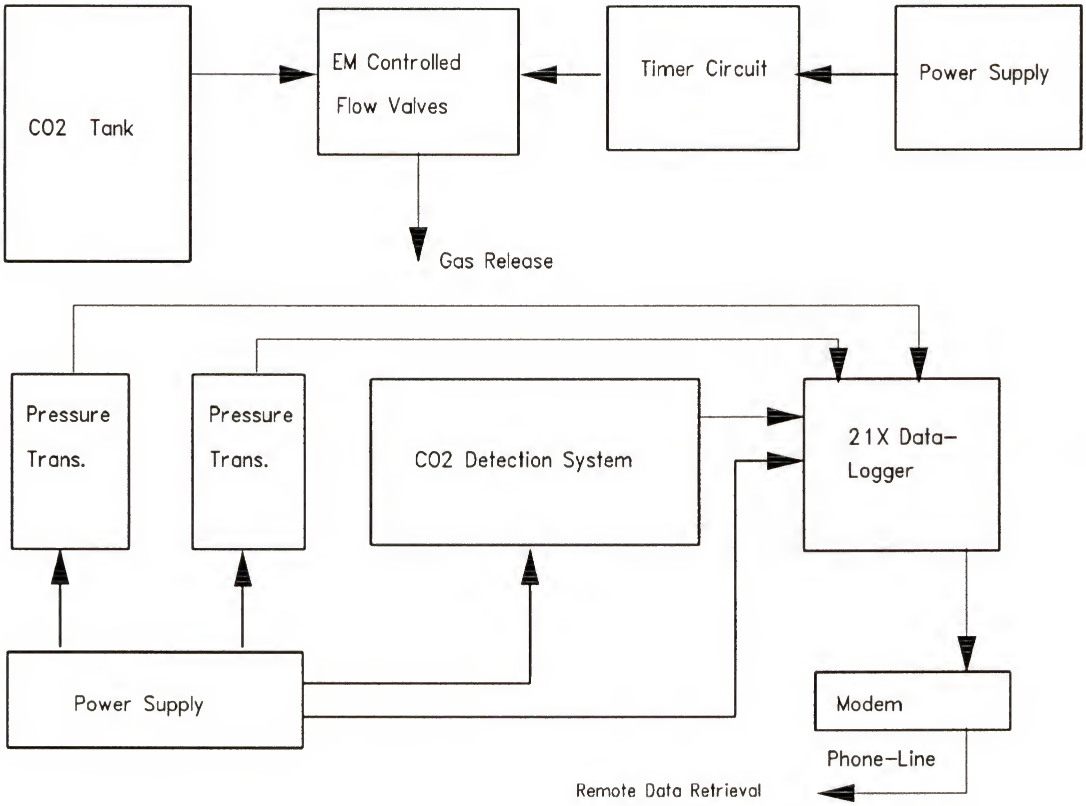
CO2 Tank
EM Controlled
Flow Valves
Timer Circuit
Power Supply
Gas Release
Pressure
Trans.
Pressure
Trans.
CO2 Detection System
21X Data-
Logger
Power Supply
Modem
Phone-Line
Remote Data Retrieval

FIGURE 3-11: The block diagram of the CO_2 pulsed injection tracer gas measurement system. Similar assembly was built for the SF_6 tracer gas measurements.

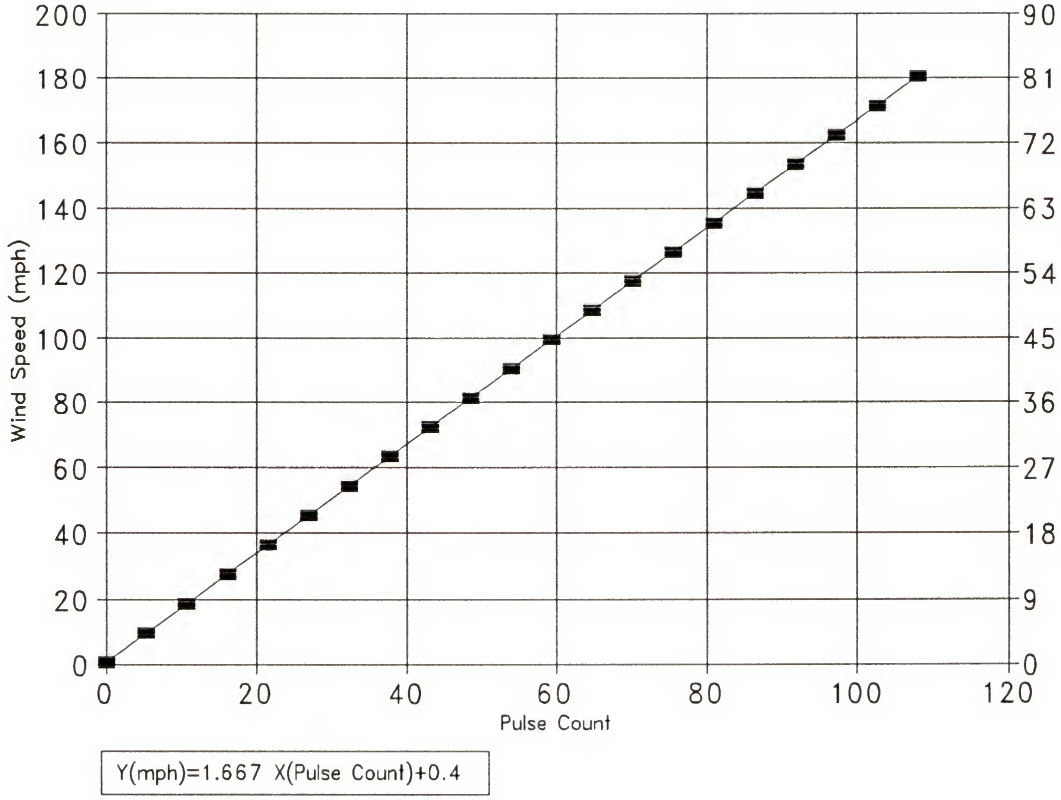

FIGURE 3-12: The linear correlation between wind speed and the anemometer pulse output monitored at the UFRRH site.

Wind direction at the site was measured simultaneously with the wind speed, and other measurements controlled by the Metrabyte system, by using of a R.M. Young (model 03301) wind sentry vane. The vane potentiometer operation was performed by supplying an excitation voltage, controlled by the 21X system to the potentiometer, and receiving the resultant circuit voltage. The latter quantity is proportional to the direction of the vane and can be expressed in degrees with respect to an established reference line. The wind direction potentiometer has a five degree dead band between 355 and 360. Figure 3-13 shows the mathematical linear relationship used to calculate the wind direction from the corresponding millivolt output collected from the potentiometer.

Rainfall measurement at the UFRRH site was performed by integrating output signals from a Texas Electronics (model TE525) tipping bucket rain gauge installed at the top of the house with the wind speed and direction equipment. The bucket is equipped with a Texas Electronics (model 525) transmitter which is a miniature adaptation of the Weather Bureau tipping bucket electric rain gauge. It has a range of 0.1 mm (or 0.01 inches) increment indication depending on the setting. The output signal is provided from the transmitter that sends pulses corresponding to switch closure derived by the collected rain. The output signal was integrated into the 21X micro logging system and measurements were simultaneously executed with the rest of parameters. Figure 3-14 shows the conversion equation used for calculating the rainfall data. Figures 3-15 A and B show the general schematic diagram of the University of Florida Radon Research House non-radiological experimental setting.

Radiological Measurements

Radiological measurements were performed at the UFRRH and a number of newly constructed residential structures. The experiments consisted of measuring radon gas in the soil and the indoor environment, measuring radon progeny in the indoor environment, and measuring gamma rays in the indoor and outdoor environments. The latter experiments were performed to obtained associated data required for performing radon measurement system calibrations.

Radon measurement experiments were designed to monitor indoor and sub-slab radon concentrations continuously in order to characterize both transient and steady state responses, as well as the spatial dependence of the radon concentrations. Three types of measurement systems were utilized for this purpose. Measurement of the spatial distribution of the soil gas was performed in the soil around the house to determine the average level of soil gas radon and characterize the radon potential zones.

Indoor radon concentrations and their spatial distributions were measured using total of six time-integrated

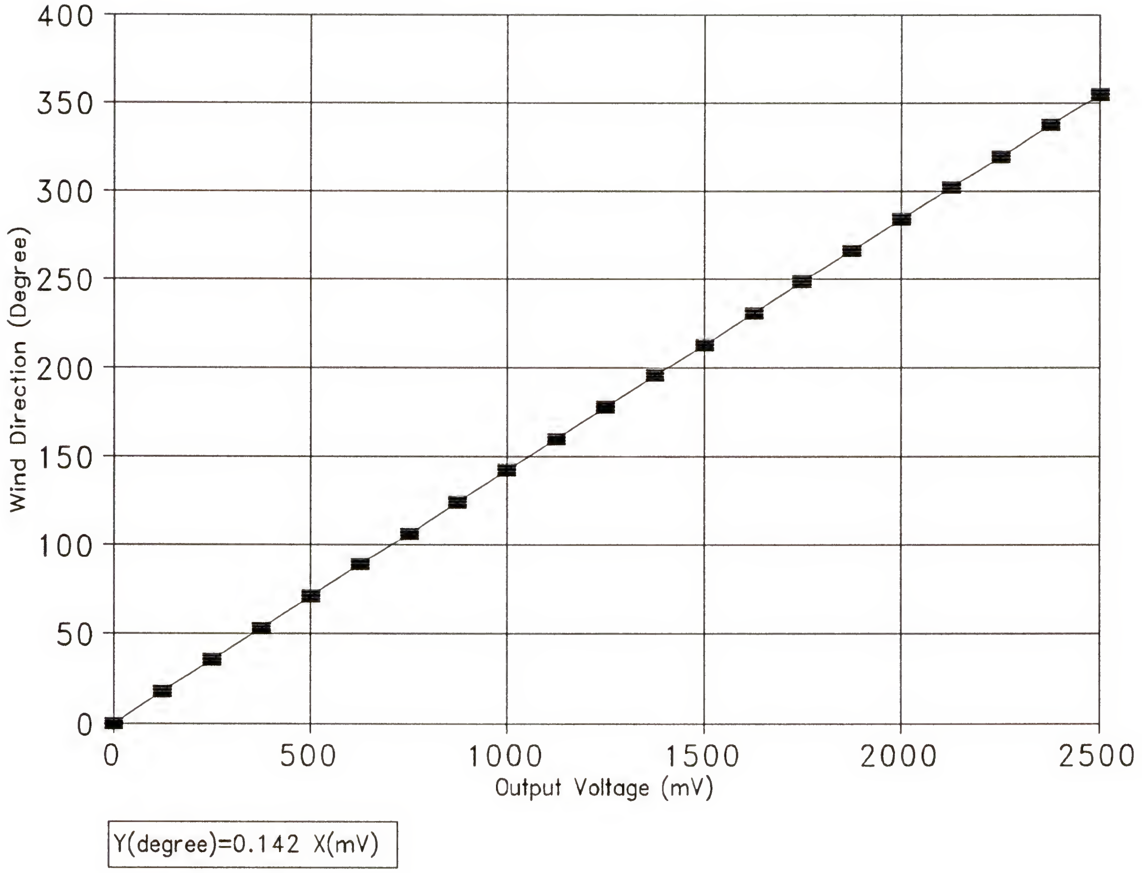

FIGURE 3-13: The linear relationship between the wind direction and the monitoring potentiometer.

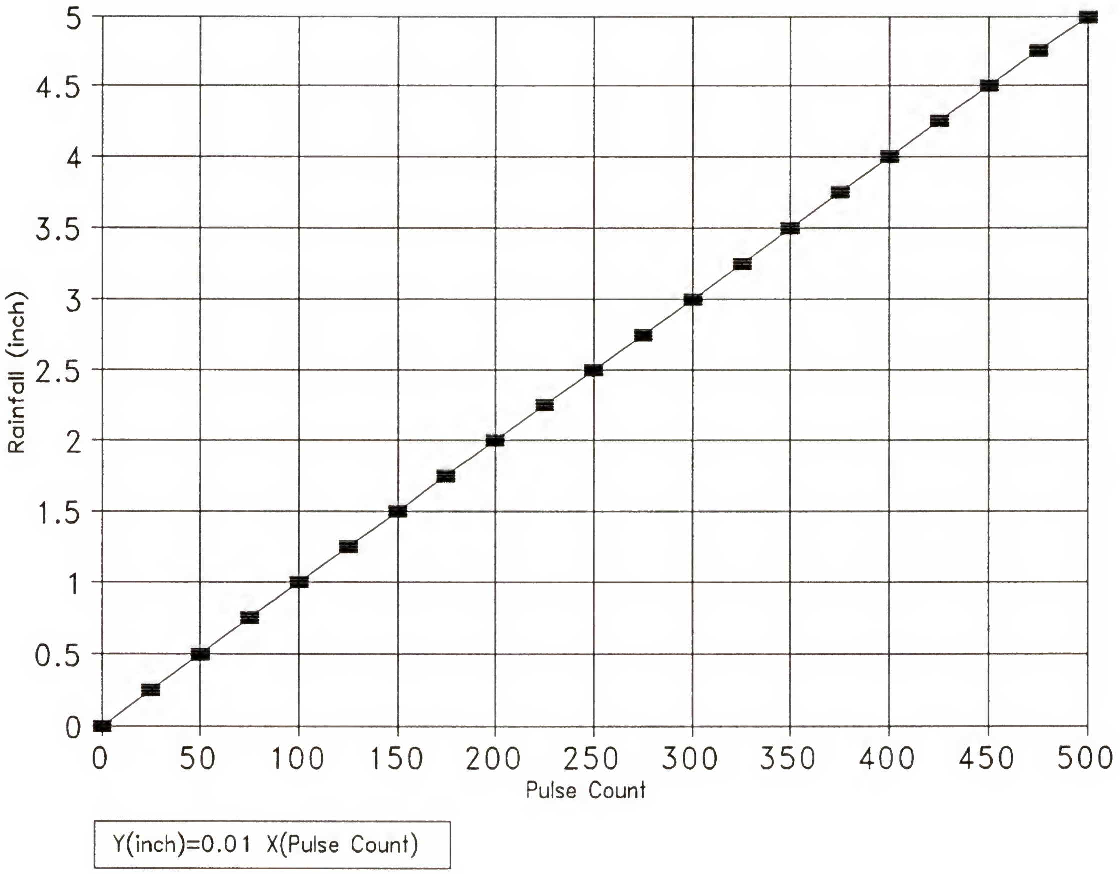

FIGURE 3-14: The linear relationship utilized to calculate the rainfall from the rain gauge pulse output at the UFRRH site.

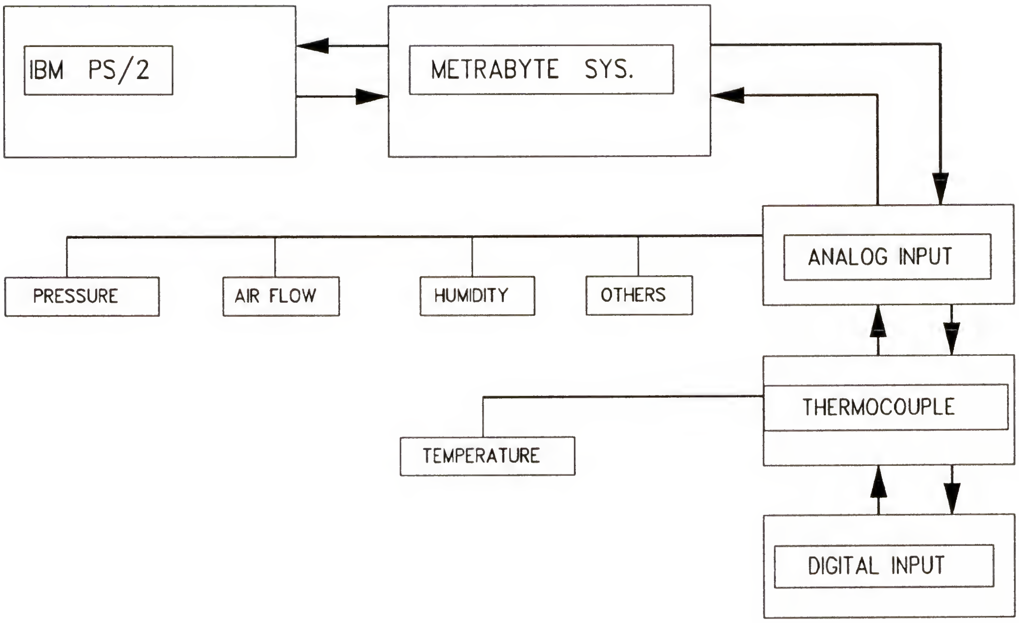
IBM PS/2
METRABYTE SYS.
ANALOG INPUT
PRESSURE
AIR FLOW
HUMIDITY
OTHERS
THERMOCOUPLE
TEMPERATURE
DIGITAL INPUT

FIGURE 3-15 A: The schematic diagram of the UFRRH non-radiological experimental setup.

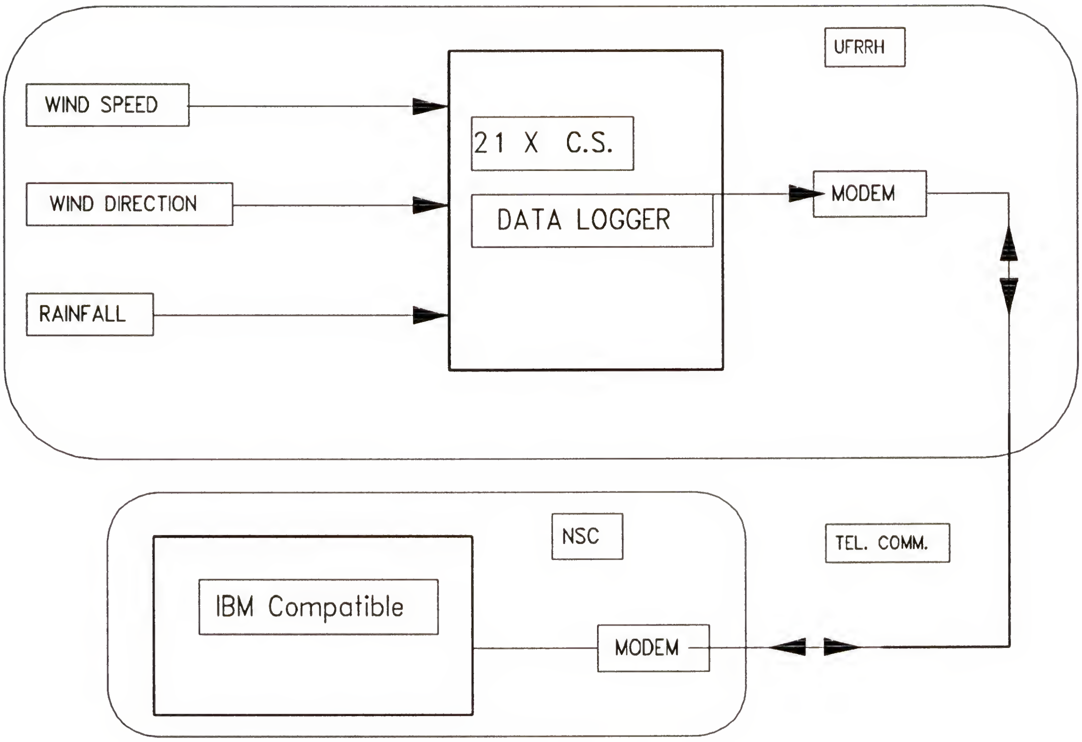
UFRRH
WIND SPEED
WIND DIRECTION
RAINFALL
21 X C.S.
DATA LOGGER
MODEM
NSC
TEL. COMM.
IBM Compatible
MODEM

FIGURE 3-15 B: The schematic diagram of the weather parameters and tracer gas ventilation experimental setup.

Honeywell, two standard (AT-Ease/models 1020 and 1021) and, four professional (model A9000A) radon monitors. These monitors use the time accumulated effect of radon to measure the concentration, and the professional model can provide resolved measurement for four-hour time intervals. These monitors are classified as continuous passive radon monitors that employ solid state technology.

Radon diffuses into the radon chamber on the monitor through filters installed in the chamber walls that allow free radon movement but prevent the entry of its decay products. Because of the diffusion process, the concentration in the test chamber is assumed to be equal to the radon concentration in the surrounding environment for the time period encountered in the operation of these monitors. Once the radon gas has decayed inside the test chamber, the generated alpha particles are counted through contact with a silicon chip inside the chamber. The number of alpha pulses that occur during every measurement time interval is counted and the radon concentration is computed in pCi/l by a microprocessor in the monitor. The monitor provides a measurement over the range from 0.1 to 999 pCi/l (0-36963 Bq/m^3).

Another type of time-integrated device used at the UFRRH is the Rad Elec (E-PERM) Electret ion chamber monitor. The device operates utilizing a charged Teflon disk (electret) which has a measurable surface voltage. The electret is then installed in an electrically conducting chamber. The electrostatic field generated from the initial disk charge, typically around 700 V, starts to collect alpha ionization products when radon disintegrates inside the chamber, and consequently decreases its electrostatic voltage. Therefore, the device operates on a time-integrated basis as the charged disk acts not only as a source of the electric field but also as a sensor.

Radon diffuses into the ion chamber from the surrounding environment through a filter opening. The filter stops radon decay products, dust, and humidity from entering the chamber. The radon concentration is calculated by measuring the drop in the electret voltage over time using a suitable voltage reader. The relationship between the drop in the electret voltage and radon concentration is linear for the range from 200 volts to 700 volts. However, when electret voltage drops below 200 volts, the resultant electrostatic field in the ion chamber is too low for efficient collection of the ions results in a non-linear relationship between the voltage drop and the radon concentration.

Continuous time-dependent measurement of indoor and sub-slab radon concentrations was performed by a Pylon (model AB-5) portable radon monitoring system. Measurements were designed to observe both the transient and steady state behavior of sub-slab and indoor radon concentration versus different indoor and outdoor conditions. This system is a portable programmable microprocessor-based data acquisition photo-multiplier radiation monitor equipped with modular accessories that can be used for measuring radon and thoron gas, airborne alpha particles, beta and gamma radiations, and surface contamination. However, its primary use is in measuring airborne radon concentration.

In this research, sample collection accessories of Passive Radon Detector cells (model PRD-1), Lucas scintillation cells (models 300 and 300A), Continuous Passive Radon Detector cells (model CPRD), Pylon adapters (model ABA), Lucas Cell adapters (model LCA-2), and others were used. Measurements using the CPRD cells were performed by allowing the indoor air to diffuse through a light-proof polyurethane foam barrier into the cell volume. The barrier also prevents airborne alpha particles from entering the CPRD cell.

An equilibrium time of approximately 0.5 is required for the CPRD cell volume to achieve a radon concentration the same as the gas level present in the surrounding air, and approximately 2.5 hours in the UFRRH indoor volume. The cell is lined with ZnS(Ag) scintillator material on the internal metal surface. Light pulses are generated when the alpha particles emitted from radon strike the scintillator surface. The cell is fitted to a photo-multiplier window coupler by the use of an ABA adapter, where generated pulses are collected and computed.

Continuous sniff sampling and grab sampling were both performed in measuring indoor and sub-slab radon concentrations by using Lucas scintillation cells. Air samples were collected by using a built-in vacuum pump in the AB-5 system. The air is passed through a 0.8 μm-powdered surface paper filter that prevents radon progeny, air moisture, dust, and other aerosol materials from entering the cell. The inner surface of the cell is lined with a ZnS(Ag) scintillator and the cell operates by the same process explained above for the CPRD cell.

Soil gas radon concentration measurement samples were collected using a soil probe at different depths in the soil but averaging about 0.76 m. In addition to the continuous measurement that can be performed during the soil gas pumping, grab sampling was utilized. In the latter sampling, the flow through the cell is left for a time period, typically about 10 minutes, that is long enough to collect a homogenous air sample from the source term. The cell is closed and left for a minimum of four hours before starting to count for a minimum of 30 one-minute consecutive readings. The readings are corrected for the decay of radon in the cell and the radon concentration is calculated based on the weighted average of the readings.

The sub-slab radon concentration measurements were performed using the Pylon at various slab points. Further, sub-slab measurements were taken from an opening of a fourinch PVC pipe access to the approximately 30-cm radius hemispherical-shaped hole, "the central hole", located immediately under the slab near the center of the house. The hole is a part of the Active Soil Depressurization (ASD) radon mitigation system installed in the house.

The Pylon counts were accumulated over 600-second measurement intervals, stored in the monitor memory at the end of each interval and downloaded to an IBM PC at the end of the experiment period. The experimental period of typically 96-hour was used to perform the measurements. This period provided information on the parameters' transient response in the house system as well as after the house system had stabilized.

Radon progeny measurements in this research were only used to support indoor radon measurement, i.e., no individual radon product measurements were performed. Progeny measurements are more significant when radon and progeny energy depositions and lung dosimetry are to be considered. However, its use to reflect indoor radon concentration provides information about the radon-progeny equilibrium ratio behavior. Such changes in the equilibrium ratio behavior are relatively limited for unoccupied, unfurnished houses like the UFRRH. Measurements were performed by using a Thomson & Nielsen Electronics Radon WL Meter (model TN-WL-02). The instrument operates by sampling air from the environment at a constant rate determined by a built-in pump. The pump is usually calibrated at 1 liter/min at the beginning of each experimental period.

The sampled air is passed through a 0.8 μm filter where radon daughter products are collected, and the alpha particles emitted from the filter are detected and counted by the system. The system employs a silicon detector and the resulting counts represent the time-integrated alpha counts from the radon products. Radon working level (WL) and time-averaged radon concentrations can then be calculated by dividing alpha counts by the time of the measurement and calibration factors.

Collection and Classification of the Experimental Raw Data

Large amounts of data are associated with the work in this research. Collection, processing and classification of the raw data, as well as calibration processes were carefully conducted to insure the quality of the experimental data and the data analysis. Most of the experimental raw data were collected by the UFRRH industrial scale Keithly Metrabyte data acquisition and control system and controlled by the dedicated PS/2 computer system at the site.

Data associated with the Metrabyte network represent most of the differential pressure measurements, barometric pressure measurements, temperature measurements, duct air flow measurements, wall and duct temperature and relative humidity measurements, and HVAC power consumption measurements. Data collected by the Campbell Scientific data-logger represent measurements of weather parameters, indoor/outdoor (portable mode) differential pressures, and ventilation rates.

Sets of control and operation programs using BASIC, QuickBASIC, VisualBasic, and Assembler were developed for handling and processing of the collected experimental raw data. A Radon Data Collection and Control Program (RDCCP, versions 1.0 & 2.0), have been developed to manage and control the data collection by the Metrabyte system. The program handles all required pointers for the input/output boards and channel pointers on each board, controls the data transfer, computes the equivalent analog value from the returned binary format, controls all time segments of the Metrabyte operation, and writes the collected data to output files using a pre-indexed ASCII format.

RDCCP can read a very large number of input channels with a wide selection of measurement intervals and has the flexibility to write the collected data in separate output files, as well as controlling the input channels. If needed, mathematical operations can also be performed before storing the data in the output files. Furthermore, the subroutines used by the program can be easily modified to control the Metrabyte output channel boards for different control purposes.

Each output file represents a specific type of raw data such as temperature, inside/sub-slab differential pressure, etc. The program can write the collected data in any ASCII format but if the data set is large, continuous ASCII files are preferred. The output format also depends on the available memory in the computer system. Therefore, intermediate processing may be needed. The processing is necessary if the raw data is collected as continuous ASCII files. The output data files must be read and rewritten in a form that is importable by analysis software. Figure 3-16 shows a schematic diagram of the program.

At the conclusion of each experimental run, a group of output data files were generated. Another set of programs; PYCONV (Pylon Converter), PTCONV (Pressure Transmitter Converter), and TECONV (Temperature Convertor) were developed to read the collected raw data files; convert them, and write them back into output files in column format structures. These programs keep track of each specific channel, extract the value of the parameter reported by that channel, provide columns from these values, and insert the time column with the data files. The output of these intermediate function programs are called the processed data files, versus the raw data files collected directly from the Metrabyte system. These processed files are able to be imported into spreadsheet-type graphics software for plotting and analysis.

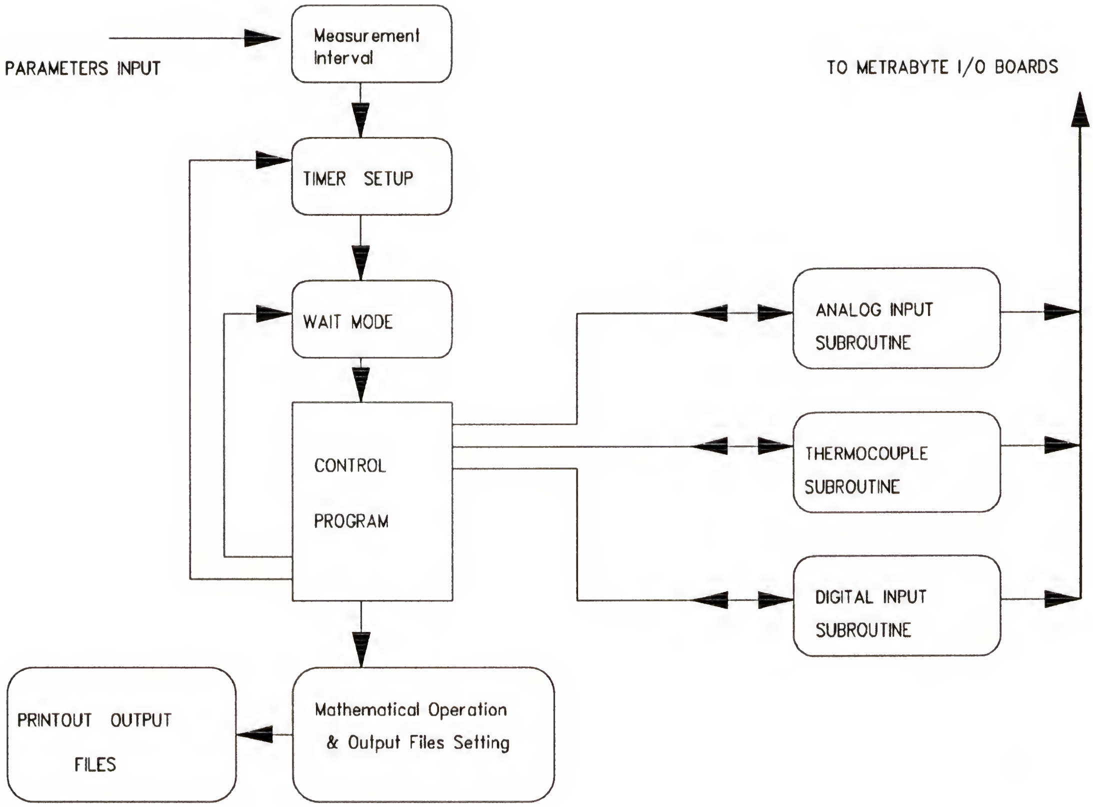
PARAMETERS INPUT
Measurement Interval
TIMER SETUP
WAIT MODE
CONTROL PROGRAM
Mathematical Operation & Output Files Setting
PRINTOUT OUTPUT FILES
TO METRABYTE I/O BOARDS
ANALOG INPUT SUBROUTINE
THERMOCOUPLE SUBROUTINE
DIGITAL INPUT SUBROUTINE

FIGURE 3-16: The block diagram of the radon data collection and control program (RDCCP).

The time intervals of the experiment are provided during this intermediate processing step as the first column in a matrix form. The other columns represent each measurement point where the value of the measurement is written corresponding to its time of measurement. The modifications also include calculations to the equivalent engineering value corresponding to the collected voltage or current according to the calibration curve of a particular instrument. Modification to the continuous ASCII output data files can also be made using other suitable software such as Word Perfect.

Since the number of raw and processed data files collected from the experiments is large, and for easy access to these files, a file name classification procedure was developed. The classification system aimed to provide clear file indexing and maximum information implementation in the file name. This information consists of the file content, type of data, and the time frame of the experiment in which these data are collected.

The raw and processed data files name classification system follows the format,

[1][2]-[3][4][5][6].[7][8][9]

where [1]&[2] digits are used to state the month in numbers, for example 10 (October). If the month consists of one digit 1-9, the first digit [1] can be neglected or used as zero, i.e., 02, 05, etc. [3]&[4] are used to state the day in the month. If the day is one digit, i.e., 1-9, the third digit can be neglected or used as zero. [5] is used to identify the general kind of the file content and [6] is for more specific determination according to special abbreviations (e.g., R=Radon, P=Pressure,...,etc). Other abbreviations can be used according to a specific need by using same letter in both digits with different meaning.

Digits [7]&[8] are used as extensions to the file name and the last digit [9] should be D to identify the file as raw data. This extension provides flexibility for additional information such as the address number of the I/O board, specific points in the slab or building, and magnitude of pressurization or depressurization.

The classification system used for the intermediate processing, the processed raw data files, is exactly the same as the classification described above except the last digit [9] is typically listed as M instead of D to indicate the data has been modified.

Processing of the Final Output Data Files

The final form of the output data was produced by reconstruction in spreadsheet (QuattroPro) files with the extension .QWX, X=1,2,3,...,9; for plotting, exchange and analysis purposes. The structure of each file is defined as seven lines of documented information followed by the collected data starting at line (8), then calculations or graphs inserted. The first seven lines of the information area include the following:

line (1) is the raw data file Name;

line (2) is the data type (ex. differential pressure across the slab in Pa);

line (3) is used for the time of the experiment (the start and end of the measurement period) in the following form:

(M/D/Y) AT (HH:MM) TO (M/D/Y) AT (HH:MM).

Line (4) describes the conditions of the experiment(s);

line (5) is for notes or/and comments (if they exist); and,

line (6) is the column title. When more than one raw data file is used in a final spreadsheet file, the first raw data file should start from HOME position and one column should be left empty between one file and another.

Final output data files can include one or more raw data files depending on the size of the raw data file and the particular purpose of the analysis. Two formats were utilized, one-to-one file format represents files that have one raw data file or several raw data files in the same measurement conclusion. This format was used to analyze the time dependent behavior of the radon concentrations with a number of measured key parameters. Usually, samples of the collected data were provided in this format to show the behavior of one or more parameters as other factors change over the same measurement period.

The general format final output data files usually represent several files of the raw data having the same type of information collected over different time intervals. This format permits analysis of the long time behavior of a specific parameter compared to the typical experimental period of 96 hours. In addition, it can be used to analyze the same measurement parameter in different spatial locations, for two or more experimental periods.

A classification system was developed to name these processed output files. This system provides sufficient information about the file content from the file name for both formats; the one-to-one format was constructed as,

[1][2][3][4][5][6][7].WQX   X=1,2,3,...,9

[1]&[2] are used to state the month in letters as January= JA, March= MA, June= JE, May= MY and July= JY. The rest of the months are stated by dropping the first digit [1] and using the first letter of the month name. [3]&[4] are used to state the day of the month in numbers which represent the end of the measurement period. The third digit [3] can be neglected or used as zero, for the days 1-9. [5][6]&[7] are reserved for abbreviations as necessary.

Most of the one-to-one format files contain different kinds of information such as pressure, temperature and radon concentration measured over the same time interval. All the abbreviations used in the raw data classification can be used here as well as a special abbreviation of three letters can be used for specific purposes. The general format was constructed as,

[1][2][3][4]-[5][6][7].WQX X=1,2,3,...,9

[1]&[2] represent the first letter of the month, except for the one letter months as above. [3]&[4], and [5]&[6], represent numbers at the beginning and end of the experimental period, respectively. In case of one digit, number [3] and/or [4] can be dropped or used as zero. [7] is the last character in the format and is a letter representing the general category of the data file content. When more space is available, an optional character [8] may be used to provide more information.

In the special case that occurs when data from two months, each needing two letters to be represented, and two days each needs two digits also, the general format will need more than eight digits to represent the data file. In this case the data should be arranged in two WQ files instead of one. If one of the months can be represented by one digit and the other by two, the second digit can be neglected because that will be understandable from the time sequence in the format if the days need two digits to be represented.

Final output data files should be constructed according to the following sequence of raw data files for different applications: radon concentration, pressure, temperature, wind speed, wind direction, rainfall, air velocity, flow rate and working level. Raw data files, processed data files and WQ files were stored in time sequence according to the date of the measurement (that can be seen easily from the file name). In case of the same time of measurement for different types of data, the file should be stored according to its contents as described above.

Experimental Error Assessment and Quality Control of the Measurements

Assessment of Experimental Error

This section deals with the procedures of calibrating devices and equipment used for performing the non-radiological testing and measurement during this research. It also specifies the error or uncertainty that might occur during the measurement. Errors associated with any experimental data can be divided into two major categories: human and system generated errors. The first category results from the experiment conductor activity that may cause the system to malfunction or cause an error during data collection, processing, analysis, and/or interpretation. The second category of possible errors results from the fact that no system is perfect, and from uncertainties developed by the distribution of the variable being tested. Elimination of the first category of possible errors in this research was based on two strategies: performing the experiment carefully and repetition of the testing.

Minimization of the second type of possible errors was based on three strategies: first is the second strategy above, second is the careful design of the experimental setup including the selection of instrumentation, and third is performing continuous equipment calibration as often as needed and cross checking experimental results for different types of devices that measure the same parameter. The same error control strategies were also utilized for the radiological measurements performed during this research.

In most of the testing and measurements performed at the UFRRH, the following error estimates were utilized to evaluate the overall system performance, for both radiological and non-radiological measurements, with regard to the accuracy of the measurements and associated error calculations. The estimators applied in the assessment process are as the follows:

(1) hysteresis: the maximum difference in the system signal output, at any measured value within the specified range, when the value is approached first when increasing and then decreasing of the variable under measurement;

(2) linearity: the maximum deviation of any calibrated point on a specified straight line (represent the best straight line fit), during any one calibration cycle;

(3) repeatability: the ability to reproduce output readings when the same variable under measurement is applied consecutively, under the same conditions, and in the same direction;

(4) thermal error: the maximum change in output, at any value of the measured variable within the specified range, when the temperature is changed from room temperature to a specified temperature extreme;

(5) thermal zero shift: the zero shift due to changes of the ambient temperature from room temperature to the specified limits of the operating temperature range;

(6) overall thermal error: combined error of thermal zero shift and thermal error calculated based on the root sum of the squares (RSS) statistical method;

(7) accuracy: combined error of repeatability, hysteresis, and linearity calculated based on the RSS method; and

(8) overall combined error: the combinations of all the previous possible error when applicable calculated based on the RSS method.

Calculation of the overall experimental error is computed based on the statistical RSS method. Most of equipment used during this research had inherent hardware corrections to the errors in their output signals that result from thermal driven factors. Such inherent corrections may cause changes to applied correction levels of approximately 70-100 % for the device output signals depending on the particular instrument and the condition of the experiment.

However, in the following assessment of the overall experimental error the maximum possible overall thermal error (OTE) was used in the computation resulting in 0% correction level consideration from the instrument inherent corrections. Therefore, the utilized assessment is conservative by implementing a built-in safety consideration of 0% thermal correction on the part of OTE, and using maximum possible error that might be driven from non-linearity, non-repeatability, and hysteresis factors for computing the combined accuracy error (CAE). The assessment criteria developed to compute the overall combined experimental error (OCEE) associated with the measurements performed during this research is,

$$OCEE = [OTE^2 + CAE^2 + OSE^2]^{0.5}$$

where OSE represents all other possible sources of system error that are individually based on particular instrumentation and/or particular applications such as errors induced by the fluctuations of external power supply voltage.

Quality Control of Non-Radiological Measurements

Errors associated with the testing of pressure differentials in many applications at the UFRRH and the other newly constructed residential structures are those of the Setra C264 pressure transmitters since those devices were exclusively used for these measurements. There is another built-in error in the collected differential pressure data, and all other measurements controlled by the Metrabyte data acquisition and control system, developed by the data collection system itself. This latter error results from converting the channel analog input voltage at the Metrabyte I/O boards into a digital binary number during reporting to the computer. Such error is very small, on the order of 2^{-12}, at least six orders of magnitude lower than the OCEE resultant from the sensor errors; therefore it is negligible. Overall Thermal error associated with the Setra C264 is <± 0.0033 % from the full scale (FS) per each temperature degree different than the factory adjusted calibration temperature of 21.1 °C (70 °F). The range of temperature that experiments were performed during this research is -1.1 to 37.78 °C (30 to 100°F) giving maximum temperature difference of 4.45 °C (40 °F) from the factory adjusted temperature. This difference results in a maximum overall temperature-induced error (TIE) of (0.0033% FS/degree x 40 °F = 0.132 % FS) in the transmitter output signal.

The transmitter has an infinite resolution factor and repeatability factor of < 0.3% FS. The combined RSS statistical accuracy error (CAE) value of the system is < ±1.0 % of the full scale. Since the C264 transmitter regulates current rather than voltage as an output signal, its circuit current may be introduced with an error resulting from variations in the power supply voltage. This error corresponds to 0.02 mA change in the transmitter's current output, per volt change in the power supply. A Hewlett Packard (model HP 6294A) DC power supply was used to power all transmitters networked to the Metrabyte system. This power supply has a maximum uncertainty of 0.1% from the constant (selected) voltage output. A 24-volt supply was delivered at the power input of each transmitter which resulted in a maximum possible power line voltage-induced error (VIE) of,

$$\text{VIE} = 0.02\text{mA} \times 24\text{volts} \times 0.001\text{FS Error/volt} = 0.00048 \text{ mA FS.}$$

The percentage representation with respect to the full scale transmitter output signal of 20 mA results in a VIE value of 0.0024 % of FS. The overall combined experimental error (OCEE) based on the maximum possible errors associated with pressure differential measurements at the UFRRH and other testing sites is therefore,

$$\text{OCEE} = (\text{OTE}^2 + \text{VIE}^2 + \text{CAE}^2)^{0.5} = < \pm 1.009 \text{ \% FS}$$

All pressure transmitters were calibrated for both zero and span adjustment. The standard calibration procedure is used for zero adjustment by applying a factory selected 24 volts from the HP power supply (by voltmeter) and a 250 ohms load for the MAI-16 analog input channel and the line resistance. The output current was then adjusted to 12 mA, the operating point for these measurement, for bi-directional range from the zero adjustment screw in the transmitter, when both pressure ports are connected by a flexible tube.

The span, or full scale output, adjustment was modified from the standard procedure to match the research house circumstances. The calibration is performed by closing the high pressure port of the transmitter to atmosphere and using the blower door/calibrated fan to apply depressurization/ pressurization to the full scale range of the pressure transmitters. The full scale value ±25 was compared with a MP20SR Neotronics digital micromanometer (1% accuracy of the full scale). Then the output current was adjusted to 20 mA for the positive side and 4 mA for the negative side by the span adjustment screw.

The error in the barometric pressure measurement at the UFRRH is that associated with the Setra model 270 (600-1100 mbar) high accuracy barometric pressure transducer. The transducer has an infinite resolution limited only by output noise level of 0.005 % FS. It has a hysteresis error factor of 0.01 % FS, repeatability error factor of 0.01 % FS, and linearity error factor of < ±0.05 %, which produced a CAE value of < ±0.052 % FS.

The transducer has a thermal zero shift of < ±0.002 % FS/°F and thermal error of < ±0.001 % FS/°F resulting in a combined thermal error for the possible 40 °F range of temperature swing at the UFRRH as TIE = < ±0.014 % FS. The transducer has circuitry that minimizes the effect of power supply (24 VDC) line variations to a maximum of < ±0.005 % FS output signal change. The latter value represents experimental error that might be induced by the fluctuation of the transducer power supply voltage (VIE). The overall experimental error associated with barometric pressure measurement therefore is,

$$OCEE = (OTE^2 + VIE^2 + CAE^2)^{0.5} = < \pm 0.054 \% FS$$

All temperature measurements were performed using the T-type thermocouple wire and collected by MTHERM20 input boards in the Metrabyte system. The cold built-in reference junction compensation (CJC) point is calibrated by adjusting voltage points in the board with a digital voltmeter. The voltage reference error is 25 μV/°C (max.) and the CJC temperature error is 0.5° C for the maximum possible temperature swing of 0-50 °C. The board automatically computes the temperature from the measured input voltage, applies CJC using an on-board microcomputer, and the results are stored in a RAM unit through a 12-bit, dual-slope integrating A/D converter with ±1 bit resolution.

Error associated with the T-type thermocouple wire itself is 0.75 % of the reported reading or 1.0 °F whichever is greater for the temperature range above 32 °F. Measurements at the UFRRH were performed in a possible temperature range of 30-100 °F which corresponds to -1.1 - 37.78 °C. Using a conservative assessment of an upper end temperature value of 100 °F, the resultant error in the thermocouple wire reading is 0.3 °C. Combining the maximum possible errors from the thermocouple wire and the MTHERM20 board, the resultant combined overall experimental error of the temperature measurements is < ± 0.58 °C. Both thermocouple wires and the board connection outputs were verified and checked using a MICROMITE (Thermo Electric Instruments) thermocouple calibrater.

Temperature measurements performed by the Vaisala duct mounted HMD 30UB/YB and wall mounted HMW 30UB/YB transmitters have a linearity error factor < 0.1 °C, and overall thermal error of ± 0.02/°C. The overall accuracy factor of the system is ± 0.2° C. Utilizing the same upper end temperature of 37.78 °C (100 °F), the resultant maximum uncertainty in the signal output due to the thermal zero shift and thermal errors is 0.75 °C. Therefore, the overall combined experimental error associated with these temperature measurements is OCEE = < ± 0.78 °C.

Vaisala duct and wall mounted transmitters mentioned above also provide relative humidity measurement simultaneously with the temperature output. The output signal for the relative humidity channel has an overall thermal error factor of ± 0.04 % FS/°C, and an overall accuracy, including linearity and repeatability factors, of ±2 % FS for relative humidity range of 0-90 % and ±3 % for relative humidity range from 90-100 %. Since the maximum possible measurement error developed by temperature is ± 1.508 % FS, the maximum combined experimental error of the relative humidity measurements is OCEE = < ± 2.5 % FS for relative humidity range from zero to

90 %, and < ± 3.6 % FS for relative humidity range from 90 to 100 %.

Continuous air velocity measurements performed in the UFRRH duct system by the Kurz 435DC linear air velocity transducers have a repeatability error factor of ± 0.25 % FS and an accuracy of ± 0.5 % for the linear output signal. The maximum overall experimental error associated with the system is OCEE = < ± 0.56 % of the full scale value. The latter error associated with air flow measurements using the Alnor balometer is OCEE = < ± 5 % of the full scale range (1400 cfm).

Experimental error associated with CO_2 and SF_6 gases measurements can be estimated from the error in the Gaztech Telaire 1050 ventilation efficiency meter and the Miran 203 specific vapor analyzer output signals, respectively. The Miran 203 system has an overall error OCEE = < ± 5 % of the full scale output. The Telaire 1050 system has an overall error of ± 5 % of the output reading or ± 50 ppm, whichever is grater. The system has a maximum possible output corresponding to 1,999 ppm which results in approximately ± 2.5 % FS when 50 ppm error is employed. Since this figure is smaller than the first error estimation, the OCEE number used for this system is < ± 5 % FS.

Quality Control of Radiological Measurements

The three types of radon monitors used in this research are EPA-listed devices. To be listed, devices must pass EPA testing criteria to ensure accuracy in measuring radon concentration before they can be used for formal testing of radon by certified commercial radon contractors. The plan of inter-calibration activities for devices used to measure radon in this research was implemented on three levels: internal, external, and comparison.

The internal level consists of calibration activities which are performed internally during the research by using local radon sources as a part of the quality assurance program implemented during this research. All devices in internal calibration activities are exposed to the same radon source, which is either the UFRRH at all-systems-off configuration or a radon drum source. The latter source is a drum half-filled with radium dials and radium-based aircraft paints.

The external level consists of participation in the inter-calibration activities provided by the Department of Energy (DOE) Environmental Measurement Laboratory (EML) facilities. In this level, four scintillation cells are periodically (every six months) sent to the EML facility where they are filled with an undisclosed radon concentration and returned to the sender with the filling conditions such as temperature, pressure, and relative humidity. The sender then measures the radon concentration in the cells and reports the result to EML. After receiving the reported measurements from participating facilities, EML publishes the results including disclosure of the actual radon fill concentration for the cells. The conversion factors associated with the calibration program in this research have been adjusted using these numbers.

The third level of calibration as a part of the quality assurance program consisted of performing back-checking on the drum source and other devices used in the internal calibration level against the calibrated (adjusted) scintillation cell conversion values obtained from the EML inter-comparison activities (external level).

Case examples of each of the three levels of calibration activities in the quality assurance program utilized in this research are illustrated here. First, conversion factors are only needed for the scintillation cells of the Pylon AB-5 radon monitors. Compared to E-PERM Electret and the Honeywall professional radon monitors, which report radon concentration in pCi/l, Pylon monitors report the alpha counts rather than alpha concentration. Since counts are measured for a period of time, count rates need to be calculated to the unit of count/minute (cpm) and then converted into concentration unit pCi/l or Bq/m^3.

The procedure utilized to obtain scintillation cell conversion factors consisted of two steps. The first step was to obtain an initial estimation for the conversion factor of each cell by using factory calibrated Honeywell and E-PERM monitors with the cells exposed to the same source, the UFRRH, under the same configuration. The second was adjusting these factors according to the corrections obtained from the EML inter-comparison calibration activities.

An example of the second level calibration activity performed at the UFRRH is illustrated below. The activity was conducted to calculate the conversion factors between the count rate in the Pylon and the actual radon concentration in pCi/l (or Bq/m^3) for two Pylon passive diffusive cells. Ten E-PERM electrets, four Honeywell radon monitors, and two Pylon AB-5 units with PRD-1 cells were used in this calibration activity. All electrets and Honeywell monitors were placed with the two sets; Pylons I.D. SN 286 with cell I.D. SN 131, and Pylon I.D. SN 415 with cell I.D. SN 130; and the indoor conditions were maintained very stable. This calibration activity was performed for a time period of 3.286 days.

The results of both types of monitors were compared with the Pylon count rate. The final calibration factors were calculated for each device-cell unit by weighting the radon concentration results of both monitors according to their statistical variances. Table 3-2 shows the results for Honeywell monitors. The second column is the radon concentration for the last four hours of the measurement, and the third column is the average radon concentration during the measurement. Statistical calculations of the results are also shown.

Ten SE-series short term electrets were used in S-type chambers. The calibration factor was calculated for each electret according to the test information available from Rad Elec as:

$$S\text{-}CF = 1.8864+.000638(MPV)$$

where MPV is the mid-point voltage. Correction for gamma ray background was made for each electret by measuring gamma rays in the same location for two hour intervals. The 12 collected readings averaged 6.2 μR/h and that value was used for the gamma ray correction. Another correction for the area elevation was made. Table 3-3 shows the results of the calculations, radon concentrations and the associated statistics.

TABLE 3-2: The results of Honeywell radon monitors and their statistical parameters.

Monitor #	Current Rn Concen. pCi/l (Bq/m^3)	Average Rn Concen. pCi/l (Bq/m^3)
1	71.0 (2627.0)	46.6 (1724.2)
2	76.3 (2823.1)	48.8 (1805.6)
3	75.7 (2793.5)	47.7 (1764.9)
4	67.4 (2493.8)	42.2 (1561.4)

<Average> = 46.3 pCi/l (1714 Bq/m^3)
Std. Dev. = 2.89 (based on 1/n-1)
Std. Dev. = 2.51 (based on 1/n)
Std. Dev. of the mean = 1.45

The two Pylon readings were initially collected in counts per ten-minute interval. The readings were changed to counts per minute for the convenient conversion to Bq/m^3 or pCi/l. Table 3-4 shows the results of these readings. The means and standard deviations of the E-PERM and the Honeywell monitors are 46.32 ± 1.45 pCi/l and 45.32 ± 0.64 pCi/l, respectively.

TABLE 3-3: Results of E-PERM measurements and their statistical parameters.

SN (SE)	Ini.V (V)	Fin.V (V)	ΔV (V)	MPV (V)	CAL. Factor	Rn-C Bq/m^3
2147	740	410	334	575	2.25325	1629.11
5999	713	372	341	542.5	2.23251	1699.78
6030	732	428	304	580	2.25644	1497.02
3844	716	370	346	543	2.17541	1770.82
3908	739	388	351	563.5	2.24591	1739.73
5999	710	376	334	543	2.23282	1664.63
6076	712	370	342	541	2.23155	1705.70
6201	739	403	336	571	2.25069	1660.93
6538	709	371	338	540	2.23092	1685.72
3830	742	396	346	569	2.24942	1711.99

<Average> = 1676.54 Bq/m^3 (45.31 pCi/l)
Std. Dev. = 2.02 (based on 1/n-1)
Std. Dev. = 1.92 (based on 1/n)
Std. Dev. of the mean = 0.64

The overall mean and standard deviation were obtained by weighting each mean over the reciprocal of its variance. Those weighting factors are,

$$W1=1/(1.4464)^2= 0.48$$

$$W2=1/(0.6400)^2= 2.44$$

then, the weighted mean = (46.36*0.48+45.32*2.44) /W1+W2 = 45.49 and, and the standard deviation of the weighted mean = $(1/W1+W2)^{0.5}$ = 0.59. The mean of each pylon reading is compared with the overall obtained mean to give the conversion factor for each PRD-1 cell. The conversion factors were obtained for Pylon SN 415 with PRD-1 SN130 as 30.11 Bq/m^3 (or 0.81 pCi/l) per count/m and Pylon SN 286 with PRD-1 SN131 as 28.75 Bq/m^3 (or 0.78 pCi/l) per count/m.

The PRD-1 cells were always with a specific Pylon to maintain the most accurate conversion factors. The previous calculations are applicable to normal/Poisson distributions. The obtained means of radon concentrations for both E-PERM and Honeywell monitors were calculated from a linear combination of the actual measurements, i.e., the mean is not an independent value. The overall mean was calculated by weighting both the E-PERM and Honeywell monitors means over the reciprocal of their variances. This statistical treatment gives the minimum possible error since the standard deviation depends on the value of the mean, which is dependent on the actual measurements.

The same argument can be applied for calculating E-PERM and Honeywell mean results by weighting over the reciprocal of their variances for each reading as in the overall mean, instead of taking the arithmetic means. However, for each average reading (Honeywell) and electret reading (E-PERM), the actual reading contains the accumulated effect of the disintegrations during a period of time, which cannot be divided into the actual effect per time interval.

An illustrative example of an inter-comparison calibration activity (external level) is provided below. Four Pylon scintillation cells were usually sent to the EML facility for filling with an undisclosed radon concentration. In this exercise, two sets of fillings were performed with a time difference of 2.5 hours between them. Counting to determine the cells' unknown radon concentrations were started at 34.2, 38.86, 35.38, and 36.22 hours after the cell filling. These periods between the filling and counting times are shown in Table 3-5 for each of the four cells along with the calibration data. In this calibration activity, 41 readings were taken for each cell. The first reading is reported at the end of the first minute after the elapsed time between filling time and reading time for each cell.

Pylon counts per minute (cpm) for the first reading and the consecutive forty readings were corrected for the decay of radon. The arithmetic mean and standard deviation were 15.33±2.88, 14.54±2.63, 14.90±3.70, and 15.61±3.80 for the four cells 575, 576, 577, and 578, respectively. As seen in the table, the arithmetic means of the 41-element reading set and its standard deviations were used to calculate a weighted mean, 15.02±1.57 pCi/l, based on the reciprocal method of the

TABLE 3-4: The statistical parameters of the pylon readings

Value	P.SN 145 & PRD SN130	P.SN 286 & PRD SN131
Mean	55.89 count/m	58.53 count/m
Std. Dev.	21.07	21.47
Std. Err.	0.97	0.99
Sum	26490.0	27743.6
Maximum	93.4	95.8
Minimum	18.6	20.0

sample standard deviations.

The adjusted conversion factors for Pylon scintillation cells were then used to calibrate the drum source for cross checking to its radon concentration. Tables 3-6 A, B, and C show the type of data and calculations associated with a drum calibration activity. Four 300A-type and three 300-type scintillation cells were used in the activity. After cleaning the cells, sniff sampling was applied for 14 continuous minutes with a flow rate of 3.7 l/min and samples from the drum air were collected for each of the seven cells. The sampling was performed in a closed loop path so no reduction to the drum concentration would occur by mixing with fresh air. The cells were then left for intervals of at least four hours and radon activities were measured for a continuous 14 minutes for the grab sampling. The latter measurements were corrected for the radon decay half-life of 3.825 days and converted to radon concentrations using the factors previously calculated during the cell calibration at the UFRRH.

The overall combined experimental errors in the radon working level measurements performed at the UFRRH were estimated for two different working periods of the Thomson & Nielsen Radon WL system used. Since the alpha activity on a new filter will build up with air sampling time, the increase of this activity is a function of a (mean) half-life of radon daughter products. Although more than the half-life is involved, the net effect is a characteristic build-up function representing the percentage of total activity that could be reached on the filter after starting the air sampling. The OCEE during the activity build-up period (approximately 40 minutes) is ± 10% of the total alpha counts, while the OCEE values after the activity had built up on the filter is ±2 % of the total alpha counts.

TABLE 3-5 A: Results of the first two cells of intercomparison calibration activity performed with four scintillation cells.

Cell I.D. # 575 Readings after 2052 min. of filling			Cell I.D. # 576 Readings after 2092 min. of filling		
end of min.	cpm	pCi/l	end of min.	cpm	pCi/l
2053	13	10.76	2093	14	11.66
2054	17	14.07	2094	21	17.49
2055	21	17.38	2095	15	12.50
2056	18	14.90	2096	15	12.50
2057	17	14.07	2097	17	14.17
2058	24	19.87	2098	16	13.33
2059	18	14.90	2099	10	8.33
2060	24	19.87	2100	14	11.67
2061	24	19.88	2101	20	16.67
2062	17	14.08	2102	23	19.18
2063	22	18.23	2103	22	18.35
2064	19	15.74	2104	22	18.35
2065	24	19.89	2105	15	12.51
2066	22	18.23	2106	20	16.68
2067	17	14.09	2107	20	16.69
2068	16	13.26	2108	15	12.52
2069	15	12.44	2109	14	11.68
2070	26	21.56	2110	20	16.69
2071	11	9.12	2111	21	17.53
2072	16	13.27	2112	18	15.03
2073	18	14.93	2113	21	17.53
2074	23	19.08	2114	18	15.03
2075	15	12.44	2115	19	15.87
2076	24	19.91	2116	17	14.20
2077	18	14.94	2117	13	10.86
2078	17	14.11	2118	11	9.19
2079	15	12.45	2119	20	16.71
2080	20	16.60	2120	13	10.86
2081	15	12.45	2121	18	15.04
2082	15	12.46	2122	16	13.37
2083	20	16.61	2123	19	15.88
2084	20	16.61	2124	17	14.21
2085	15	12.46	2125	23	19.23
2086	18	14.95	2126	15	12.54
2087	22	18.28	2127	17	14.22
2088	17	14.13	2128	14	11.71
2089	16	13.30	2129	18	15.06
2090	14	11.64	2130	20	16.73
2091	20	16.63	2131	18	15.06
2092	18	14.97	2132	18	15.07
2093	17	14.14	2133	17	14.23

TABLE 3-5 B: Results of the other two cells of intercomparison calibration activity performed with four scintillation cells shown in Table 3-5 A.

Cell I.D. # 577 Readings after 2123 min. of filling			Cell I.D. # 578 Readings after 2173 min. of filling		
end of min.	cpm	pCi/l	end of min.	cpm	pCi/l
2124	18	15.99	2174	20	17.09
2125	21	18.66	2175	21	17.95
7126	23	20.44	2176	20	17.09
2127	20	17.77	2177	16	13.68
2128	22	19.55	2178	26	22.23
2129	15	13.33	2179	17	14.54
2130	22	19.56	2180	17	14.54
2131	12	10.67	2181	14	11.97
2132	12	10.67	2182	15	12.83
2133	23	20.46	2183	17	14.54
2134	19	16.90	2184	10	8.56
2135	23	20.46	2185	22	18.83
2136	21	18.68	2186	16	13.69
2137	16	14.24	2187	20	17.12
2138	15	13.35	2188	29	24.82
2139	12	10.68	2189	27	23.12
2140	11	9.79	2190	22	18.84
2141	12	10.68	2191	24	20.55
2142	13	11.57	2192	20	17.13
2143	19	16.92	2193	19	16.27
2144	14	12.47	2194	22	18.85
2145	13	11.58	2195	10	8.57
2146	14	12.47	2196	12	10.28
2147	14	12.47	2197	18	15.43
2148	26	23.17	2198	21	18.00
2149	15	13.37	2199	17	14.57
2150	10	8.91	2200	22	18.86
2151	16	14.26	2201	17	14.58
2152	19	16.94	2202	14	12.01
2153	19	16.94	2203	25	21.44
2154	13	11.59	2204	18	15.44
2155	15	13.38	2205	16	13.73
2156	11	9.81	2206	19	16.30
2157	25	22.30	2207	13	11.16
2158	13	11.60	2208	19	16.31
2159	18	16.06	2209	10	8.58
2160	14	12.49	2210	18	15.45
2161	16	14.28	2211	13	11.16
2162	18	16.07	2212	14	12.02
2163	15	13.39	2213	20	17.17
2164	19	16.96	2214	17	14.60

TABLE 3-5 C: Statistics of the inter-comparison calibration activity shown in Table 3-5 A and B.

Mean of the cpm readings

cell I.D. # 575 = 15.33 pCi/l
cell I.D. # 576 = 14.54 pCi/l
cell I.D. # 577 = 14.90 pCi/l
cell I.D. # 578 = 15.61 pCi/l

Standard deviation of the samples

cell I.D. # 575 = ±2.88 pCi/l
cell I.D. # 576 = ±2.63 pCi/l
cell I.D. # 577 = ±3.70 pCi/l
cell I.D. # 578 = ±3.80 pCi/l

Weighting factors of the samples

cell I.D. # 575 = 0.12
cell I.D. # 576 = 0.14
cell I.D. # 577 = 0.07
cell I.D. # 578 = 0.07

Weighted Mean (WM) = 15.02 pCi/l

Standard deviation of the WM = ±1.57 pCi/l

TABLE 3-6 A: Pylon count rate (cpm) during sniff sampling for seven scintillation cells and their statistical data.

Cell I.D.# / Sampling Time

SN577 2:37pm	SN576 2:53 pm	SN578 3:06pm	SN575 3:19pm	SN203 3:40pm	SN783 3:52pm	SN720 4:10pm
234	248	226	248	301	219	233
301	301	282	289	291	272	264
317	306	329	321	277	288	320
327	355	363	392	322	298	329
362	361	387	395	329	379	292
380	372	349	393	330	340	341
398	404	393	372	349	387	349
406	429	397	412	356	395	368
416	406	388	370	394	399	346
396	383	423	381	394	400	386
430	445	443	392	343	366	356
460	412	442	392	399	402	375
451	409	391	411	401	398	383
447	397	401	417	398	367	366

Mean (cpm)

380.36	373.43	372.43	370.36	348.86	350.71	336.29

Standard Deviation (± cpm)

63.04	53.20	58.04	47.98	41.47	56.43	43.82

TABLE 3-6 B: Pylon count rate (cpm) during grab sampling for the seven scintillation cells and their statistical data.

Cell I.D.# / Reading Time

SN577	SN576	SN578	SN575	SN203	SN783	SN720
8:21pm	8:35pm	8:51pm	9:06pm	9:21pm	9:36pm	9:53pm
747	722	782	738	711	779	727
735	736	790	776	733	725	685
776	769	782	727	706	705	723
787	794	766	761	743	765	700
748	771	721	747	678	707	627
748	785	800	753	729	663	667
759	741	774	759	718	706	688
737	751	764	819	660	730	658
755	733	740	756	682	708	668
789	770	739	722	700	753	691
722	752	751	718	679	718	689
763	783	748	762	686	730	724
767	776	756	740	669	738	701
754	769	737	753	721	736	699

Mean (cpm)

756.21	760.86	760.71	752.21	701.07	725.93	689.07

Standard Deviation (± cpm)

18.52	21.03	22.11	24.43	24.92	27.90	26.65

TABLE 3-6 C: Decay-corrected grab sampling measurements in pCi/l.

At the End of Period # (first column)

Δt (min.)

	344	342	345	347	341	344	343
	SN577	SN576	SN578	SN575	SN203	SN873	SN720
1	468.09	452.31	490.08	462.62	482.47	504.41	493.46
2	460.63	461.14	495.16	486.50	497.47	469.50	465.01
3	486.38	481.87	490.20	455.84	479.20	456.61	490.86
4	493.34	497.60	480.24	477.22	504.38	495.53	475.31
5	468.95	483.25	452.08	468.50	460.31	458.02	425.79
6	469.01	492.09	501.68	472.32	495.00	429.57	453.02
7	475.97	464.56	485.43	476.15	487.59	457.49	467.34
8	462.23	470.89	479.22	513.85	448.26	473.10	447.02
9	473.58	459.66	464.23	474.38	463.26	458.90	453.87
10	494.97	482.93	463.66	453.11	475.55	488.13	469.55
11	452.99	471.70	471.25	450.65	461.34	465.50	468.25
12	478.78	491.20	469.42	478.33	466.15	473.34	492.10
13	481.35	486.87	474.50	464.58	454.66	478.59	476.53
14	473.25	482.54	462.64	472.80	490.06	477.35	475.23

Mean (pCi/l)

474.25	477.04	477.13	471.92	476.12	470.43	468.09

Standard Deviation (± pCi/l)

11.62	13.26	13.72	15.31	16.81	18.06	18.10

Weighting Factors (W.F.)

0.01	0.01	0.01	0.00	0.00	0.00	0.00

Coefficient Factors

3.51	2.71	2.53	2.01	1.68	1.44	1.43

Sum of Weighing Factors = 0.03
Sum of Coefficient Factors = 15.33
Weighted Mean (WM) = 474.17 pCi/l
Standard Deviation of the WM = 5.56 pCi/l

CHAPTER 4
RESULTS AND DISCUSSION

Observations of Physical Parameters Related to Indoor Radon

Initial Characterization of the Research Site

Initial characterization of the UFRRH site consisted of three activities; characterization of the soil-gas radon concentration, characterization of the gamma ray distribution around the house and the indoor, and characterization of the differential pressure field developed across the house concrete slab by the installed high vacuum pump (ASD system) at the central hole.

Initial characterization of the soil area surrounding the UFRRH for soil-gas radon concentration was performed by the use of Pylon and Lucas scintillation cells. Fifty-three testing locations around the house were utilized for this purpose as illustrated in Figure 4-1. A soil probe was used to penetrate the soil to a depth of approximately 0.76 m (2.5 feet) where the soil gas was grabbed at a flow rate of approximately 4 liters per minute.

Distances of approximately 3 m (10 feet) separate the testing locations parallel to the house length, except

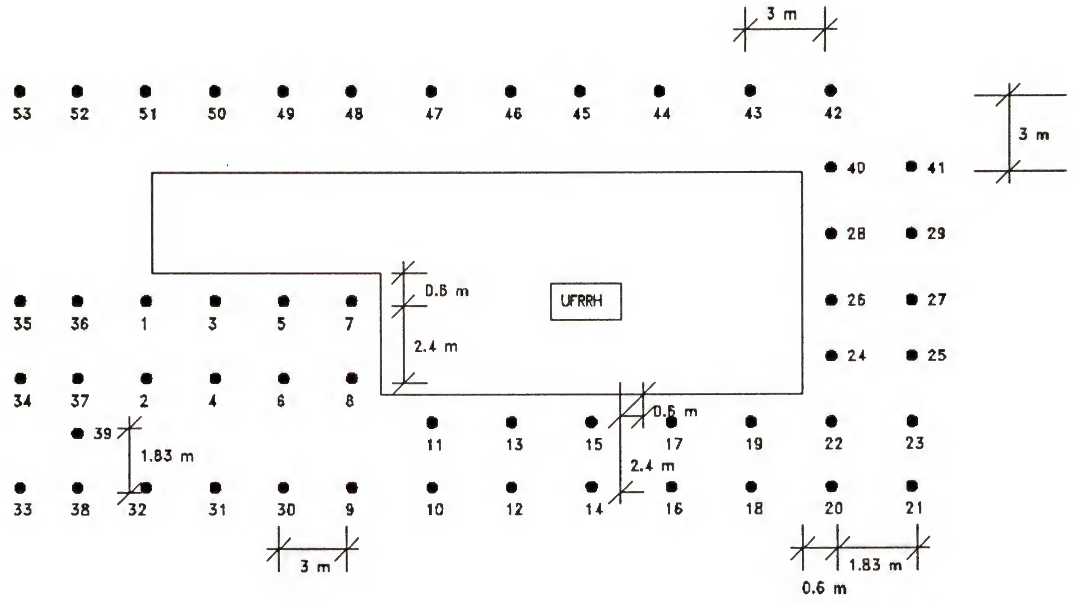
3 m
53
52
51
50
49
48
47
46
45
44
43
42
3 m
40
41
28
29
0.6 m
UFRRH
35
36
1
3
5
7
26
27
2.4 m
24
25
34
37
2
4
6
8
0.6 m
39
11
13
15
17
19
22
23
1.83 m
2.4 m
33
38
32
31
30
9
10
12
14
16
18
20
21
3 m
1.83 m
0.6 m

FIGURE 4-1: An illustration to the testing locations utilized for initial radon soil gas measurements at the UFRRH.

between the last testing location and the previous one on the north side of the house because of the fence. Distances of approximately 2.4 m (8 feet) between testing locations parallel to the house width, and 0.6 m (2 feet) between testing locations and the house exterior block walls were utilized during this characterization. Table 4-1 shows the Pylon counts per minute and the corresponding soil-gas radon concentration results obtained from this characterization activity. The arithmetic mean of all measurements is approximately 6332 pCi/l (234284 Bq/m^3) with a sample standard deviation of approximately ±1226 pCi/l (45362 Bq/m^3). This summaries the initial characterization of the soil-gas radon concentration and soil-gas distribution at the UFRRH site.

Characterization of the mechanically induced pressure differentials across the house slab were performed by activating the suction pump of the ASD system described elsewhere for a period of seven days before readings were taken. This period provides enough time for the air volume pressure underneath the slab, the sub-slab air volume pressure, to reach equilibrium with the forced vacuum pressure applied by the system. Table 4-2 shows the average pressure differentials collected at each of the sub-slab tubes. Figure 4-2 shows the three-dimensional representation of the differential pressure map across the foundation due to the operation of the ASD system.

Figure 4-3 illustrates a contour map of the differential

TABLE 4-1: The results obtained from the initial soil gas characterization at the UFRRH (rounded to the nearest figure).

Point (#)	Average (cpm)	Average (pCi/l)
1	4683	5620
2	3959	4750
3	4791	5749
4	4065	4878
5	5069	6082
6	4300	5161
7	6141	7370
8	5243	6291
9	4226	5071
10	4672	5606
11	6324	7588
12	6376	7651
13	5458	6550
14	6019	7222
15	5564	6677
16	5629	6754
17	6634	961
18	6269	7523
19	7351	8821
20	4810	5772
21	3599	4318
22	4051	4861
23	3073	3688
24	5016	6019
25	4463	5356
26	6099	7319
27	5316	6379
28	7148	8578
29	6724	8069
30	4515	5418
31	4598	5518
32	4643	5571
33	4735	5682
34	4900	5880
35	5031	6037
36	4901	5881
37	4765	5718
38	4728	5673
39	4669	5603
40	7318	8781
41	7105	8526
42	6289	7546
43	5958	7150
44	5345	6414
45	6445	7734
46	7654	8105
47	5745	6894
48	5146	6176
49	5988	7186
50	4876	5851
51	4652	5582
52	4100	4920
53	3423	4107

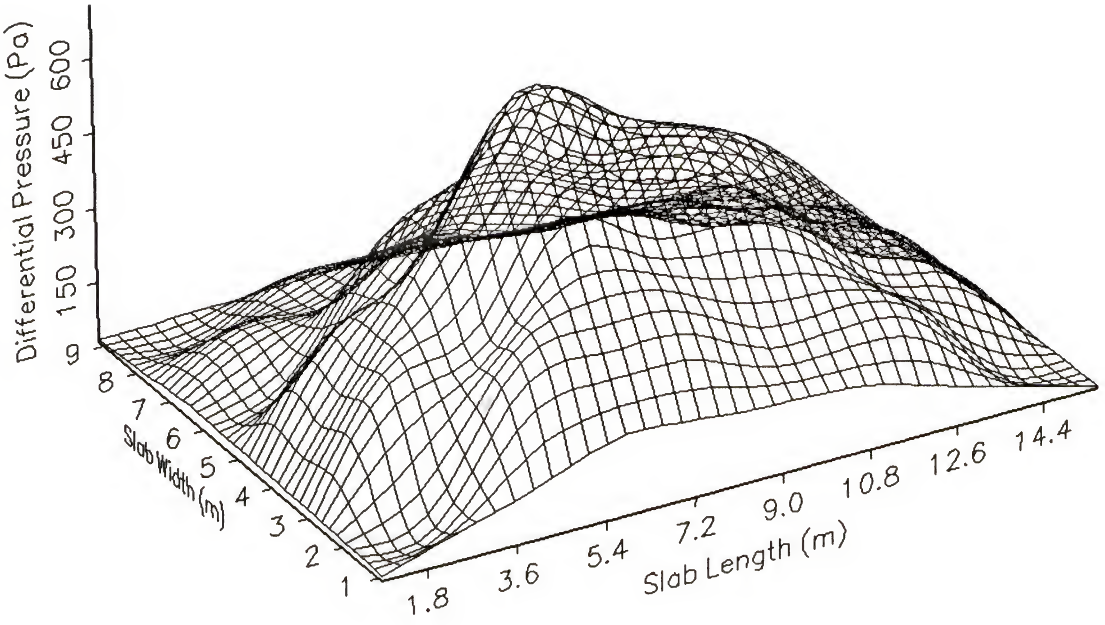

FIGURE 4-2: The spatial distribution of the time-averaged differential pressure across the slab developed by the active soil depressurization (ASD) system.

TABLE 4-2: Results of the pressure differentials developed across the slab due to operation of the ASD system.

Sub-Slab Tube #	Pressure Differential (Pa)
1	37.3
2	37.3
3	54.8
4	34.8
5	59.8
6	286.4
7	702.4
8	184.3
9	156.9
10	490.7
11	206.7
12	44.8
13	29.9
14	44.8
15	49.8
16	32.4

pressure distribution across the foundation due to the ASD operation. As seen in the figure, the suction pressure produced maximum pressure difference of 680 Pa between the immediate area under the slab and the indoor at the location of sub-slab tube 7. Testing at the location of sub-slab tube 10 shows the next highest pressure difference value of about 466 Pa. These points are nearest to the location of the center hole where the pump suction pressure is applied. The suction pressure has a value of approximately 2000 Pa measured at the testing opening in the duct of the ASD system. This duct along with the central hole and radon testing access is shown in Figure 4-4.

The distance between the center hole and sub-slab location tube 7 is approximately 1.67 m (5.5 feet). The longest distance is between the central hole and the sub-slab location tube 13 at the north-west corner of the structure, and is approximately 10.97 m (36 feet). The pressure differential at this location is about 9.9 Pa. Since the indoor pressure is reasonably spatially flat during this measurement, the change in the sub-slab air volume pressure for the longest measured distance is approximately 99.5%. This figure corresponded to a 2.76% pressure drop approximately per 0.3 meter (foot) of the soil in the sub-slab structure area.

If the above calculations are employed to compute the pressure drop corresponding to the shortest testing distance, between sub-slab location tube 7 and the central hole, an overall pressure drop of 66% is obtained which corresponds to a pressure drop of approximately 12% per 0.3 meter (foot) of the soil. The two examinations of the pressure drop per foot of the soil do not match, the calculations performed for the shortest and longest distance configurations of the testing.

The slope in pressure difference reduction, which corresponds to the sub-slab air volume pressure reduction, is

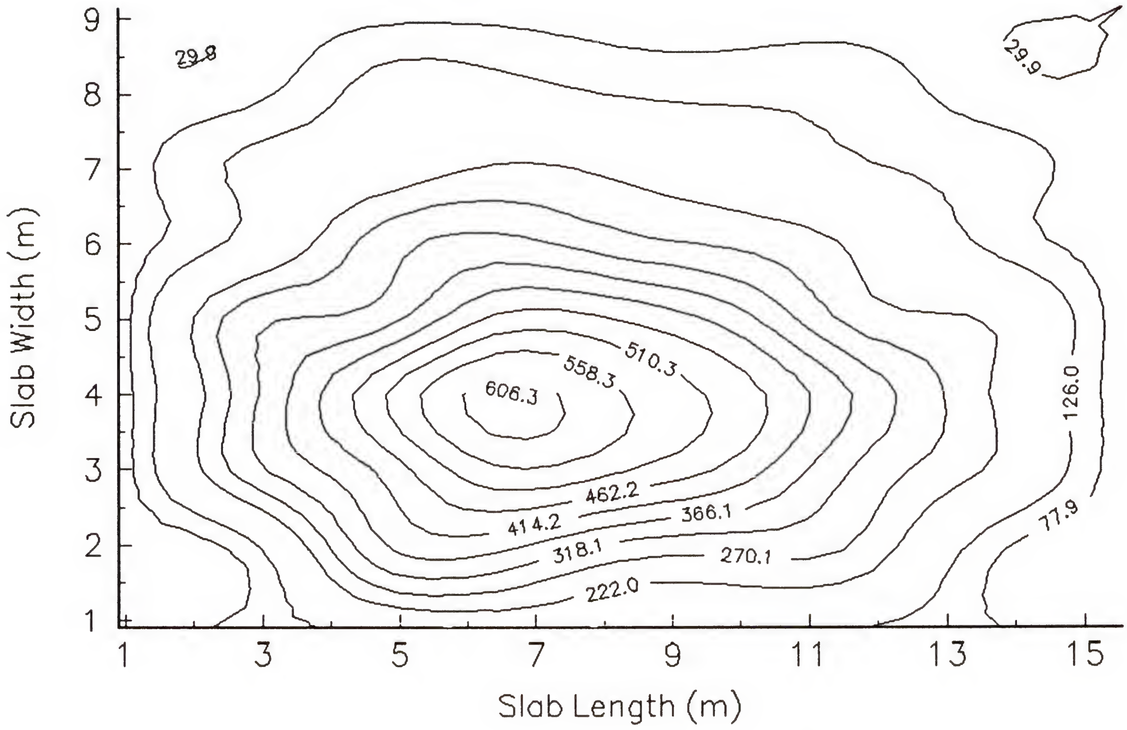

FIGURE 4-3: The contour map plotting of the differential pressure distribution across the slab developed by the ASD system.

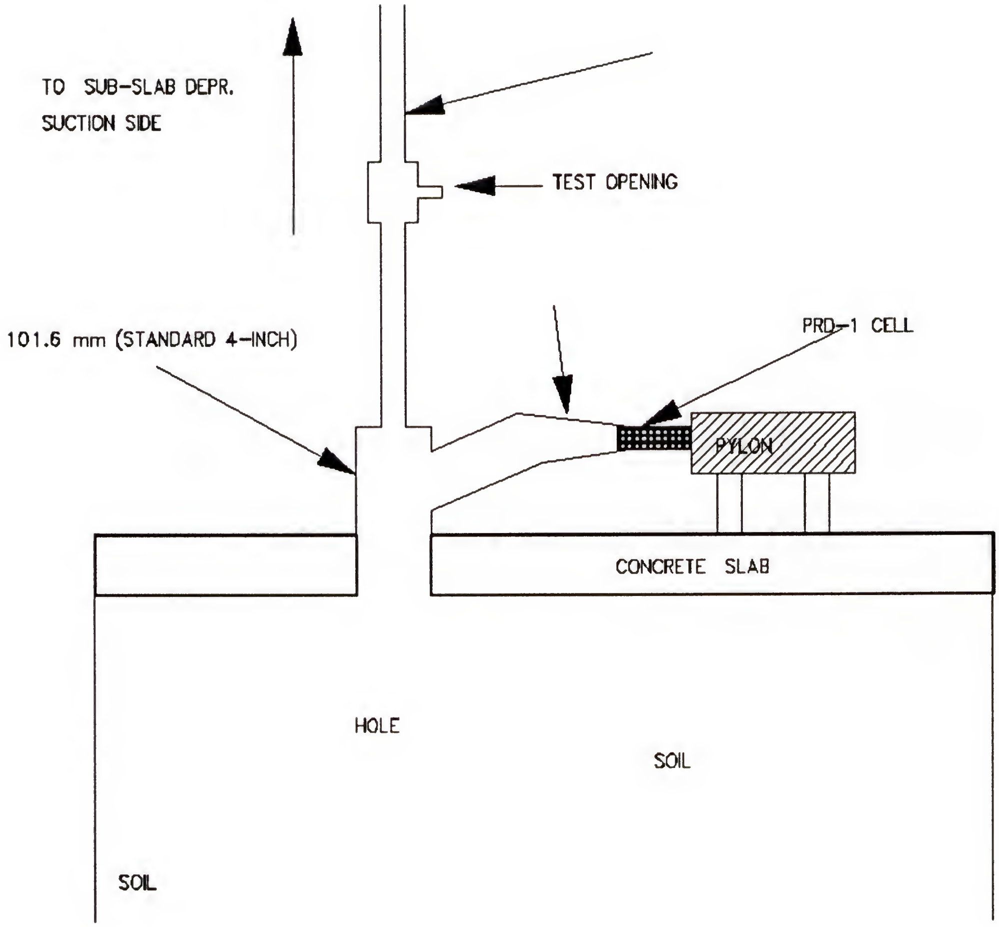
TO SUB-SLAB DEPR.
SUCTION SIDE
TEST OPENING
101.6 mm (STANDARD 4-INCH)
PRD-1 CELL
PYLON
CONCRETE SLAB
HOLE
SOIL
SOIL

FIGURE 4-4: The experimental setup of sub-slab radon concentration measurements and active soil depressurization system installation at the central hole.

approximately 4.3 times larger for the long distance in the soil configuration compared to the short distance configuration. The other important observation that can be noticed here is that the pressure difference drop at the short distance testing (66%) reaches about two thirds of the total possible drop (100%) in the first 15% of the total distance in the sub-slab soil area tested in this measurement.

These observations of the pressure difference across the UFRRH, and consequently the sub-slab air volume pressure behavior, indicate that this volume significantly dampens the pressure field as a function of the distance. Furthermore, the difference in the results of the slopes of pressure difference as a function of the sub-slab soil distance indicate that this drop is not linear. More importantly, the significant drop in the pressure that occurred for short distances in the sub-slab soil system and then slowly approach to the total possible drop suggests that the behavior of such pressure drop is exponential. This fact will be employed, in later sections, during the development of the sub-slab air volume pressure modeling structure.

The third characterization activity at the UFRRH consisted of performing a gamma ray survey. Outdoor gamma measurements were performed at the site and classified with respect to the distances from the house outside walls. Figure 4-5 illustrates the direction of movement during the measurement and the set of distances. In the north direction, parallel to the house west and east sides, two sets of readings were taken for both the front and the back of the house.

Approximate distances of 1.1 and 4.3 m (3.5 and 14 feet) from the back wall, and 1.5 and 3 m (5 and 10 feet) from the front wall were used. These distances were selected to provide most uniform measurements while accommodating obstructions such as the house porch and front entrance stairs. Measurements parallel to the north side of the house were performed on approximately 1.22 and 2.1 m (4 and 7 feet) distances from the wall. Tables 4-3 A,B, and C list the gamma ray measurement results outside the UFRRH. All outside gamma measurements were performed on the surface of the soil. Gamma testing in the UFRRH interior was performed in locations adjacent to the sub-slab tubes on a height of 1.4 meters for a period of two hours. The range of the measurement varied between 5 and 7 μR/h, and an average value of 6.2 μR/h was obtained.

Time and Spatial Dependence of Pressure Differentials

The construction of the differential pressure maps was performed by dividing the slab area into four fields and measuring the differential pressure using the sixteen tubes which penetrated through the slab into the sub-slab area, as shown in Figure 3-1. Experiments were performed to observe the time dependence of pressure differences monitored in each

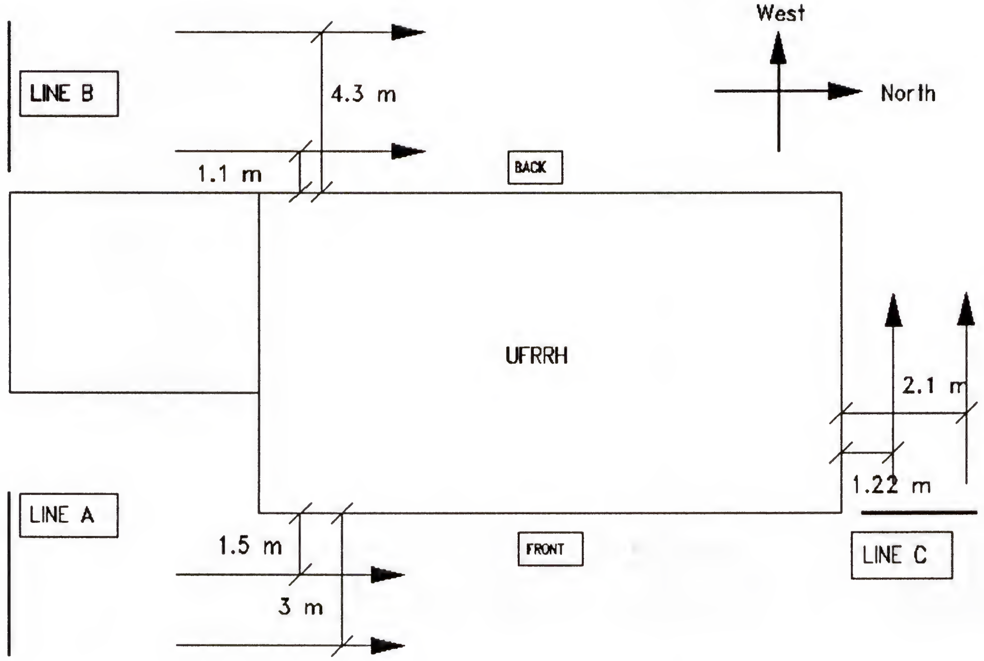
West
North
LINE B
4.3 m
1.1 m
BACK
UFRRH
2.1 m
1.22 m
LINE A
1.5 m
3 m
FRONT
LINE C

FIGURE 4-5: The distances and locations used for the initial characterization of the gamma ray field at the UFRRH.

TABLE 4-3: Results of gamma-ray survey at the UFRRH exterior.

Distance from line A (meter)	Rate μR/hr 1.5 m from the wall east side	Rate μR/hr 5 m from the wall east side
0	10	11
1.5	10	10
3	10	9
4.6	10	9
6	9	9
7.6	8	8
9.1	8	8
12.2	9	9
15.2	9	8
18.3	8	9
21.3	10	11

Distance from line B (meter)	Rate μR/hr 1.1 m from the wall west side	Rate μR/hr 4.3 m from the wall west side
0	9	11
1.5	10	11
3	9.5	12
4.6	9	12.5
9.8	8	12.5
11.3	9	12.5
13.7	11	12

Distance from line C (meter)	Rate μR/hr 1.22 m from the wall north side	Rate μR/hr 2.1 m from the wall north side
0	12	12
3	12	13
6	12	12
9.1	12	11.5

of the sub-slab tubes for different mechanically induced pressure conditions. The latter conditions were introduced and maintained by the blower door. At any point in time during the measurement period, the spatial dependence of the differential pressure across the slab can be examined from the collected data for all sub-slab points.

Experimental results collected in this research are extensive and only small sample representing a major experimental setup will be shown. Figures 4-6 A,B, and C show the time dependent behavior of the differential pressure taken at sub-slab tubes 1,2 and 3, when the house experienced depressurization to 3 Pa. Figures 4-7 A,B, and C show the pressure difference behavior for sub-slab tubes 4, 5, and 6 at indoor to outdoor pressure difference of 6 Pa. depressurization.

Figure 4-8 A,B, and C shows measurement results collected from sub-slab tubes 7, 8, and 9 when the blower door induced a depressurization of 10 Pa. Figures 4-9 A and B show the time dependent pressure differences measured at sub-slab tube 7 and 13 for 12 and 14 Pa depressurization. Examination of these figures indicates that there is a dependence between the magnitude of the pressure differences and the spatial location of the sub-slab area at all levels of depressurization applied during the experiments.

Figure 4-10 illustrates the time-averaged pressure difference (for periods of 8 hours) observed at slab-slab

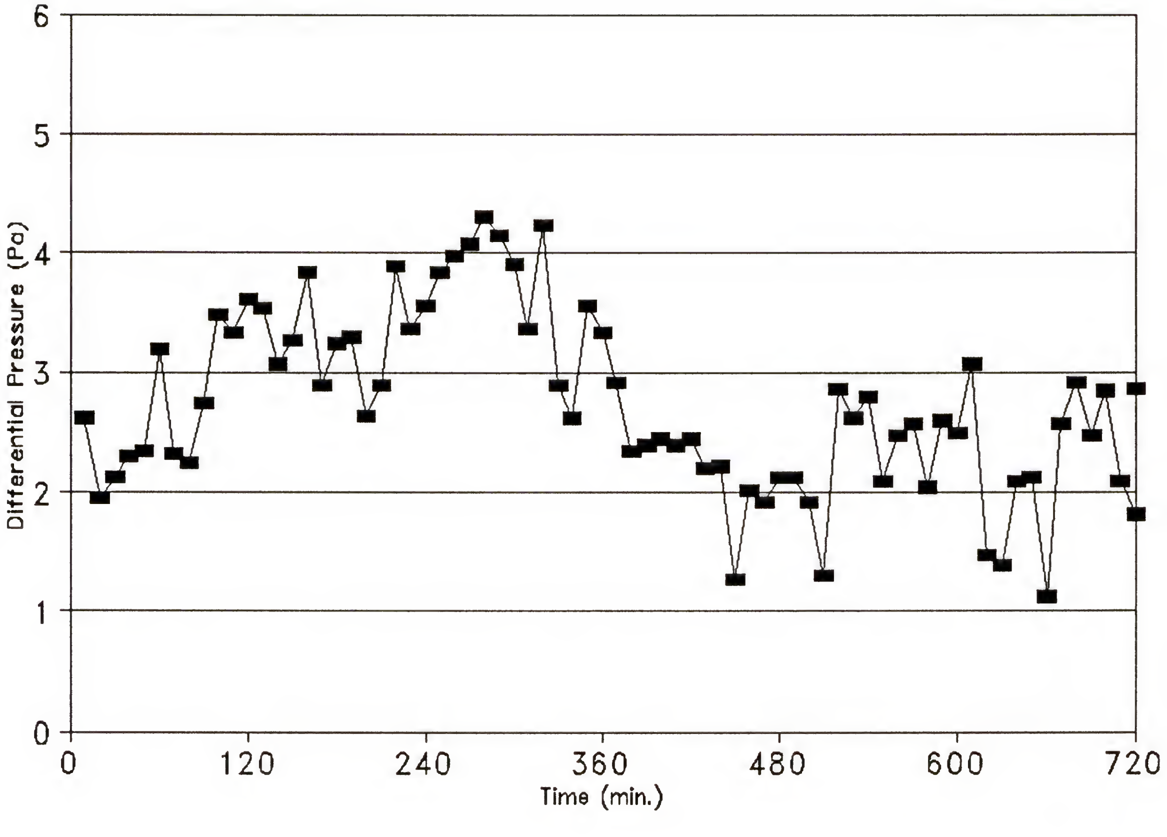

FIGURE 4-6 A: The time dependent behavior of the differential pressure across the slab measured from sub-slab tube 1, field 1, when the structure is subject to 3 Pa depressurization.

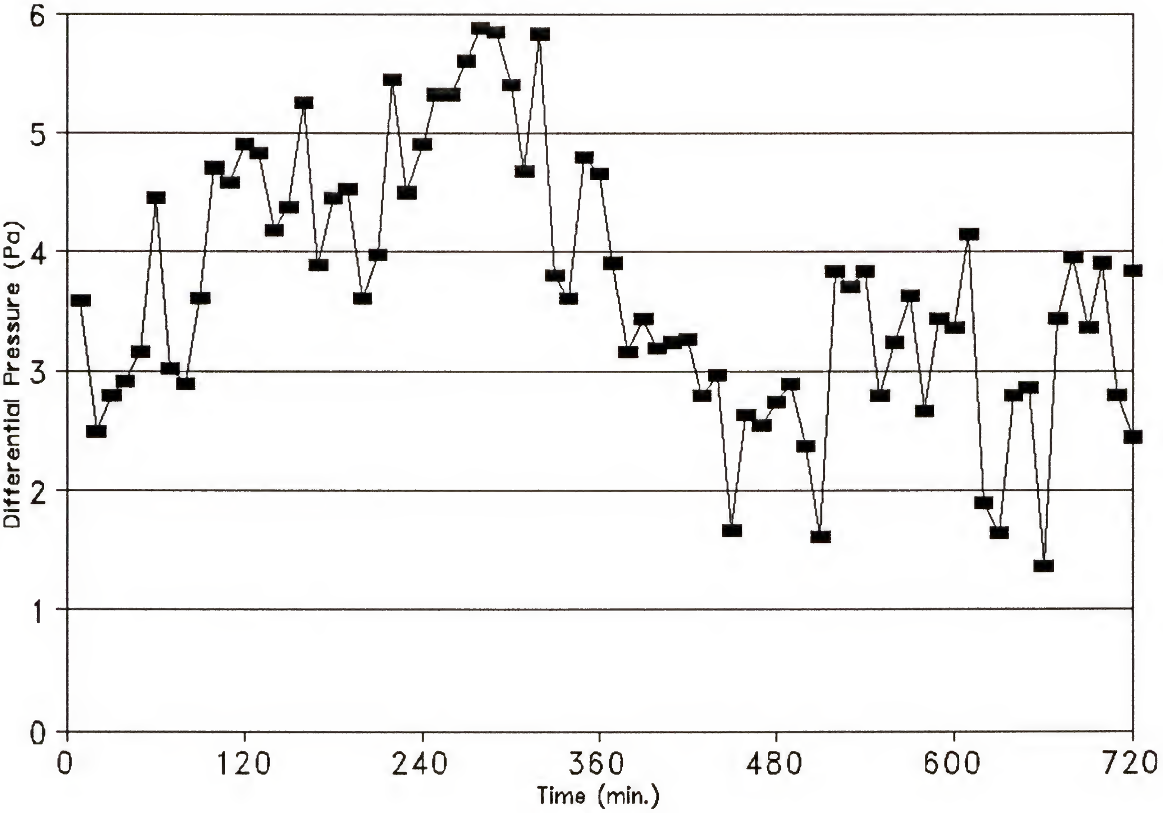

FIGURE 4-6 B: The time dependent behavior of the differential pressure across the slab measured from sub-slab tube 2, field 1, when the structure is subject to 3 Pa depressurization.

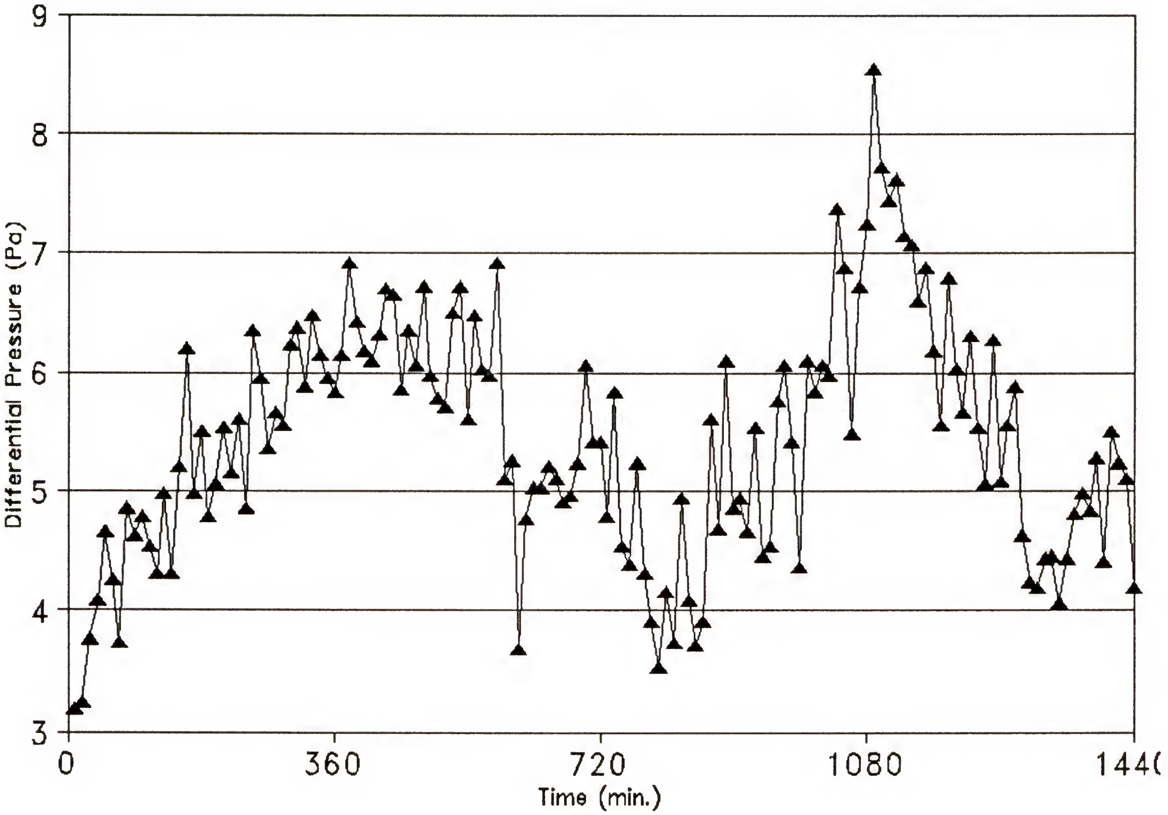

FIGURE 4-6 C: The time dependent behavior of the differential pressure across the slab measured from sub-slab tube 3, field 1, when the structure is subject to 3 Pa depressurization.

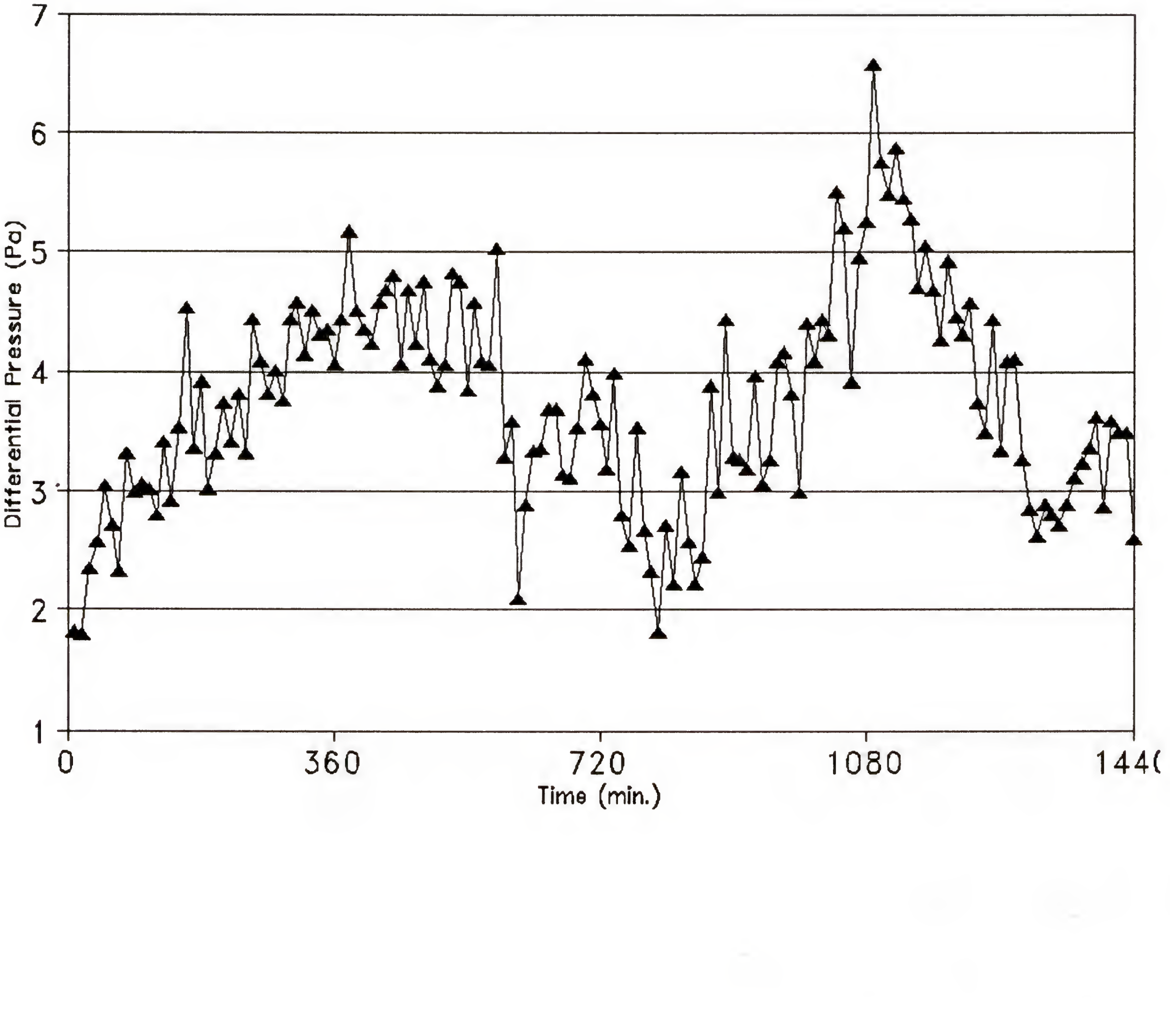

FIGURE 4-7 A: The time dependent behavior of the differential pressure across the slab measured from sub-slab tube 4, field 2, when the structure is subject to 6 Pa depressurization.

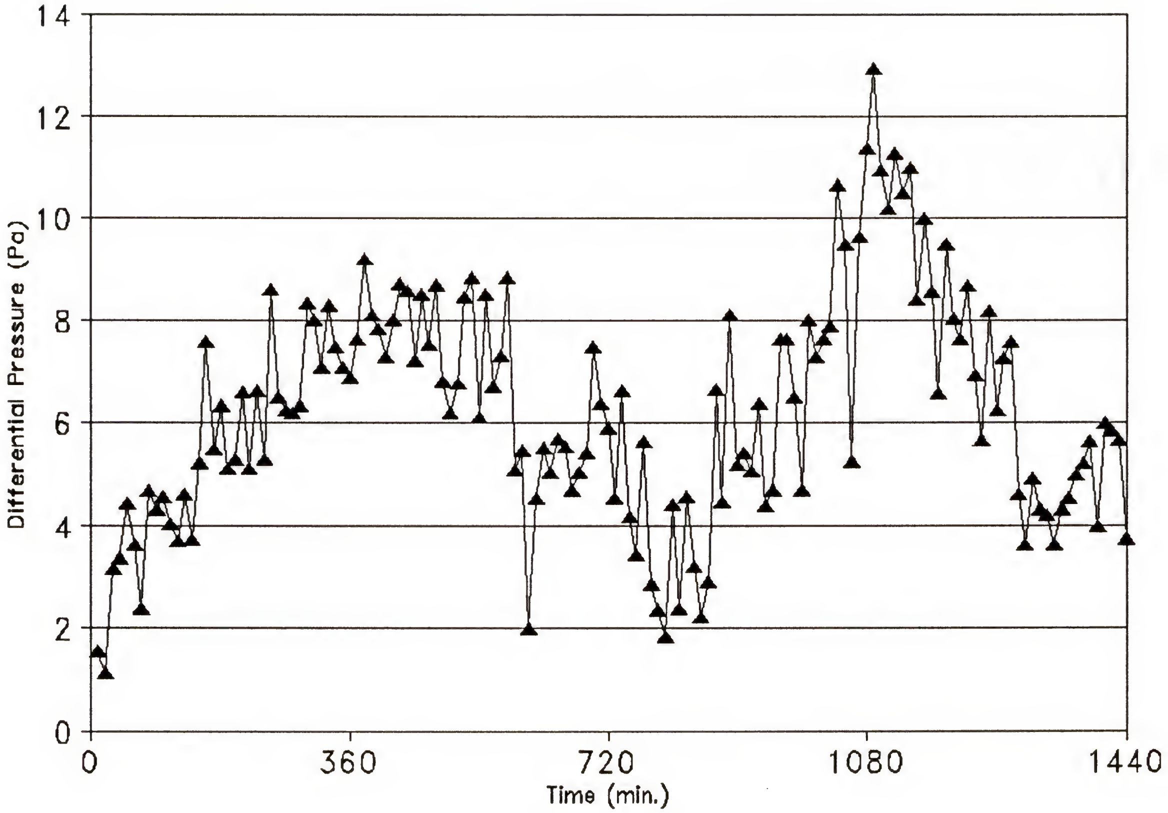

FIGURE 4-7 B: The time dependent behavior of the differential pressure across the slab measured from sub-slab tube 5, field 2, when the structure is subject to 6 Pa depressurization.

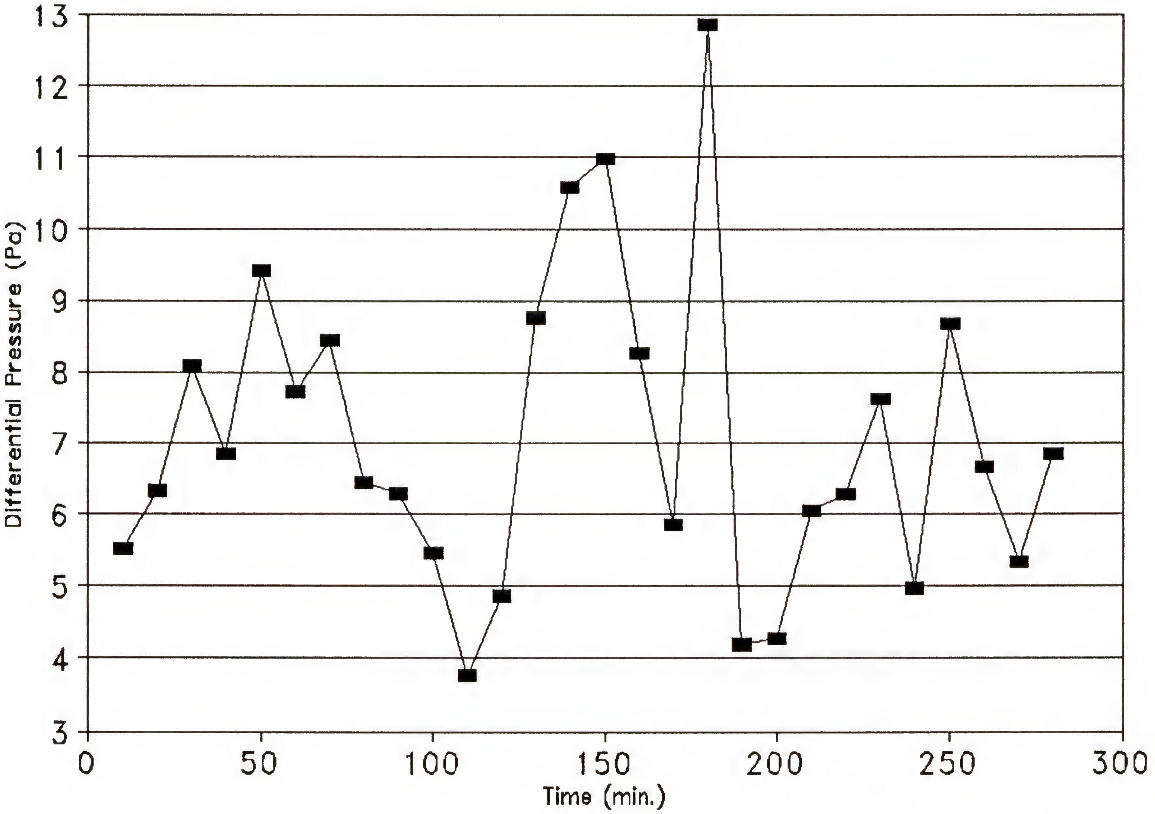

FIGURE 4-7 C: The time dependent behavior of the differential pressure across the slab measured from sub-slab tube 6, field 2, when the structure is subject to 6 Pa depressurization.

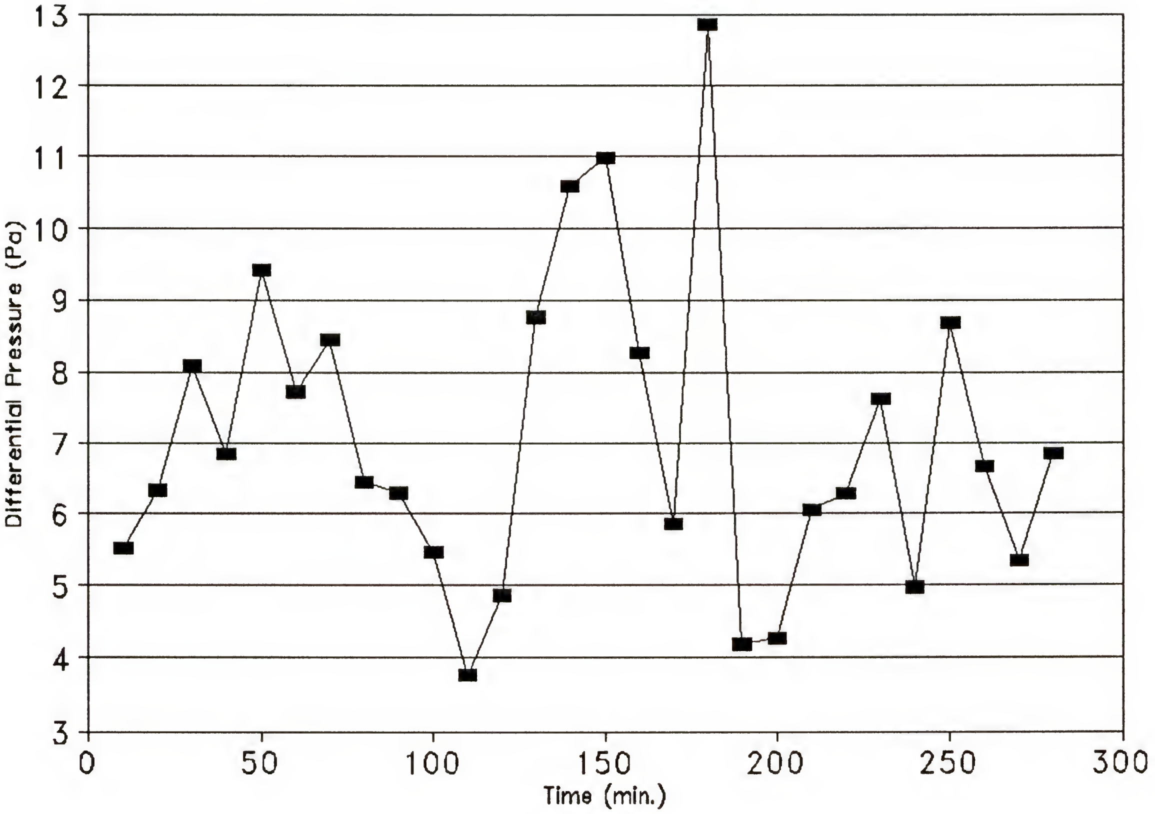

FIGURE 4-8 A: The time dependent behavior of the differential pressure across the slab measured from sub-slab tube 7, field 3, when the structure is subject to 10 Pa depressurization.

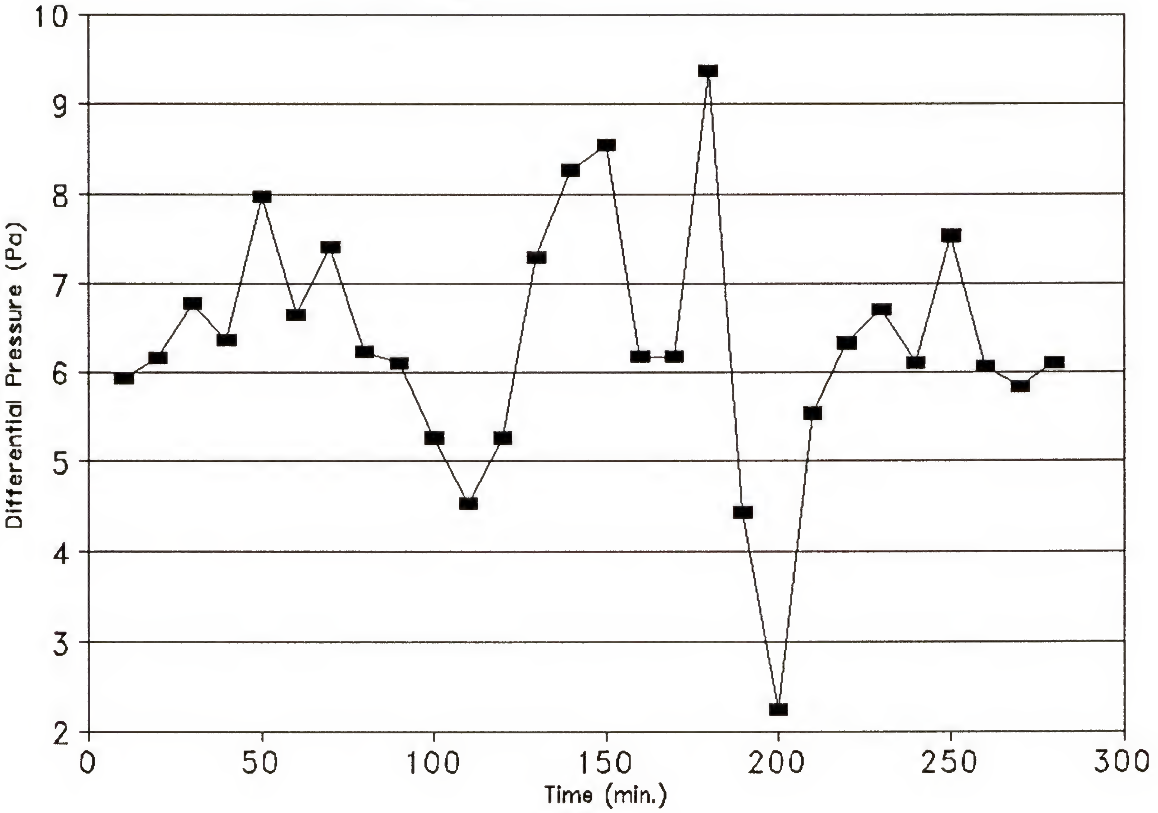

FIGURE 4-8 B: The time dependent behavior of the differential pressure across the slab measured from sub-slab tube 8, field 3, when the structure is subject to 10 Pa depressurization.

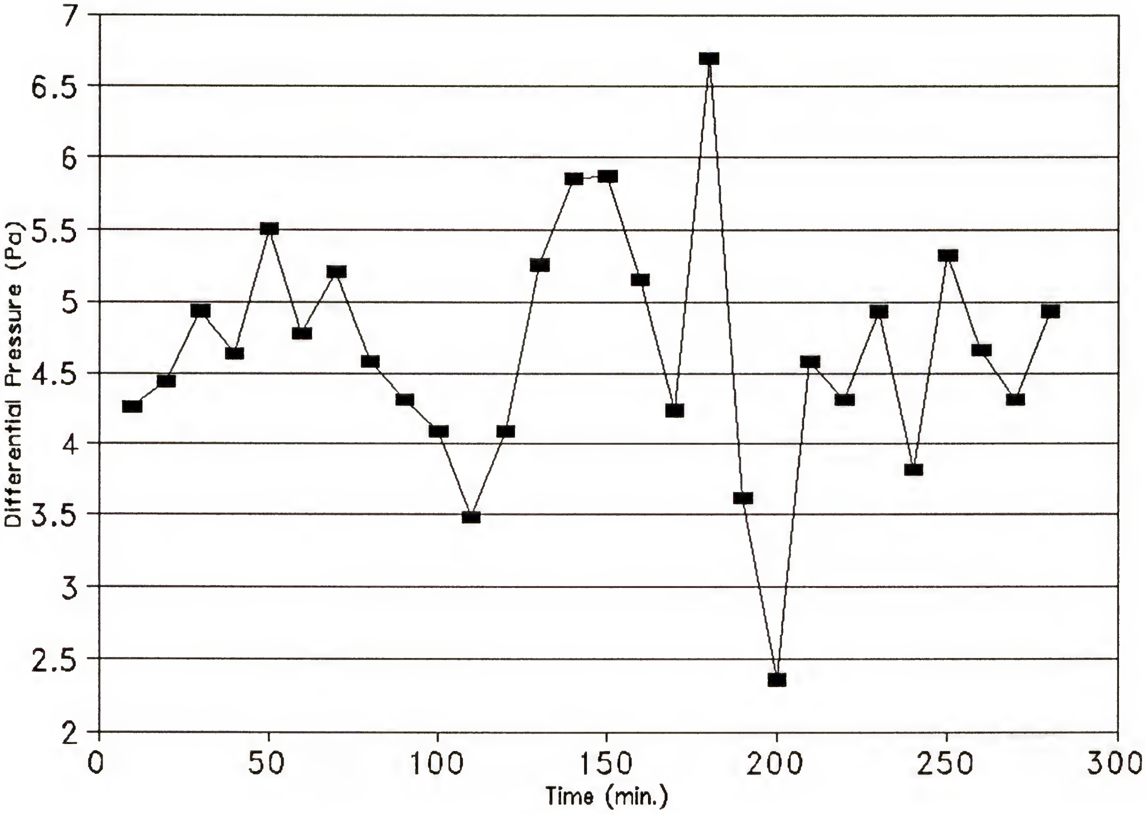

FIGURE 4-8 C: The time dependent behavior of the differential pressure across the slab measured from sub-slab tube 9, field 3, when the structure is subject to 10 Pa depressurization.

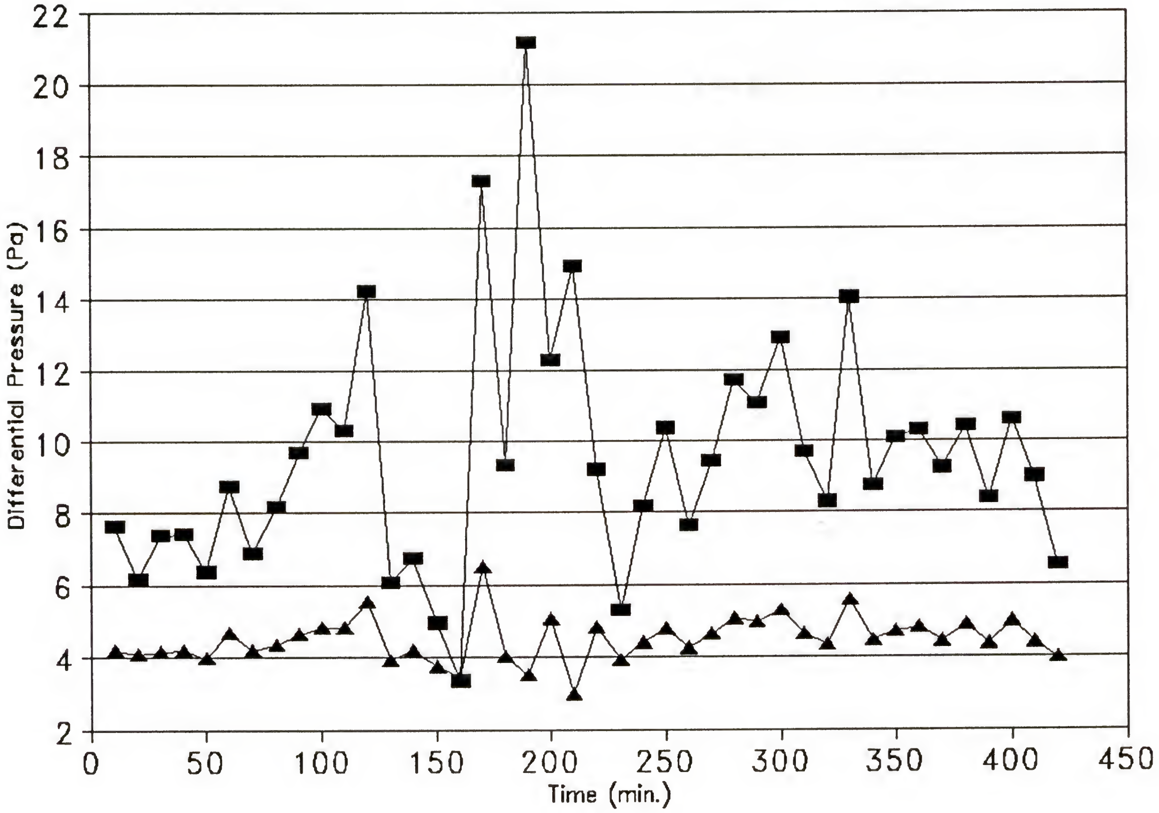

FIGURE 4-9 A: The temporal variations of differential pressure monitored from sub-slab access locations 7 (square) and 13 (triangle) when the structure experiences a depressurization of 12 Pa.

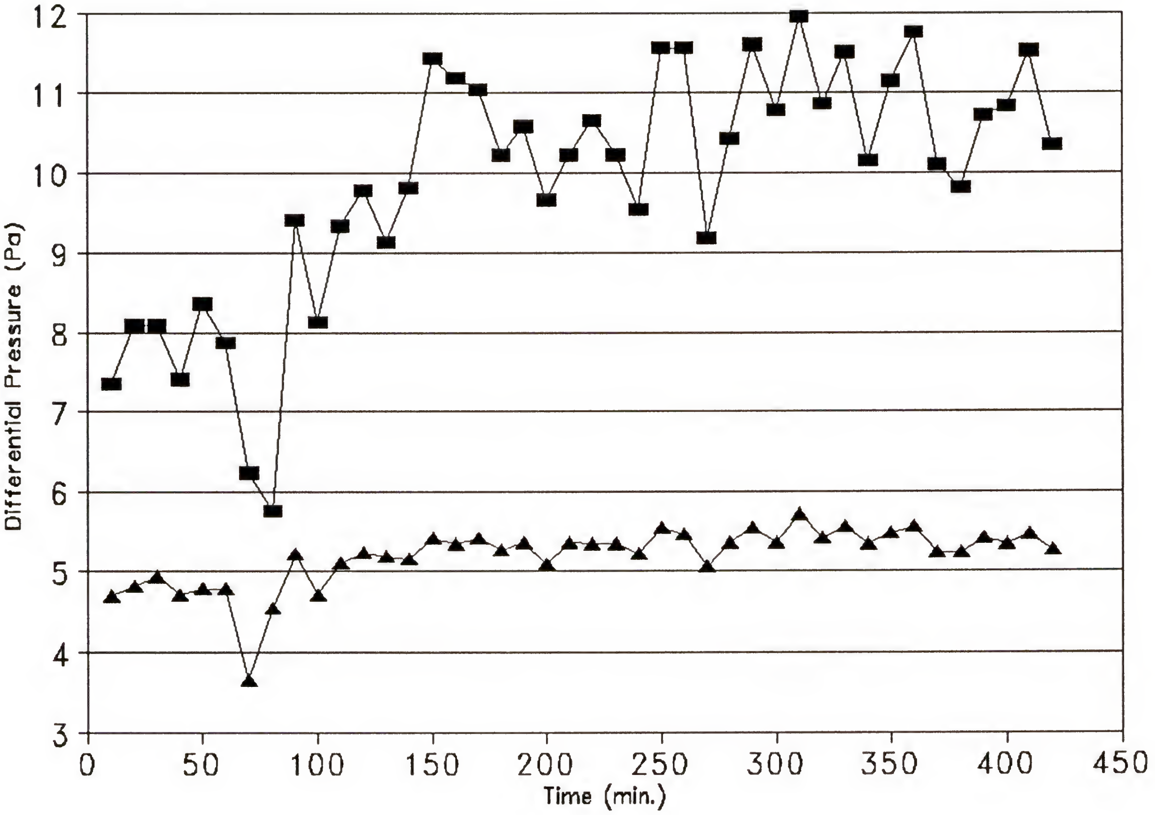

FIGURE 4-9 B: The temporal variations of differential pressure monitored from sub-slab access locations 7 (square) and 13 (triangle) when the structure experiences a depressurization of 14 Pa.

point 9 when the house is subject to depressurizations of 2, 4, 6, 8, 10, 12 and 14 Pa, respectively. This figure indicates a linear relationship between the structure depressurization, i.e., the indoor/outdoor differential pressure, and the time-averaged differential pressure that was generated across the foundation slab due to depressurization.

The time-averaged value of pressure differentials across the slab is expected to reach zero under the theoretical conditions of exact out-of-phase fluctuations around a reference line that might correspond to a constant component in the responses. However, the results illustrated in Figure 4-10 indicate that there is a slight linear dependence toward increasing magnitudes of the time-averaged pressure difference across the slab as the magnitude of indoor depressurization increases.

This result suggests that the percentage of the out-of-phase alternating fluctuations in the pressure difference cycle across the slab increases with indoor depressurization. This behavior induces a greater contribution to the soil-gas driving force across the slab into the indoor for a larger magnitude of indoor depressurization. Based on this observation and the time dependent behavior of pressure differences across the slab, one can conclude that increasing the magnitude of structure depressurization increases soil gas radon entry into structures not only by increasing the driving

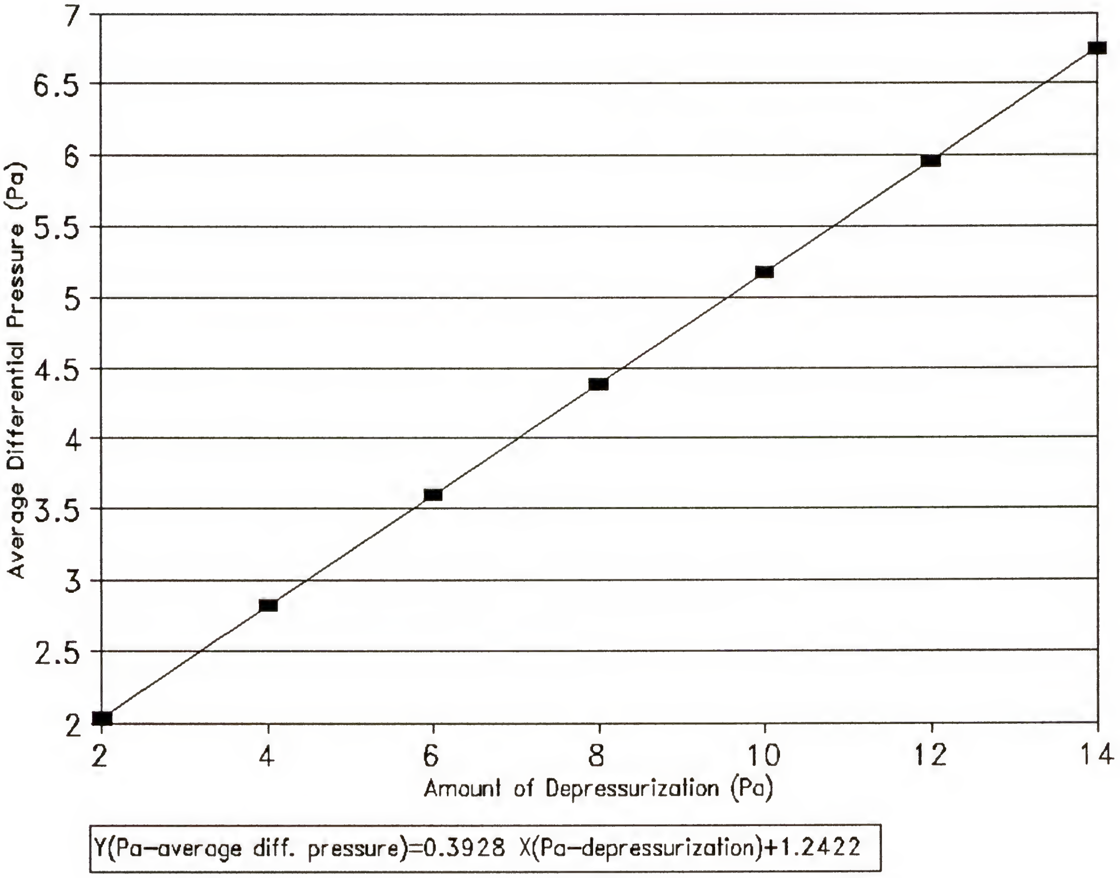

FIGURE 4-10: The linear relationship between the time-averaged differential pressures measured from sub-slab location 9.

forces, but also by increasing the contributions of the pressure cycle differences across the slab.

During these experiments, pressure differences generated across the walls were also monitored. The amplitudes of these differences were found to be of a magnitude similar to the magnitude of pressure difference across the house shell developed by the blower door. However, some fluctuation could still be seen around the time-averaged value of the response. Figures 4-11 A and B show samples of a one-day response monitored when the blower door was applying 6 Pa depressurization between the house interior and the outdoors. Unlike the differential pressure across the slab, these pressure differences show clear bias towards the pressure difference developed by the blower door.

The time-averaged values of the responses in Figures 4-11 A and B are -5.7 Pa and -6 Pa, respectively. Figure 4-11 B shows the response across the west side wall of the house, the same wall where the blower door is installed, while Figure 4-11 A shows the response across the east wall of the house. These responses and others collected in analogy to other depressurization testing activities suggest three observations. First, pressure differences across the wall closely follow the pressure differences that are mechanically induced by the blower door, evident from the time averaged values of these responses which are very similar to the pressure difference developed by the blower door. This observation was found for all depressurization levels ranging from 2 Pa to 40 Pa; therefore, any pressure differences but the blower door component are relatively weak when compared with the differential pressure across the slab.

Second, even though pressure differences across the wall are strongly driven by the blower door, a small amplitude fluctuation around the averaged component can still be observed indicating the existence of another independently driving force component. The latter component follows a pattern which can be described as diurnal.

Third, the independent component is not developed from wind since two opposite walls of the house show very similar phase responses in all the measurements. These observations leave the temperature cycle as the candidate independent driving force of the fluctuations around time-averaged responses of the differential pressure across the structure shell.

The spatial dependence of the pressure difference measurements can be examined from the 16-point grid pattern tubes distributed across the slab at a specific point in time. Figures 4-12 A and B illustrate the tendency of differential pressure across the slab spatial dependence. As seen from the graphs (4-6, 4-7, 4-8, 4-9, and 4-11), pressure measurement at sub-slab tube locations 1, 2, 3, 4, 5, 8, 9, 12, 13, 14, 15, and 16 experienced time averaged values smaller than locations 6, 7, 10, and 11. This indicates that the mechanically

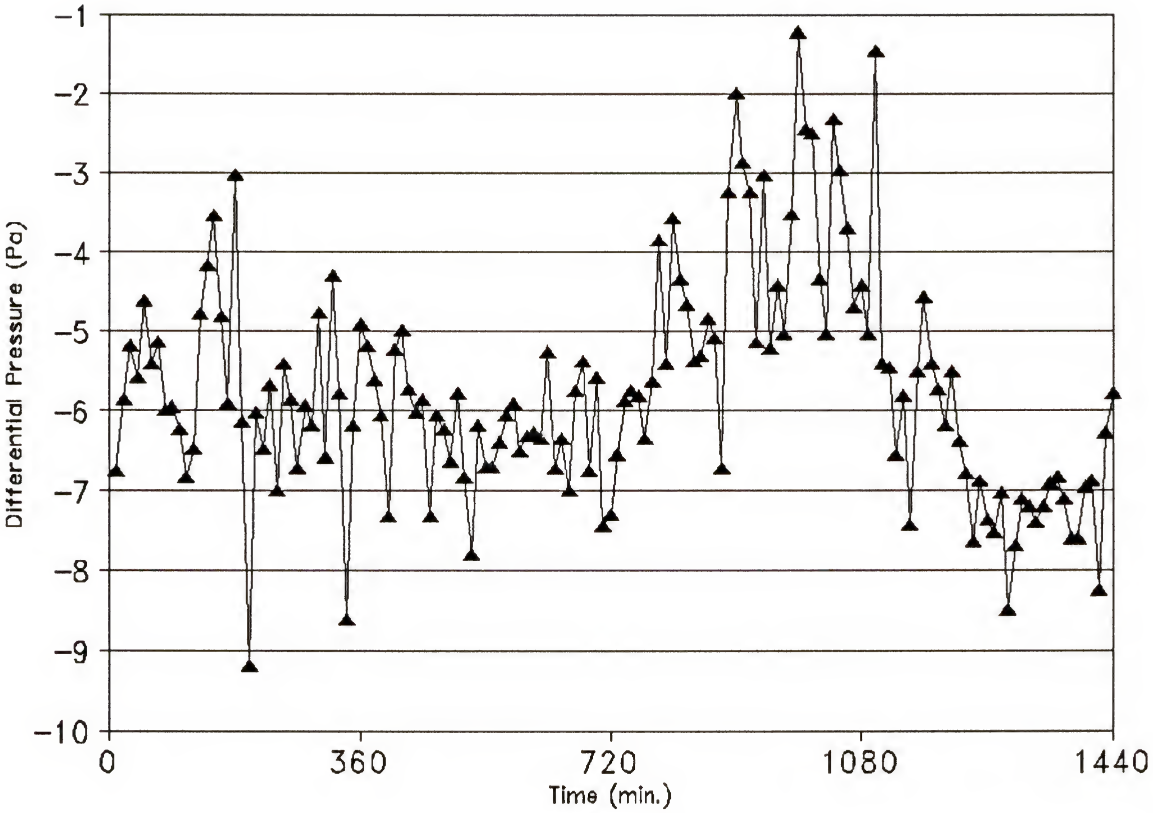

FIGURE 4-11 A: A sample of the temporal variations of differential pressure across the east wall of the UFRRH when the structure is subject to 6 Pa depressurization.

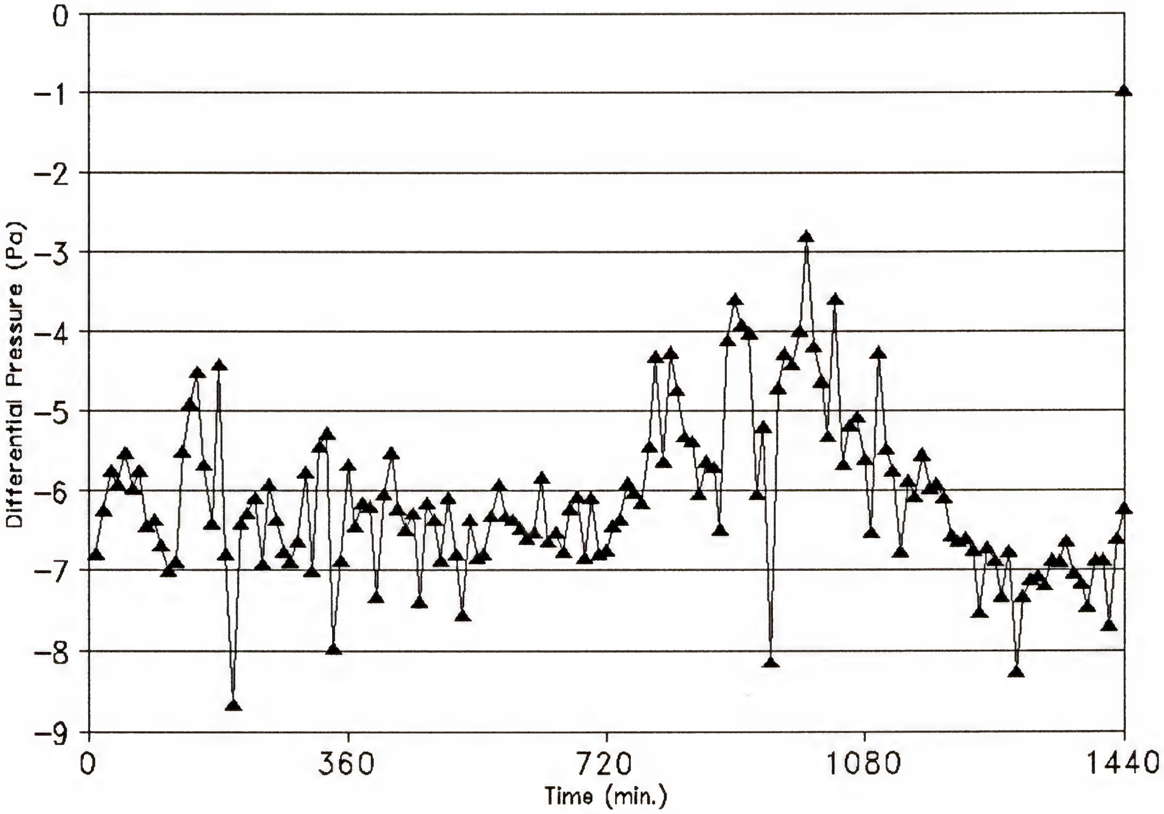

FIGURE 4-11 B: A sample of the temporal variations of differential pressure across the west wall of the UFRRH when the structure is subject to 6 Pa depressurization.

induced pressure differences generated across the central area of slab between the indoor and outdoors is greater than that generated near the slab edge.

To better visualize the pressure difference distribution across the slab, differential pressure maps can be developed from the testing grids for any point in time. The differential pressure maps of the sub-slab area when the whole house is maintained at a constant 10 Pa by depressurization and pressurization relative to the outdoors are shown in Figures 4-13 A and B, respectively. As seen in the graph, the differential pressure across the center line of the slab and the center area exhibits a greater magnitude than at the slab margins. This is expected because of the slab-soil interface around the slab perimeter. The interaction of the sub-slab area with the outdoors is different near the slab edge versus the center because of the soil permeability and under-structure fill materials. Notice that the differential pressure transmitter pressure magnitudes (above the zero base line) represent the indoor depressurization relative to the sub-slab.

Maintaining various steady, mechanically induced pressure difference levels between the indoor and outdoor has shown similar profiles in the differential pressure maps across the slab with different scaling. If the indoor pressure is uniform throughout the house, then the differential pressure

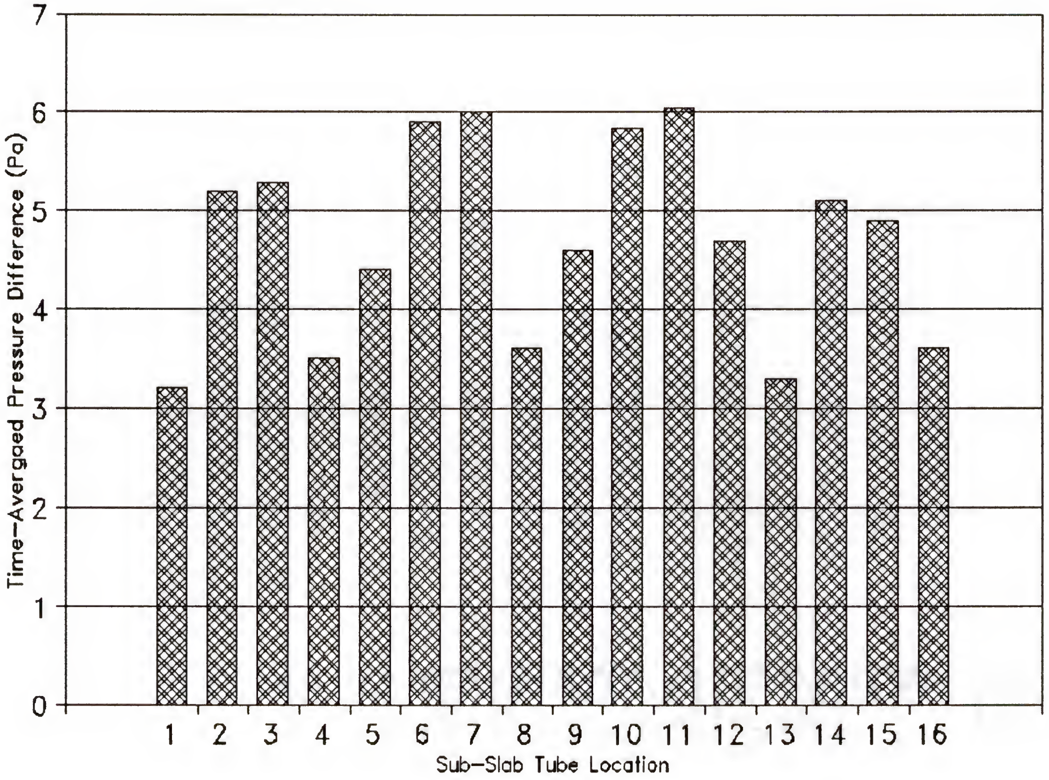

FIGURE 4-12 A: The tendency of spatial dependence of the time-averaged differential pressure across the slab for a structure pressure condition of -6 Pa.

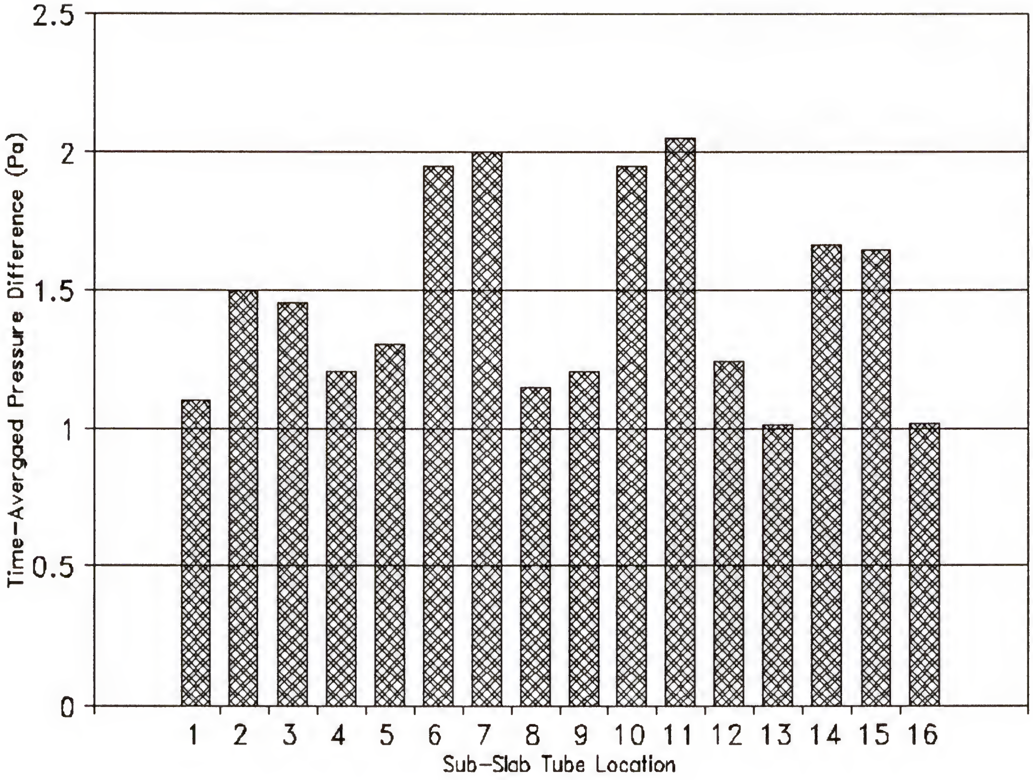

FIGURE 4-12 B: The tendency of spatial dependence of the time-averaged differential pressure across the slab for a structure pressure condition of -2 Pa.

map represents the spatial distribution of the sub-slab air volume pressure.

Upon observation of the differential pressure maps across the UFRRH, however, it is seen that the sub-slab air volume pressure is not equivalent to the outdoor pressure, at least for certain time intervals. The induced uniform indoor pressure across the slab is associated with a nonuniform pressure distribution in the sub-slab area. In fact, the profiles in Figure 4-13 represent the nonuniform differential pressure maps of the sub-slab area shifted and scaled by a constant for different indoor pressure levels.

After examining the time and spatial dependence of pressure differences developed by mechanically induced depressurization or pressurization, examination of the behavior of pressure differences under conditions of no mechanically induced pressures were needed to better resolve the independent component that seemed to exist in the pressure difference responses. These components in particular produce the semi-diurnal behavior in the pressure differentials across the slab and a diurnal behavior in the pressure differential across the structure shell.

Experiments similar to the ones described above were performed under neutral pressure conditions. These conditions are defined to exist when there are no sources of mechanical pressurization or depressurization operating in the structure. Such sources include, but are not limited to, blower doors,

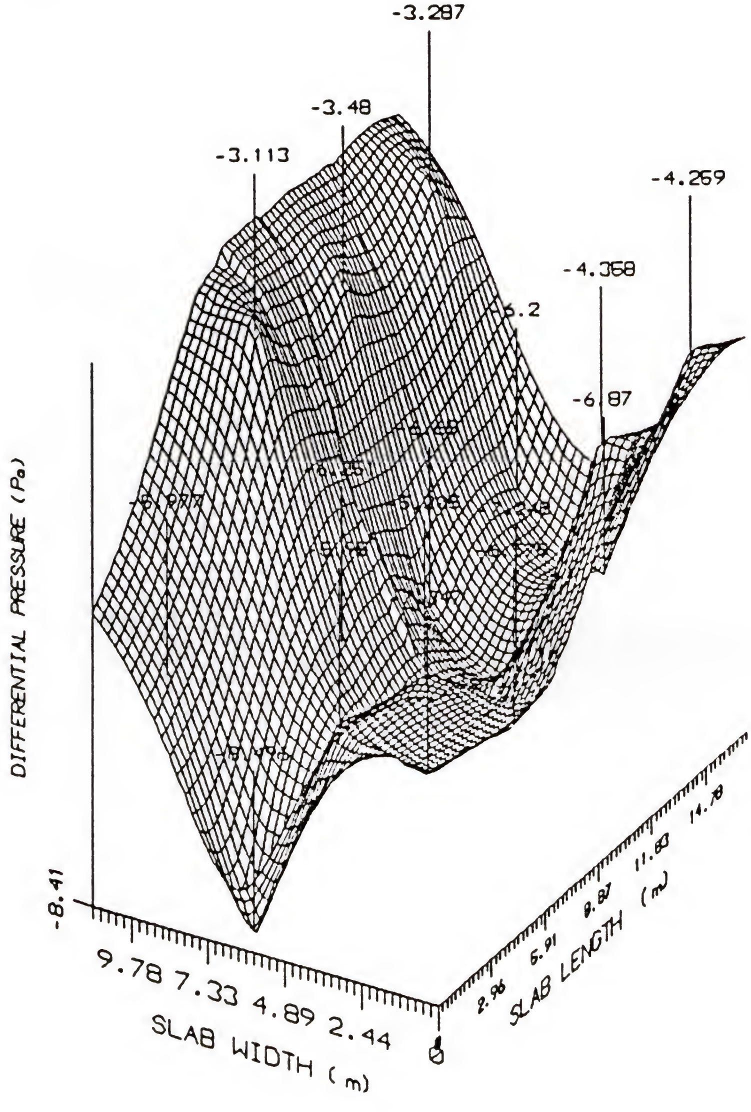

FIGURE 4-13 A: The differential pressure map across the slab when the structure is under 10 Pa depressurization.

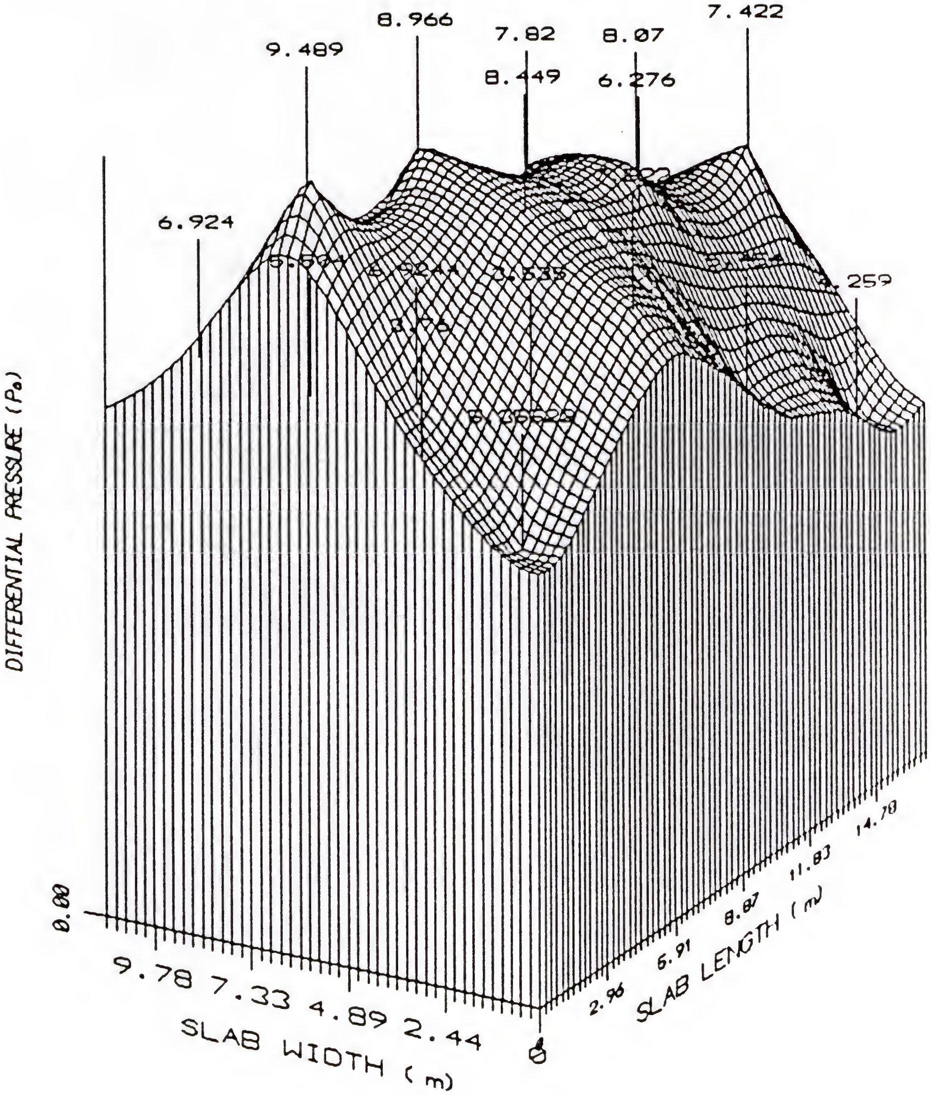

FIGURE 4-13 B: The differential pressure map across the slab when the structure is under 10 Pa pressurization.

suction fans, HVAC systems, fire places, and other household appliances that might cause a pressure difference between the structure interior and the outdoor exceeding one pascal.

Figures 4-14, A to H show the time-dependent pressure difference responses for a period of two days. Two sub-slab locations are shown for each of the four pressure fields of the UFRRH slab. Measurements collected from sub-slab tubes 1 and 4 in field 1; 6 and 8 in field 2; 9 and 12 in field 3; and 14 and 16 in field 4 are shown in the graphs A to H of Figure 4-14, respectively. In all pressure differential responses across the slab in the above figures and in similar measurements performed at the UFRRH, a semi-diurnal periodicity was observed. This cycle has a high and a low peak in any given 12-hour period. Since such a cycle was experienced under all structure pressure conditions, it must derive from an independent component associated with pressure changes. This observation will be utilized in a later section during the construction of the sub-slab area air volume pressure and the differential pressure driving forces modeling.

Time and Spatial Dependence of Radon Concentrations

Time and spatial dependent measurements of indoor radon and sub-slab soil gas radon concentrations were simultaneously performed with the other monitored parameters. The relationship of indoor radon concentrations to the structure pressure condition is to be studied here. Measurements were designed to observe the effects of mechanically induced pressure conditions, neutral pressure conditions, operation of the household appliances such as the HVAC system, and configuration of the indoor environment such as the opening and closing of interior doors.

Figures 4-15 A and B show a 2.5-day sample of time-dependent sub-slab radon concentration collected at the structure center hole, and the simultaneous indoor radon concentration collected at the house when all the systems were off. The latter plot represents the spatial averages of the indoor radon concentration collected by three Pylons with passive diffusive radon detector cells. For the same configuration of an all-system-off run condition, Figures 4-16 A, B, C, and D illustrate the corresponding differential pressures measured across the slab.

A similar fluctuation, but with smaller amplitudes, was observed for radon concentrations measured from a tube access to the sub-slab area. Figure 4-17 shows these concentrations measured from sub-slab tube 7 in field 2. Generally radon concentrations measured at sub-slab access locations are about six to eight orders of magnitude smaller than sub-slab concentrations measured at the structure central hole, depending on the particular spatial location under the slab.

In Figure 4-17, the radon concentration measured from tube 7, was multiplied by an arbitrary factor of seven so it

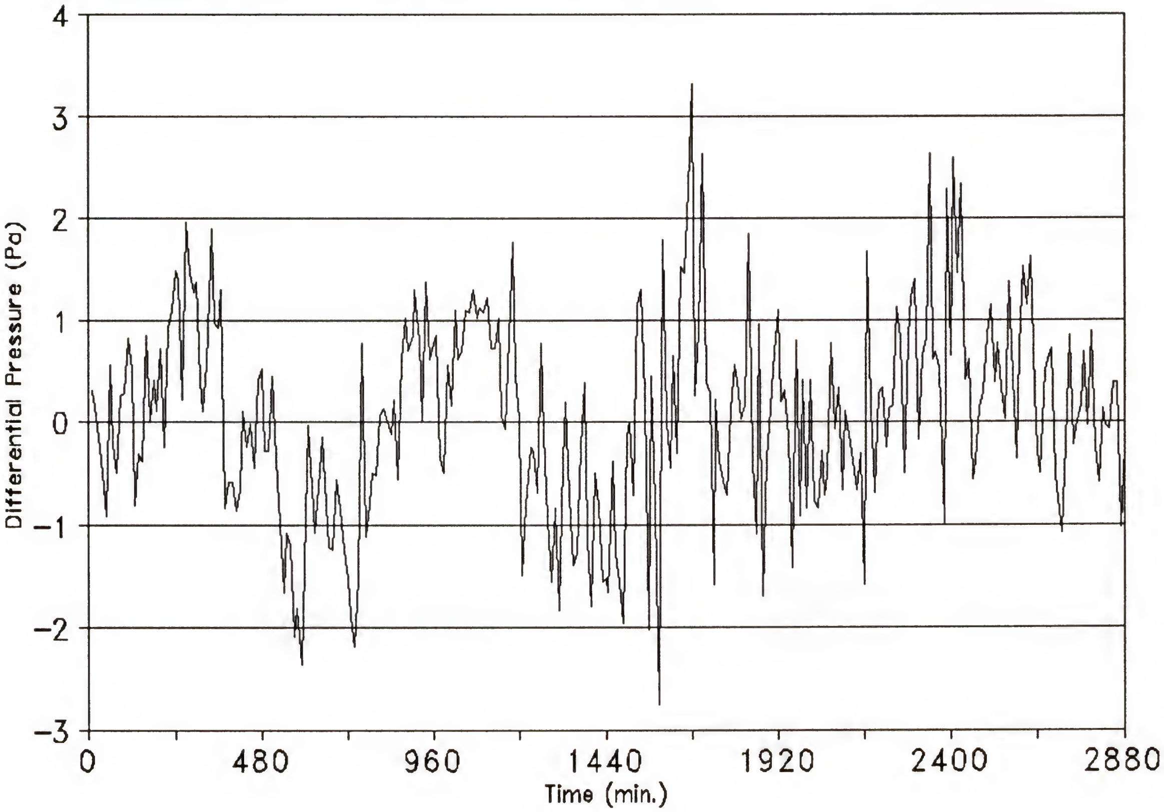

FIGURE 4-14 A: A 2-day sample of temporal variations of pressure differences measured across the slab at location 1, field 1, under neutral pressure conditions.

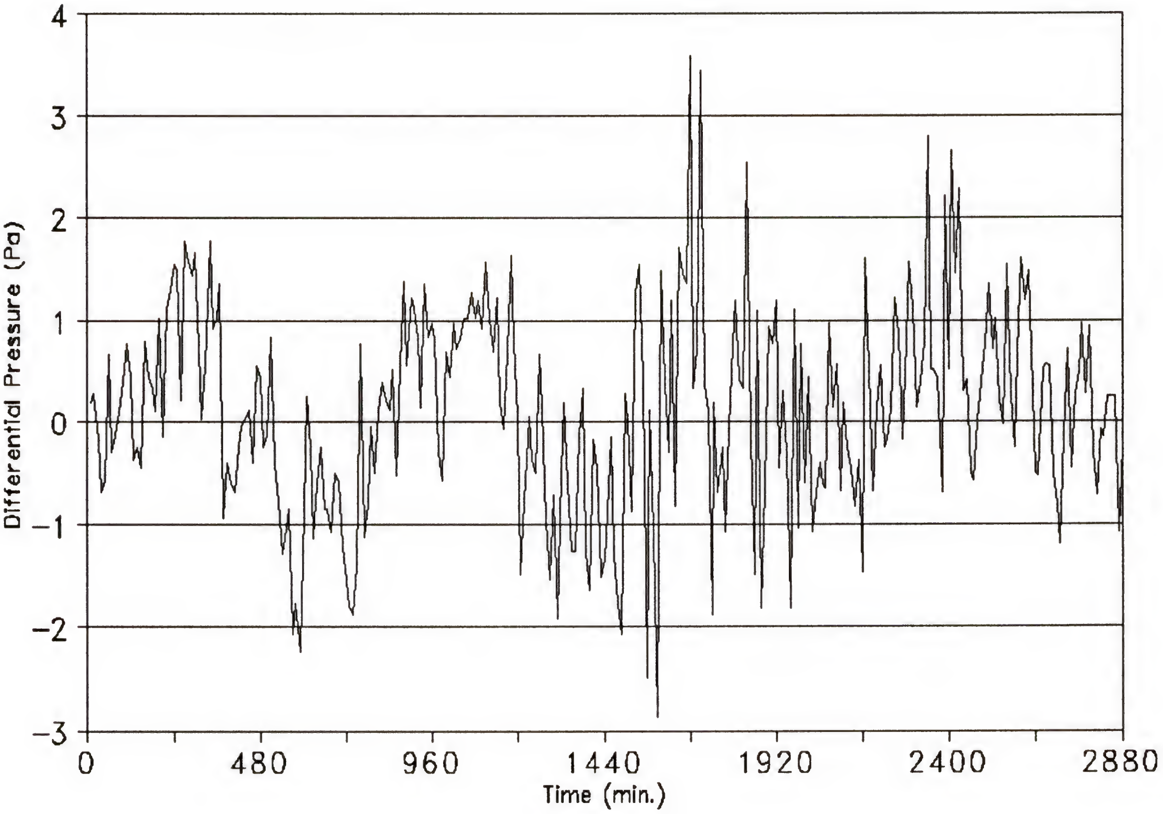

FIGURE 4-14 B: A 2-day sample of temporal variations of pressure differences measured across the slab at location 4 field 1, under neutral pressure conditions.

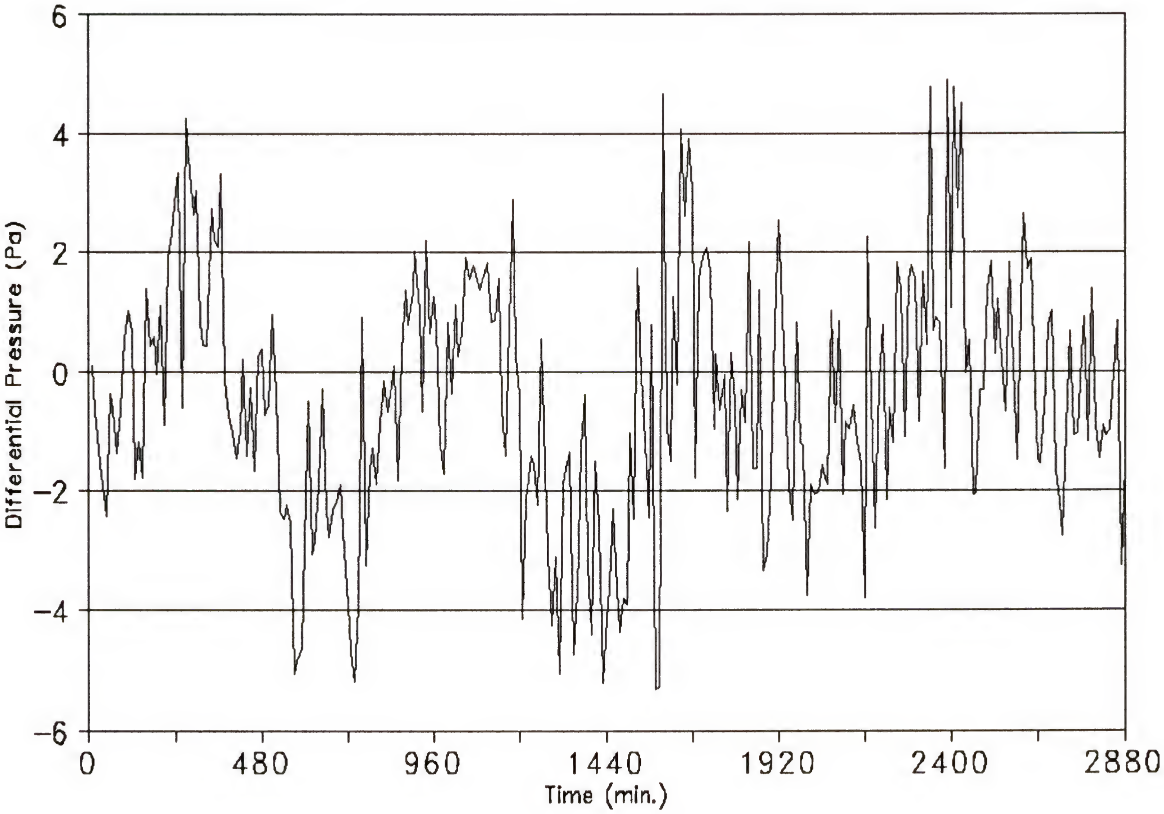

FIGURE 4-14 C: A 2-day sample of temporal variations of pressure differences measured across the slab at location 6 field 2, under neutral pressure conditions.

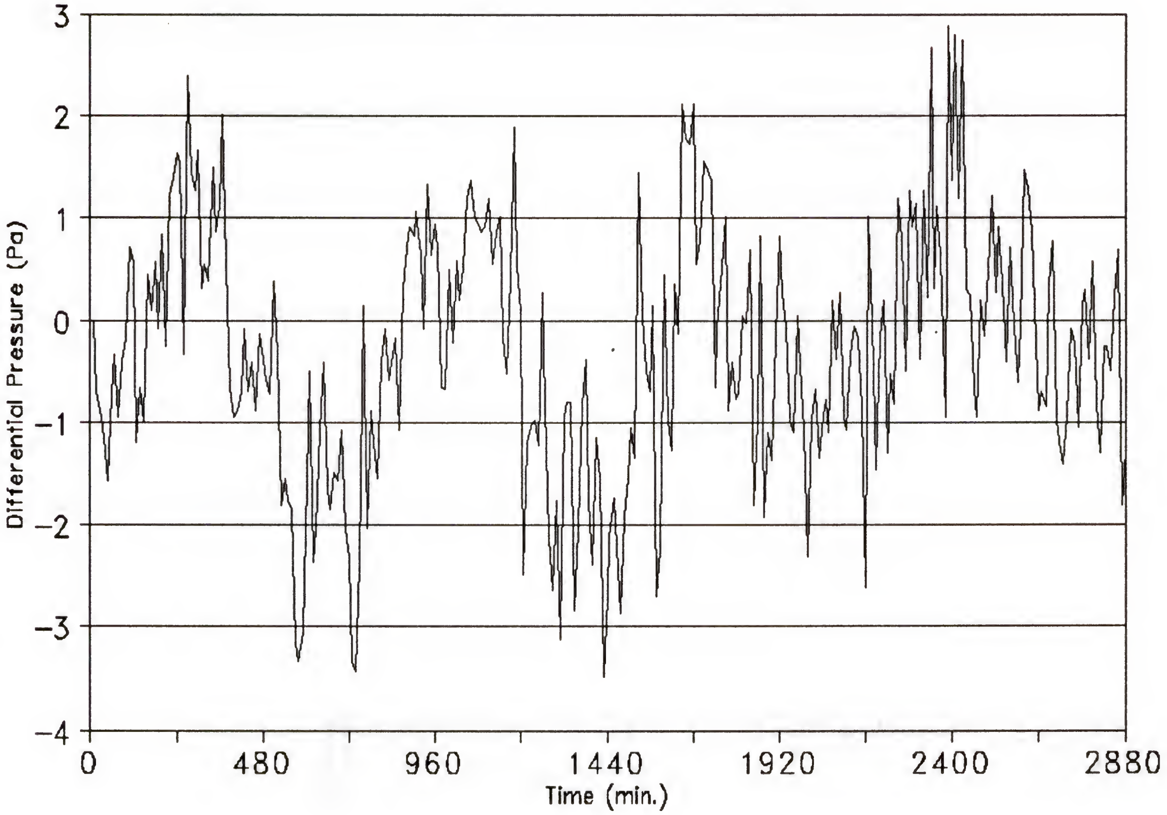

FIGURE 4-14 D: A 2-day sample of temporal variations of pressure differences measured across the slab at location 8 field 2, under neutral pressure conditions.

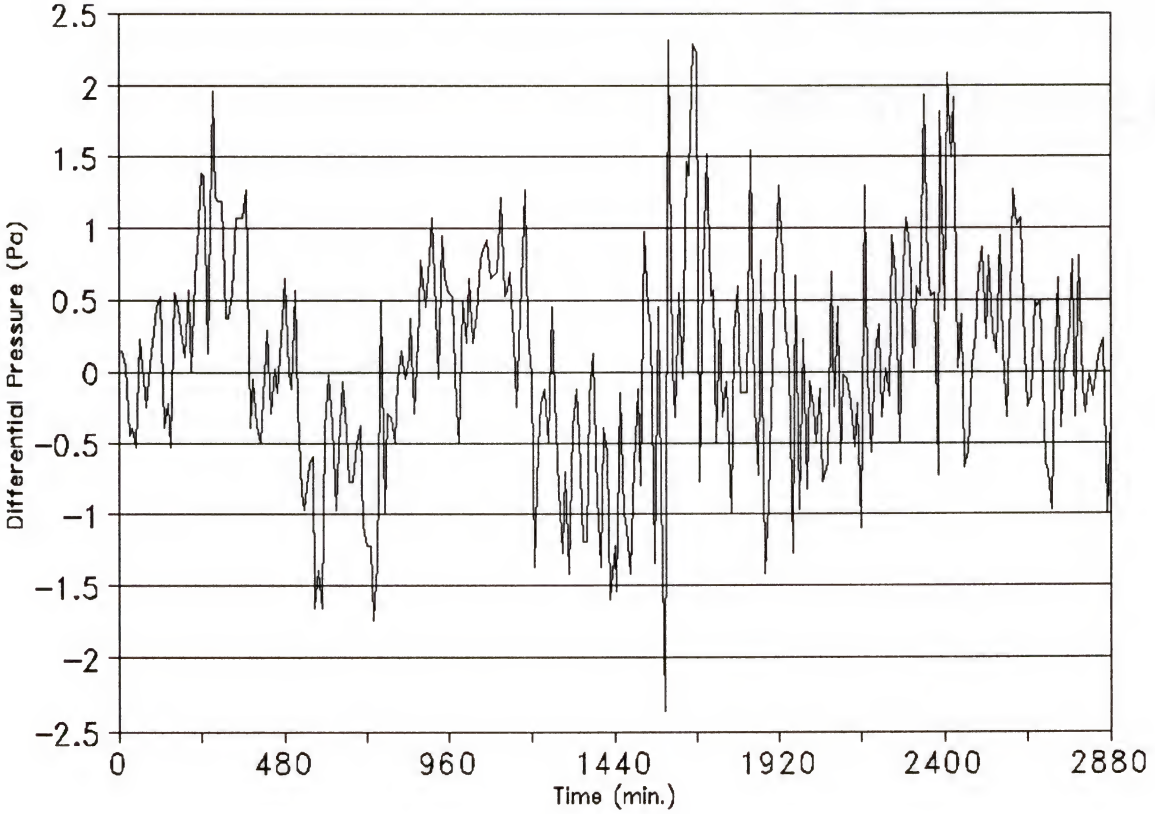

FIGURE 4-14 E: A 2-day sample of temporal variations of pressure differences measured across the slab at location 9 field 2, under neutral pressure conditions.

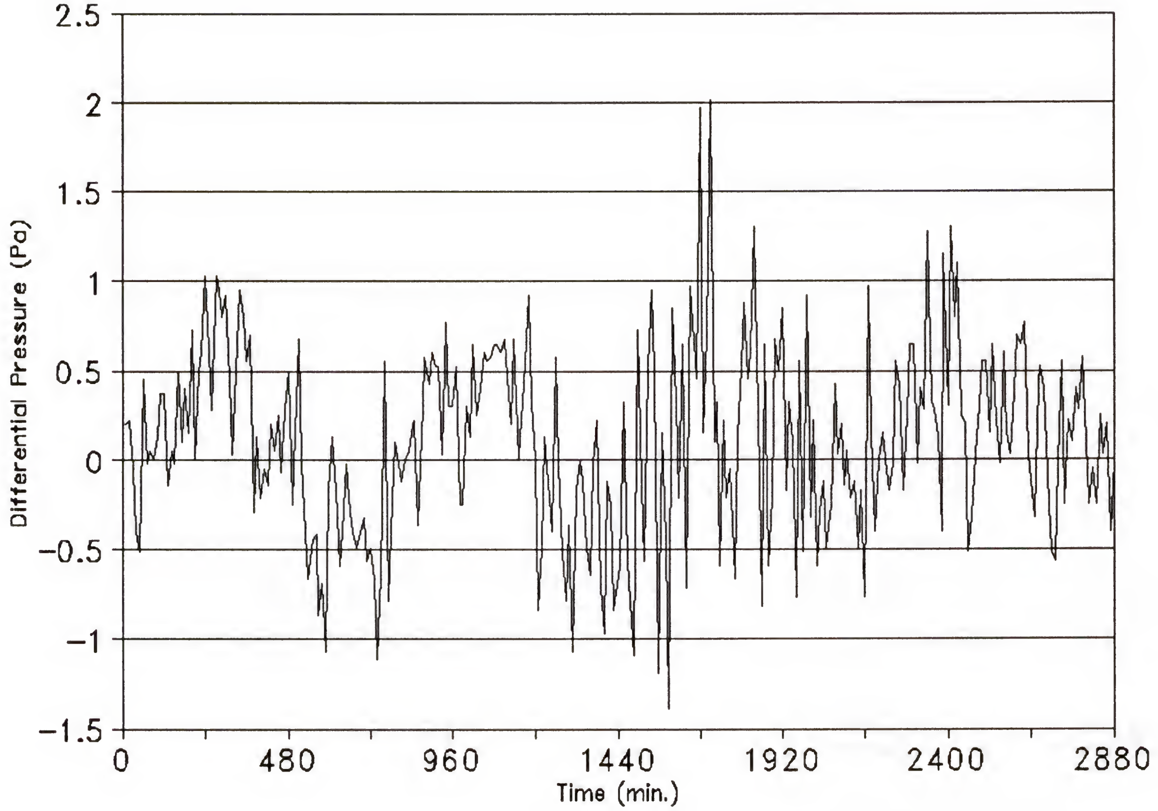

FIGURE 4-14 F: A 2-day sample of temporal variations of pressure differences measured across the slab at location 12 field 3, under neutral pressure conditions.

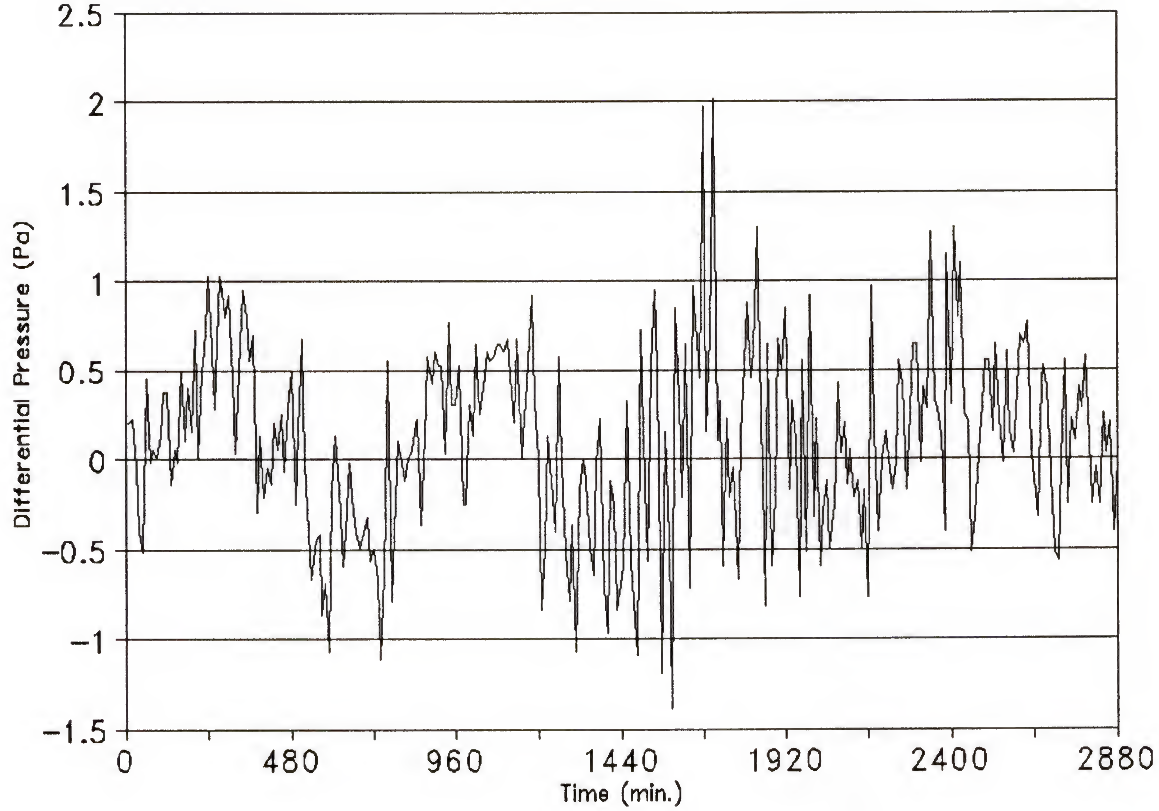

FIGURE 4-14 G: A 2-day sample of temporal variations of pressure differences measured across the slab at location 14 field 4, under neutral pressure conditions.

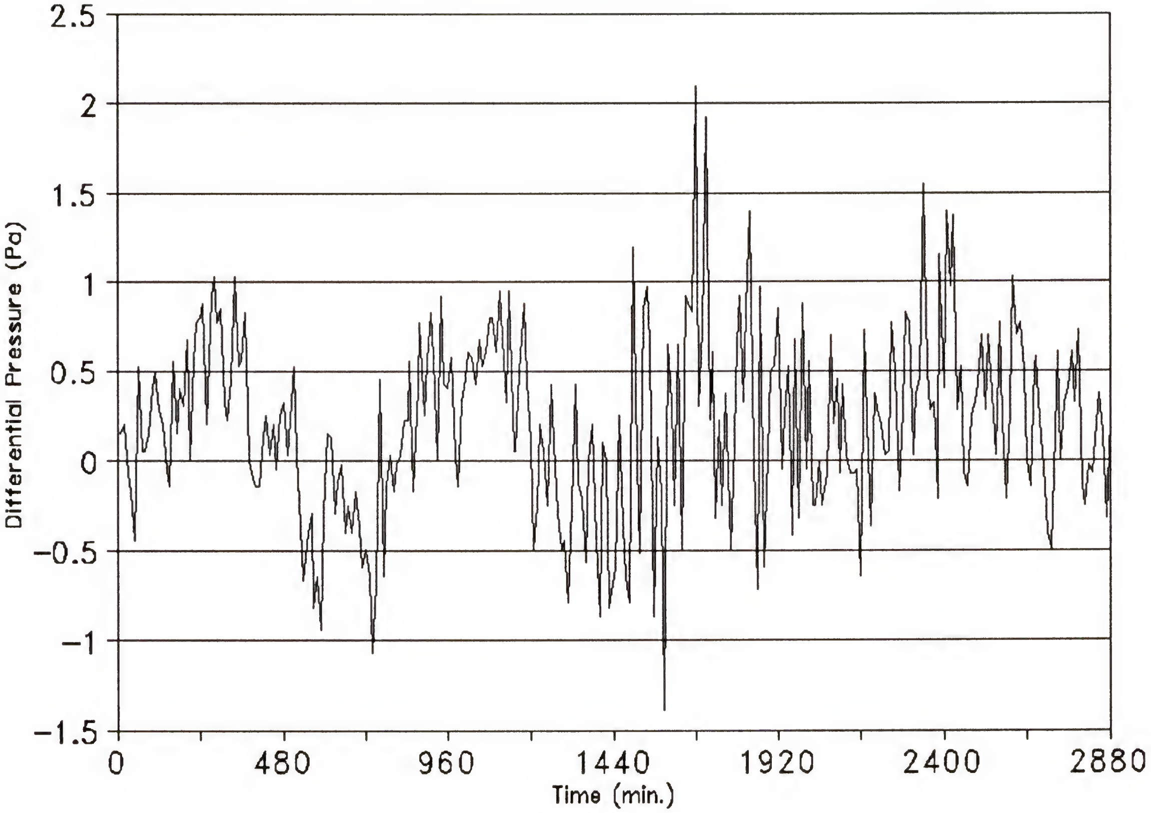

FIGURE 4-14 H: A 2-day sample of temporal variations of pressure differences measured across the slab at location 16 field 4, under neutral pressure conditions.

could be plotted in the same graph with the sub-slab radon concentration measured at the center hole. In all cases, both concentrations experienced a semi-diurnal fluctuation corresponding to the fluctuations observed from differential pressure measurements across the slab.

Figures 4-15, 4-16, and 4-17 illustrate measurement under neutral pressure conditions. The temporal response of the sub-slab radon concentration measured from sub-slab location 7, when the structure was slightly pressurized to 2 Pa is shown in Figure 4-18. The figure also shows the behavior of the radon concentration when pressurization is stopped approximately 80 hours from the start of the experiment. Figures 4-19 A,B, and C show the temporal response of the sub-slab radon concentrations measured at two sub-slab locations (2 in field 1, and 10 in field 3) representing a different spatial configuration when the HVAC system was operating continuously (fan, no air-conditioning) with interior doors opened and then closed.

As seen in the graph, a distinct difference in the radon concentration responses could be seen shortly after closing the interior doors and it continued to be significant. These observations suggest two points: first, that most of the crack distributions and their communications with the sub-slab area are not homogeneous because of different openings and soil permeability. Second, utilizing the HVAC system with various indoor configurations, could result in a redistribution of the

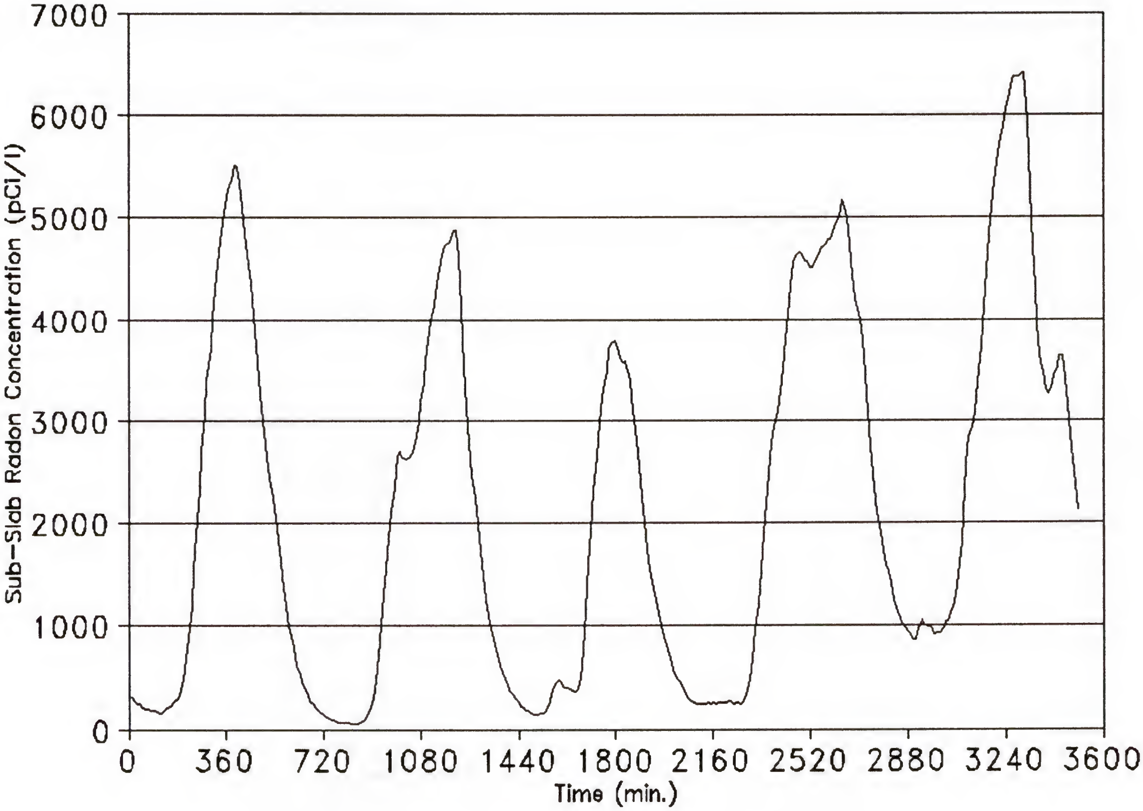

FIGURE 4-15 A: A 2.5-day sample of temporal variations of sub-slab radon concentration monitored at the central hole when the structure is under neutral pressure conditions.

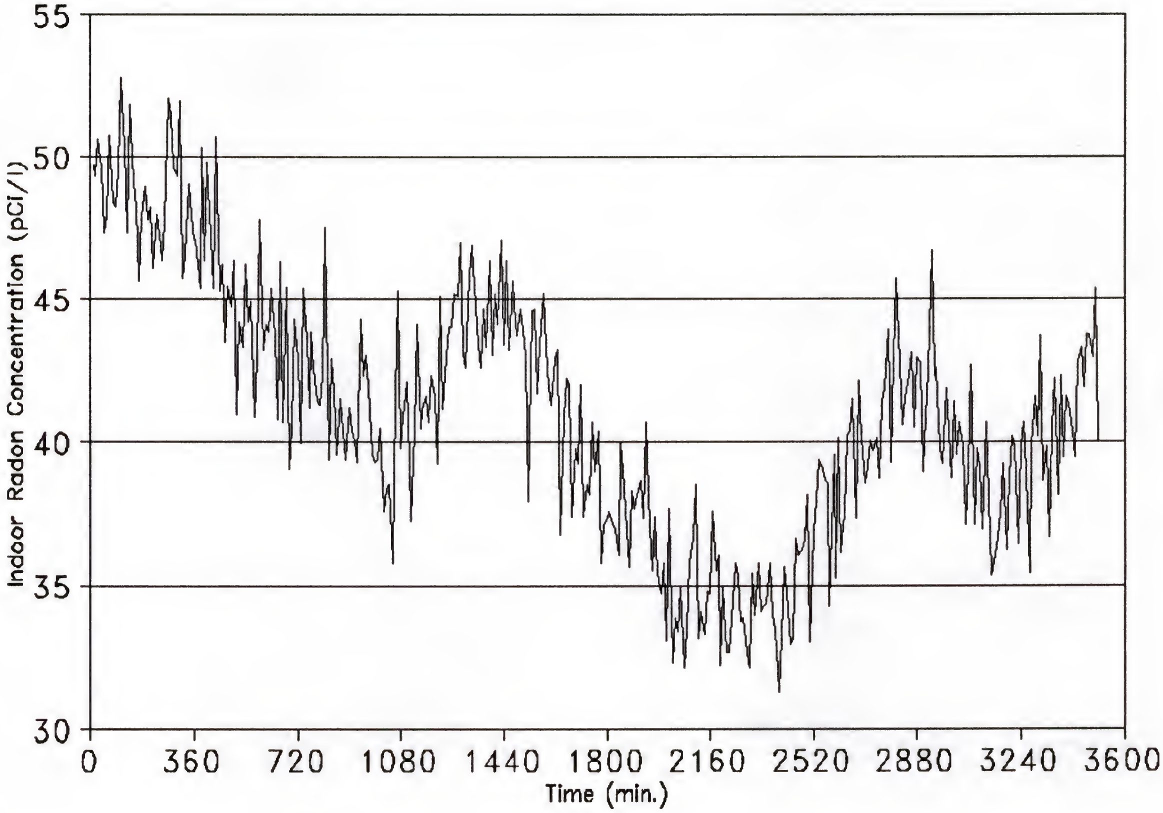

FIGURE 4-15 B: A 2.5-day sample of temporal variations of the indoor radon concentration monitored at the same time of Figure (4-15 A). The structure is under neutral pressure conditions.

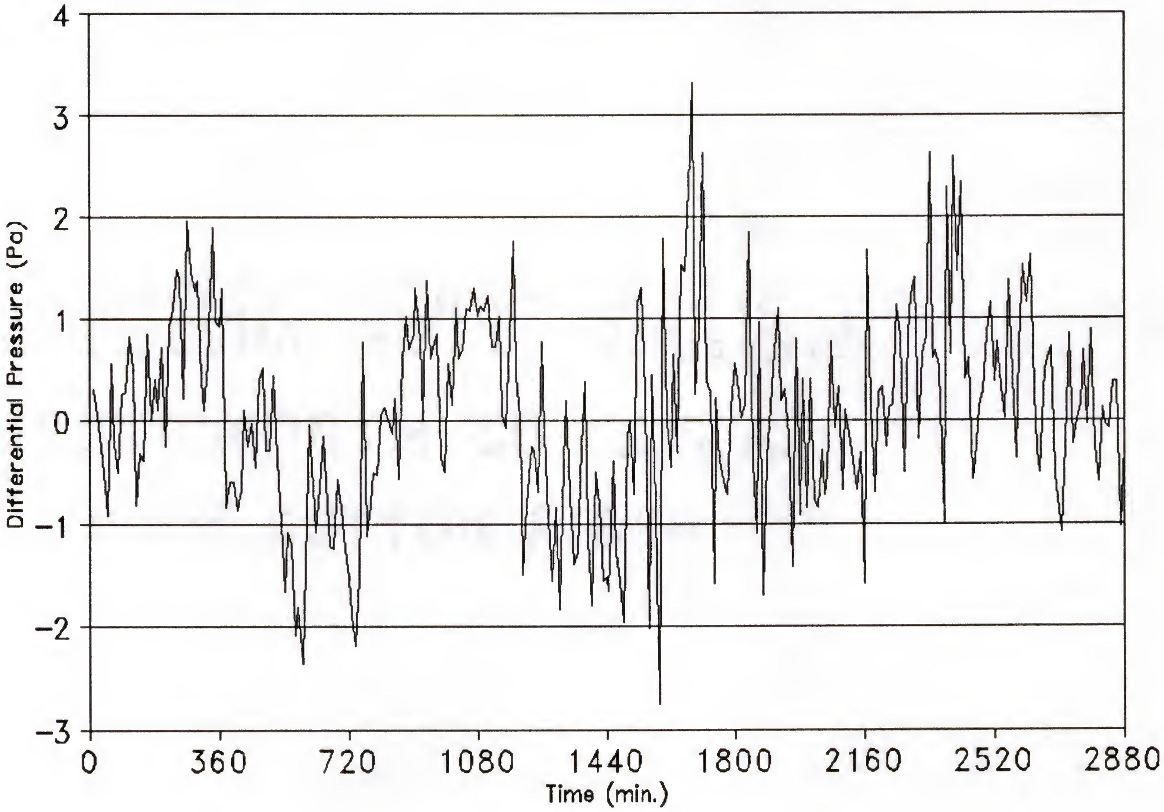

FIGURE 4-16 A: Temporal variations of the average differential pressure in field 1 for the first two days in Figure (4-15).

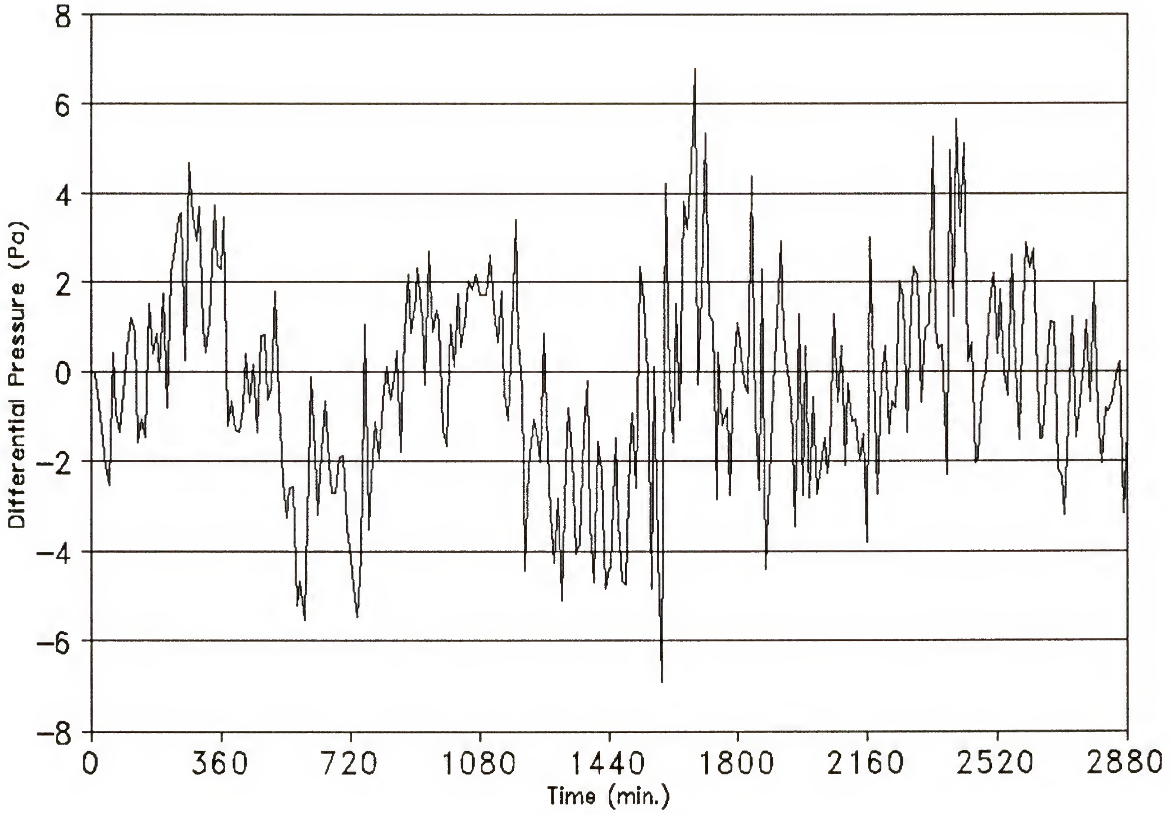

FIGURE 4-16 B: Temporal variations of the average differential pressure in field 2 for the first two days in Figure (4-15).

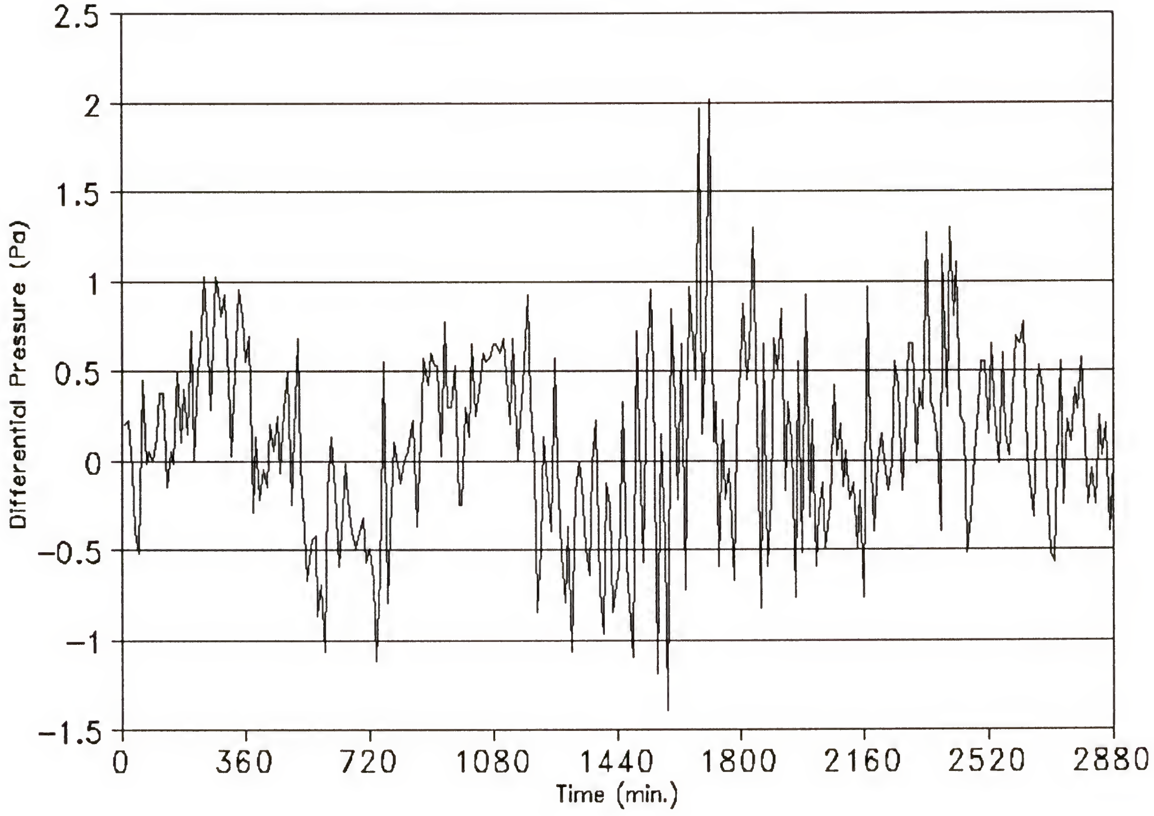

FIGURE 4-16 C: Temporal variations of the average differential pressure in field 3 for the first two days in Figure (4-15).

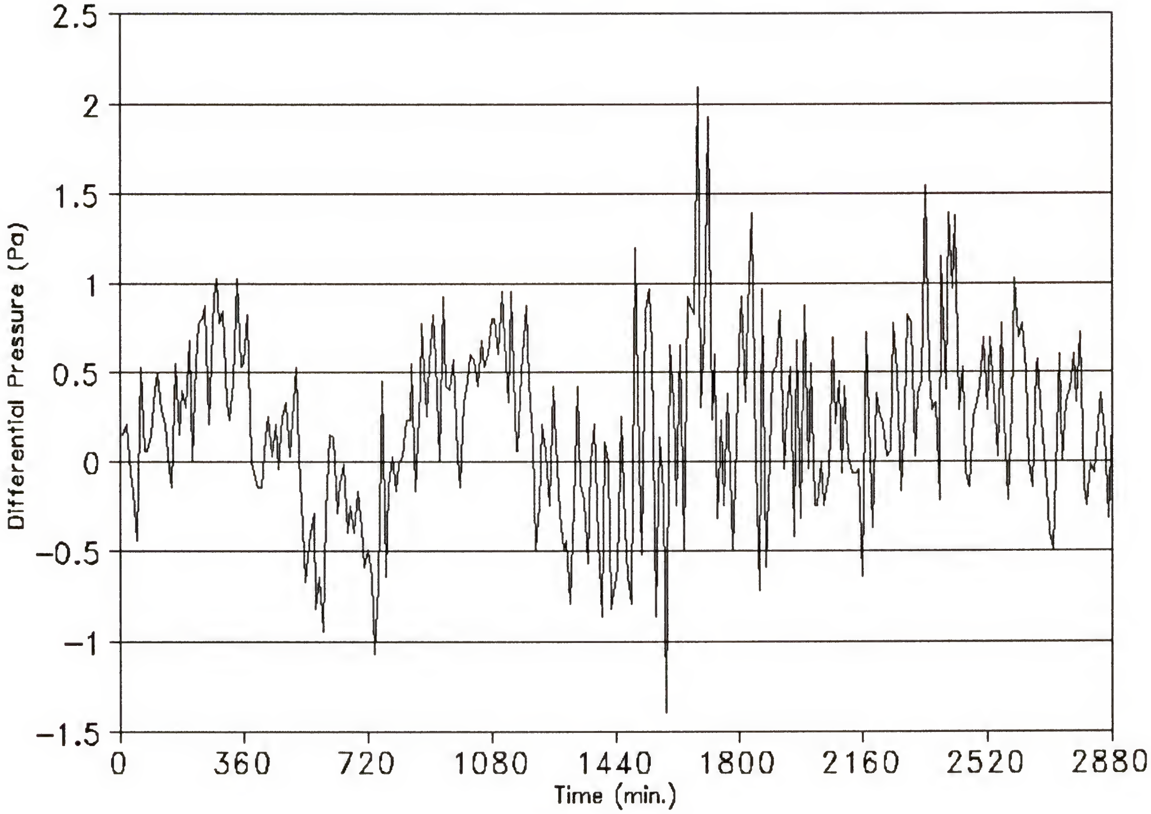

FIGURE 4-16 D: Temporal variations of the average differential pressure in field 4 for the first two days in Figure (4-15).

differential pressure field across the slab and consequently affect sub-slab radon entry into the indoor environment. These observations will be used in the development of the house pressurization physical model and implemented in the design of radon prevention and mitigation systems in later sections of this chapter.

Many experiments were designed and performed to cover possible configurations that might exist in the structure and might affect indoor radon concentrations. Each item under indoor radon concentration represents the arithmetic mean of all time-averaged measurements performed for that configuration. A minimum of four runs were performed for each configuration.

The average of the spatial and time dependent measurements of the radon concentrations, over at least 24 hours after reaching equilibrium, for configurations associated with creating pressurization and depressurization of the whole house is shown in Figure 4-20. The graph also shows the interesting result that occurs when the house is subject to no mechanically induced pressurization or depressurization.

The highest average indoor radon concentration was found when the house was maintained under the neutral pressure conditions. Neutral pressure conditions were defined to exist when the structure shell experienced only very small pressure differences between the indoors and the outdoors.

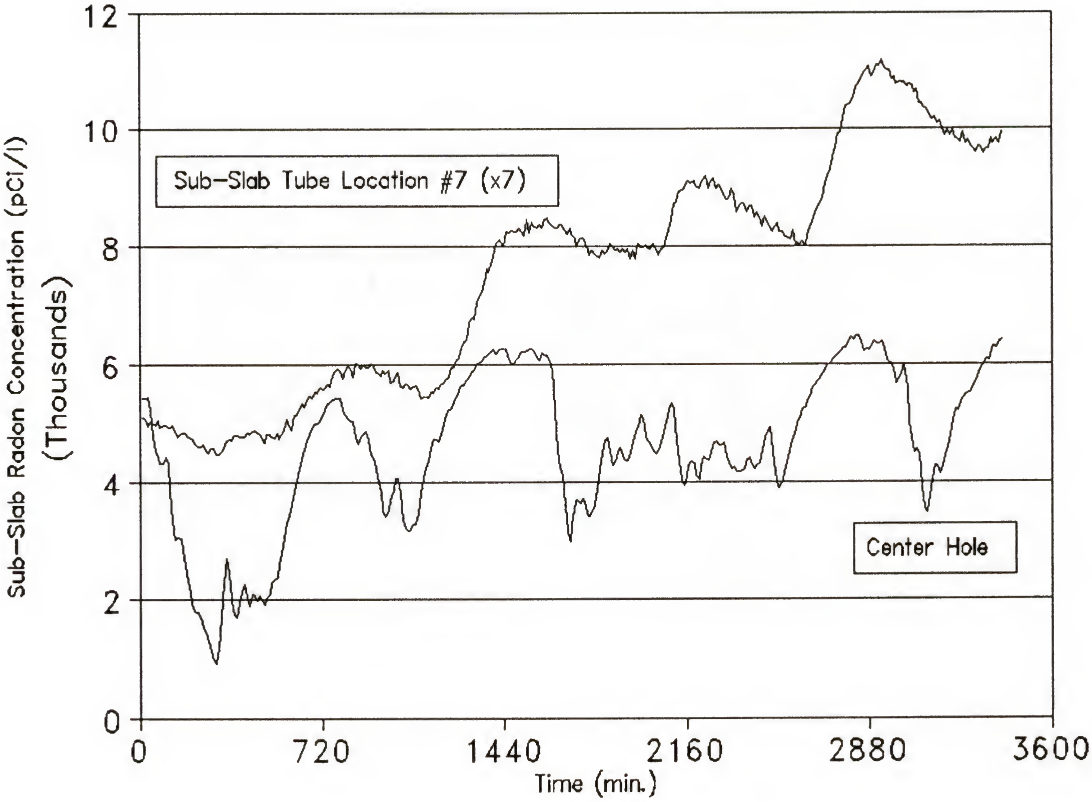

FIGURE 4-17: The temporal variations of the sub-slab radon concentrations measured from sub-slab tube 7 and the structure central hole. Response from tube 7 was multiplied by 7 so it could be shown in the plot.

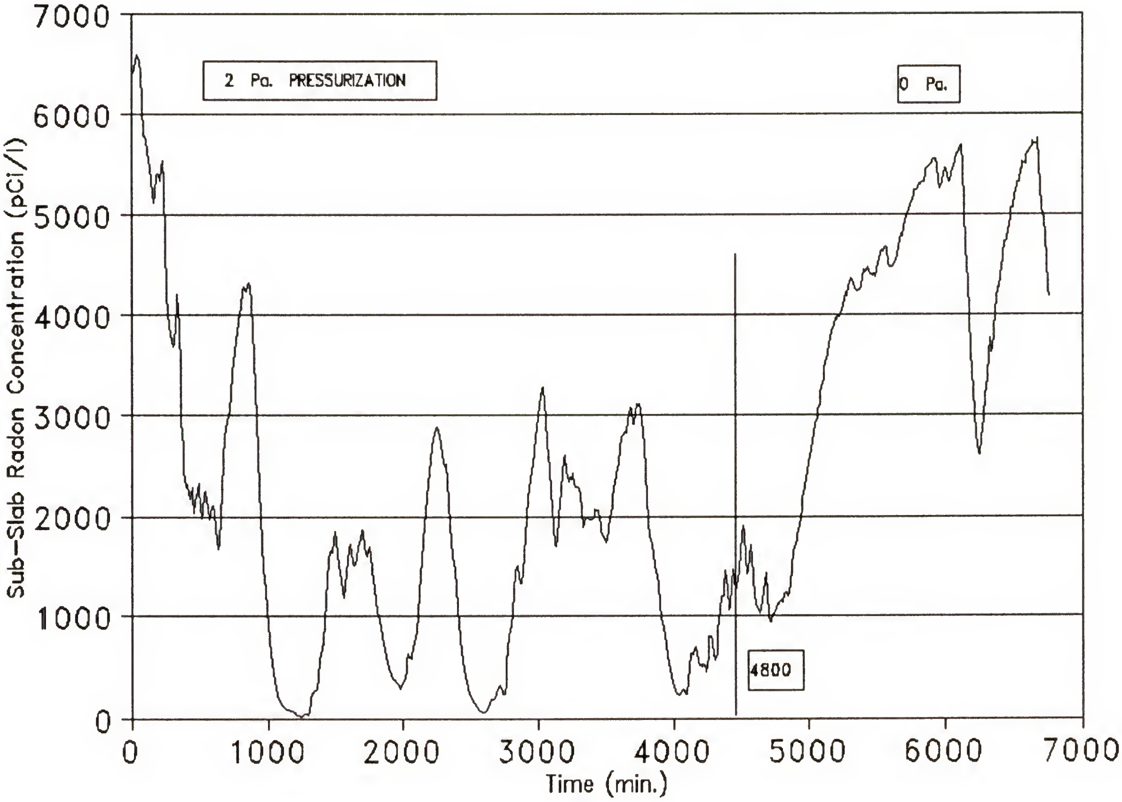

FIGURE 4-18: The temporal variations of the sub-slab radon concentrations measured from sub-slab tube 7. The structure was maintained under 2 Pa pressurization for the first 80 hours of testing.

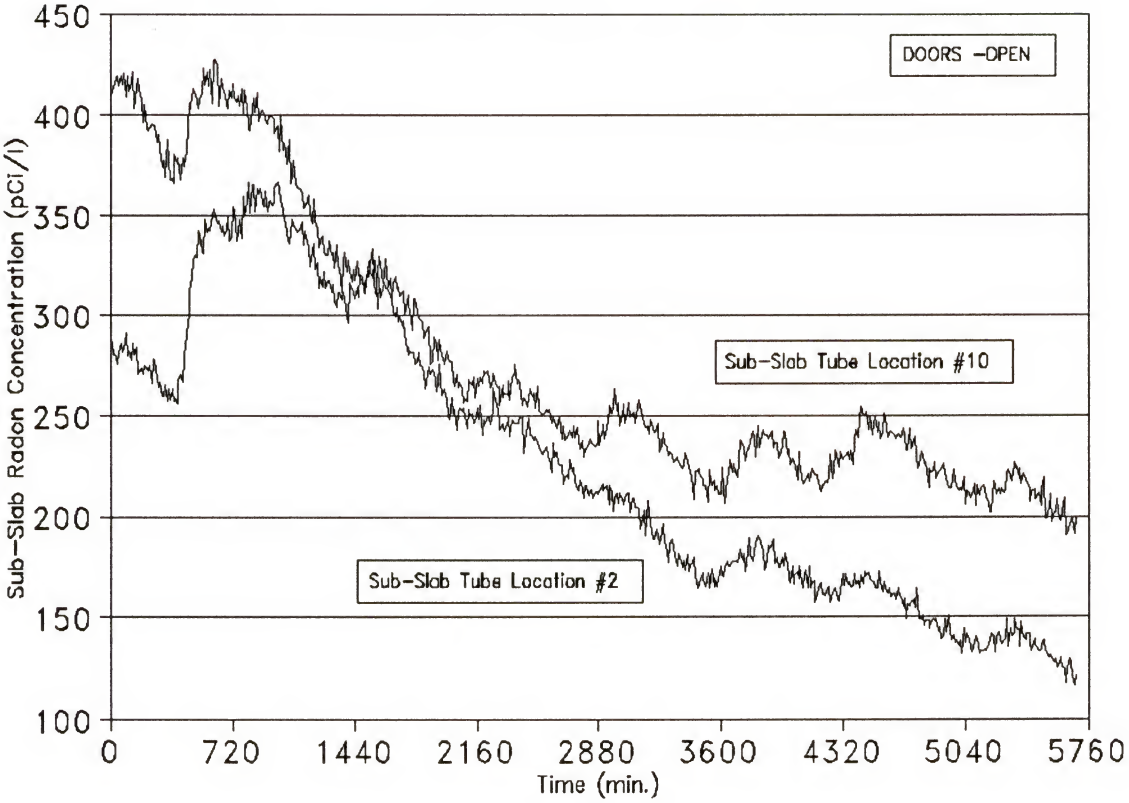

FIGURE 4-19 A: The temporal variations in the sub-slab radon concentrations measured from sub-slab tube 2 and 10. The structure was maintained under neutral pressure conditions and the interior doors were opened.

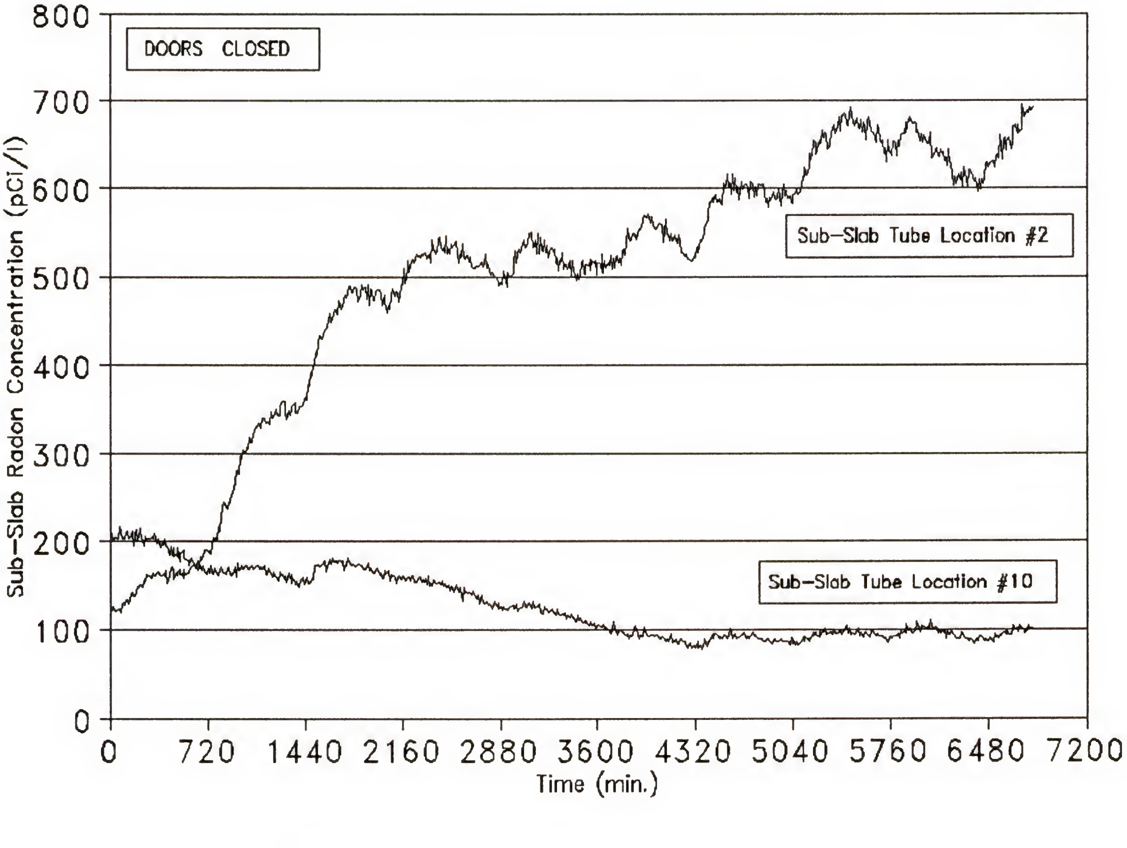

FIGURE 4-19 B: Continuation of temporal variations in sub-slab radon concentrations measured from sub-slab tubes 2 and 10 (Figure 4-19 A). The structure interior doors were closed approximately 96 hours after the start of the experiment.

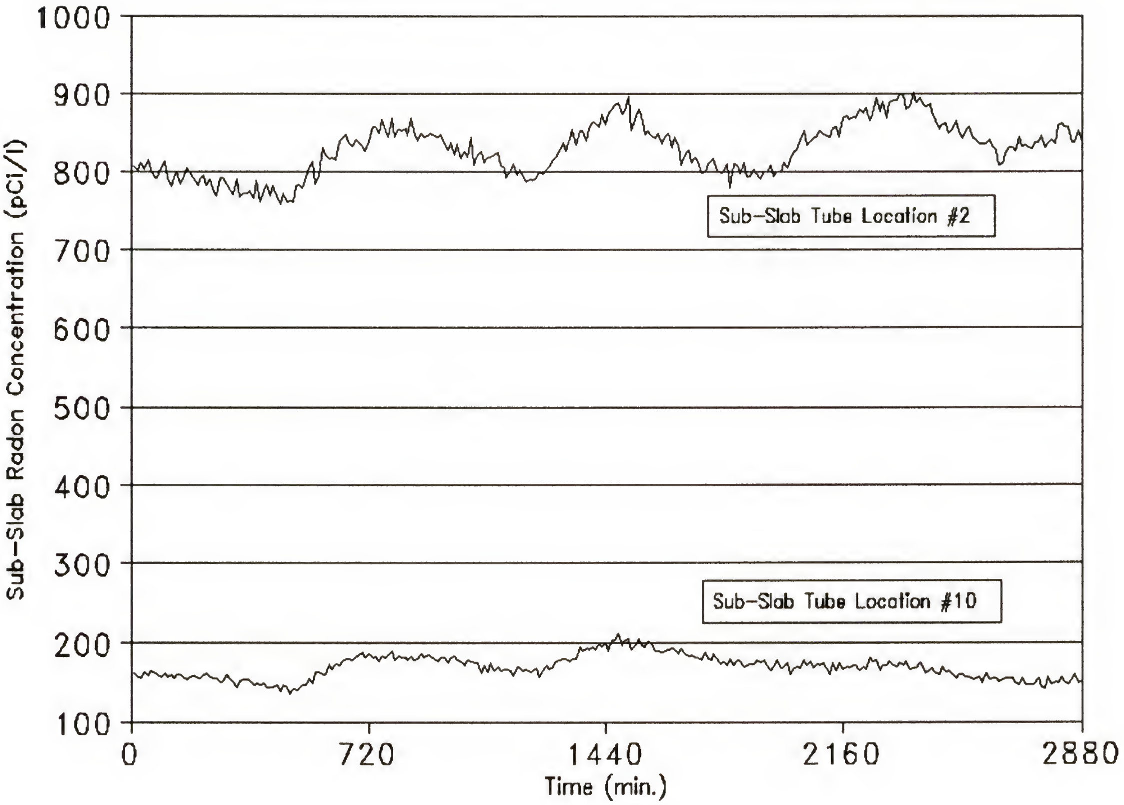

FIGURE 4-19 C: Continuation of temporal variations in sub-slab radon concentrations measured from sub-slab tubes 2 and 10 (Figure 4-19 B) for the next 48 hours.

These differences are typically on the order of one Pascal.

The convective components of radon transport, as discussed in the mathematical considerations of Chapter 2, have been considered responsible for elevated radon concentration levels in indoor atmospheres, since no diffusion components were found capable of producing such elevated levels. The contribution of the pressure driven airflow mechanisms, the forces responsible for the convective components, have been ignored by radon researchers for neutral or low pressure differentials. However, small pressure differentials across the research house slab seem to be associated with elevated indoor radon concentration under neutral pressure conditions.

As seen in Figure 4-20, the steady state indoor radon concentrations are correlated to the house depressurization levels. In the house shell, when the indoor pressure became lower than the outdoor pressure, the convective transport component was enhanced, bringing the radon rich soil gas from the sub-slab area into the structure. The increase in the radon entry rate as a result of the interior depressurization corresponds, at the same time, to the enhancement of the radon ventilation rate by bringing more infiltration air from outside into the structure through the overall house shell leakage area. The increase in the rate of radon entry in this case is larger than the increase in the radon removal rate

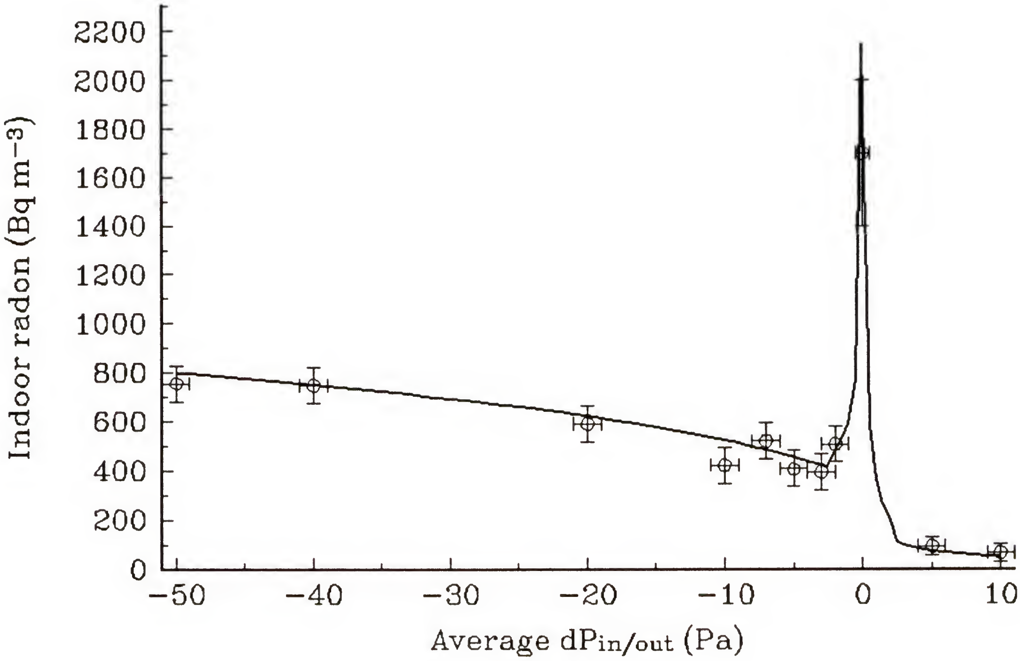

FIGURE 4-20: Time-Averaged Indoor Radon Concentrations As a Function of Whole House Pressure Conditions.

(ventilation rate), causing a buildup in the radon concentration (accumulation rate).

The increase in the radon accumulation became very slow and tends to saturate after reaching a certain level of the interior depressurization. This level is a function of the total house shell leakage area, the sub-slab characteristics, and the radon content in the soil. No prevention for the radon entry source term exists for the house depressurization conditions. The radon entry source terms, for the purpose of this research, are defined to be the radon concentrations immediately below the slab which are subject to the effects of the slab and house shell conditions.

The steady-state indoor radon concentrations decrease as the depressurization level decreases until some point at a small depressurization level. Then the radon concentration starts to increase very rapidly toward a maximum level. This "critical" point is on the order of a few pascal and depends on the particular conditions of the structure. For the University of Florida radon research house, a critical point of house depressurization exists at approximately 5 pascal or less.

Modelling of Physical Parameters Related to Indoor Radon

Barometric Pressure-Induced Pressure Differentials

The average indoor radon concentration decreases dramatically from its maximum level when the house shell experiences pressurization. Indoor pressurization was performed by pushing fresh air from the outside into the house shell using the blower door described in the experimental design and methodology. House pressurization enhances the radon ventilation rate and, consequently, the radon removal rate. If the indoor pressure is modeled as a downward force on the structure's slab, and acts as a spatially distributed load across the slab surface, then this force can cause a significant reduction in the radon entry source terms. Illustration to this model is shown in Figure 4-21. The distributed load is represented by thin arrows applied on the house slab.

When the indoor pressurization increases, the applied forces interact with the slab and the sub-slab area, as illustrated by the thick arrows in Figure 4-21. If the cracks, holes and openings in the slab, as well as the sub-slab area, are uniform, the radon concentration will continue to decrease until reaching a constant, very small level, ideally equal to the outdoor background level.

If the spatial distribution of the slab openings and the sub-slab materials become physically nonuniform with respect

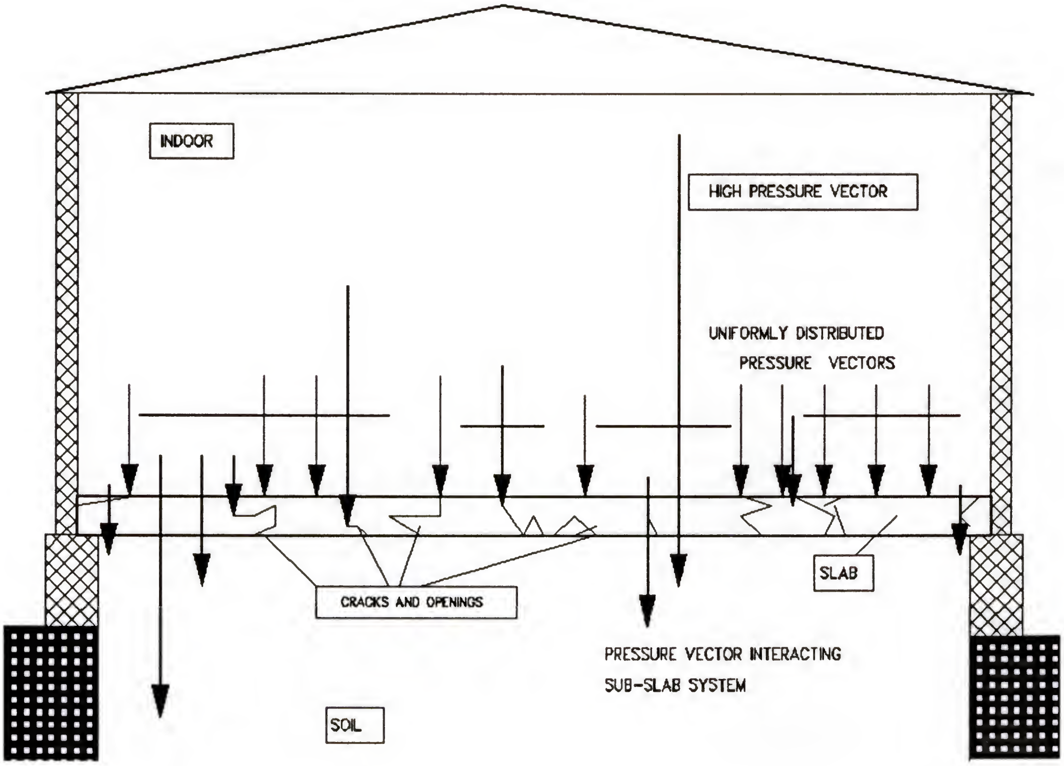
INDOOR
HIGH PRESSURE VECTOR
UNIFORMLY DISTRIBUTED PRESSURE VECTORS
SLAB
CRACKS AND OPENINGS
PRESSURE VECTOR INTERACTING SUB-SLAB SYSTEM
SOIL

FIGURE 4-21: An Illustration of A Model for The Interaction During Interior Pressurization Between the Indoor and the Sub-Slab Areas.

to the penetrating vectors of the airflow driven pressure forces, the radon concentration is expected to start to increase again. This is the result of the generation of a nonuniform pressure differential across the slab area developed by different levels of interaction between the applied load and the slab/sub-slab system. The differential pressure across the slab will be higher in the area where the applied load has more difficulty penetrating the slab sections into the sub-slab area.

The average rate of change of the radon concentration is expected to be slower during pressurization of the whole house from a few pascal and up. The critical point in the pressurization condition, analogous to the depressurization critical point, is given the name the "mirror" point. The mirror point occurs at an amount of pressurization on the order of that of the depressurization critical point for a particular structure. The mirror point does not necessarily represent the minimum possible indoor radon concentration, for the case of pressurization, but it reflects a turning (inflection) point of dramatic change in the radon concentration between neutral pressure conditions and itself.

The transient response of the radon concentration was examined during the house pressurization and depressurization experiments. Figure 4-22 shows the rapid response of the sub-slab radon concentrations to whole house depressurization, measured from the hemispherical shaped hole immediately under the slab by the experimental configuration illustrated in Figure 4-4. The concentration responded quickly and reached stable levels in a short time. The response of the sub-slab radon concentration with a pressurization level is shown in Figure 4-23.

In most cases the radon concentration reached its steady state concentration in less than 12 hours with a level corresponding to the whole house pressurization or depressurization level. In Figure 4-22, the slower response time corresponds to a 20 Pa depressurization. This time was about 70% of the 12 hour interval, while the response time for the 50 Pa depressurization took approximately 26% of the 12 hour interval to reach stabilization. Therefore, waiting for a 24 hour interval and then averaging radon concentration levels over the next interval of 24 hours (or more) provides suitable results for determining radon concentration levels corresponding to the whole house pressure conditions. Figure 4-24 shows the transient response of the indoor radon concentration for a 5 Pa steady pressurization.

It is important to notice that the radon concentration measured in a certain volume (leaking container, such as the sub-slab system) depends on the measurement technique and the characterization of that volume. The volume characterization can significantly affect the convective component of the radon transport if the volume is not completely isolated from the surrounding environment.

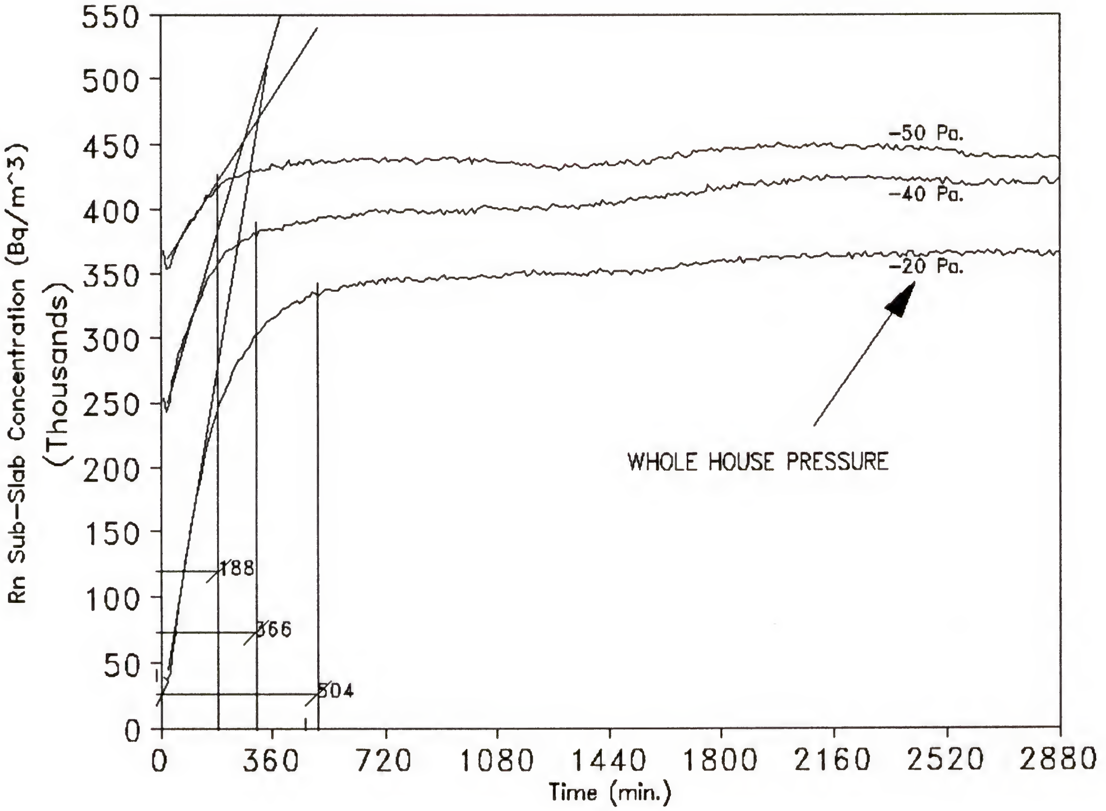

FIGURE 4-22: The transient response of the sub-slab radon concentration in the central hole for different whole house depressurization levels.

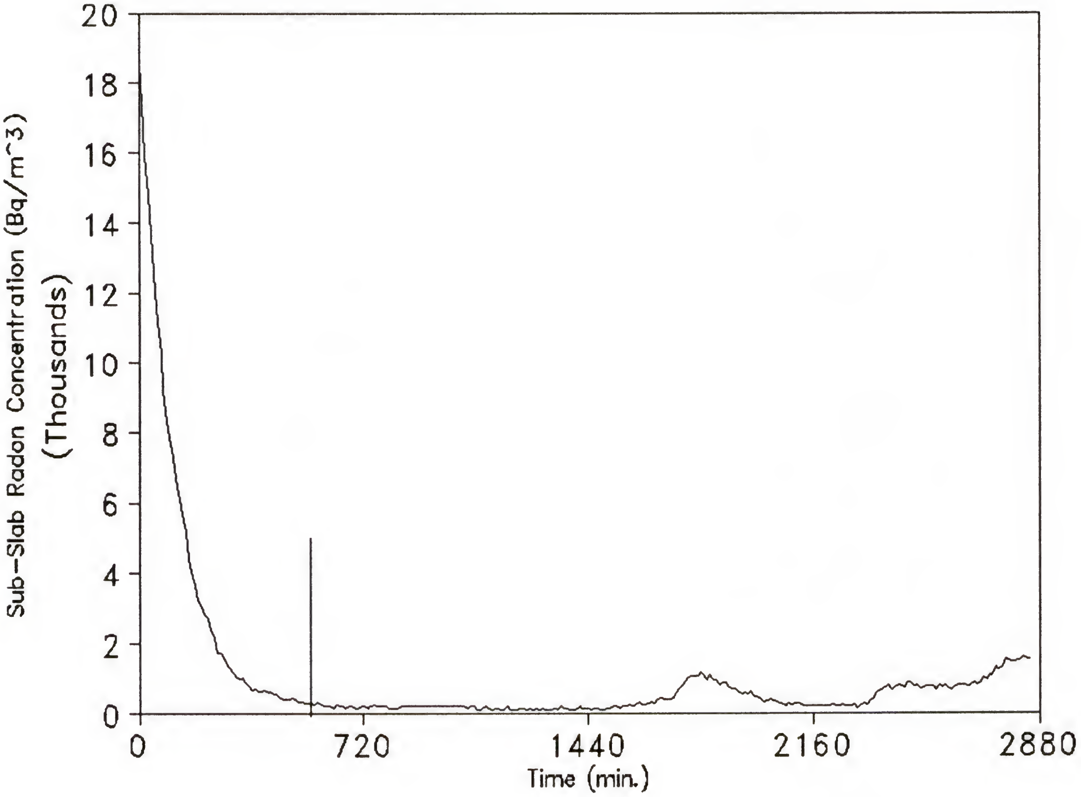

FIGURE 4-23: The transient response of the sub-slab radon concentration in the central hole for 5 Pa. whole house pressurization.

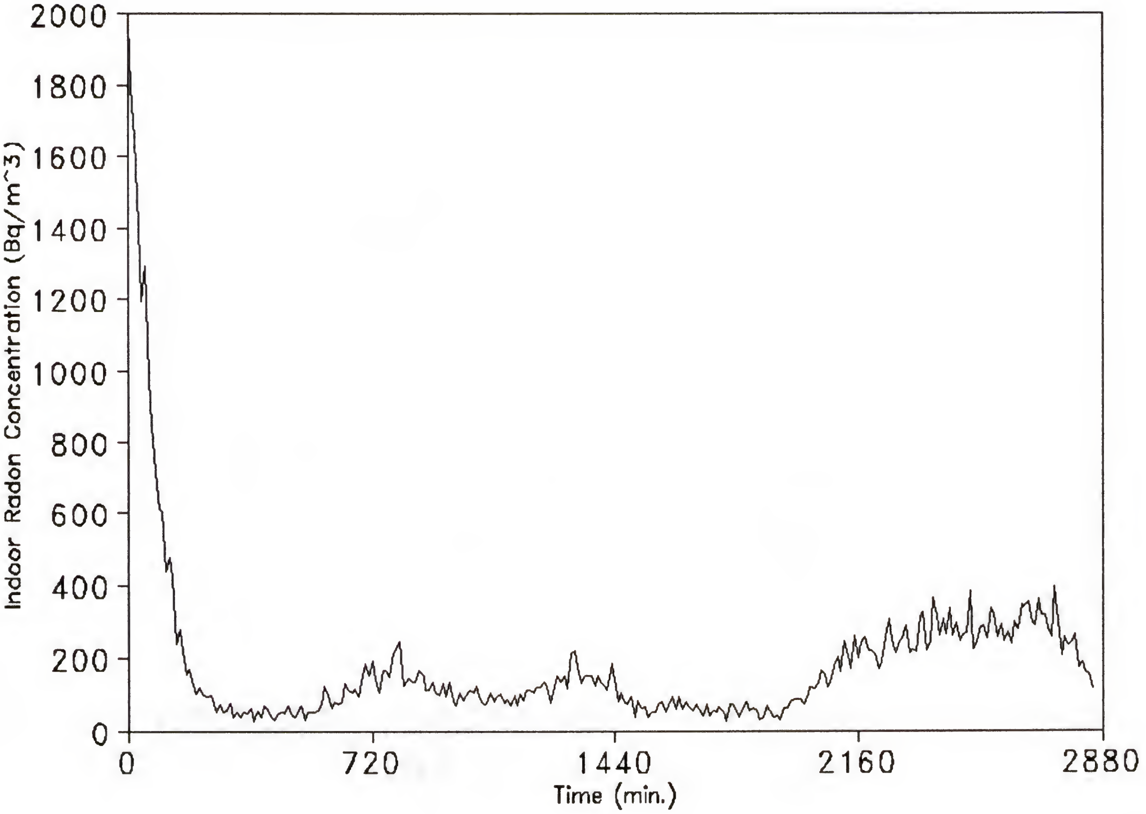

FIGURE 4-24: The transient response of the indoor radon concentration for whole house pressurization of 5 Pa.

The volume leakage affects the radon ventilation rate and, consequently, the removal rate. If the radon entry source term is defined at the boundary between the volume surface and the surrounding medium, the total leakage area could significantly affects the radon entry rate. Thus, the radon measurement in a leaking volume does not necessarily represent the radon concentration in the surrounding medium, especially if the surrounding medium has different characteristic conditions, such as permeability. Using this characteristic volume with respect to radon measurements can provide an excellent means of estimating and studying the radon concentration in areas where taking the actual measurements for each particular point, such as opening holes in the slab-system, is not practical.

The sub-slab hemispherical shaped hole (the central hole) was used to measure the effects of external conditions on the radon concentration, as set up in Figure 4-4. The leakage effects of that characteristic volume played a role in the discovery of the regular cycling in the (source term) radon concentration. This discovery was made during an investigation of the elevated indoor radon concentrations under the neutral pressure conditions (Al-Ahmady 1992a).

A strong semi-diurnal cycle in the sub-slab radon concentration was observed in the central hole, using the experimental measurement set-up of Figure 4-4. Samples of the radon behavior are illustrated in Figure 4-25. As seen in the graph, the radon cycle has two peaks in a period of 24 hours, with approximately a 12 hour difference. The amplitude of the radon cycle varies from several hundred thousand to several tens of thousands of Bq/m^3.

These large differences in the sub-slab radon concentration magnitudes do not agree with the research house soil gas radon measurements and the initial characterization of the soil radon content, which is typically on the order of 10^5 Bq/m^3. This suggests that the radon concentrations in the sub-slab central hole are dramatically affected by external forces applied to the convective component of radon transport.

Since no mechanically-induced depressurization or pressurization exists, the observed 12-hour cycle fluctuations in fact, are not generated by the house system but rather by external forces. Further investigation has shown, as will be seen later, that the external influencing forces are generated by the atmospheric tidal barometric pressure variations.

The radon cycles were also observed in the radon measurements from the slab accesses, which represent a very small volume (point simulation) in the sub-slab area immediately under the slab. The observed radon cycles under neutral pressure conditions, as expected, also exhibit semi-diurnal variations, with smaller variations in amplitude, as shown in Figure 4-26. The absolute fluctuation in the amplitude is, however proportional to the average radon concentration. Figure 4-26 shows the radon cycles measured from tubes or points 3 and 11 under neutral pressure conditions.

The differences in radon cycle amplitudes that are observed between the hemispherical shaped central hole under the slab and the slab tubes exist as a result of different volume characterizations. If a force is applied to the leakage area of the characteristic measurement volume, and the radon is primarily transferred by convection, then airflow must pass through the leakage areas, affecting radon transport.

The leakage areas of the experimental settings simulate the cracks, holes, and openings in the slab that air allow in penetration. The penetrating airflow fraction depends on the available penetrating paths and the applied driving forces. If the applied driving forces are directed upward (vector direction from low to high), then the radon rich soil gas will have more difficulty penetrating from the soil into the indoors through the available penetrating paths. This effect decreases the radon transport through the control of the leakage area and, consequently, yields the radon levels measured in the lower part of the cycle.

If the leakage area represents a similar possibility of penetration through the cracks, then these radon measurements actually represent the radon entry source term to the interior by application of prevention mechanisms to the overall source term in the soil. The penetrating paths, in some cases, are

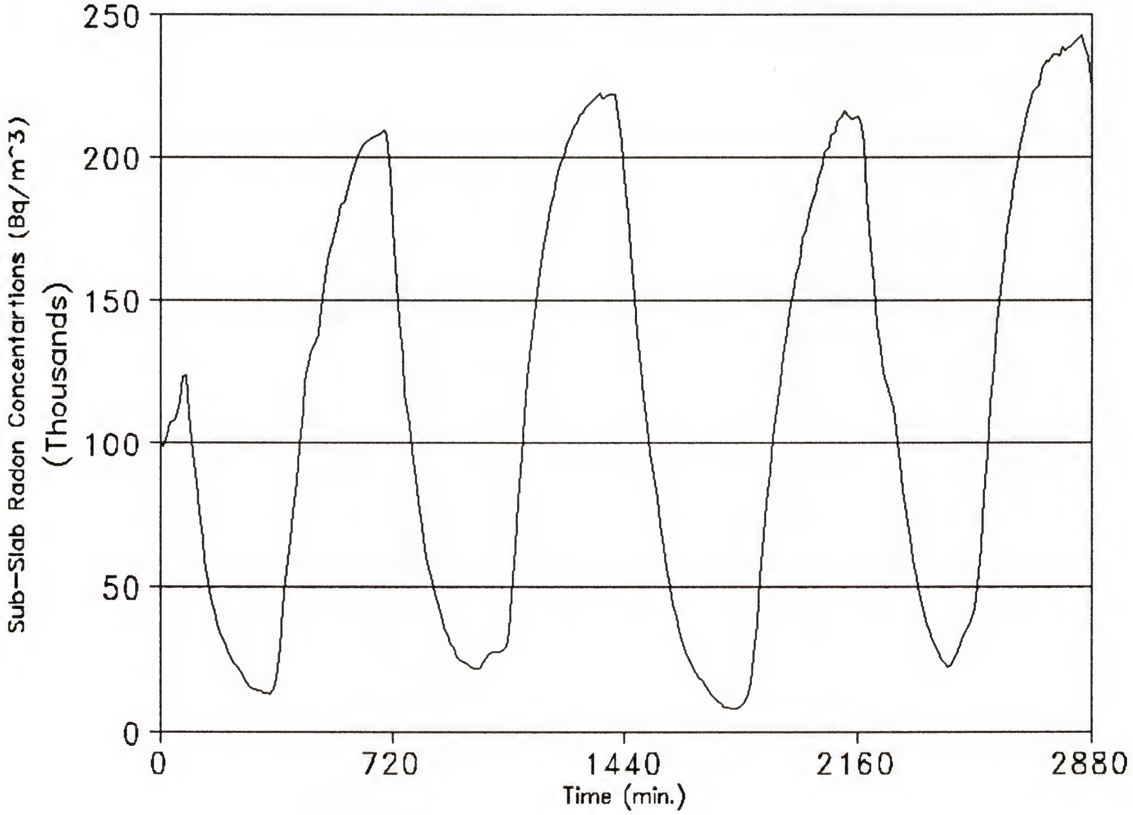

FIGURE 4-25: The temporal variations (semi-diurnal) in the sub-slab Radon concentrations measured at the central hole.

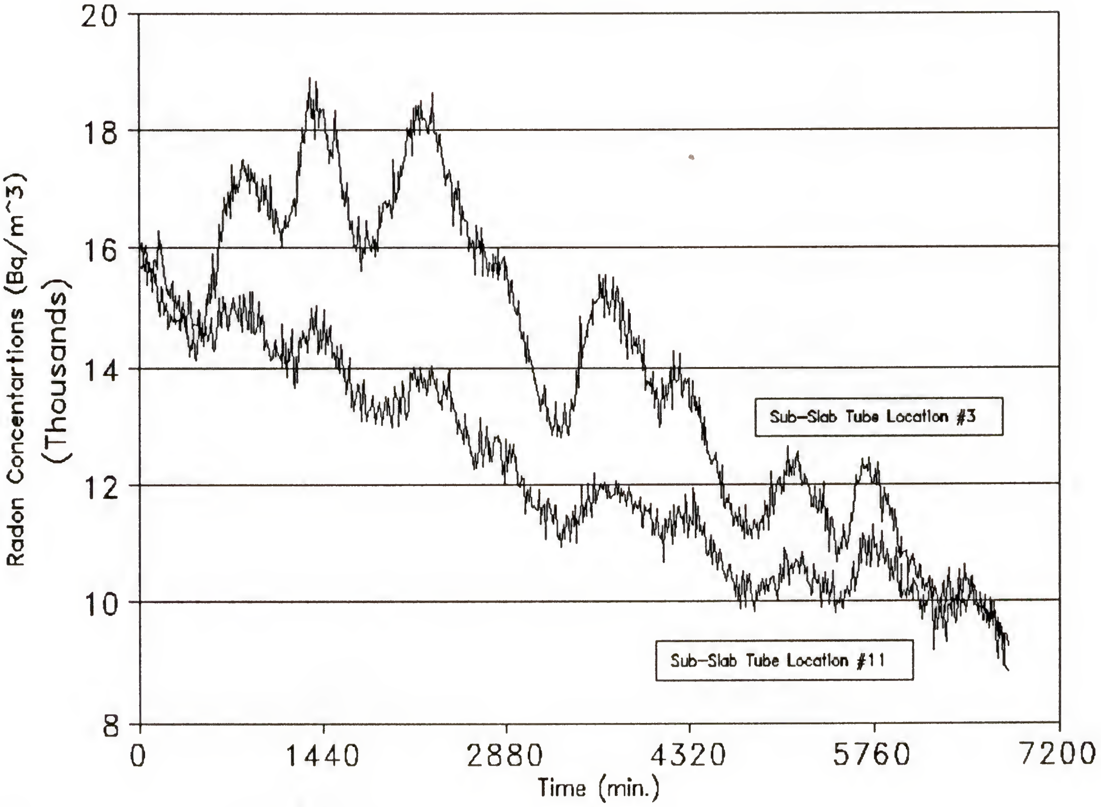

FIGURE 4-26: The temporal variations (semi-diurnal) in the sub-slab radon concentrations measured in two sub-slab locations under normal pressure conditions.

themselves functions of the applied driving forces. The overall possibility of penetration represents the influence of the effective leakage area on the soil gas flow rate through the slab cracks, holes, and openings. If a differential pressure is applied across the leakage volume, the volumetric flow rate (m^3/s) through the slab opening is given as,

$$Q = k\,A_e\,(\Delta P)^n \tag{4-1}$$

where,

k is a constant and equal to 1.29 for SI units,

A_e is the effective leakage area (m^2),

n is a dimensionless number and,

ΔP is the pressure difference applied to the leaking volume.

As seen in Equation 4-1, the flow rate is proportional to the effective leakage area, which itself may be a function of the applied differential pressure. The effective leakage area can be calculated as the integral of the response curve of the volumetric flow rate versus ΔP, plotted on a log-log scale.

Furthermore, the slope of the tangent to this curve, at any point of interest, is equal to n. If the response curve of the flow rate versus ΔP is a straight line on the log-log scale, the slope will be constant and n equal to 1 for dominant viscous flow and 2 if inertial forces dominate flow. Therefore, if downward applied forces exist, the soil gas will penetrate more easily into the structure by enhancing the convective component in the radon transport. Enhancement of the radon entry source terms exist, and increases in the radon concentration are detected by the experimental setup.

It is important to notice that the effects of the leakage area influence both the volumetric flow rate and the radon source terms which exist within the leakage volume boundaries. Enhancement of both quantities occur and consequently affect the radon entry rate and the indoor radon concentration. A mathematical statement of this is the following,

$$E_{Rn} = [S_{Rn}]\ [Q] \tag{4-2}$$

E_{Rn} is the volumetric radon concentration entry rate as a function of the radon source terms $[S_{Rn}]$ and the volumetric flow rate [Q]. $[S_{Rn}]$ is not necessarily constant, but likely to change as a function of the effective leakage area.

Further experiments are needed to characterize the radon source term response as a function of the differential pressure. These experiments should be designed to measure the time dependent response of the volumetric flow rate from the leaking volume (the possibility that the slab will be penetrated) for various pressure differences. The effective area response curve versus ΔP can then be constructed.

If the experiments allow successful calculation of the individual effect of the volumetric flow rate on the enhancement of the measured radon concentration, then the difference between the measured and calculated radon concentrations represents the enhancement to the radon source terms. The relation between the radon source terms and ΔP

may, therefore, be generated and, consequently, the response of the radon source terms to the change in the effective leakage area.

Since pressure is the major driving force for radon transport from the soil into structures, the applied forces that drive the radon cycle under neutral pressure conditions should, also, be pressures. Investigation of the suggested pressure forces has been performed by examining a small amplitude pressure differential variation across the house shell and the slab.

The pressure differential between the indoors and outdoors across the walls (the house shell) has been found to be well coupled in the case of no mechanically-induced indoor pressure conditions. The pressure differential between the outdoors and the sub-slab air volume has been found to be not well coupled.

Most models for radon entry assume that the outdoor pressure and the sub-slab air volume pressure are identical. However, Hintenlang and Al-Ahmady provide experimental evidence demonstrating that this assumption is not accurate for the UFRRH, and generally for houses built over low permeability soils and fill materials (Hintenlang and Al-Ahmady 1992).

Figure 4-27 illustrates the average indoor/outdoor and indoor/sub-slab differential pressures, monitored for the same time interval. Samples of the time dependence of the differential pressure across the slab at points 3,6,11, and 13 (from pressure fields 1,2,3, and 4) are shown in Figures 4-28 A, B, C, and D, respectively. Figures 4-28 E and F show these responses at points 2 and 10 (from fields 1 and 3 respectively) measured at a different time intervals than in Figures 4-28 A, B, C, and D.

As seen on the graphs, under neutral pressure conditions, the differential pressure across the slab is larger near the center than at the slab edges as mentioned in the beginning of this chapter. The time dependent behavior for all the monitored points (results collected by the differential pressure transmitters described the experimental design and methodology) is almost identical in the time steps, with different amplitudes, depending on the relative location on the slab.

Figure 4-30 shows the time dependent differential pressure measurements for four points from pressure field 3 plotted on the same graph. Samples of the spatial distribution of the differential pressure across the slab during the high and low peaks for the particular times indicated in Figure 4-30 are shown in Figures 4-31, 4-32, 4-33, and 4-34.

The corresponding contour map graphs are provided in Figure 24 A, B, C and D, respectively, and these maps can indicate easily the location of the maximum pressure differential across the slab.

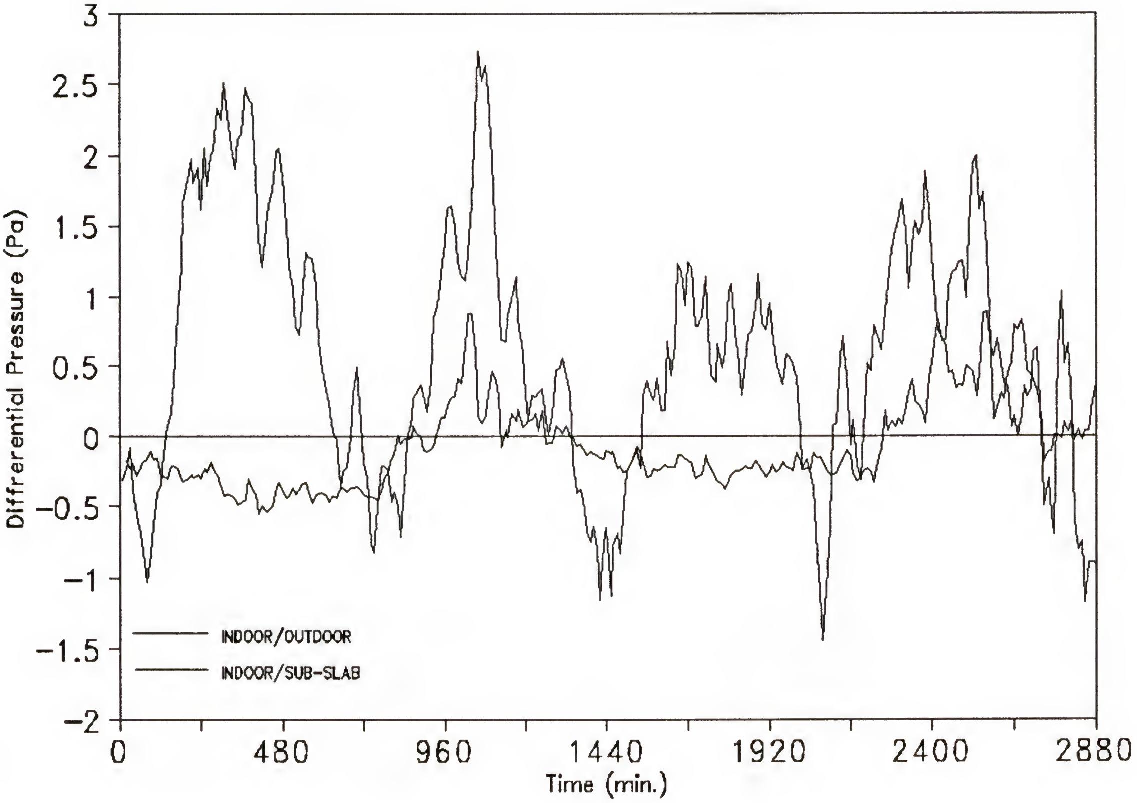

FIGURE 4-27: The temporal variations of the average indoor/outdoor and indoor/sub-slab differential pressures monitored for the same time interval.

The indoor/outdoor pressure differential of Figure 4-27 has a peak amplitude of approximately 0.5 Pa. The measurements of the differential pressure across the walls show differences on the order of 1 Pa. If these differences are averaged, it becomes evident that no substantial effects exist between the indoors and the outdoors as a result of the wind. However, the UFRRH is located in a wooded area that mitigates the effect of the wind, as described in the research house selection criteria. Other houses located in similar wind damping environments, or those that experience only weak winds, may be expected to have comparable pressure differences.

As the measured air changes per hour at 50 Pa (ACH_{50}) was 7.6 and the effective leakage area at 4 Pa (ELA_4) was 0.06 m^2, the indoor response to the outdoor pressure variation was almost instantaneous. As indicated in the comparison between the indoor/ sub-slab and indoor/ outdoor pressure differentials, the sub-slab air volume pressures are not well coupled to the indoor pressure and, consequently, to the outdoor pressure.

The result of the previous analysis suggests that the outdoor pressure conditions can provide the driving force required to bring the radon from the soil into structures under the neutral pressure conditions. An analysis of the barometric pressure data shows a semi-diurnal 12 hour cycle variations.

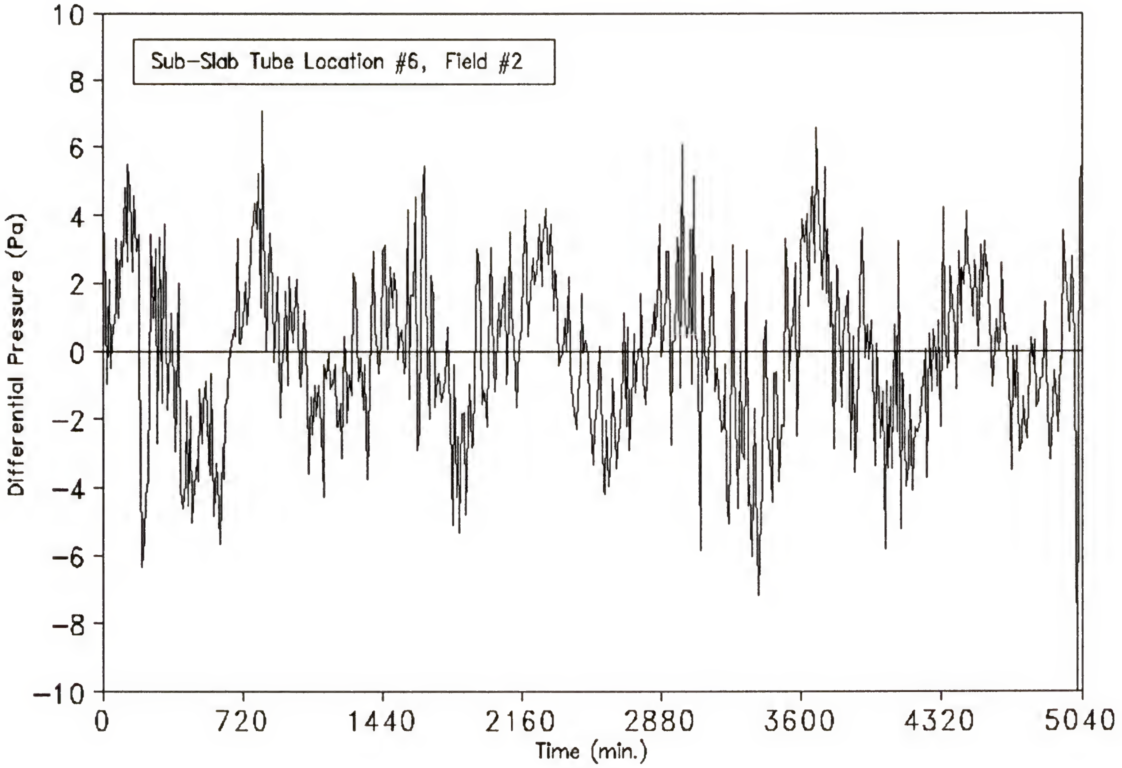

FIGURE 4-28 B: The temporal variations of differential pressure across the slab monitored at sub-slab location 6, field 2.

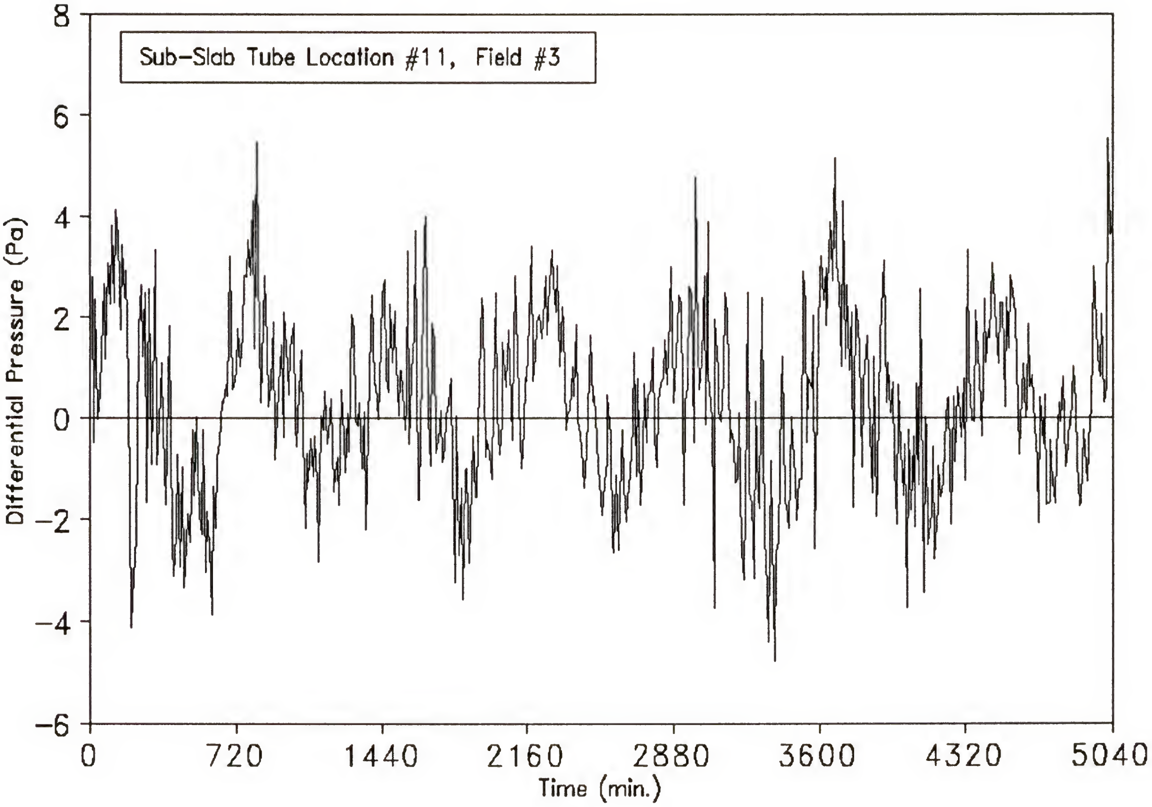

FIGURE 4-28 C: The temporal variations of differential pressure across the slab monitored at sub-slab location 11, field 3.

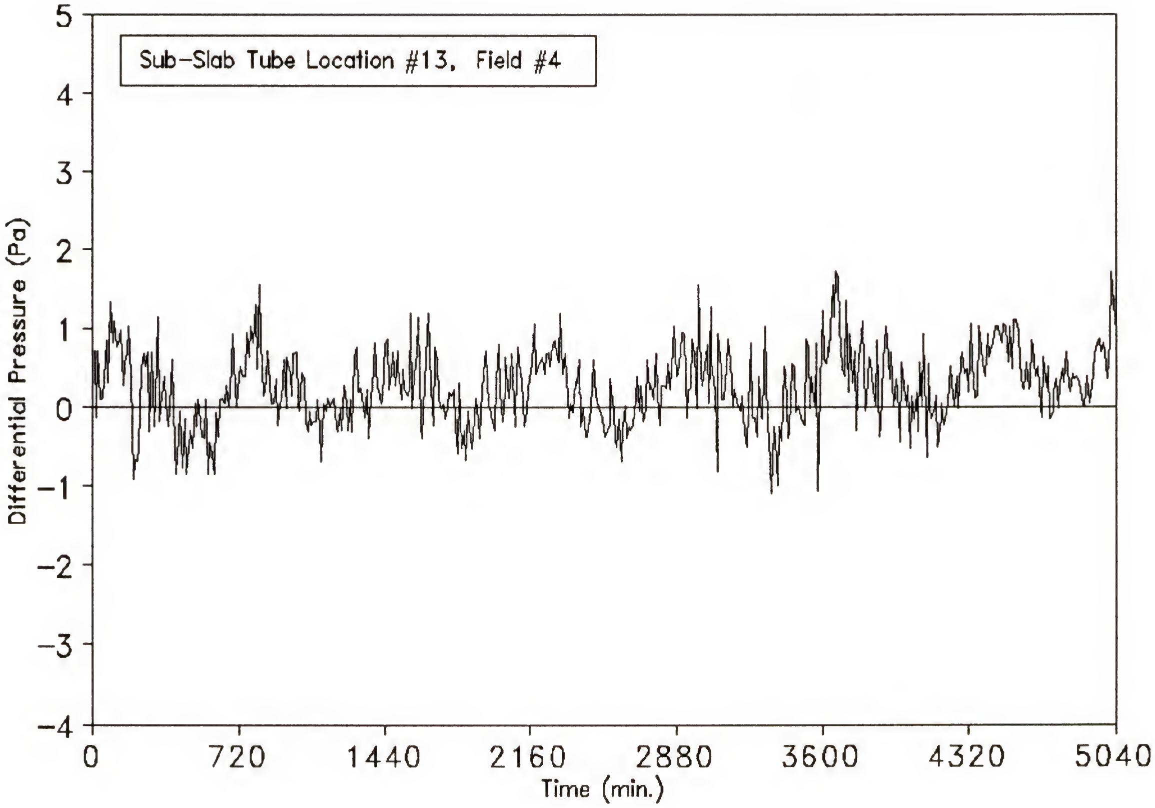

FIGURE 4-28 E: The temporal variations of differential pressure across the slab monitored at sub-slab location 13, field 4.

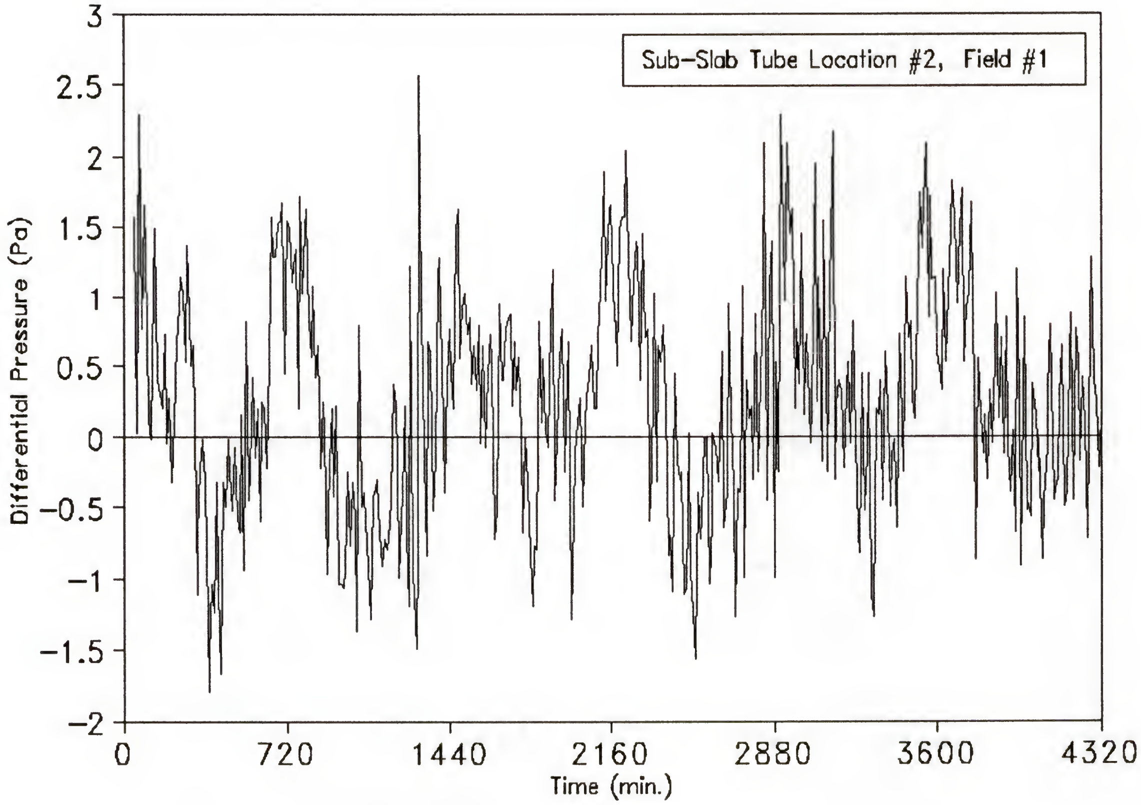

FIGURE 4-29 A: The temporal variations of differential pressure across the slab monitored at sub-slab location 2, field 1.

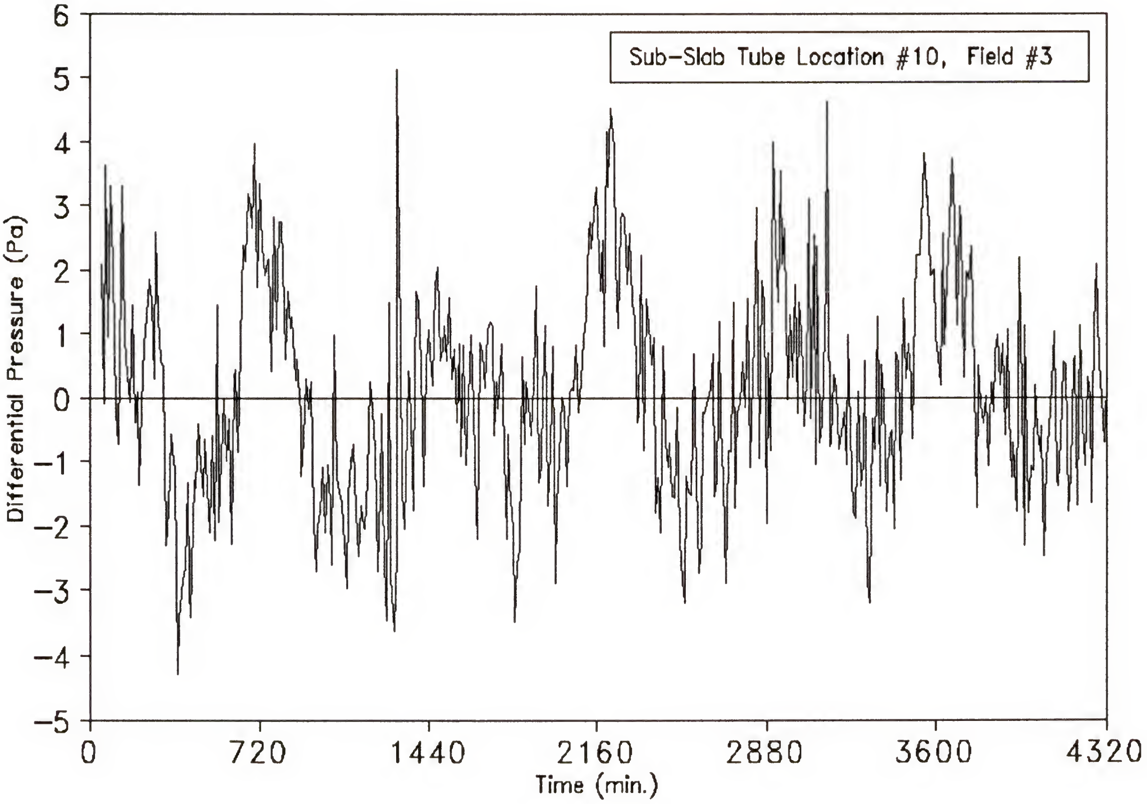

FIGURE 4-29 B: The temporal variations of differential pressure across the slab monitored at sub-slab location 10, field 3.

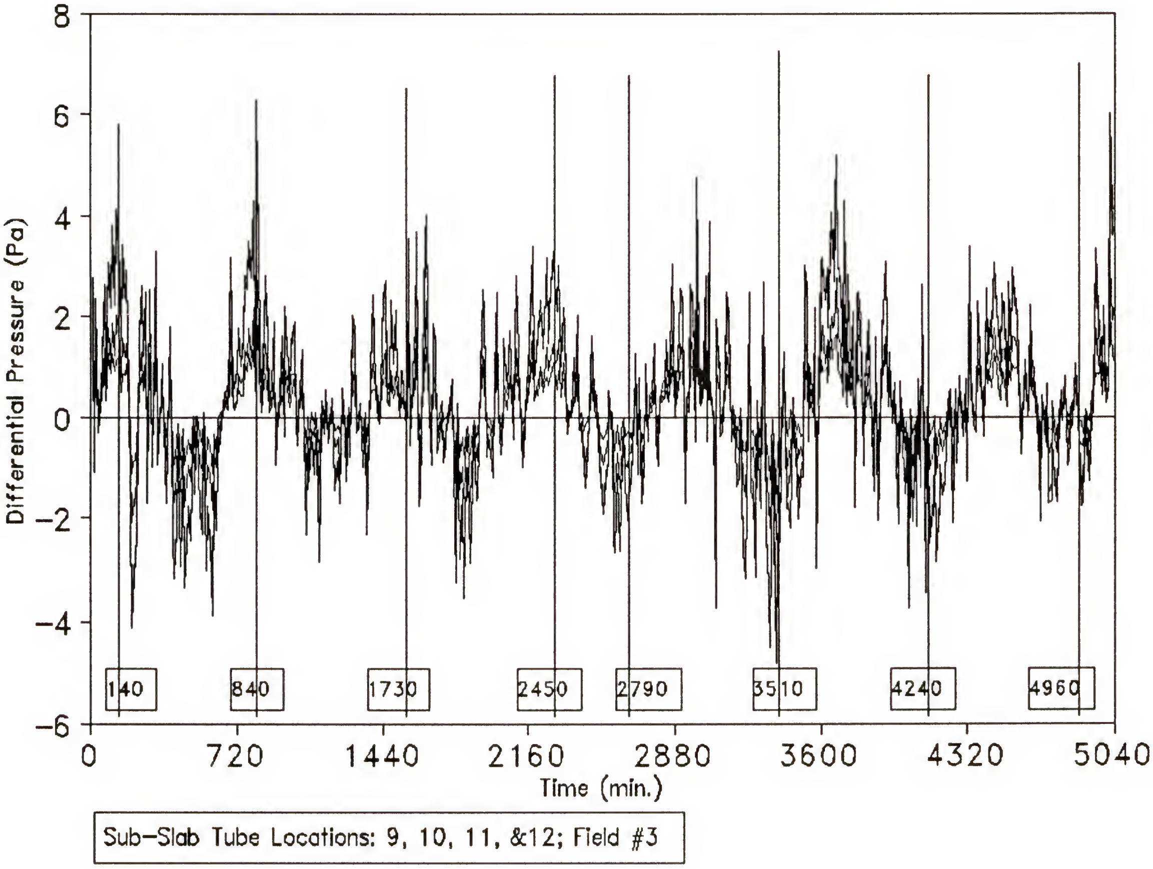

FIGURE 4-30: The temporal variations of the differential pressure map across the slab in field 3.

Some researchers have analyzed barometric pressure data having diurnal variations (24 hour cycle) and the consequent effects on radon concentration (Tsang & Narsimhan 1991). However, under typical conditions, the semi-diurnal variation of the barometric pressure is a well documented result of the atmospheric tides resulting from the solar heating and coriolis forces on the earth (Beer 1976, Fejer 1967).

The observed radon concentrations in the central hole and the slab tubes, as well as the differential pressure across the slab, exhibit a semi-diurnal 12 hour cycle. Comparison between the time dependence of these observations and the absolute barometric pressure data collected during the same time intervals shows that the two cases match very well, except for a slight shift that exists between the observations and the collected barometric pressure data. This result indicates that the atmospheric tidal barometric pressure variations are the suggested driving force under neutral pressure conditions. In fact, it provides the dominant force for the elevated indoor radon concentrations in many houses built over low permeability soils and fill materials.

The atmospheric tidal barometric pressure variations are frequently small in amplitude compared to the pressures associated with the changing meteorological conditions. The effect of this force has been largely ignored by radon researchers looking for radon entry mechanisms, because it was considered that low or small pressure differences are not

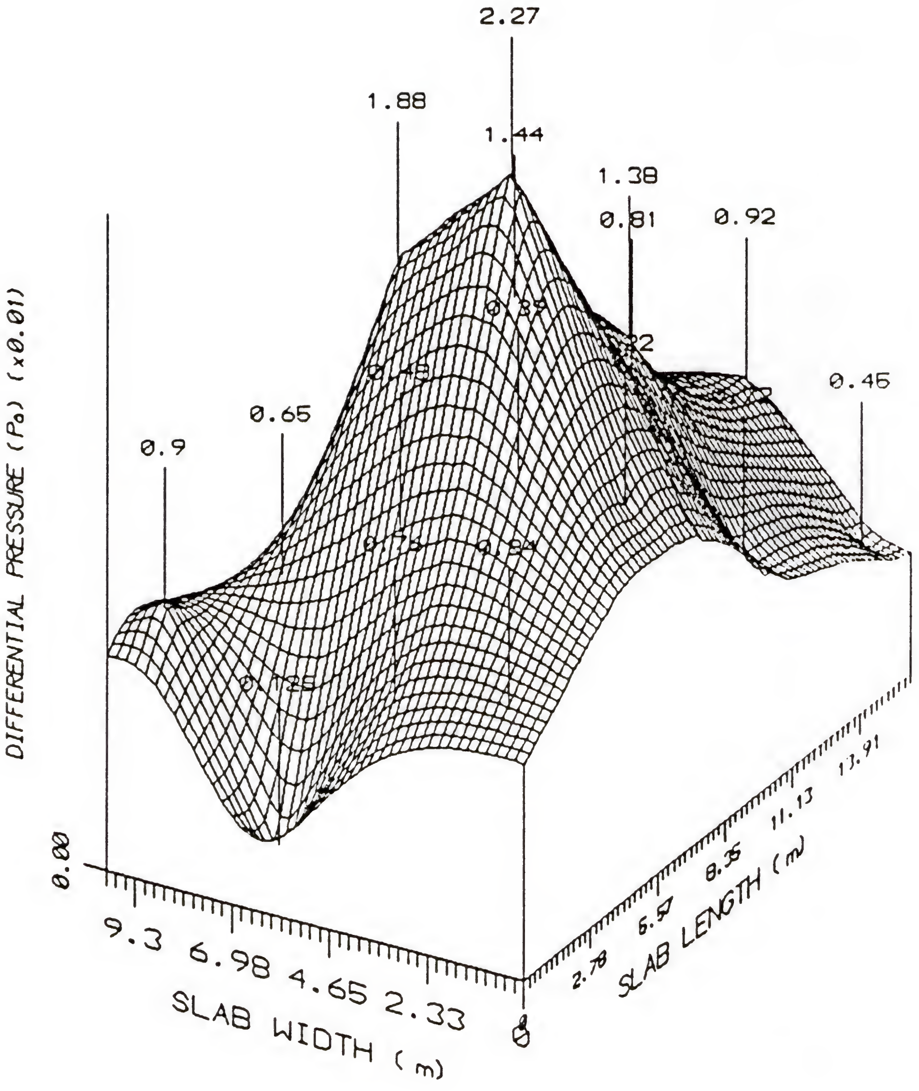

FIGURE 4-31: The spatial distribution of the differential pressure across the slab at the 140-minute mark in Figure (4-30).

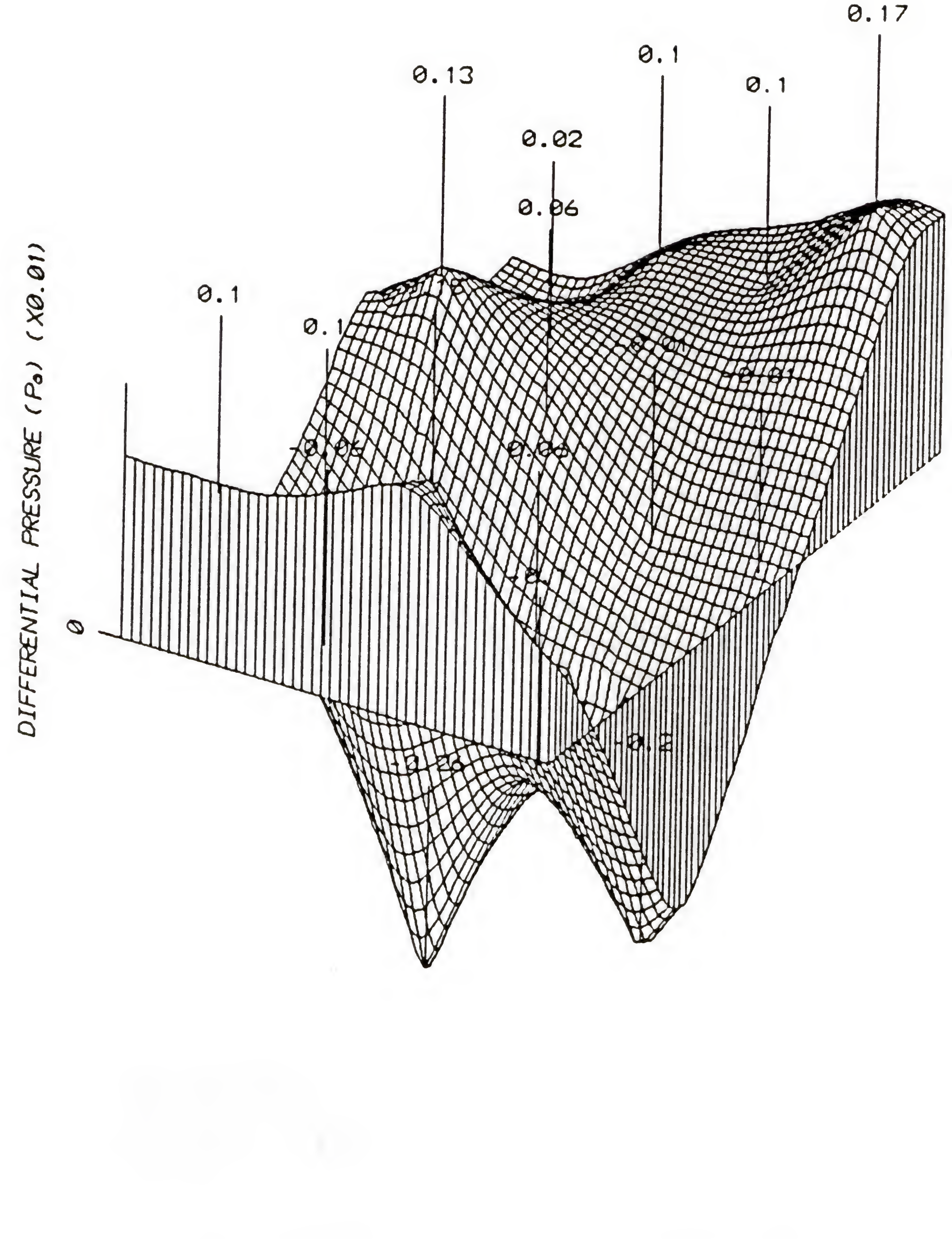

FIGURE 4-32: The spatial distribution of the differential pressure across the slab at the 1730-minute mark in Figure (4-30).

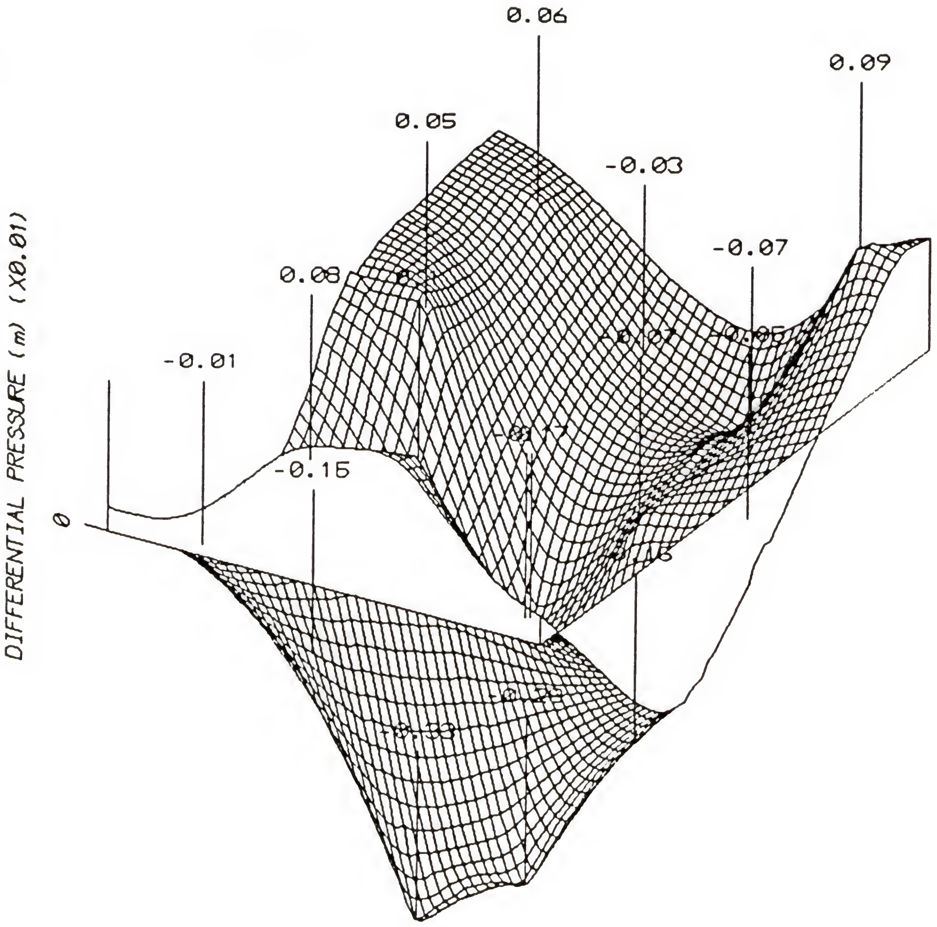

FIGURE 4-33: The spatial distribution of the differential pressure across the slab at the 2970-minute mark in Figure (4-30).

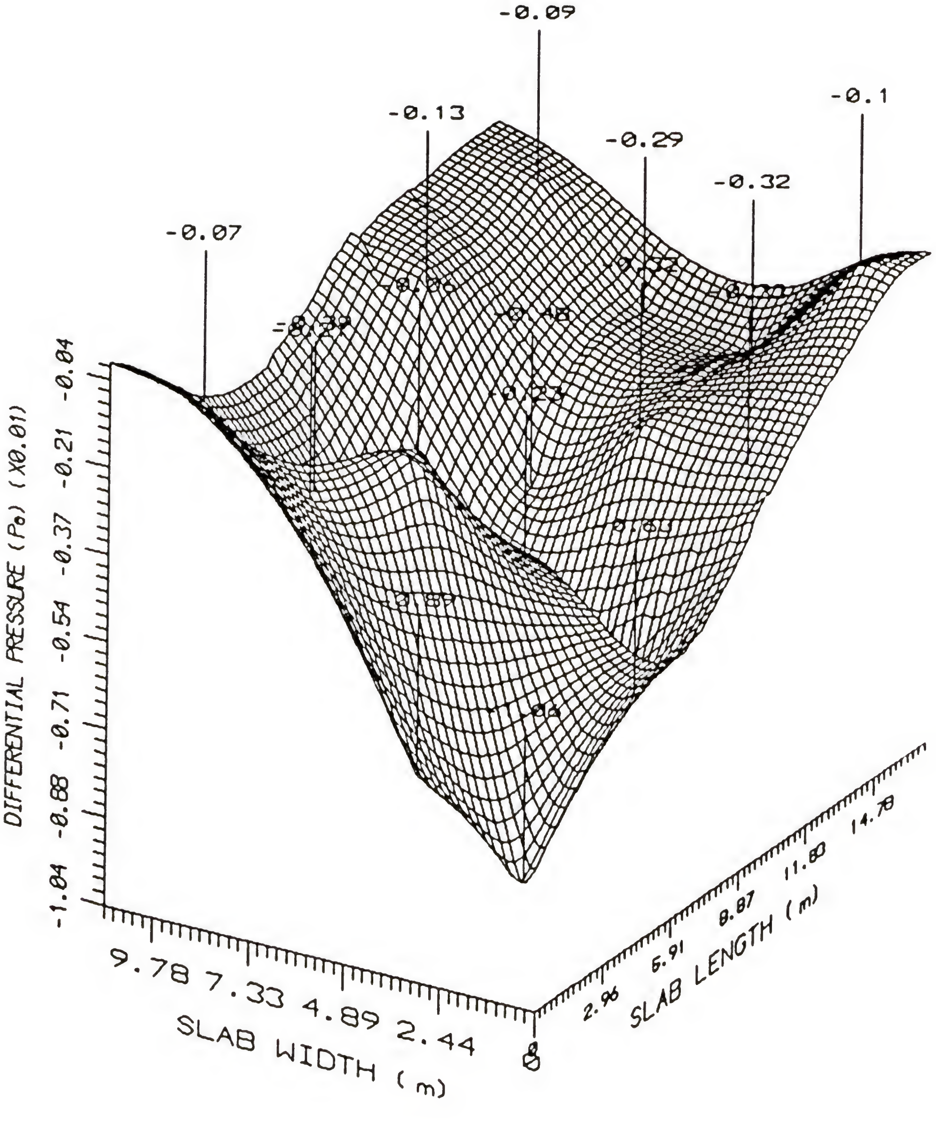

FIGURE 4-34: The spatial distribution of the differential pressure across the slab at the 3510-minute mark in Figure (4-30).

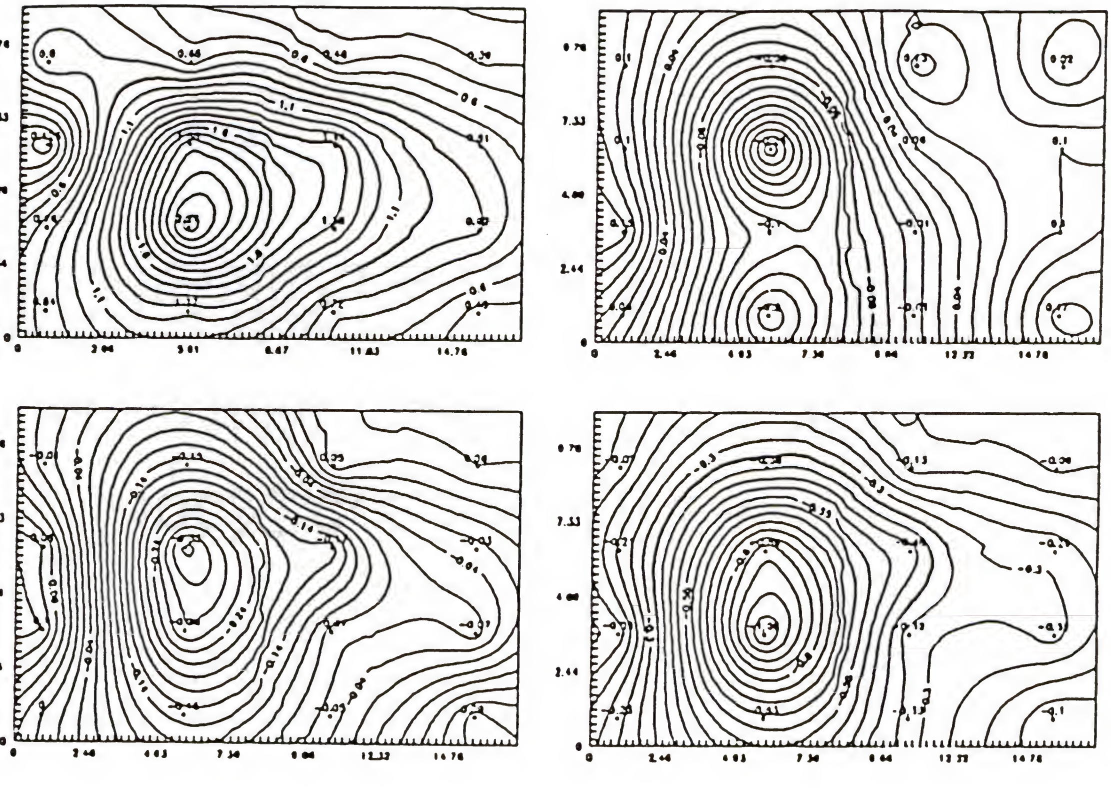

FIGURE 4-35: The contour maps of the spatial distributions illustrated in Figures 4-31, 4-32, 4-33, and 4-34.

capable of inducing high radon concentrations compared to those induced by depressurization conditions.

In fact, small pressure differentials generated by the atmospheric tidal barometric pressure variations are applied across the slab between the indoors and the sub-slab area, not between the indoors and outdoors (the house shell), and provide natural pumping of the radon-rich soil gas from low permeability soils into the structure. Although the radon entry rate associated with this mechanism may be small, it is present at all times. Tsang and Narsimhan predicted that the barometric pressure fluctuation can increase the radon entry into a basement by up to 120% of the steady radon inflow due to a steady depressurization of 5 Pa, based on mathematical considerations for soil of homogenous permeability (Tsang & Narsimhan 1991).

The low amplitude atmospheric tidal barometric pressure driving force can induce a significant increase in the indoor radon concentration by the natural pumping mechanism, without depressurizing the interior of the structure relative to the outdoors. This increase occurs since the indoor/outdoor pressure equalizes quickly, resulting in a build-up of the radon concentration (Hintenlang and Al-Ahmady 1992). Other mechanisms can bring more radon into the house, but they also increase the infiltrating air flow to dilute the indoor radon concentration significantly.

The slow response of the sub-slab system to the change in barometric pressure results from the low permeability soil and fill materials. Using Equation 8 in Chapter 2, with typical values of soil permeability (k) and soil dynamic viscosity (μ), results in soil gas velocities on the order of less than one meter per second for barometric pressure changes of a few hundred pascal applied over several meters, the characteristic length from the edge to the center of the slab. The response of the sub-slab air volume pressure to the barometric pressure variation has been quantitatively modeled as a damped exponential response. The equilibrium of the sub-slab air volume pressure with the outdoor pressure takes a relatively long time, on the order of tens of minutes, compared to the indoor/outdoor equilibrium time, for the distances and volumes typically encountered in this research.

If the atmospheric tidal barometric pressure variations are modeled as step functions, where the step occurs at the beginning of the measurement interval, then the sub-slab air volume pressure response after each time interval Δt, is calculated by the following equation,

$$P_{ss}(t+\Delta t) = C+P_b(t+\Delta t)-(P_b(t+\Delta t)-P_{ss}(t))\ \exp(-\Delta t/T_R) \quad (4\text{-}3)$$

where, $P_{ss}(t)$ is the sub-slab air volume pressure at time t,
$P_b(t)$ is the barometric pressure at time t,
T_R is the characteristic equilibrium time, and

C is a constant to compensate for the steady state component influenced by meteorological conditions such as temperature.

The sub-slab air volume pressure will equalize with barometric pressure changes, showing the exponential response with the characteristic equilibrium time (T_R). Since the indoor pressure equalizes quickly with the change in barometric pressure, the difference between the indoor pressure and outdoor pressure will be zero after less than one minute under structure neutral pressure conditions. The difference between the sub-slab air volume pressure and the indoor pressure is therefore,

$$\Delta P_{slab} = P_{ss}(t+\Delta t) - P_b(t+\Delta t) \tag{4-4}$$

and,

$$\Delta P_{slab} = C-(P_b(t+\Delta t)-P_{ss}(t)) \exp(-\Delta t/T_R) \tag{4-5}$$

The difference between the sub-slab air volume pressure and the outdoors will exponentially decrease for the time period of T_R. When the duration of the step changes in barometric pressure occur in periods longer than T_R, the sub-slab air volume pressure at time t is, in fact, equal to the barometric pressure $P_b(t)$ for periods Δt-T_R. The difference, therefore, can be calculated from only the barometric pressure data as,

$$\Delta P_{slab} = C-(P_b(t+\Delta t)-P_b(t)) \exp(-\Delta t/T_R) \tag{4-6}$$

This model can be used to predict the differential pressure across the slab by using only the barometric pressure data collected over the same time period Figures 4-36 A and B show the predicted sub-slab air volume pressures for two different experimental periods.

The solid line is the calculated sub-slab air volume pressure near the absolute barometric pressure measurements. Since the indoor/outdoor pressure equalizes quickly, the difference between the absolute barometric pressure and the calculated sub-slab air volume pressure using the above model can predict the indoor/sub-slab pressure differential at each point across the slab and gives, consequently, the differential pressure map across the slab.

The barometric pressure data were applied to the above model, and the result is a family of predicted graphs for different characteristic equilibrium times, T_R. Each graph fits specific point(s) in the slab system, generating the time dependent differential pressure map across the slab. The characteristic equilibrium time is longer for the points near the center of the slab. Figures 4-37 A, B, and C show the predicted differential pressure responses for different characteristic equilibrium times.

Analysis of the characteristic equilibrium time indicates that this parameter is not always constant for the same point under the slab at different barometric pressures, as might be expected. Although the equilibrium time represents the

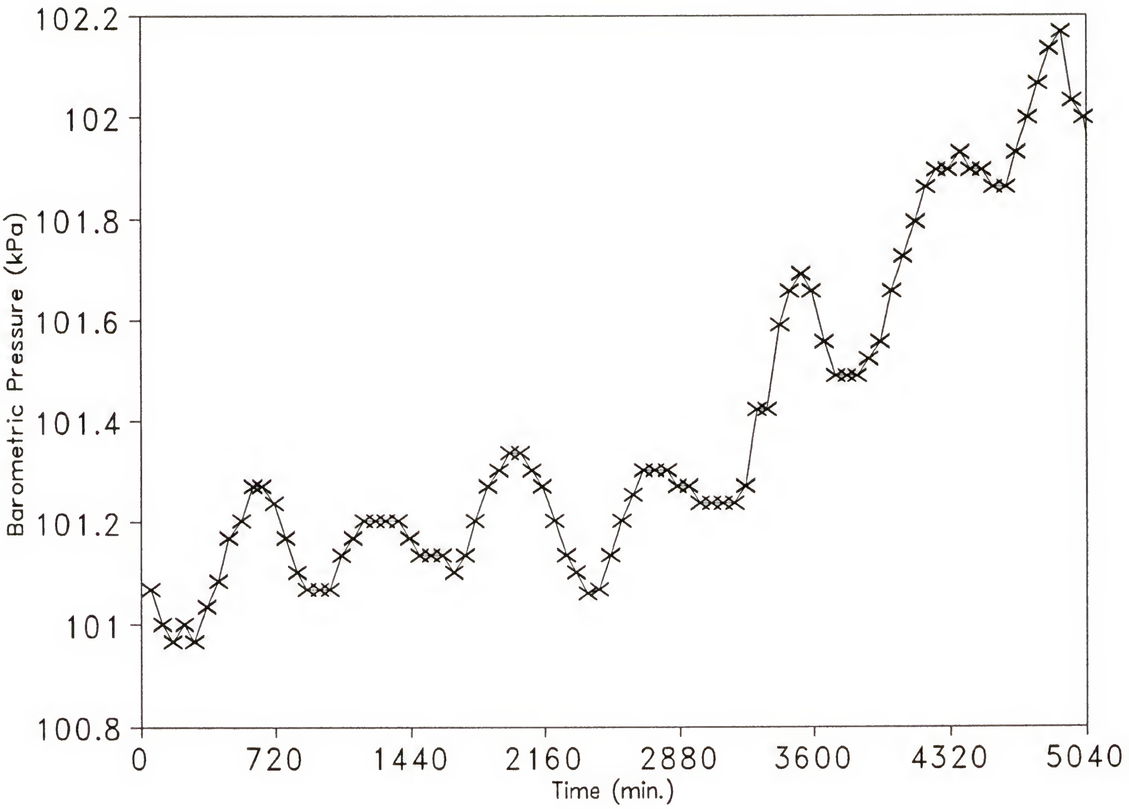

FIGURE 4-36 A: The time variations of a 4-day sample of barometric pressure measurement data (x) and the predicted sub-slab air volume pressure (solid line).

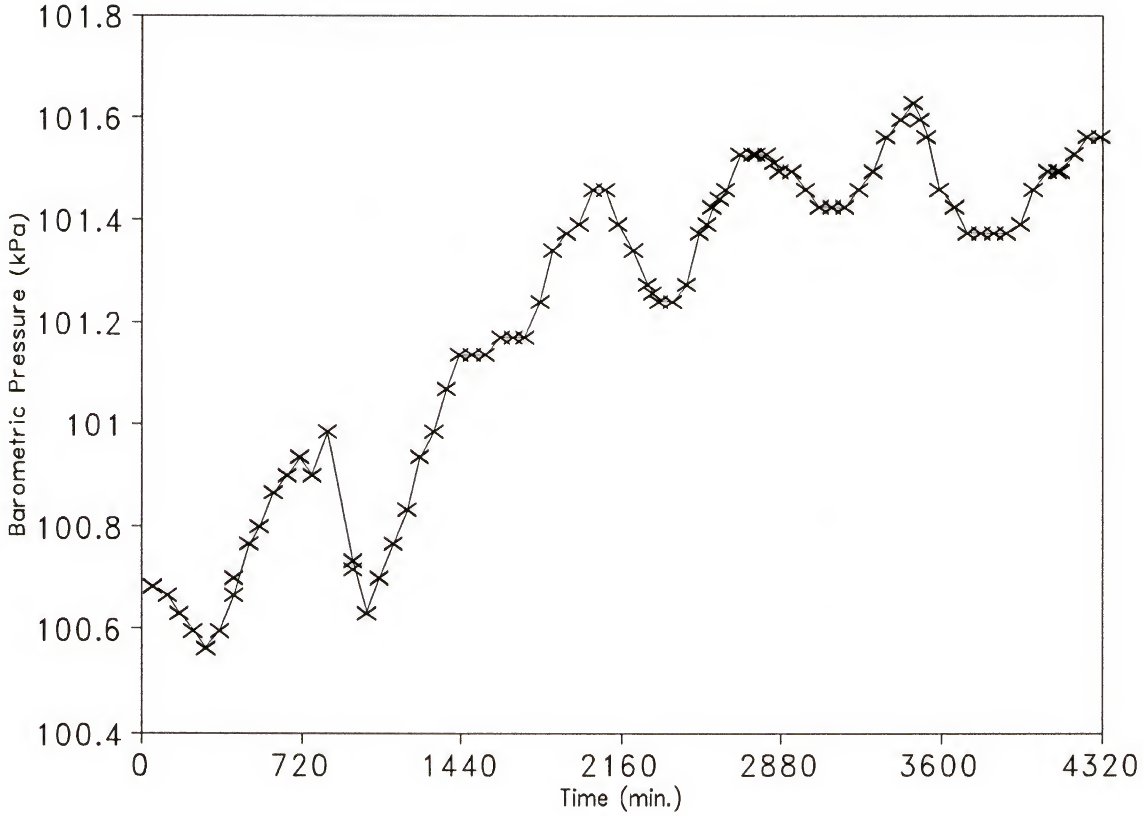

FIGURE 4-36 B: The time variations of a 3-day sample of barometric pressure measurement data (x) and the predicted sub-slab air volume pressure (solid line), for a testing period different than Figure 4-36 A.

damping effect on the sub-slab system on the variation in the barometric pressure, it is not only a function of the soil characteristics, but also of the barometric pressure itself.

In fact, the gaseous paths in the soil are functions of soil parameters such as porosity and emanation coefficients, which are themselves affected by different factors such as moisture content. The amplitude of the barometric pressure variation in each step and the actual position in time compared to the measurement time are expected to affect the characteristic equilibrium time T_R.

For this research, different values of T_R are applied to generate predicted patterns; fitting using the suitable T_R can then produce the measured differential pressure across the slab. The constant (C) in the model equation is assumed initially to be zero. The purpose of this constant is to provide vertical offset to the predicted response in some cases, especially for the points near the slab edges. This offset may be needed to correct for the effect of some forces, such as temperature, that generate pressure differences.

Figures 4-38 A to E and Figures 4-39 A and B show the predicted and measured differential pressures across the slab produced by the above model. In Figure 4-38 predictions for five points (1, 3, 6, 10 and 13) were produced using equilibrium times between 14 and 20.5 and a constant value (C) of zero. Figures 4-39 A and B show the predicted pressure differential fits with the measured values for points 10 and

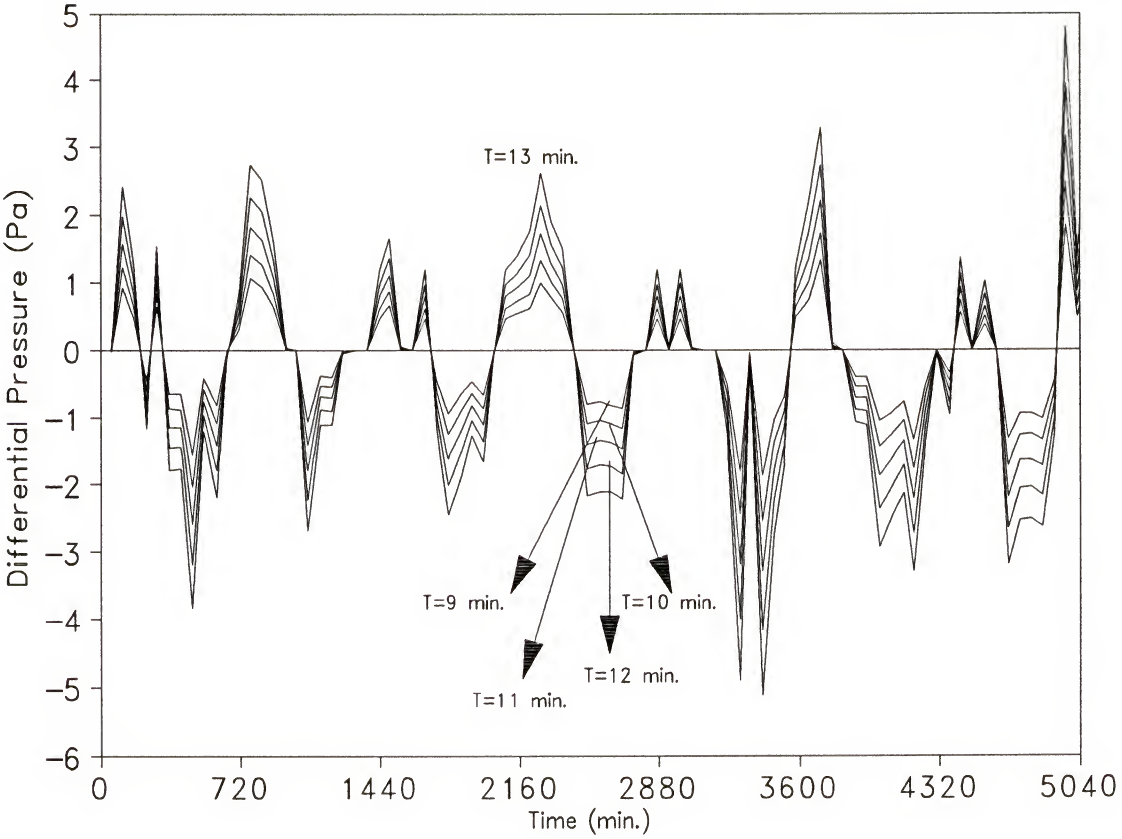

FIGURE 4-37 A: The predicated patterns of the differential pressure across the slab for sub-slab equilibrium times of 9 to 13 minutes from the barometric pressure data of Figure 4-36 A.

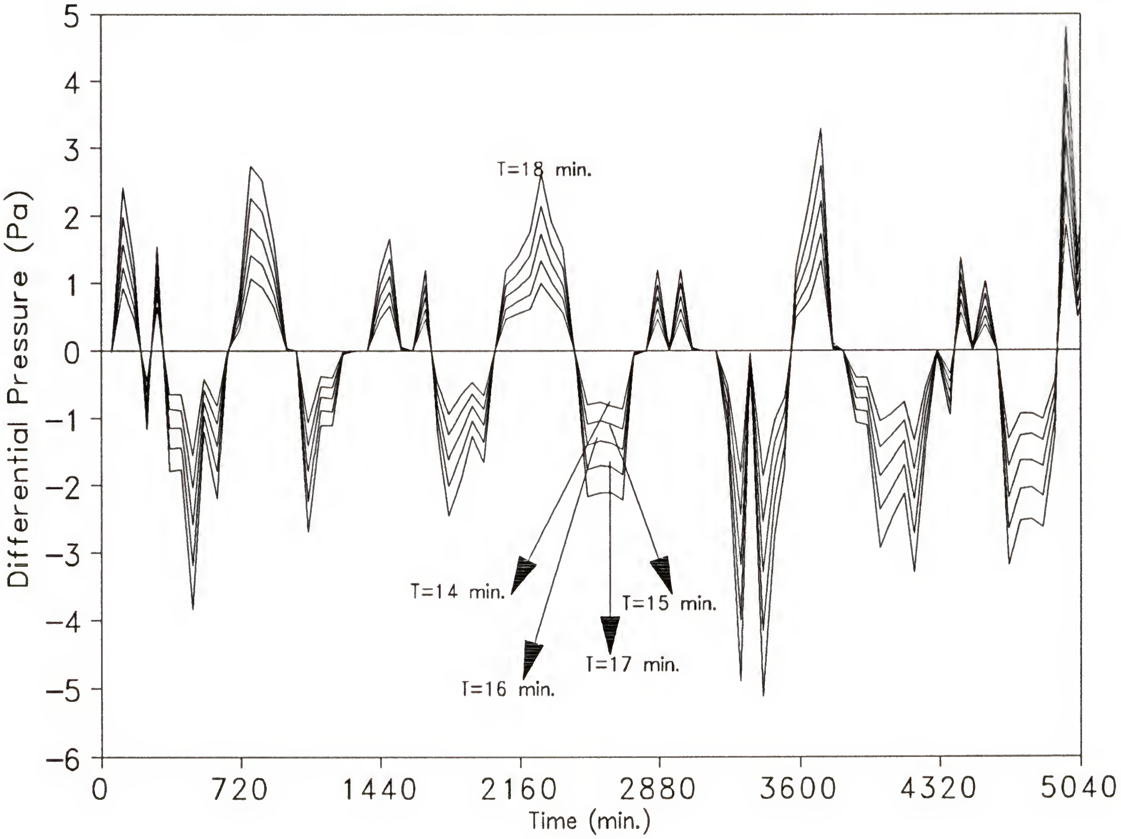

FIGURE 4-37 B: The predicated patterns of the differential pressure across the slab for sub-slab equilibrium times of 14 to 18 minutes from the barometric pressure data of Figure 4-36 A.

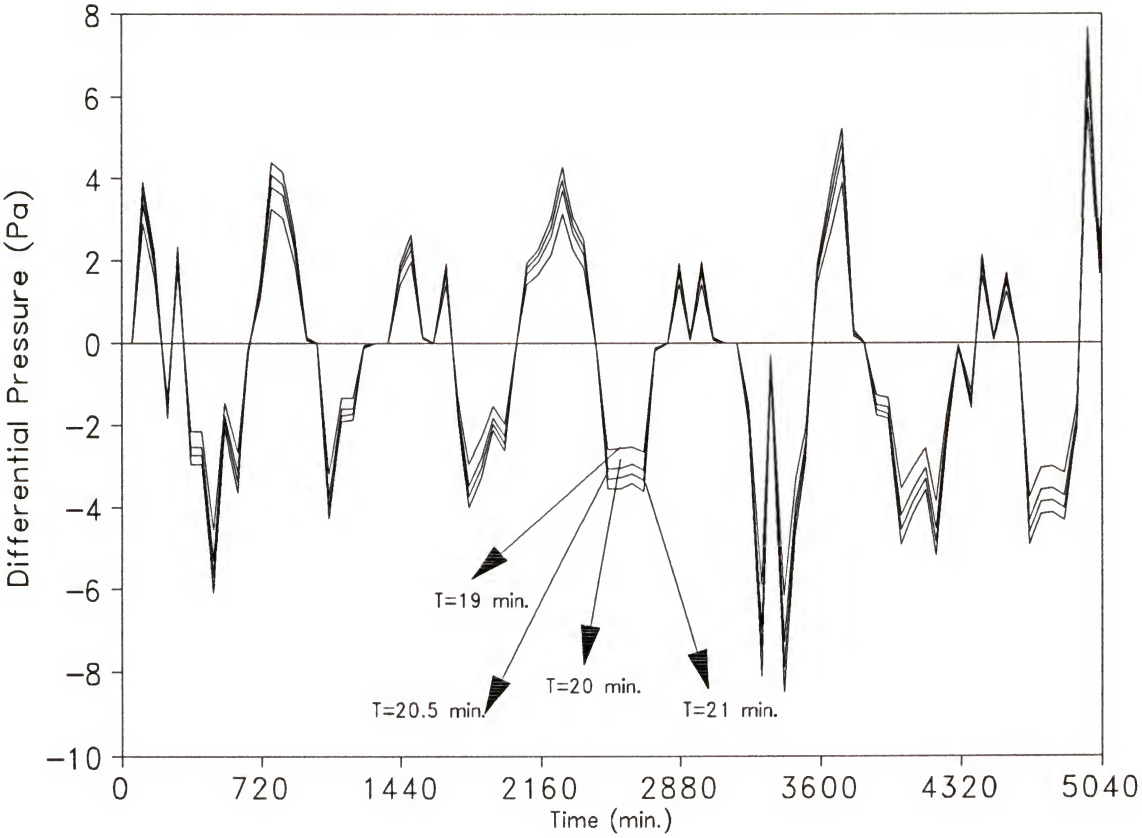

FIGURE 4-37 C: The predicated patterns of the differential pressure across the slab for sub-slab equilibrium times of 19 to 21 minutes from the barometric pressure data of Figure 4-36 A.

2 near the center and the edge of the slab, respectively, for different times from those in Figures 4-38. A characteristic equilibrium time of 16 min. was used for the fit of Figure 4-39 A, and 13 min. with a constant value of C= -0.2 Pa. was used for the fit in Figure 4-39 B.

This model is sensitive to changes in barometric pressure, since the generated pressure differentials are on the order of several pascal. Fits for the points located in (or near) the center of the slab generated better results than those located near the slab edges. The reason is the available resolution in the measured barometric pressure data. The model starts to give the same response for equilibrium times of about 8 minutes or less with the collected barometric pressure data format used in this application (##.### in Hg). If the barometric pressure data are measured with more significant figures, then the model is expected to give better resolution of the characteristic equilibrium times for the short response points (near the slab edges). For the points located near the center of the slab, the resulting fit undergoes a discernable change if the characteristic equilibrium time is changed by ±1 minute.

As seen in Figures 4-38 and 4-39, the agreement between the observed and predicted indoor/sub-slab differential pressures across the slab demonstrates the effect of the low permeability soils and fill materials in damping the sub-slab air volume pressure in response to the barometric pressure

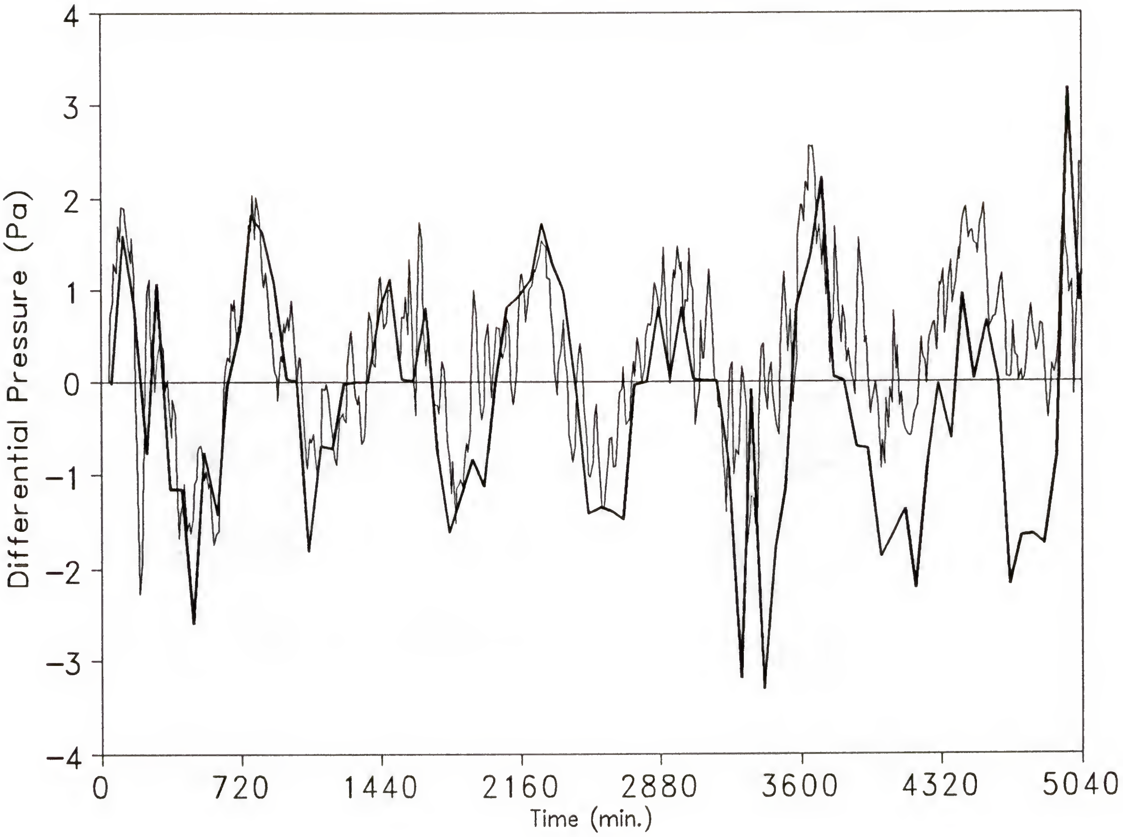

FIGURE 4-38 A: Time variations of the modeled (heavy-line) and the measured differential pressures across the slab monitored at sub-slab location 1 (Figure 4-36 A) Using T_R=16 min.

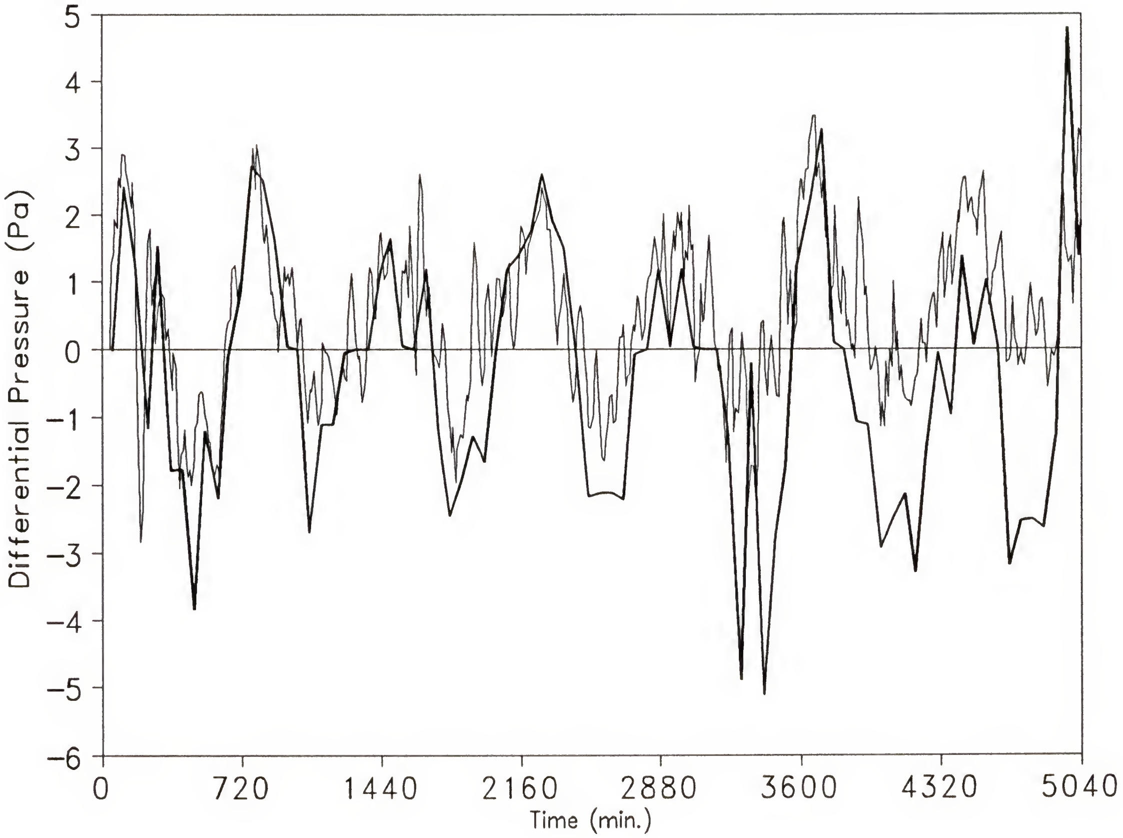

FIGURE 4-38 B: Time variations of the modeled (heavy-line) and the measured differential pressures across the slab monitored at sub-slab location 3 (Figure 4-36 A) Using T_R=18 min.

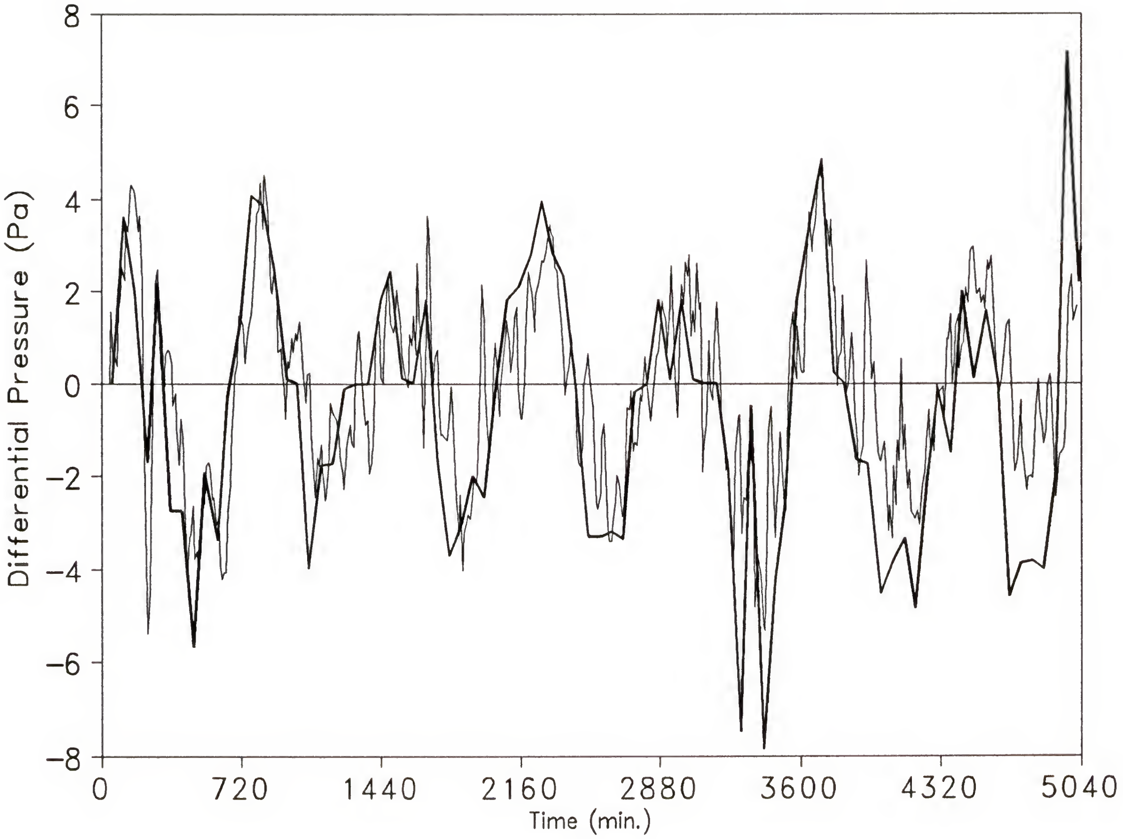

FIGURE 4-38 C: Time variations of the modeled (heavy-line) and the measured differential pressures across the slab monitored at sub-slab location 6 (Figure 4-36 A) Using T_R=20.5 min.

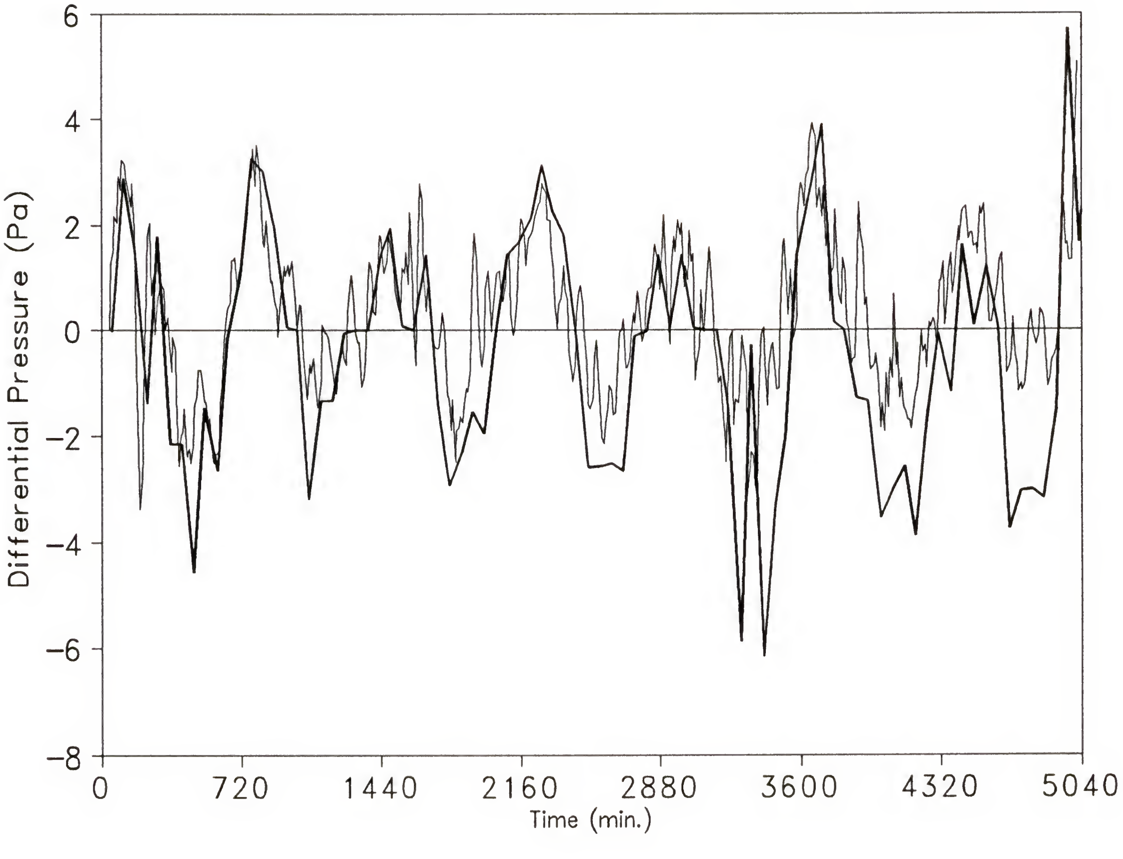

FIGURE 4-38 D: Time variations of the modeled (heavy-line) and the measured differential pressures across the slab monitored at sub-slab location 10 (Figure 4-36 A) Using T_R=19 min.

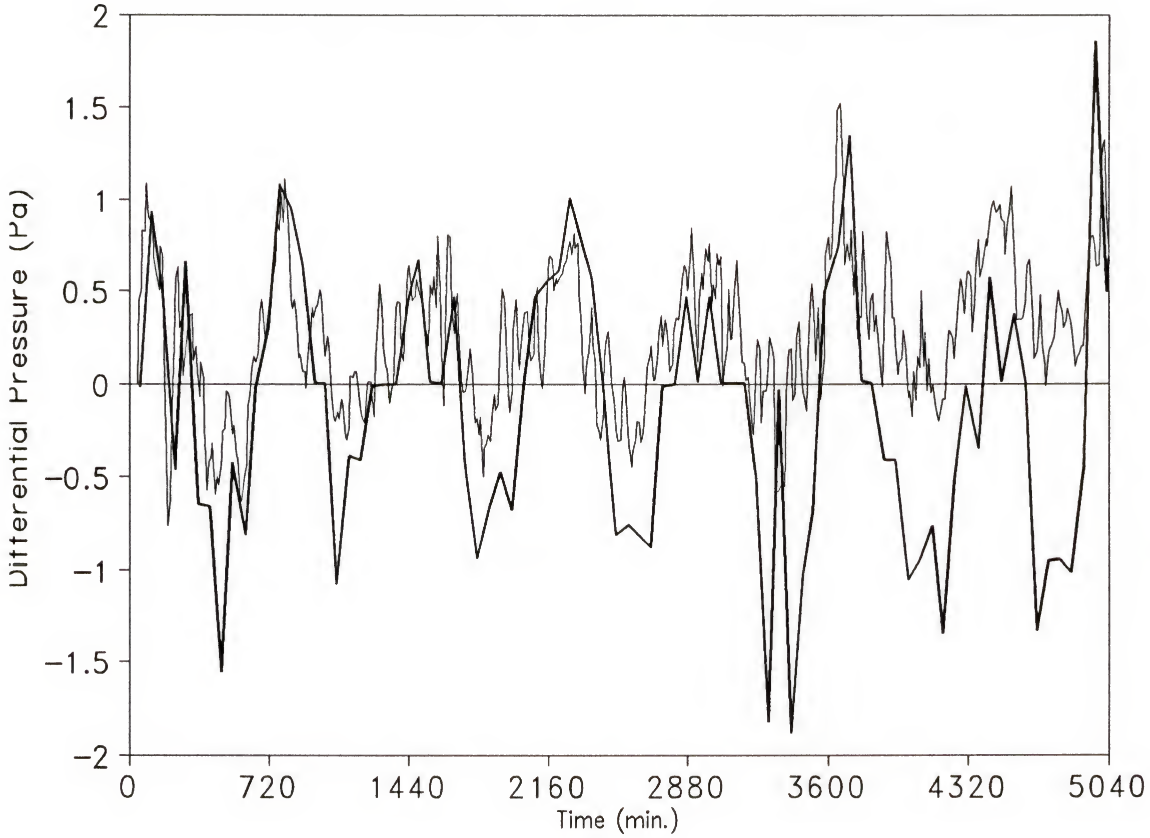

FIGURE 4-38 E: Time variations of the modeled (heavy-line) and the measured differential pressures across the slab monitored at sub-slab location 13 (Figure 4-36 A) Using T_R=14 min.

variation. Natural differences between the indoor and sub-slab pressures provide natural pumping of the radon-rich soil gas into structures.

The pumping occurs during the positive oscillation of the cycle because the indoor pressure becomes negative with respect to the sub-slab, and the radon is drawn from the soil into the building interior. The positive and negative portions of the differential pressure across the slab and, consequently, the sub-slab radon cycle are well documented results of this research, when the experimental setting is designed to simulate limited penetration in the slab area.

An experimental attempt to observe the cycle of the indoor radon concentration was performed, and there was difficultly in resolving the time dependent indoor radon concentrations generated by the natural pumping, from the time integrated effects of this pumping, using the monitors described in the Chapters 3. In fact, the measured indoor radon concentrations are damped by not only the detector response but also the whole-house volume effects. The large whole-house volume causes the radon entry inside the structure to be spatially distributed, which significantly affects the convective component of radon transport and enhances the diffusion processes of radon transport.

The characteristic time for radon transport by diffusion is much smaller than that for convection. Therefore even with the existence of relatively small convective processes, the whole-house volume can damp the effect of the time based natural pumping of radon and dominate the indoor radon transport with times characteristic of the diffusion processes under neutral pressure conditions. That produces a kind of "ramp" response when the indoor radon concentration is measured continuously over time. However, for typical conditions the semi-diurnal cycle of the indoor radon concentration is expected to exist with a lag shift in its peaks. So it should be possible in the future to observe the cycle in the indoor atmospheres experimentally, after suitable reduction of radon monitors response times.

The prediction of the indoor radon concentrations as a result of the natural pumping mechanism, induced by the atmospheric tidal barometric pressure variation under neutral pressure conditions, is the next logical step after constructing the sub-slab air volume pressure and indoor/sub-slab pressure differential prediction model above. In fact, attempts in this direction are in progress but the kinds of measurements and information required for this purpose are beyond the scope of the research described in this paper.

Experimental data characterizing the potential effective leakage areas of the house slab penetrating paths under neutral pressure conditions may be needed for this purpose. Furthermore, development of quantitative methods to resolve the time dependent indoor radon concentrations generated by the other forces that create a pressure differential, such as

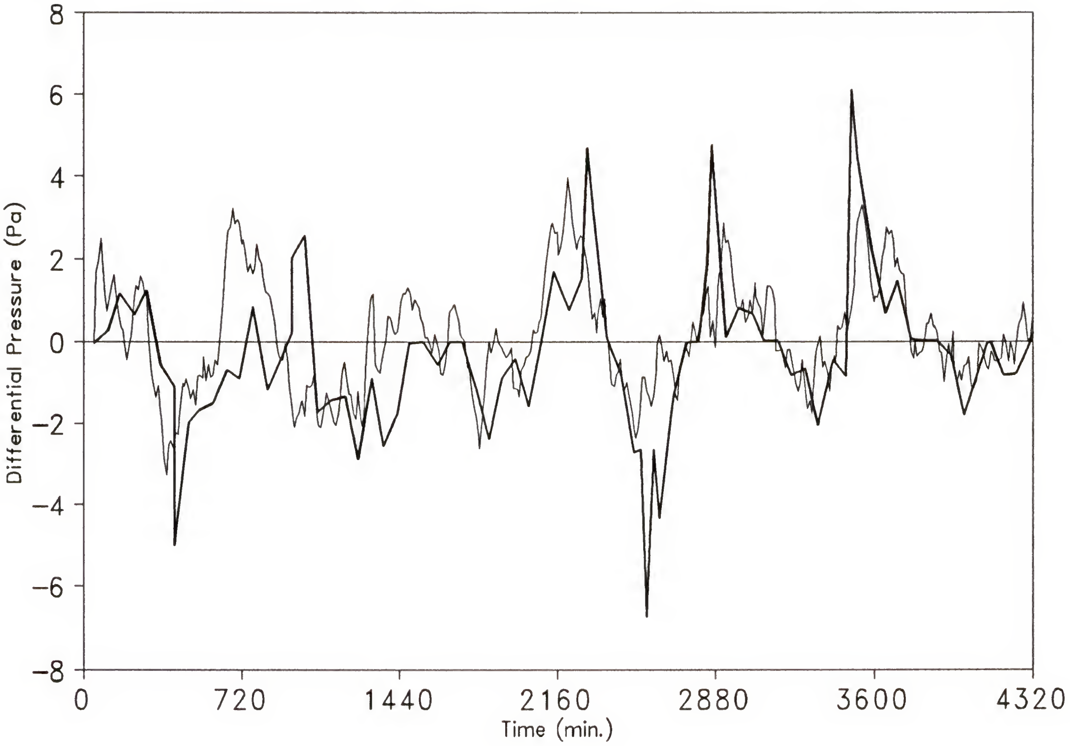

FIGURE 4-39 A: Time variations of the modeled (heavy-line) and the measured differential pressures across the slab monitored at sub-slab location 10 (Figure 4-36 B) Using T_R=16 min.

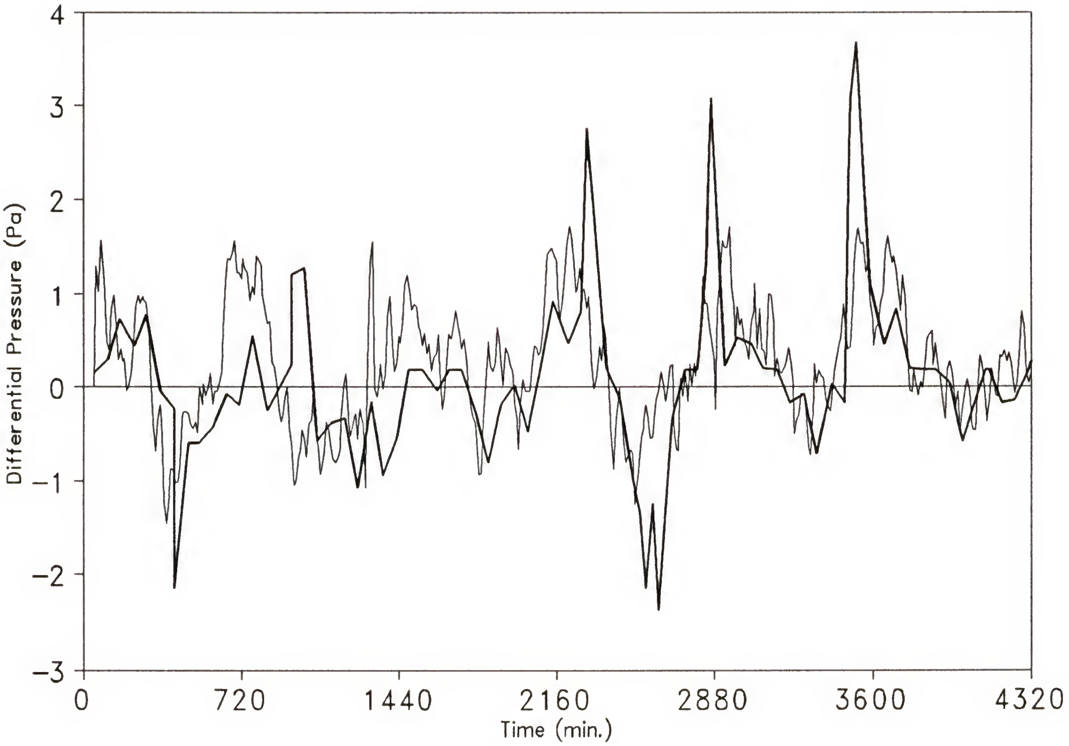

FIGURE 4-39 B: Time variations of the modeled (heavy-line) and the measured differential pressures across the slab monitored at sub-slab location 2 (Figure 4-36 B) Using T_R=13 min. and C=-0.2 Pa.

temperature or wind, may be necessary in the process of modeling the natural pumping contribution to the overall radon concentrations. The other possibility is to characterize the effect of the natural pumping mechanism directly, and from this resolve the contributions from those other forces. In addition, calculation of the air exchange rate between the indoors and outdoors and its contribution to the radon removal rate at the point of measurement are considered necessary for the prediction of the indoor radon concentration.

Calculations for the indoor radon buildup, based on the observations in the research house after total ventilation was performed, resulted in an average radon entry rate of 6.8 Bq/s. The average differential pressure of the non-uniform distribution across the slab for the particular experiments of Figures 4-28 and 4-29 and the other slab points is about 0.9 Pa. This value is applied to a simple cylindrical slab-on-grade structure model (RAETRAD) for radon transport and entry developed by Nielson and Rogers (1991).

For pressure differentials causing a 0.9 Pa depressurization and an sub-slab radon concentration of $1.3\text{x}10^5$ Bq/m^3, as observed at the UFRRH, RAETRAD predicts a radon entry rate of 7.5 Bq/m^3, compared to the above calculation of 6.8 Bq/m^3. However, the RAETRAD prediction is based on a cylindrical slab-on-grad structure built over homogenous sandy soil which is 14% smaller than the rectangular slab-on-grad structure of the UFRRH. The soil at the UFRRH site may also slightly vary from that used by RAETRAD.

Wind-Induced Pressure Differentials

Differential pressure across the structure walls which might influence indoor radon concentrations may be generated due to wind blowing across the structure shell. Wind is probably one of the most fluctuating environmental parameters that interacts with indoor radon concentrations. The relationship between the latter interaction and the generated radon driving forces is complicated. It depends on the wind speed, direction, frequency, duration, shape of the pressure wave, structural features such as wall and slab interface, particular time and location, and the structure's surroundings.

Wind-induced pressure differentials might interact with the indoor radon concentration through pressure differences generated across the structure walls and consequently contribute to the structure ventilation and radon removal rates from the indoor environment into the outdoors. Indirect interaction could also occur if the wall/slab interface with the surrounding soil can provide paths to air flow from the sub-structure area into the indoors (or the outdoors), in response to a pressure generated on the walls by wind.

Wind speed and direction were simultaneously monitored with the other parameters at the UFRRH by the use of an on-site weather station. Wind related measurements at the UFRRH were also checked with data collected by the Gainesville Flight Service Station (FSS) at the Gainesville Airport administered by the Federal Aviation Administration (FAA).

Wind-induced pressures can fluctuate significantly and therefore consideration of the frequencies of pressure waves associated with blowing wind, as well as the level to which such pressure waves can propagate and be transmitted at the surface of the soil are important to characterize. Some researchers such as Van der Hoven (1957) and Fukuda (1955), have analyzed such problems with both theoretical and experimental approaches.

Van der Hoven analyzed the spatial distribution of wind speed at Brookhaven, New York, and found that the wind energy distribution is roughly bimodal. Fukuda utilized a theoretical approach to estimate the time rate of change of pressure fluctuations when they are significantly smaller than the atmospheric pressure. In summary, previous experimental observations indicated that wind-induced pressure differences are dependent on wind wave shape, orientation, and shielding, and the wind speed (Nazaroff et. al. 1988).

At the UFRRH site, most of anemometer readings indicate wind speeds below 0.18 m/s more than 90% of the time, and the indoor/outdoor pressure responses measured across the different walls were observed to be nearly identical (in phase) throughout the experimental periods. The house is very well sheltered from the wind through dense trees in the surrounding area. For those observations it has been assumed that the influence of wind at the UFRRH site is insignificant.

However, for the integrity of the modeling effort in this research, a mechanistic approach will be utilized to derive the fundamental relationship between the wind parameter of speed and the pressure difference that might be generated across the structure walls. The effects of other wind parameters will then be lumped into a coefficient that shapes the fundamental relationship.

Starting from the physics of a fluid in motion, in this case air, the fundamental equation for conservation of fluid energy can be utilized to establish a correlation between wind speed and pressure. In this application, wind is assumed to be represented by an incompressible stream of air that has a Reynolds number much grater than one. Such conditions for this case are always satisfied.

Neglecting the shear stress between the wind stream and the ground surface, the conservation of energy (Bernoulli's equation) indicates that the total air energy under steady-state conditions must be constant at any point in the stream, therefore

$$1/2\ \rho\ v^2 + h\ \rho\ g + P = \text{constant} \qquad (4\text{-}7)$$

where P is the air pressure in Pa,

h is the height of the point in meters relative to a horizontal reference,

ρ is the air density (kg/m^3),

g is the acceleration constant due to gravity (m/s^2), and

v is the air speed (m/s).

If the above equation is applied for two points in the air system, one point in the air stream around the structure when the pressure is not affected yet by the existence of the flow obstruction, and other point at the surface of the structure wall, then

$$(0.5\ \rho\ v^2)_1 + (h\ \rho\ g)_1 + P_1 = (0.5\ \rho\ v^2)_2 + (h\ \rho\ g)_2 + P_2 \quad (4\text{-}8)$$

For the height encountered in single family residential structures and/or one-story structures such as the UFRRH, measured from the ground surface around the structure, the difference between the two quantities $(h\ \rho\ g)_1$ and $(h\ \rho\ g)_2$ is small enough to be neglected. Then Equation 4-8 can be written as,

$$P_1 - P_2 = \Delta P = 0.5\ \rho\ (v^2_2 - v^2_1) \qquad (4\text{-}9)$$

When the wind blows on the structure wall, its speed can be reasonably assumed to be zero at the surface of the wall.

If point 1 is selected to represent the area on the wall, the above equation reduces to,

$$\Delta P = 0.5\ \rho\ v^2 \qquad (4\text{-}10)$$

where v is the directional velocity of the wind stream measured by the weather station, and ΔP is the pressure difference between the wall outer surface and the pressure of the wind stream surrounding the structure. The wind stream pressure can be reasonably represented by the atmospheric pressure measured at the site and, therefore, the immediate pressure on the wall will be equal to,

$$P_{wall}(t) = P_b\ (t) + 0.5\ \rho\ v^2(t) \qquad (4\text{-}11)$$

The wind-induced differential pressure across the structure may then be calculated from,

$$\Delta\ P_w = P_{in} - P_{wall} = P_{in} - P_b + 0.5\ \rho\ v^2 \qquad (4\text{-}12)$$

Assumptions made during the preceding derivation neglect the effect of shear stress between the wind stream and the ground, the compressibility of air (particularly at the wall surface), and other factors that contribute to reduce the value of the pressure difference estimated by Equation 4-12 Therefore, this equation represents the maximum pressure difference that can be induced from wind blowing on the structure for the specific configuration. To account for the effects of the neglected factors, a constant, C_w (pressure or drag coefficient) is introduced into the equation that has a theoretical value ranging from zero to one.

The value of C_w is usually empirically determined through wind tunnel experimentation and is highly dependent on the particular cases of structure/wind configurations. Equation 4-12 is then written as,

$$\Delta P_w = C_w (P_{in} - P_b - 0.5 \rho v^2) \qquad (4\text{-}13)$$

Figures 4-40 A, B, and C illustrate the model predictions of wind-induced pressure differences developed across the wall of a structure when the indoor pressure is constant and equal to the barometric pressure. The wind is blowing with a range of speed (from 0 to 25 m/s) with wind drag coefficients of 0.56 (windward side wall), 0.49 (side wall), and -0.15 (leeward side wall), respectively.

Figure 4-40 D illustrates the model precautions for wind-induced pressure differences across the structure shell for wind speeds of 1, 3, 5, and 10 m/s, and the full range of drag coefficients. As seen from the graphs, the drag coefficient has a negligible effect for the small range of wind speed encountered at the UFRRH.

Figures 4-40 E and F illustrate the model prediction of wind-induced pressure differences generated in response to temporal variations in barometric pressure and indoor pressure equal to the time-average value of the barometric pressure for

1 and 14 m/s wind on the windward side wall and the leeward side wall of the structure, respectively.

Temperature-Induced Pressure Differentials

The initial attempt to model the temperature-driven pressure differentials involved studying the pressure differentials monitored across house shell (walls). Two experimental observations suggested that temperature is responsible for generating these pressure differentials across the structure shell. First, as evidenced from a previous section, contributions to the pressure differential that might be attributed to the wind blowing on the external walls of the structure are negligible. Second, the observed pressure differentials experienced a diurnal cycle similar to that of temperature.

Since these observations measure pressure differences, that is, the difference in the static pressure between two separated areas, the candidate physical quantity is, in fact, temperature difference. Although these pressure differences might be small in magnitude, in the range of a tenth to several pascal, they may exist continuously if temperature differences exist.

Continuous measurements were taken in order to track the time and spatial dependent responses of pressure in three separate areas during this research. Those areas are the

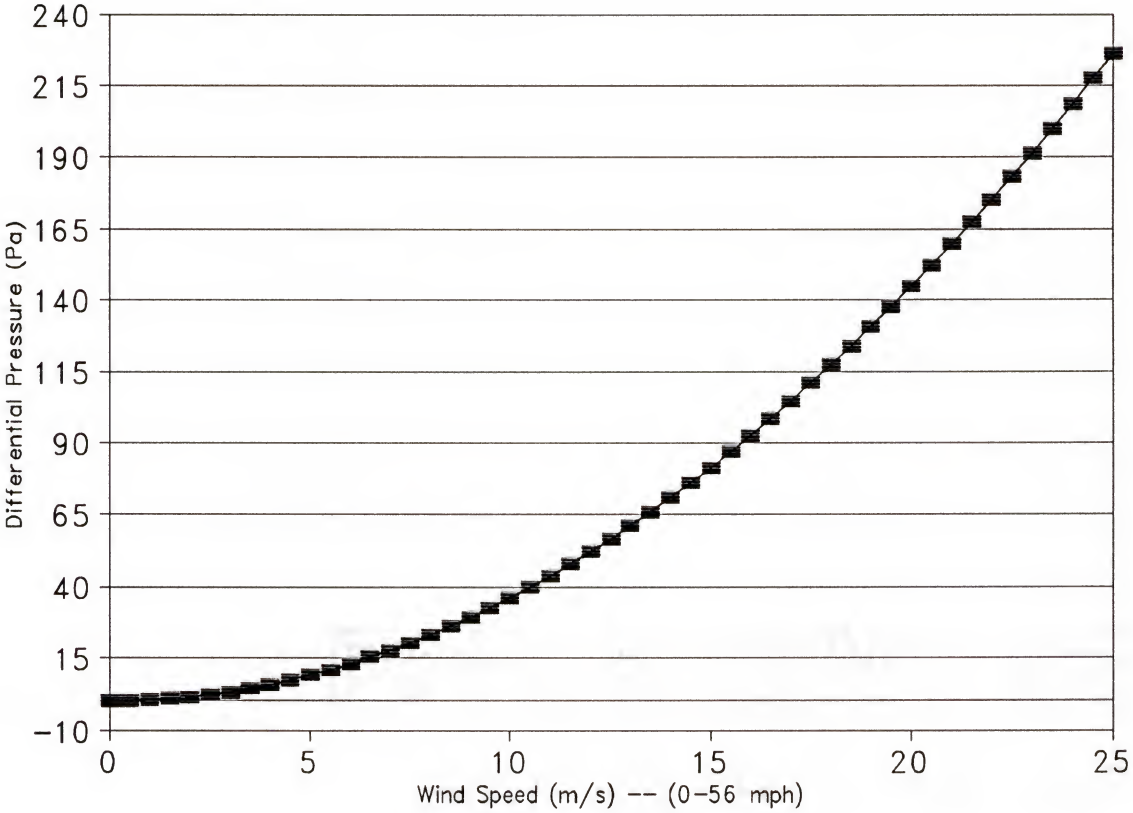

FIGURE 4-40 A: The wind-induced pressure differential predictions for a range of wind speed blowing on the windward side wall of a structure when the indoor pressure equals the barometric pressure.

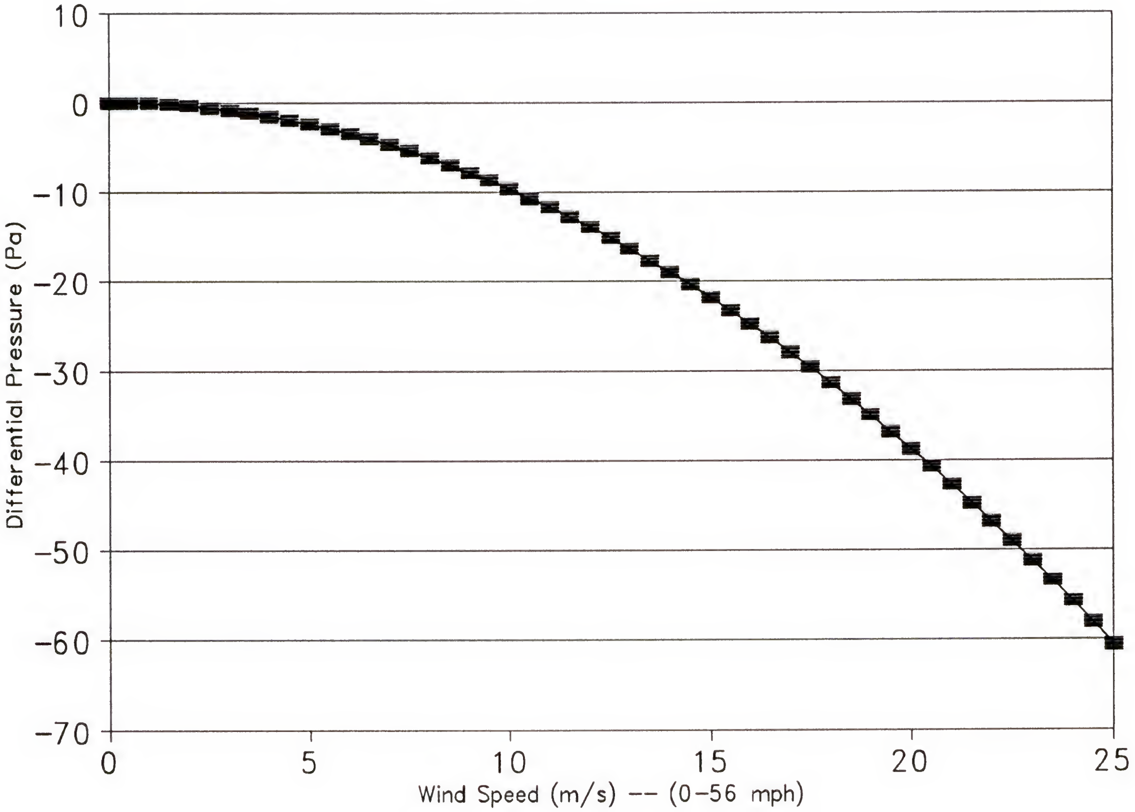

FIGURE 4-40 B: The wind-induced pressure differential predictions for a range of wind speed blowing on the leeward side wall of a structure when the indoor pressure equals the barometric pressure.

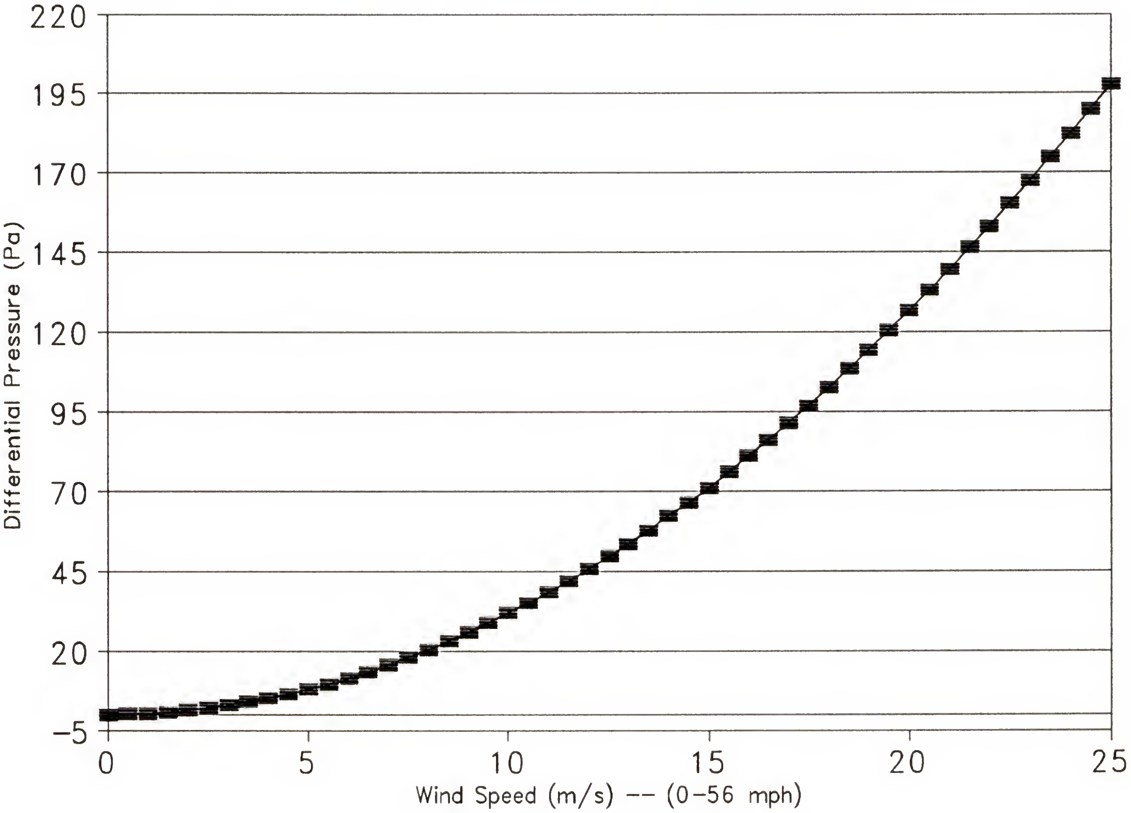

FIGURE 4-40 C: The wind-induced pressure differential predictions for a range of wind speed blowing on the side wall of a structure when the indoor pressure equals the barometric pressure.

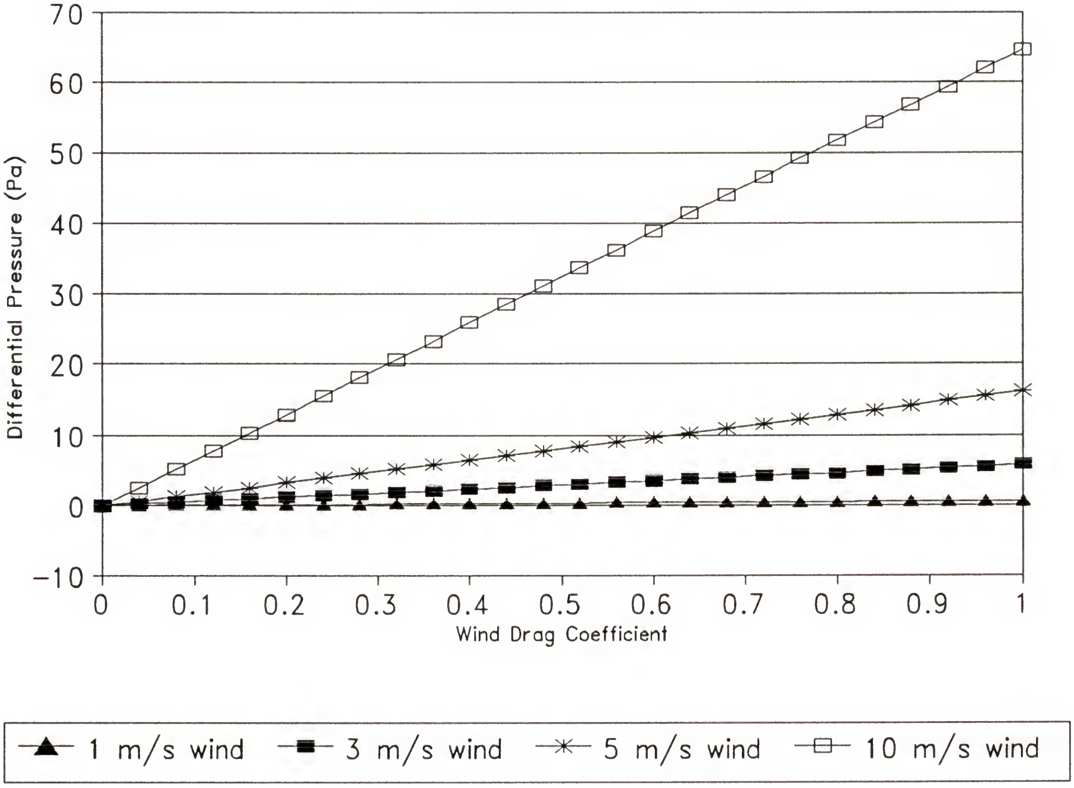

FIGURE 4-40 D: The model predictions of wind-induced pressure differences generated for several wind speeds blowing on the windward side wall of a structure as a function of the wind drag coefficient.

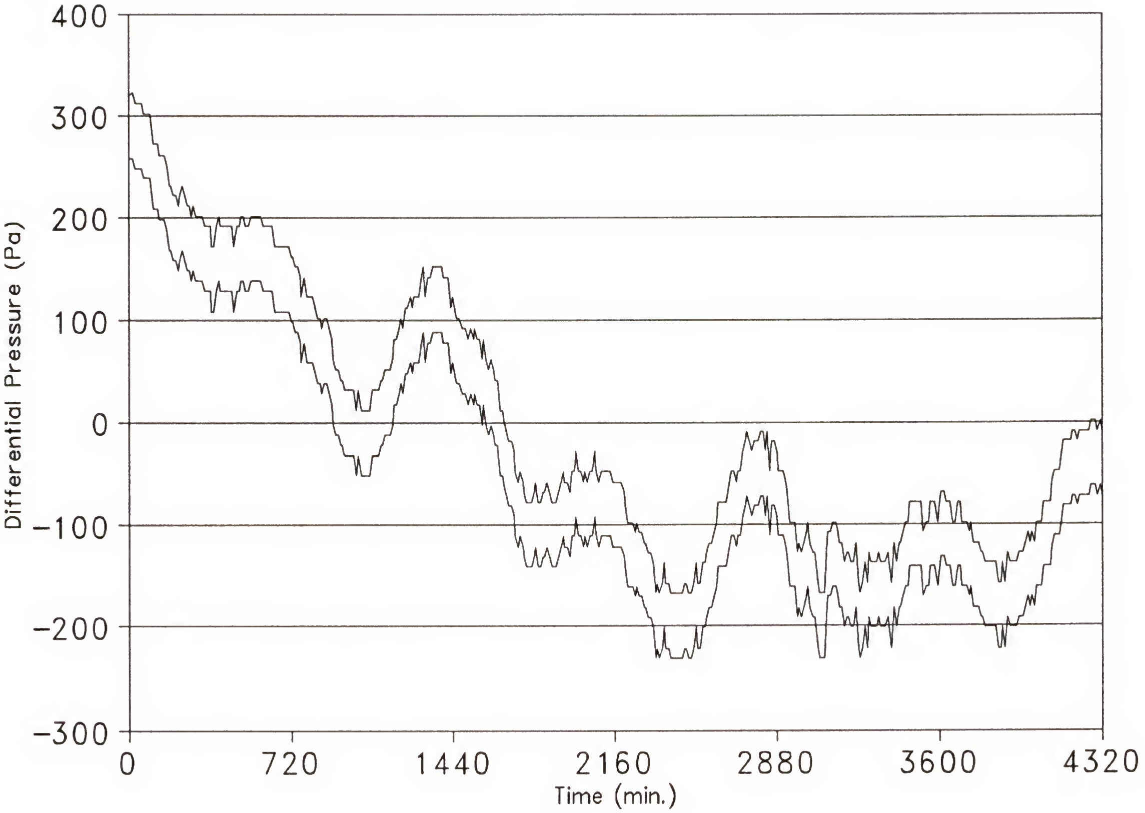

FIGURE 4-40 E: Prediction of wind-induced pressure differences in response to temporal variations in barometric pressure and indoor pressure equal to the average barometric pressure for 1 (lower curve) and 14 m/s wind on the windward wall.

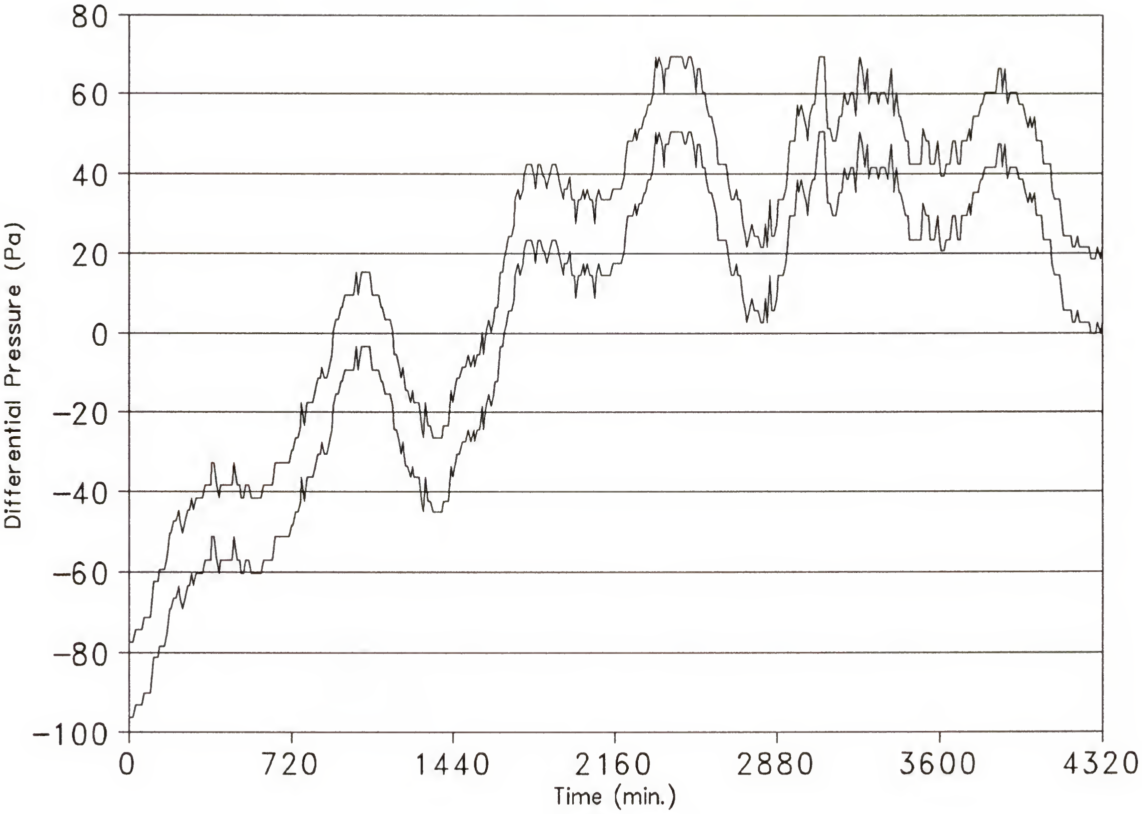

FIGURE 4-40 F: Prediction of wind-induced pressure differences in response to temporal variations in barometric pressure and indoor pressure equal to the average barometric pressure for 1 (upper curve) and 14 m/s wind on the leeward wall.

structure interior, sub-slab area, and the outdoors. As explained in the experimental design and methodology, temperature was monitored in each room, at the supply and return ducts, room register, HVAC thermostat location, attic, sub-slab area, and outdoors, using T-type, copper versus copper-nickel, thermocouple wires.

The experimental monitoring period of 96 hours along with a measurement interval of 60 seconds, averaged every 600 seconds, provided a suitable time interval over which both detailed local observation (for temperature measurement resolution), and global observations (for temperature behavior) could be performed.

Figures 4-41, A to F show samples of the temperature measurements in the attic, supply and return ducts, outdoors, indoors, and sub-slab zones. As seen in the graphs, all areas experienced a clear diurnal cycle that corresponded to one maximum and one minimum during the day. Observations for the indoor zone were very flat with respect to the spatial distribution. Only differences in the order of a tenth of a degree were experienced among different measurement locations in the indoor zones.

The absolute amplitudes (maximum peak minus minimum peak) of these diurnal cycles in the indoor environment were observed to be significantly limited when they were compared with the attic and the outdoor area as expected. The latter areas experienced the highest absolute temperature amplitude

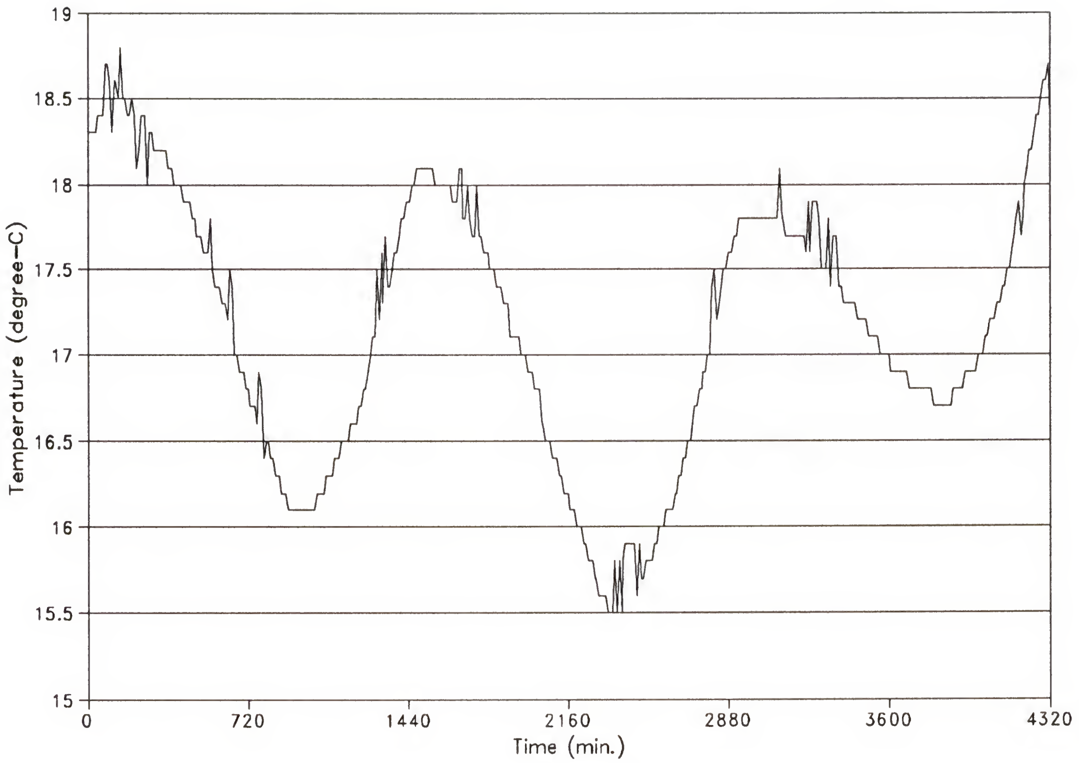

FIGURE 4-41 A: A three-day sample of the temporal variations of temperature measured in the attic zone at the UFRRH.

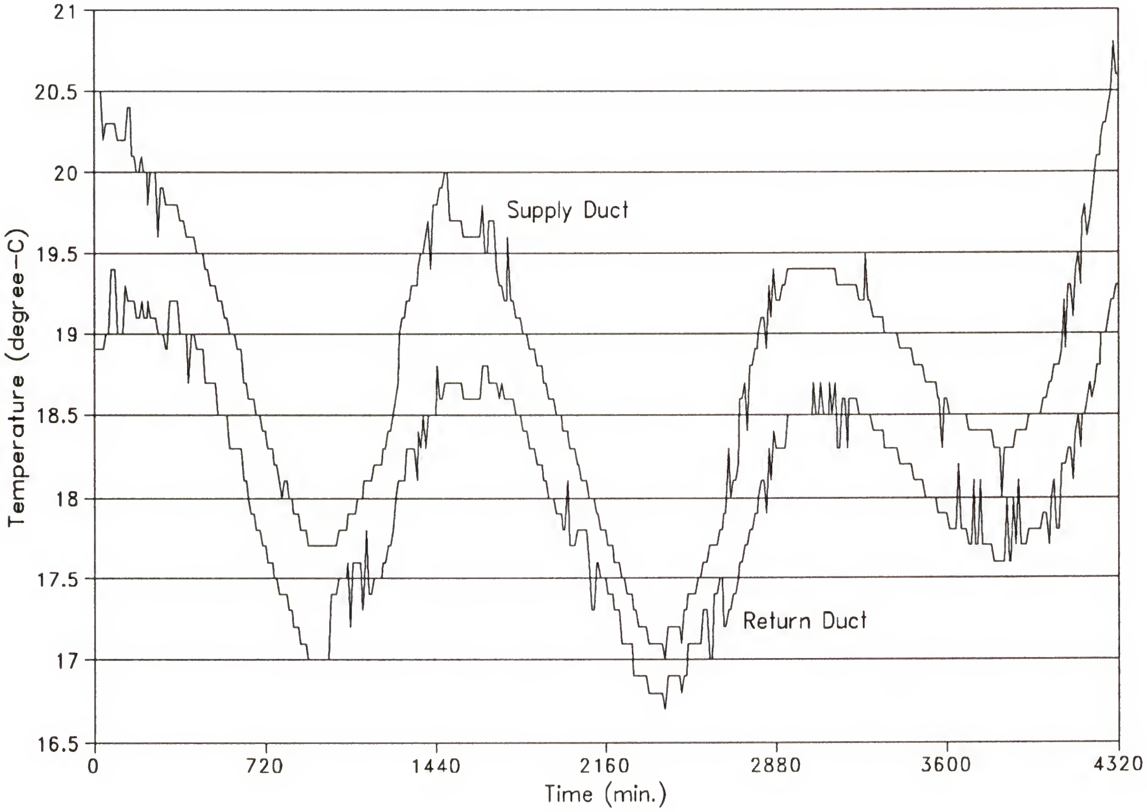

FIGURE 4-41 B: A three-day sample of the temporal variations of temperature measured in supply and return duct zones at the UFRRH.

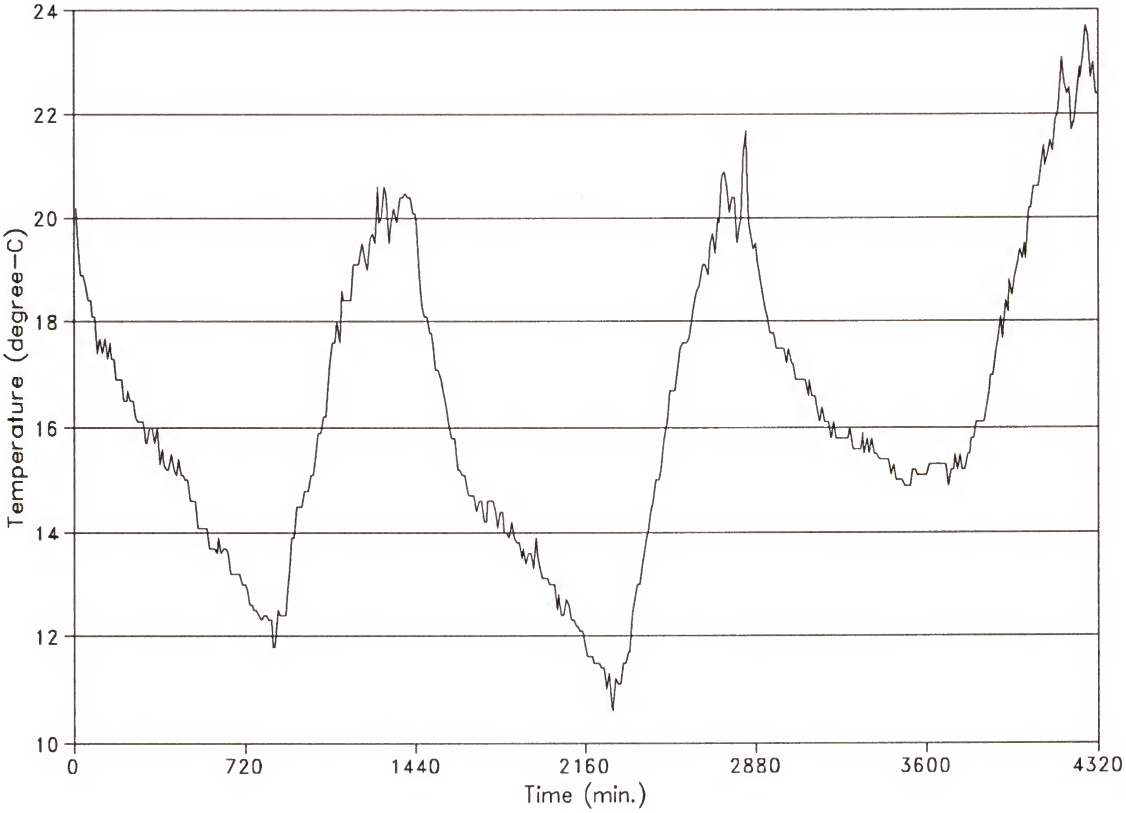

FIGURE 4-41 C: A three-day sample of the temporal variations of temperature monitored in the outdoors. Measurements were conducted in a shadowed area outside the UFRRH.

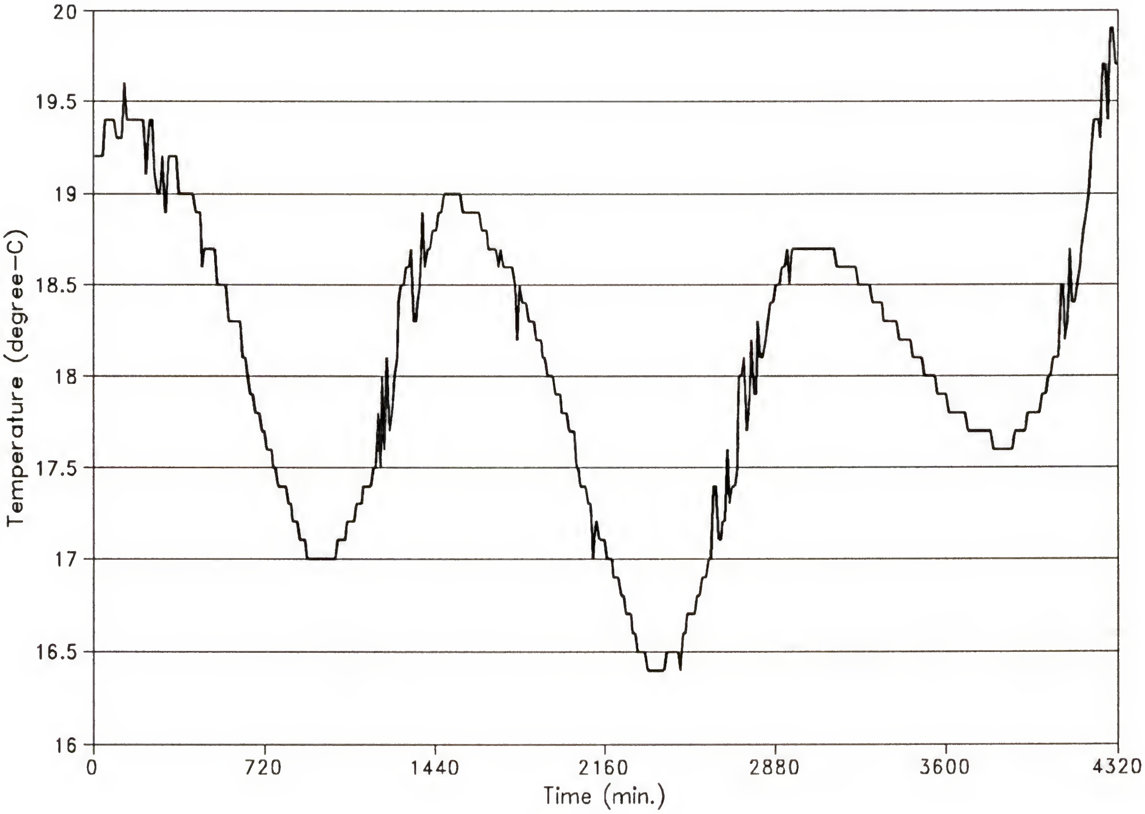

FIGURE 4-41 D: A three-day sample of the temporal variations of temperature monitored in the indoor zone. Measurements were averaged from seven locations inside the UFRRH.

difference during the diurnal cycle. Alterations of these differences between the attic or the outdoor areas were varied and were crossed depending on the particular weather patterns. Figure 4-41 G shows the temporal variations of temperatures monitored in the indoor, attic, and the outdoors when the latter temperatures varied below and above the indoor temperature, for a period of five days.

Figure 4-42 shows an illustration of the average temperature values during temperature cycles. Although theoretical consideration of a perfect diurnal cycle indicates that such averaging should be zero, the graph illustrates that a constant component exists in all cycles because of the non-equal contributions of the negative and positive portions of the diurnal cycle. Two reasons may provide support, and then conclusion, for these observations. First, the diurnal cycle is not necessarily perfect but is likely to experience changes generated from non-linear distortion of the positive and negative portions of the cycle. Second, the average (constant) component may not be the same during the positive and negative portions of the temperature cycle due to meteorological conditions.

In these particular measurements illustrated in the graph and during other temperature measurements performed in this research, the outside temperature cycle experienced the minimum non-linear distortion to its alternative portions compared with other indoor temperature cycles. This evidence

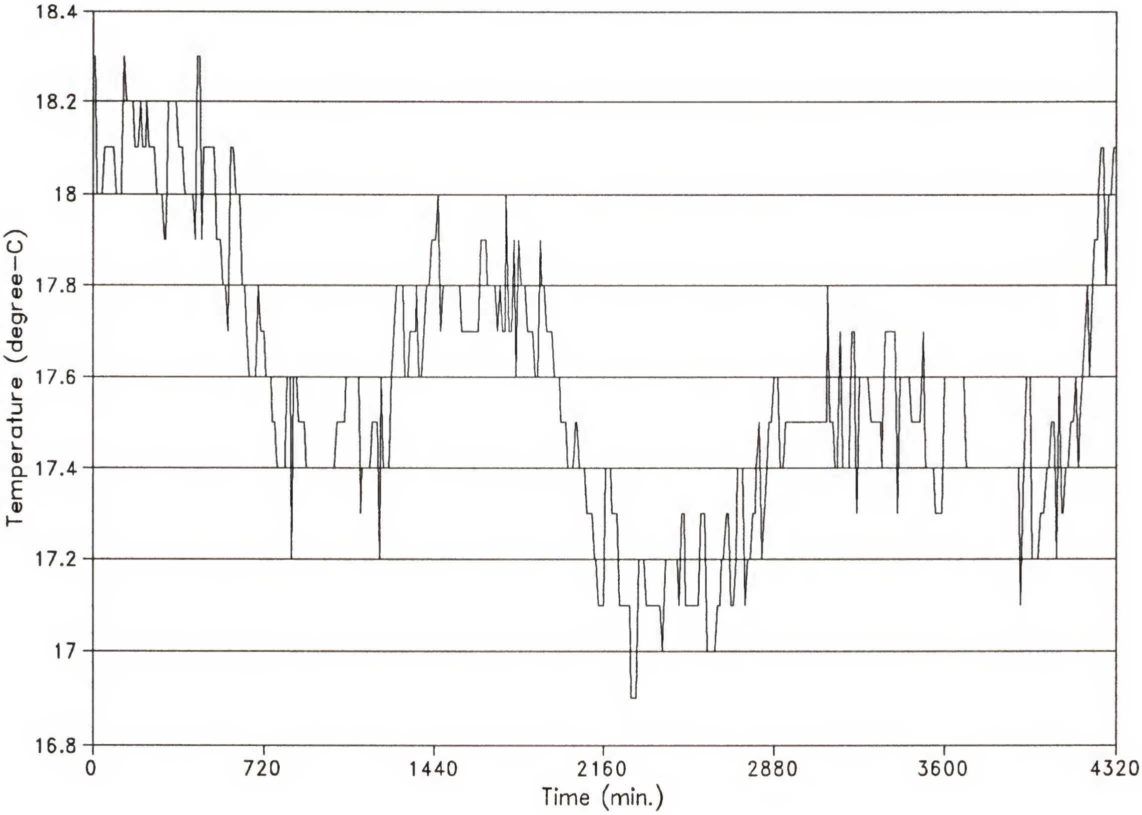

FIGURE 4-41 E: A three-day sample of the temporal variations of temperature monitored in the sub-slab zone. Measurements were conducted at a depth of approximately 1 meter at the central hole of the UFRRH.

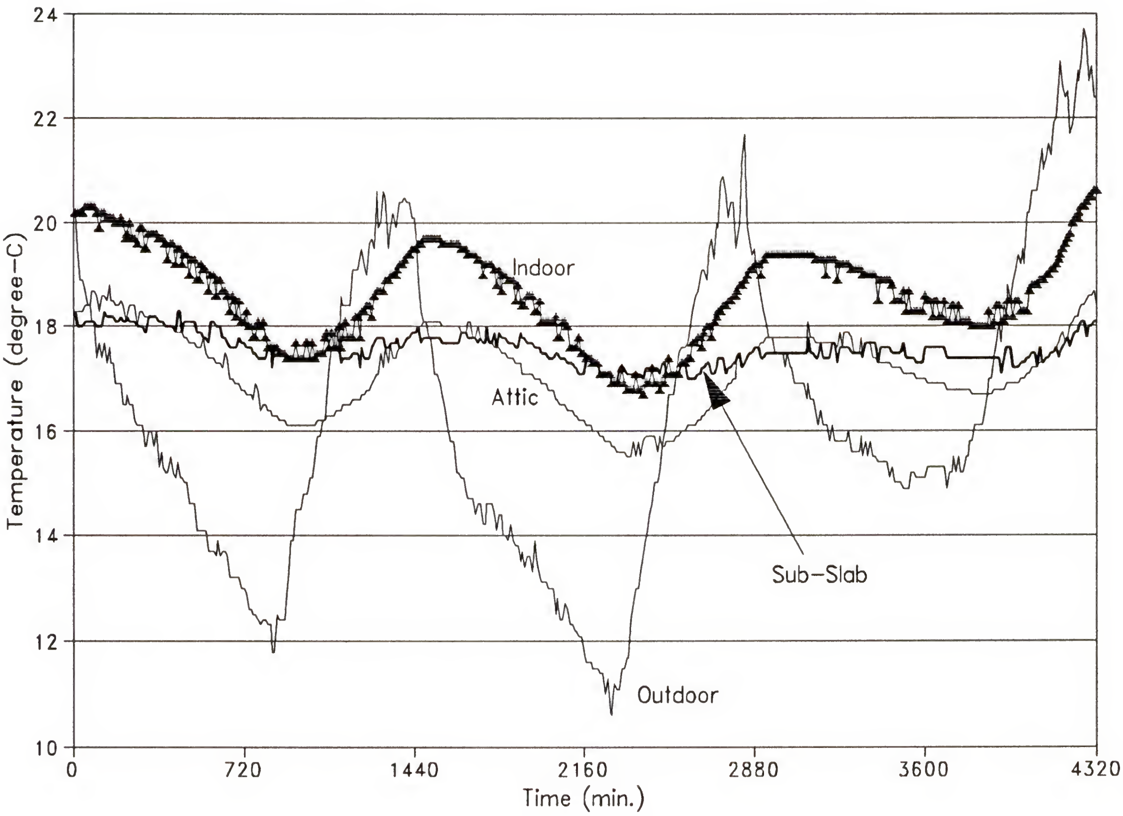

FIGURE 4-41 F: A three-day sample of the temperature temporal variations continuously collected at the temperature measurement zones at the UFRRH.

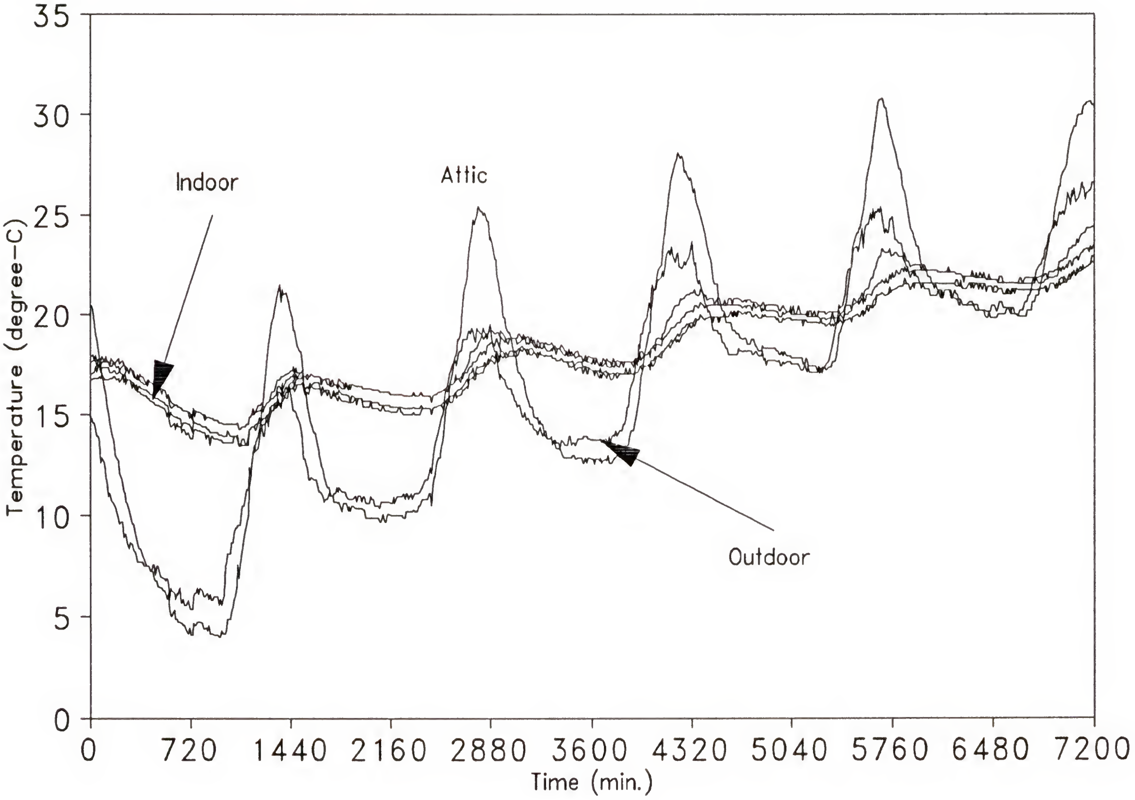

FIGURE 4-41 G: The temporal variations of temperatures at the UFRRH when a continuous increase in the average temperature was observed while outdoors and attic zones temperatures fluctuate below and above the indoor temperature zone.

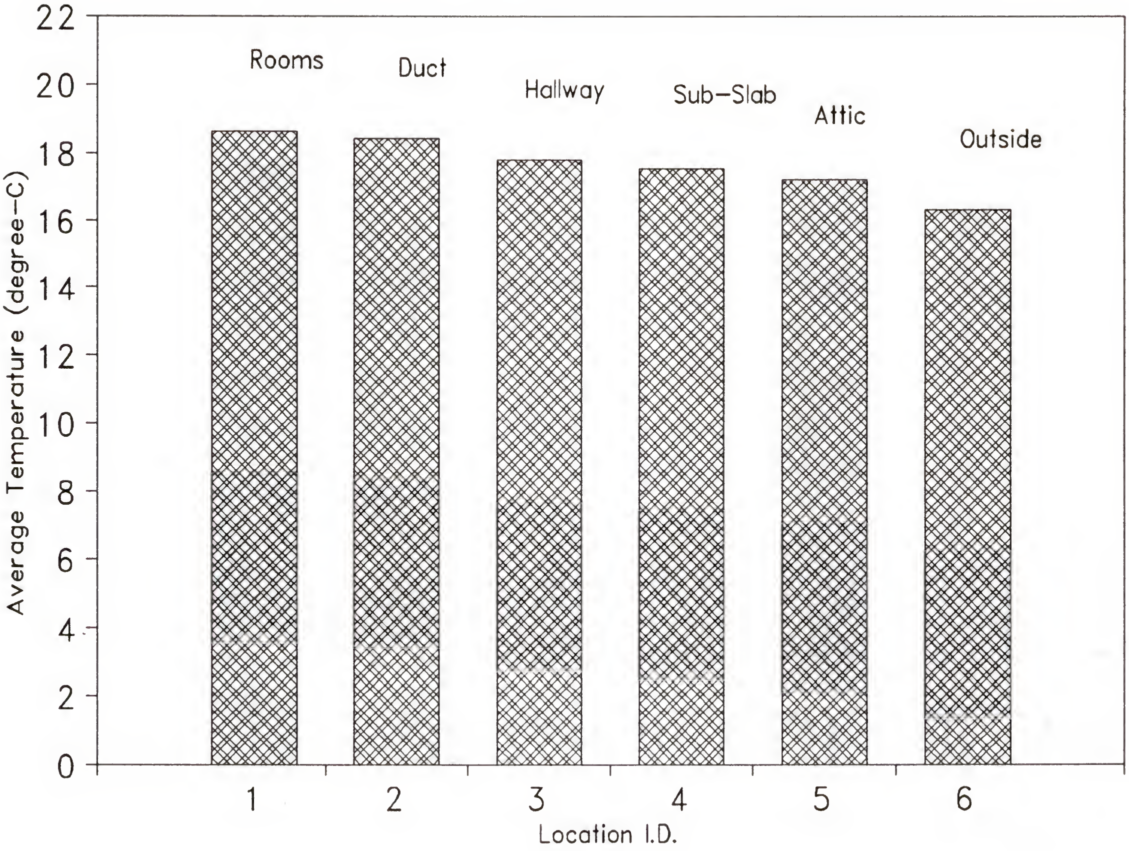

FIGURE 4-42: The average temperature values in six different temperature measurement zones at the UFRRH. Measurements were conducted during march time.

also suggests that a time shift exists between these temperature responses in different zones. Such a shift may derive from different thermal coefficients among the temperature zones (indoor, attic, sub-slab, and outdoors) tested in this work.

Although the temperatures in separate areas are generally responsible for generating pressure difference driving forces that might affect radon transport from the sub-structure and the outdoor areas into the interior, and/or radon removal from the interior into the outdoor, temperature differences as the direct component responsible for developing these driving forces need to be characterized. Figures 4-43 A and B show samples of temperature differences measured between the structure interior and the outdoors, the structure interior and the sub-slab area, the structure interior and the attic area, and the attic area and the outdoors.

As seen in the graphs, all temperature differences experience diurnal cycles. These cycles are expected to be responsible for generating the pressure differentials observed across the structure shell. Such cycles were also experienced in localized temperature measurements collected at a particular sub-slab access location. Figure 4-44 shows a sample of the time-dependent temperature responses collected at sub-slab tube location 3 (field 1), and 11 (field 3).

Figure 4-45 shows an illustration of the arithmetic average of the above cycles and other temperature measurements collected at the same time interval but at different sub-slab tube locations. The graph can be used to indicate the amount of non-linear distortion in their positive and negative portions and as a measure of the direct (constant) component of temperature difference in these difference cycles. As expected, such indications closely followed those illustrated in Figure 4-42.

Figure 4-46 shows the time dependent temperature differences among temperature measurements in the structure interior area. Although, these measurements were performed in different indoor spatial locations, there is no periodicity in the temperature behavior and the values of the difference magnitudes are very small. These values are evidence that both the spatial distribution of temperature in an unheated residential structure and the time-distribution of such temperatures are flat or relatively flat.

A sample of the temporal variations of indoor/outdoor area pressure differentials across the house shell and indoor/sub-slab area pressure differentials across the structure slab over an interval of 48 hours at the UFRRH is illustrated in Figure 4-27. Since these differences derive from different driving forces, the two differential pressure responses are not coupled.

When the differences are compared, it is found that the differential pressures across the floor slab, ΔP_{slab}, generally have larger magnitudes while the differential pressures across

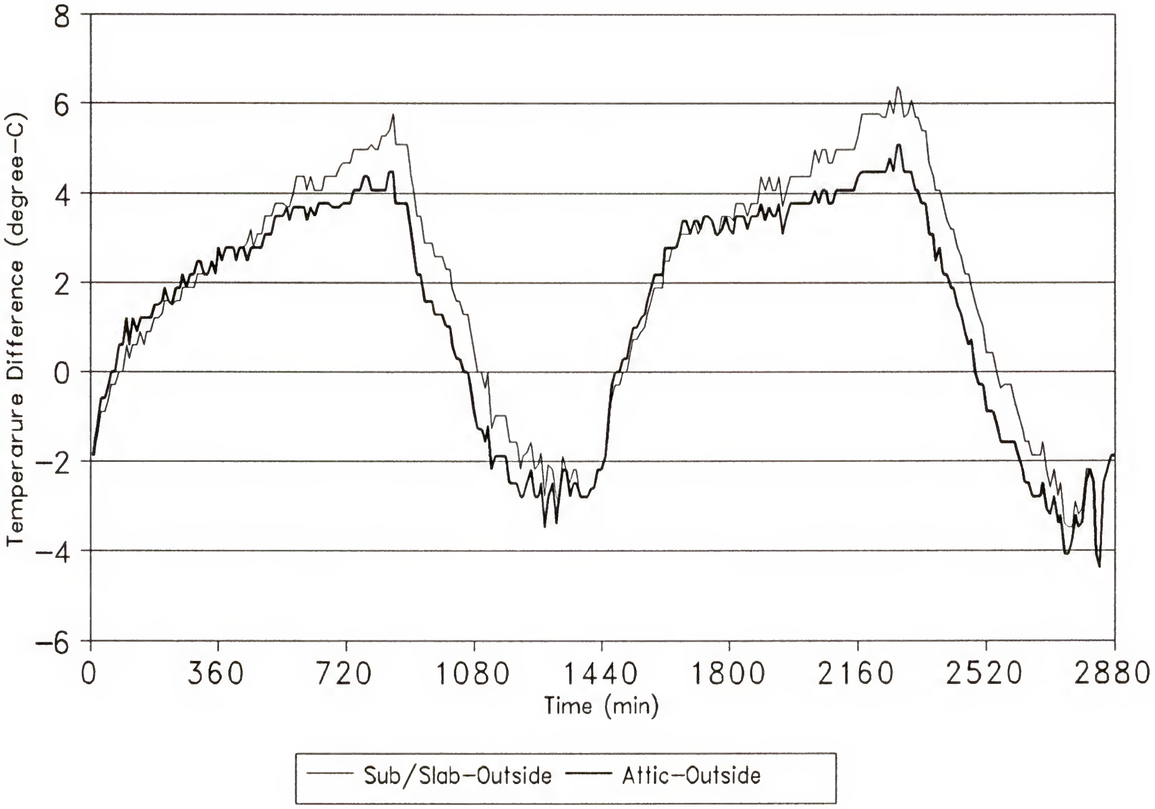

FIGURE 4-43 A: Temporal variations of the temperature differences measured between the sub-slab and the outdoors, and the attic and the outdoors.

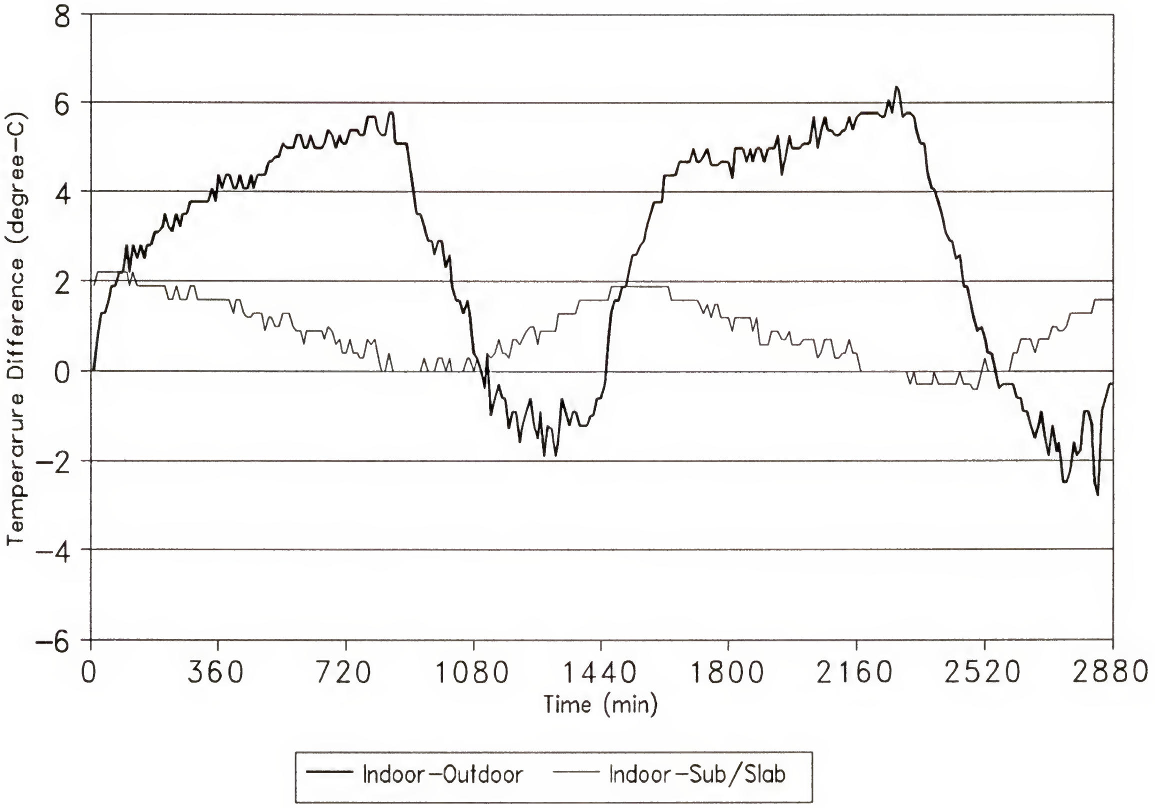

FIGURE 4-43 B: Temporal variations of the temperature differences measured between the indoor and the outdoors, and the indoor and the sub-slab area.

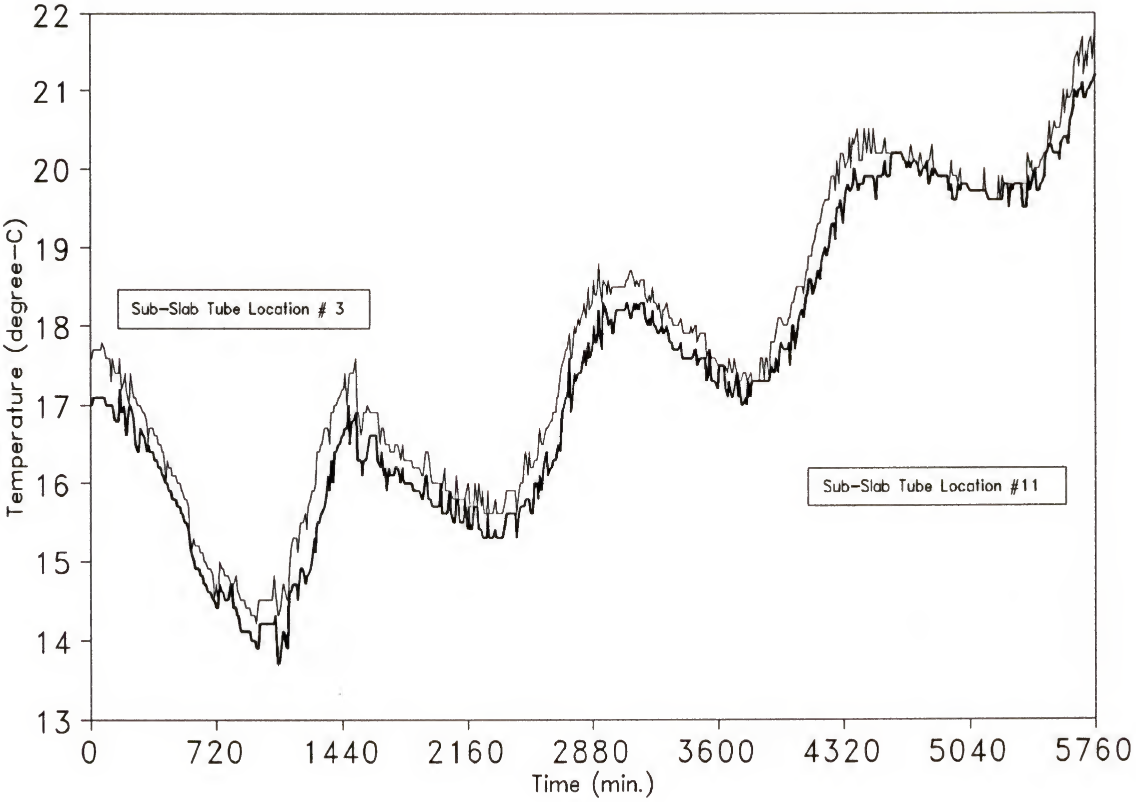

FIGURE 4-44: Samples of the time-dependent temperature responses monitored at the sub-slab tube 3, Field 1, and sub-slab tube 11, field 3.

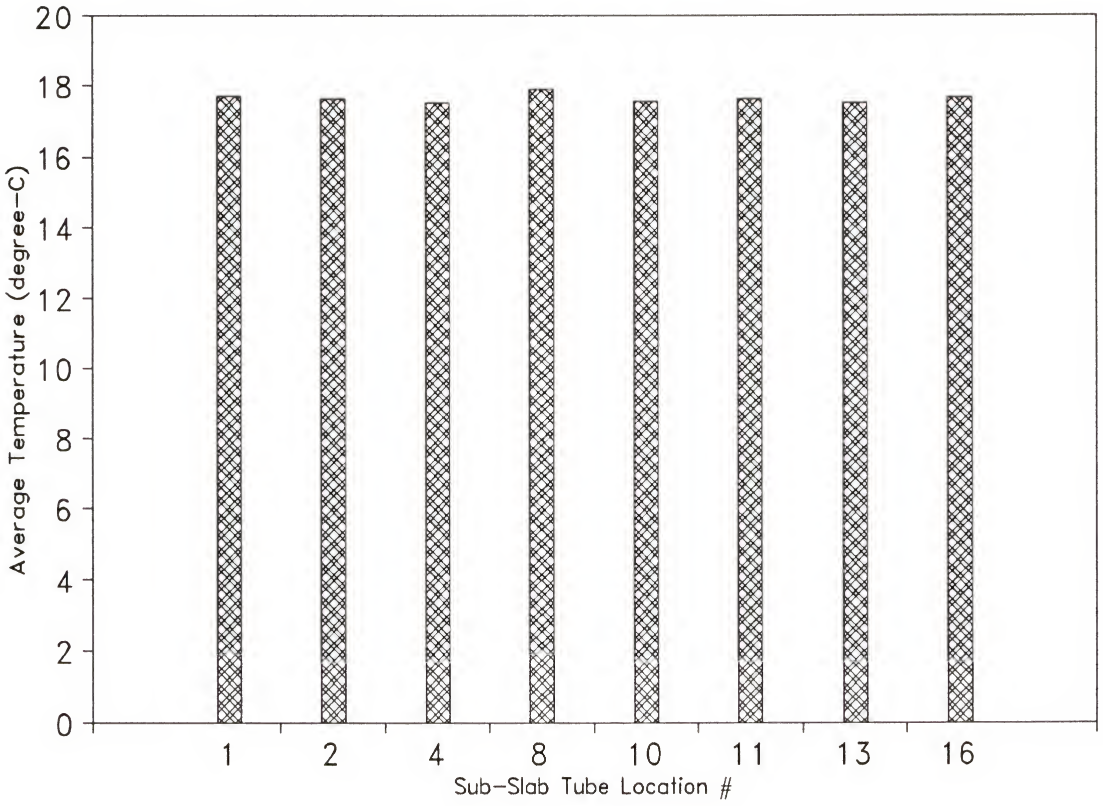

FIGURE 4-45: The average of time-dependent temperature measurements collected at different sub-slab tube Locations at the UFRRH.

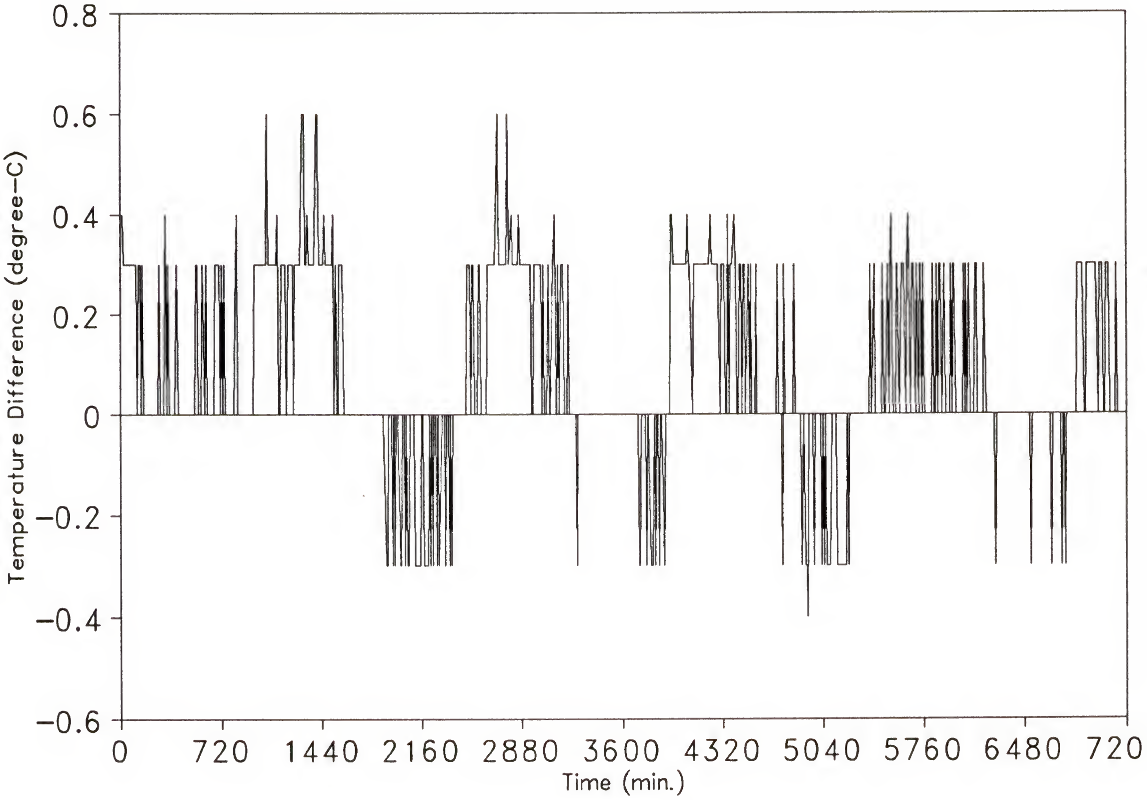

FIGURE 4-46: The time-dependent differences in temperatures measured at different locations inside the UFRRH Interior.

the house shell, $\Delta P_{i/o}$, generally have much smaller magnitudes. Differential pressures across the slab experienced semi-diurnal variations while pressure difference variations across the structure shell followed diurnal cycles, and differential pressures across the slab are dependent on the geometric location under the slab, while the ones across the wall show no differences and consequently independent of the particular location in the structure.

The indoor/outdoor pressure differential response demonstrates a diurnal cycle with a peak amplitude of about 0.4 Pa. This cycle is attributed to the variation in temperature difference between the indoor and outdoor environments that occurs throughout the day. These responses are small in magnitude because temperature differences between the indoors and outdoors remain small during the time of year in which these experiments were performed, and also because the house is well sheltered from the wind.

The temperature influence on the natural pumping driving force is obvious, since the temperature-induced differential pressures between the indoors and outdoors could result in an influencing component on the natural pumping driving force when large temperature differences, and variable weather patterns, are considered. Furthermore, temperature-induced pressure differences from large temperature differences are expected to be comparable in magnitude, in certain circumstances, to those associated with the natural pumping of sub-structure soil gas in residential structures. It is also important to characterize the effects of temperature differences that might be generated from the utilization of the structure heating, ventilating, and air-conditioning systems.

The indoor temperatures show only small variation and form a flat spatial distribution at a given height in the indoor environment. Therefore, the research structure living space may be considered a single thermal zone with the indoor temperature, T_{in}, calculated as the average of the temperature measurements from all of the indoor points.

With the house not air conditioned and unoccupied, there is a phase shift in the time response of the indoor temperature to changes of the outdoor temperature, T_{out}. Such a phase shift is also sometimes observed between the indoor temperature and the attic or sub-slab temperature. This shifting depends on several factors, such as the structure's thermal properties, the interactions between the structure's thermal zones, the magnitude of the ambient temperature changes, and the shell configuration.

From the temporal variations of indoor/outdoor (T_{in}-T_{out}) and indoor/sub-slab (T_{in}-T_{ss}) temperature differences shown in Figure 4-43 when the UFRRH was under neutral pressure conditions and no air-conditioning, the maximum indoor-outdoor temperature difference of about 9 °C was observed. During these observations, the house underwent a positive temperature difference (the indoor temperature exceeded the outdoor temperature) for approximately 75% of the day.

The time when the maximum and minimum temperatures during the diurnal cycle (24-hour) occurred was dependent on the weather pattern. Generally, during mild weather in the Gainesville area, such times are about 4 pm and 6 am, for the maximum and minimum temperatures, respectively. However, the maximum/minimum temperatures and the temperature differences depend on the time of the year and the particular location. Therefore, characterization of the temperature effects are also important in studying the seasonal effects on radon driving forces and consequently the indoor radon concentrations.

For the purpose of modeling pressures developed by temperature differences, experiments were also performed to monitor the vertical distribution of temperature in the indoor environment. Three nylon wires were used as vertical stands between the house floor and the ceiling. Each wire was divided into five equally spaced locations that held thermocouple wires. Figure 4-47 A shows the vertical (axial) distribution of indoor temperature monitored at three different locations of the UFRRH. Figure 4-47 B illustrates the range of differences among these vertical temperature measurements. The largest difference observed was 0.3 °C between the floor and ceiling thermocouple. As seen in the graphs, the vertical temperature distribution is very flat and the maximum differences between temperature at different heights in the indoor environment is negligible for this application. This observation is evidence that modeling of temperature-induced pressure difference need not consider the particular height of the structure wall at which the pressure difference is to be generated.

The general trend of the change in radon concentration with the change in temperature is shown in Figure 4-48 A and B. The simultaneous monitoring of sub-slab radon concentration and temperature at the same sub-slab tube access indicates that sub-slab radon concentration, representing a modified radon source term that is available for transport into structure with pressure differences encountered in the natural pumping in residential structures, decreases with increasing temperature. The temperature measured at the sub-slab access is very similar to the indoor temperature, and the increase in the latter may provided a slight pressurization of the structure interior, acting as a leaking container, that provides partially limits radon entry.

Characterization of temperature-driven pressure differences required developing the mathematical formulation that uses temperature difference as inputs and returns pressure differences that are developed between two separated temperature zones. By implementing the concept of conservation of forces related to pressure under hydrostatic equilibrium, a mechanistic approach can be used. The force

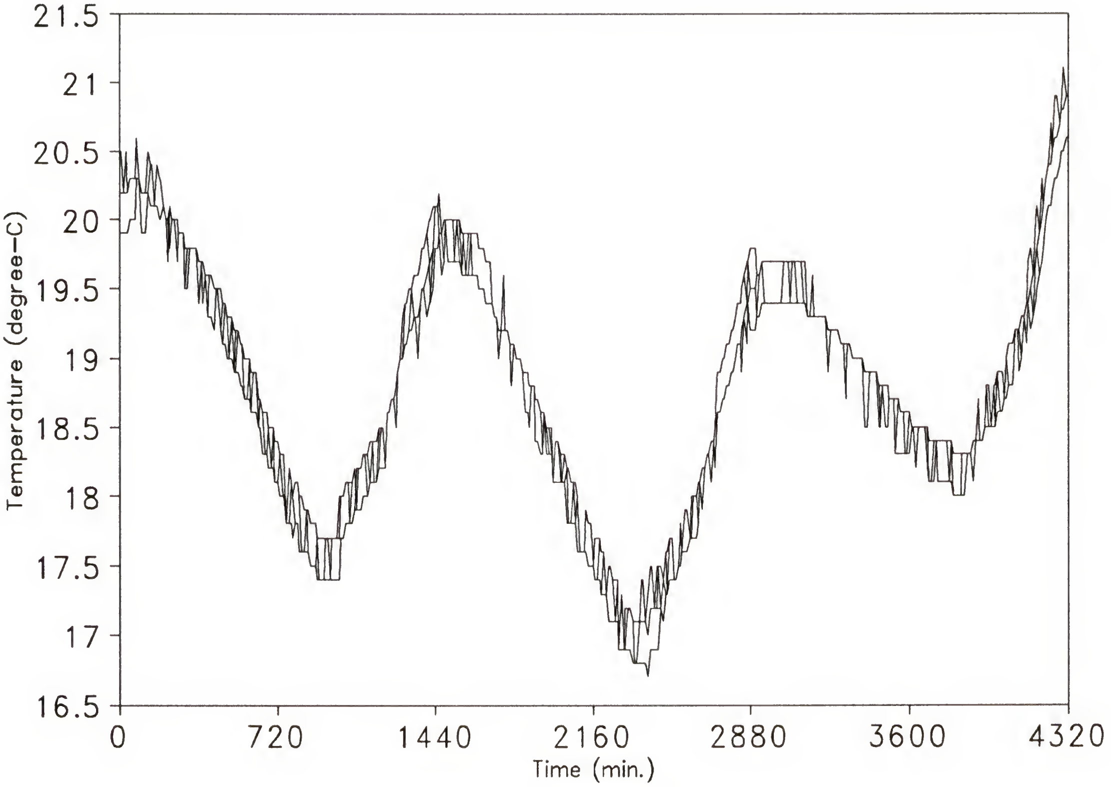

FIGURE 4-47 A: The time dependent vertical variations of indoor temperatures monitored at three different locations at the UFRRH.

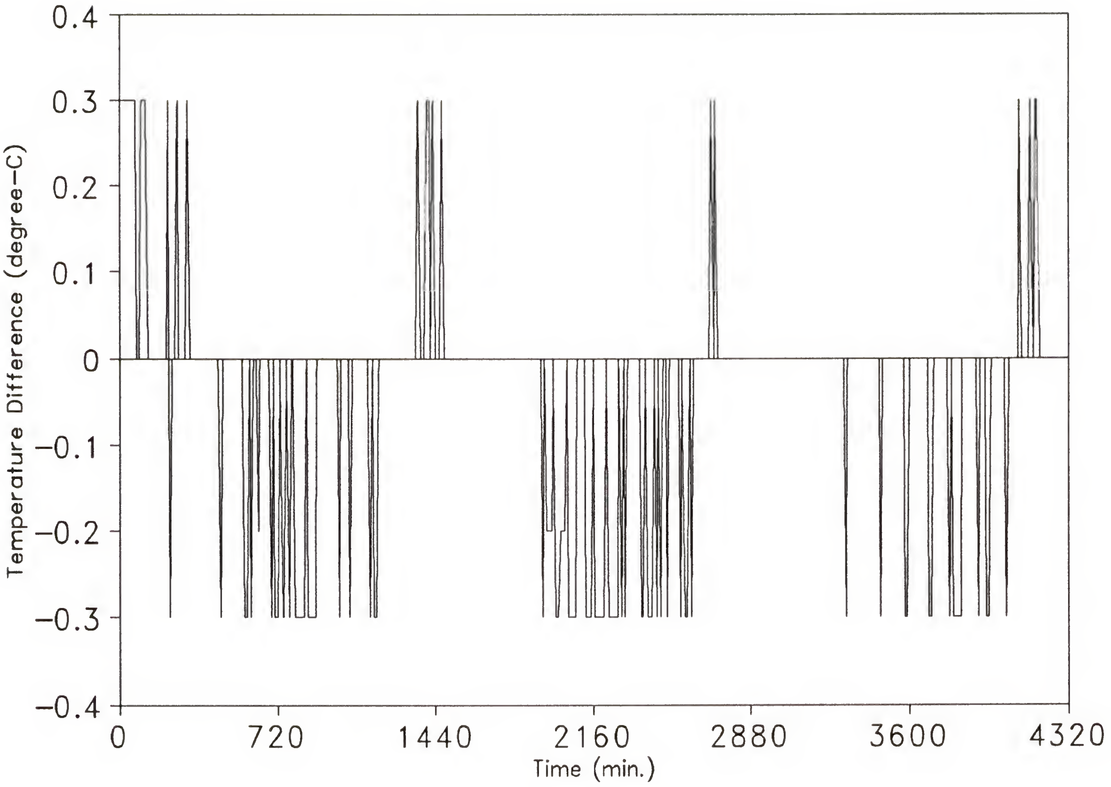

FIGURE 4-47 B: The range of differences in the time-dependent vertical variations of indoor temperatures monitored at three different locations at the UFRRH.

associated with a fluid pressure, air pressure in this application, must counteract the gravitational force under hydrostatic equilibrium. If a specific volume is considered and under such equilibrium, the net force at any point in this volume must be zero, therefore

$$dP/dh=-\rho g \tag{4-14}$$

where h is the height measured from a reference level (m),
ρ is the air density (kg/m^3), and
g is the gravitational acceleration constant ($9.8\ m/s^2$).

Air can be considered to be an ideal gas for this application, thus a utilization of the ideal gas law may be used to introduce the temperature into the above equation through the equivalent of the right hand side of Equation 4-14, ρg as

$$dP/dh=-P(mg/kT) \tag{4-15}$$

where m is the mass of air (kg),
k is Boltzmann constant (1.38×10^{-23} J/K), and
T is the absolute temperature (K). Equation 4-15 establishes the explicit relation between temperature and pressure until specific volume representing a zone in this application; however, this relation is not linear as will be shown by its solution. An analytical solution to this first order

differential equation requires application of a boundary condition. An applicable boundary condition to this implementation is $P=P_o$ at $h=0$, which yields

$$P=P_o \exp(-mgh/kT) \qquad (4\text{-}16)$$

The temperatures at the research structure were measured 1.4 m above the slab (h=1.4 m); however, it was shown earlier that the vertical variation temperature is negligible. Utilizing this height, the magnitude of the quantity (mgh/k) represents a constant of value C=0.0477 K, when m is the average molecular mass of air (28.8 u) at an atmospheric composition of approximately 80% N_2 and 20% O_2, at uniform temperature of 280 K.

Because the constant C is small, the value of the exponent on the right hand side of Equation 4-16, exp(-C/T), is approximately unity and it can be approximated as (1-C/T). Applying this treatment to two pressure conditions P_1 and P_2, which correspond to temperatures T_1 and T_2, respectively, yields

$$P_1-P_2 = \Delta P = P_o\ C\ [(T_1-T_2)/T_1T_2] \qquad (4\text{-}17)$$

the pressure difference generated between two zones of different temperatures. This equation can be used to characterize the pressure differences induced by indoor and

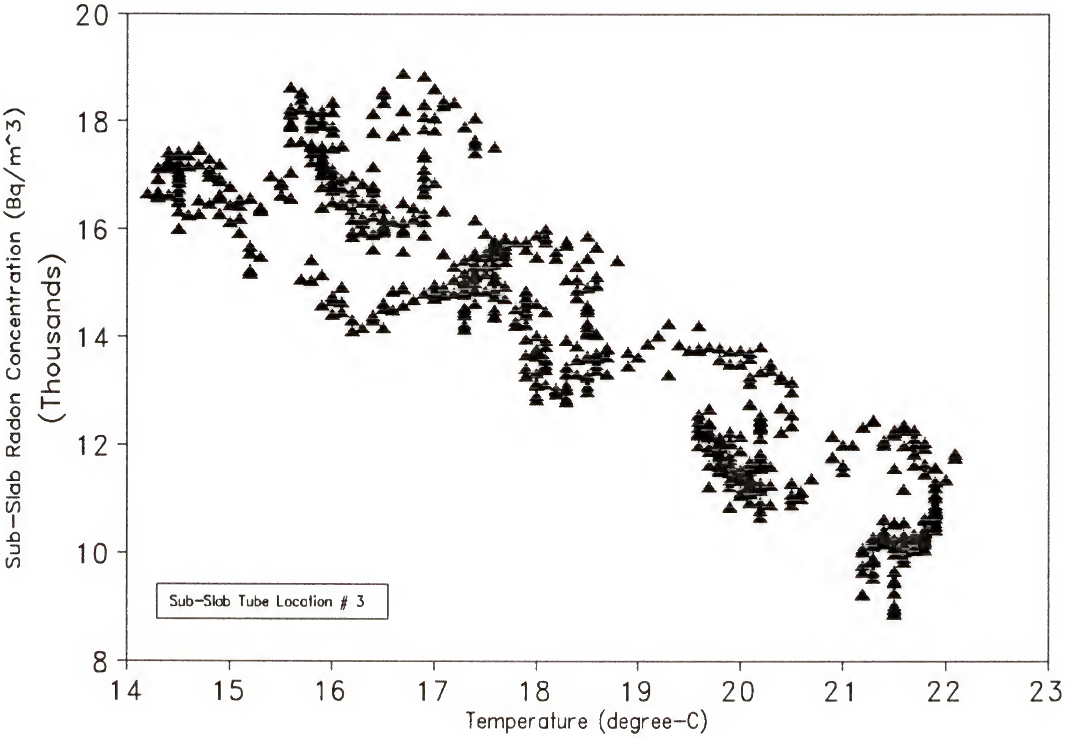

FIGURE 4-48 A: The general trend of sub-slab radon concentration measured from sub-slab location 3, with the temperature variations.

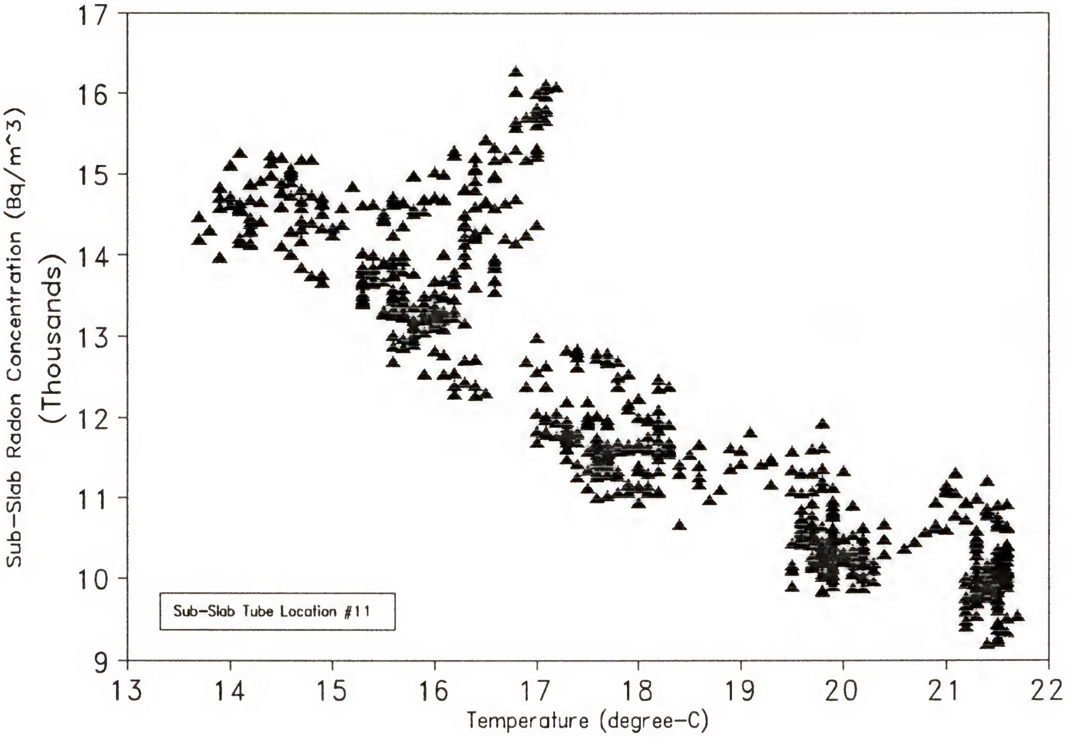

FIGURE 4-48 B: The general trend of sub-slab radon concentration measured from sub-slab location 11, with the temperature variations.

outdoor temperatures on the indoor/sub-slab pressure differentials.

Differential pressures across the slab, ΔP_{slab}, were previously calculated from the expression,

$$P_{ss}(t+\Delta t)-P_b(t+\Delta t) \tag{4-18}$$

without temperature effects, since it was assumed the indoor pressure is quickly equalized with the outdoor pressure and therefore,

$$P_{in}(t+\Delta t) = P_b(t+\Delta t) \tag{4-19}$$

at the time $(t+\Delta t)$ in response to step changes in the barometric pressure. The pressure difference between the indoors and outdoors can be estimated as,

$$\Delta P_{i/o}=P_{in}-P_{out} \tag{4-19a}$$

The barometric pressure is in fact the pressure measured outside the structure and $P_b(t+\Delta t)=P_{out}(t+\Delta t)$ can be used to calculate the indoor pressure at time $t+\Delta t$ as,

$$P_{in}(t+\Delta t)=\Delta P_{i/o}+P_b(t+\Delta t) \tag{4-20}$$

When the temperature-induced differential pressures modeled above are linearly combined with the pressure differentials across the slab then,

$$\Delta P_{slab} = P_{ss}(t+\Delta t)-[\Delta P_{i/o}(t+\Delta t) + P_b(t+\Delta t)] \qquad (4\text{-}21)$$

where $\Delta P_{i/o}(t+\Delta t)$ is calculated utilizing Equation 4-17.

Equation 4-17 can be used to predict the indoor/outdoor pressure differences, which are induced by the indoor/outdoor temperature differences. The predicted values of the pressure differential between the indoors and outdoors are in good agreement with the ones measured when applied for the same time interval. Figure 4-49 A illustrates the predictions of the above model to a sample of continuous measurements collected for a period of four days at the UFRRH. Simultaneous temperature and pressure measurements were collected every ten minutes in both the indoor and outdoor zones, then temperature differences were used to predict the measured pressure differences.

The difference between the modeled pressure differentials and the measured ones can be estimated based on the Mean Square Error (MSE) method described in the experimental design and methodology. Utilizing this criteria, the MSE associated with the Figure 4-49 A predictions is 0.011 Pa, which indicates that predicted pressure differences are in very good agreement with the measured ones.

Furthermore, to illustrate the detailed components of the errors and the associated steps in calculating the MSE, Figure 4-49 B shows the temporal variations of differences between the modeled and measured pressure differentials across the house shell for the measurements of Figure 4-49 A. Figure 4-49 C illustrates the temporal variations of the values of the differences between the predicted and modeled pressure differences used to calculate the MSE value.

Figure 4-50 A shows other predictions for differential pressure measurements conducted at different time periods than those shown in Figure 4-49 A. The MSE value for the latter prediction is 0.014 Pa, showing again an excellent agreement between the measured pressure differences across the house shell and the predicted differences from the temperature-induced pressure differential model. Figures 4-50 B and C show the temporal variations of the difference between measured and predicted values and the square of these values respectively.

The results obtained from this modeling are compared with the Furrer et. al. (1991) model that also predicts pressure differences induced by temperature differences. In this model, the differential pressure across the shell can be calculated from,

$$\Delta P = \Delta T * k * g * h \qquad (4\text{-}22)$$

where ΔP is the pressure difference in pascal developed due to temperature difference, ΔT in °C,

k is a constant representing the specific decrease in air density ($4\times10^{-3} kg/m^3K$),

g is the acceleration due to the gravity ($9.8\ m/s^2$), and

h is the height above the basement level (m).

If a height of 1.4 m is used in this model, the magnitude of the pressure differentials across the walls at the UFRRH, can be written as

$$\Delta P\ (Pa) = 0.05488 * \Delta T\ (°C) \qquad (4\text{-}23)$$

The above equation can be used to predict the pressure differences developed by temperature differences. When it is applied to the same set of data in Figures 4-49 A and 4-50 A the agreement between the two models is excellent. Figures 4-51 A and B illustrate the predictions of both models for the experimental data in Figure 4-49 A, and in Figure 4-50 A, respectively. Figures 4-52 A and B illustrate temporal variations of the error estimations based on MSE method for the temperature-induced pressure differences model predictions in Figures 4-49 A and 4-50 A.

It is worth noting that the mathematical treatment in modeling temperature-induced pressure differentials used by Furrer et. al. produced a linear relationship between the generated pressure differences and the temperature

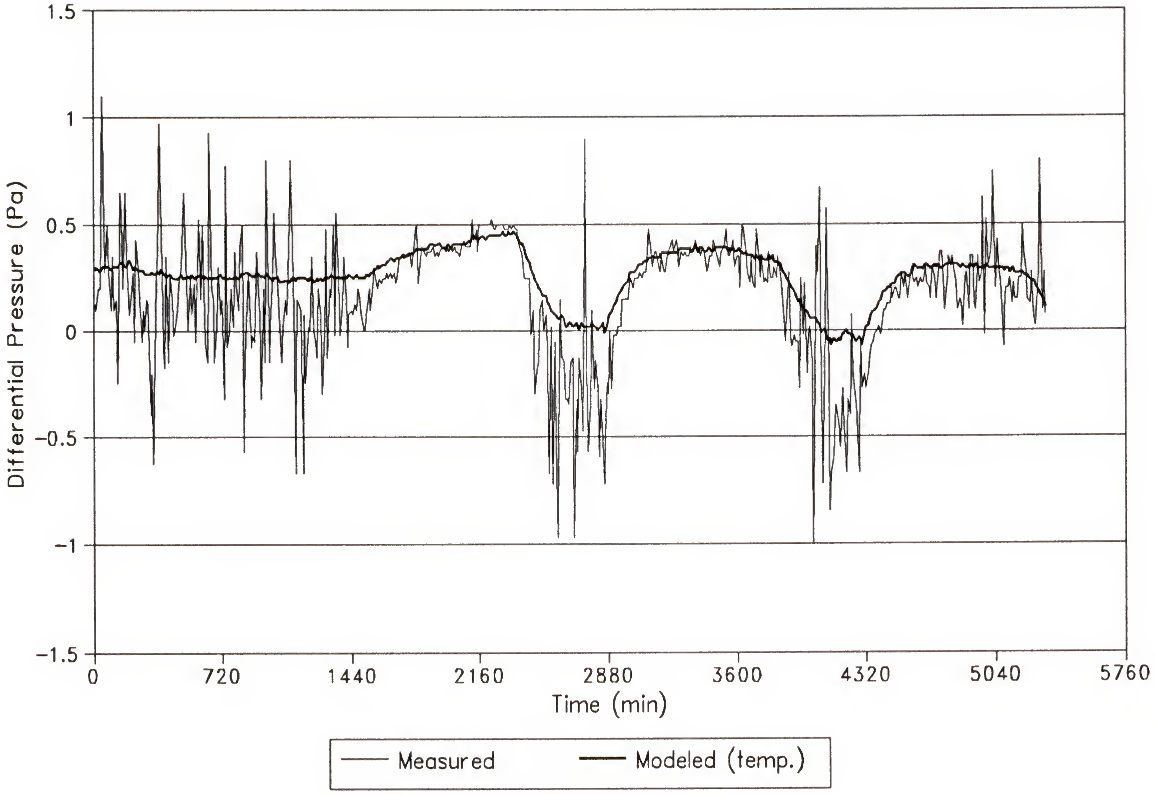

FIGURE 4-49 A: Measurements and predictions of the temporal variations of indoor/outdoor pressure differences induced by indoor/outdoor temperature differences.

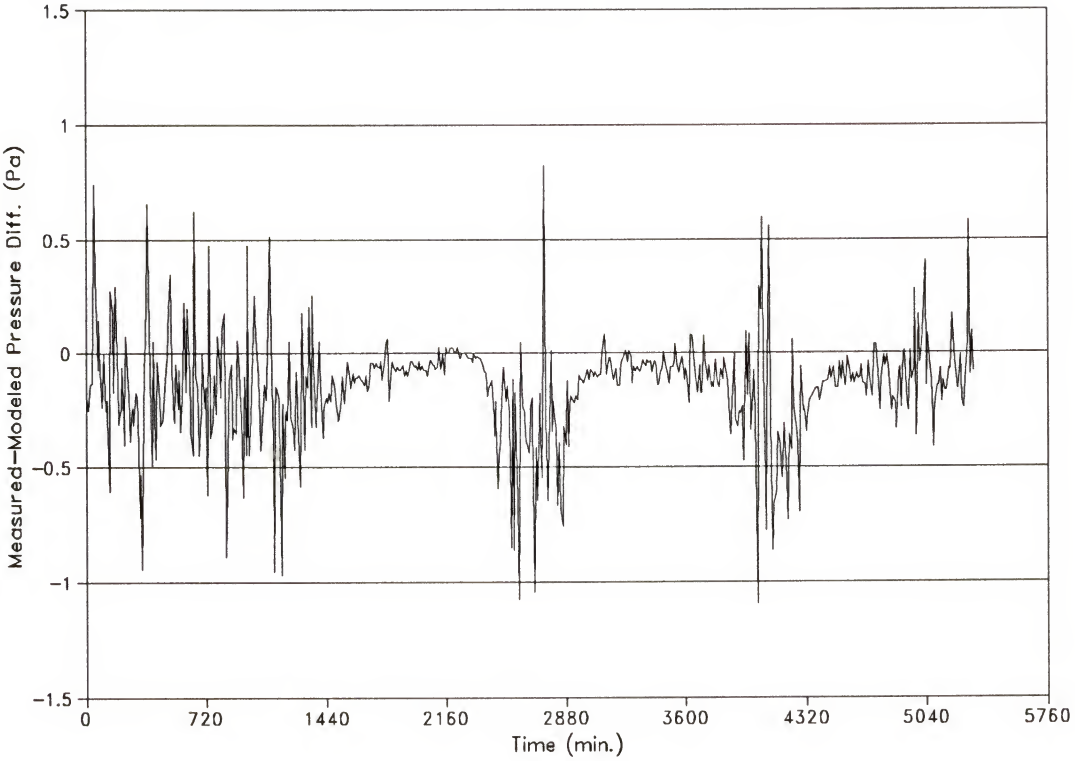

FIGURE 4-49 B: The time-variations of differences in the measured pressure differentials across the walls and the modeled temperature-induced pressure differentials for the same experimental period.

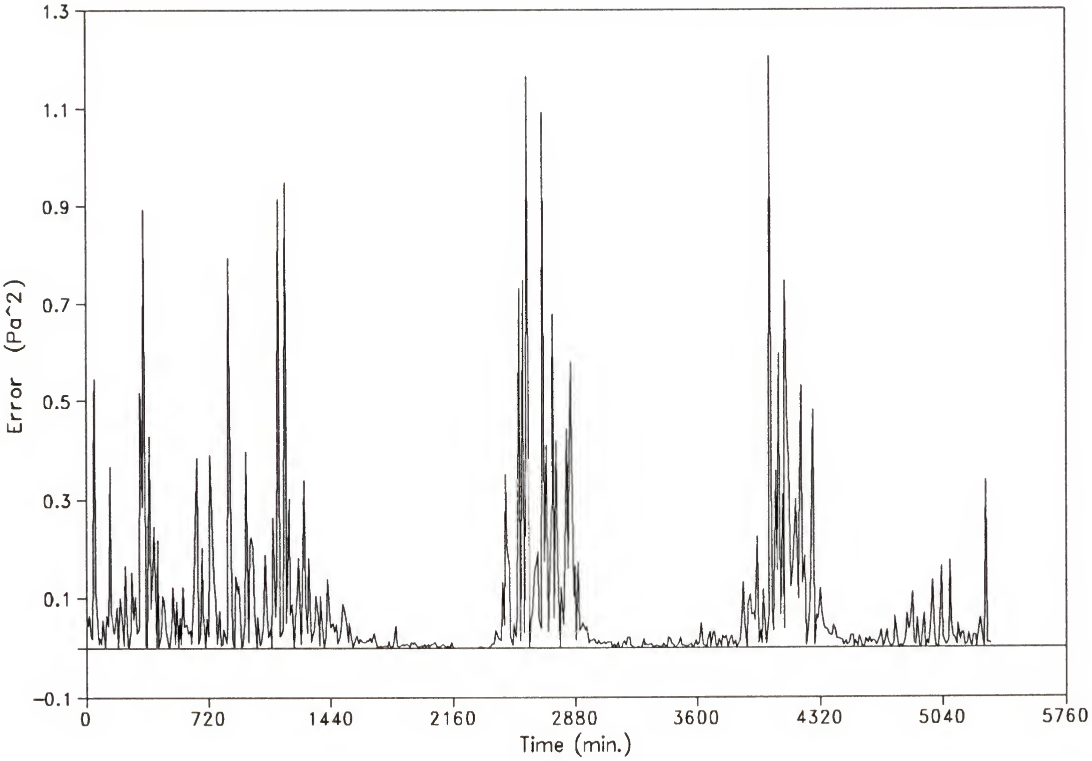

FIGURE 4-49 C: The time-variations of the square difference (SD) between the measured and the modeled differential pressure across the structure shell.

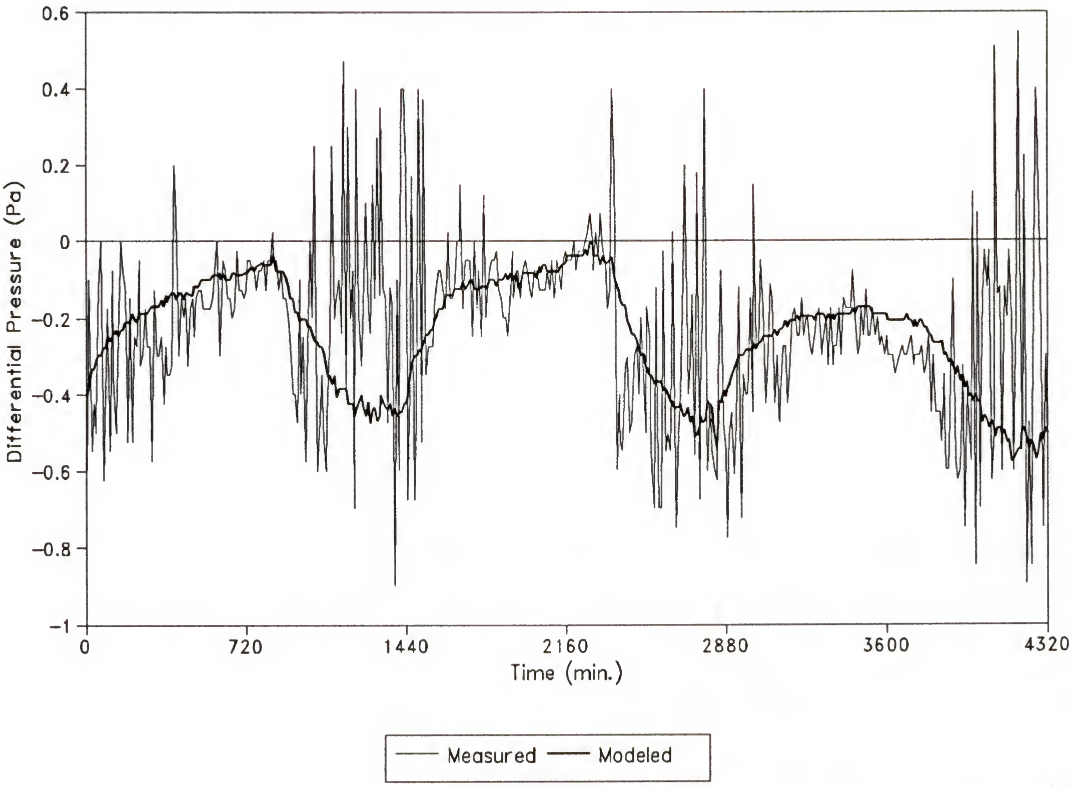

FIGURE 4-50 A: Measurements and predictions of the temporal variations of indoor/outdoor pressure differences induced by indoor/outdoor temperature differences for a different experimental period than illustrated in Figure 4-49 A.

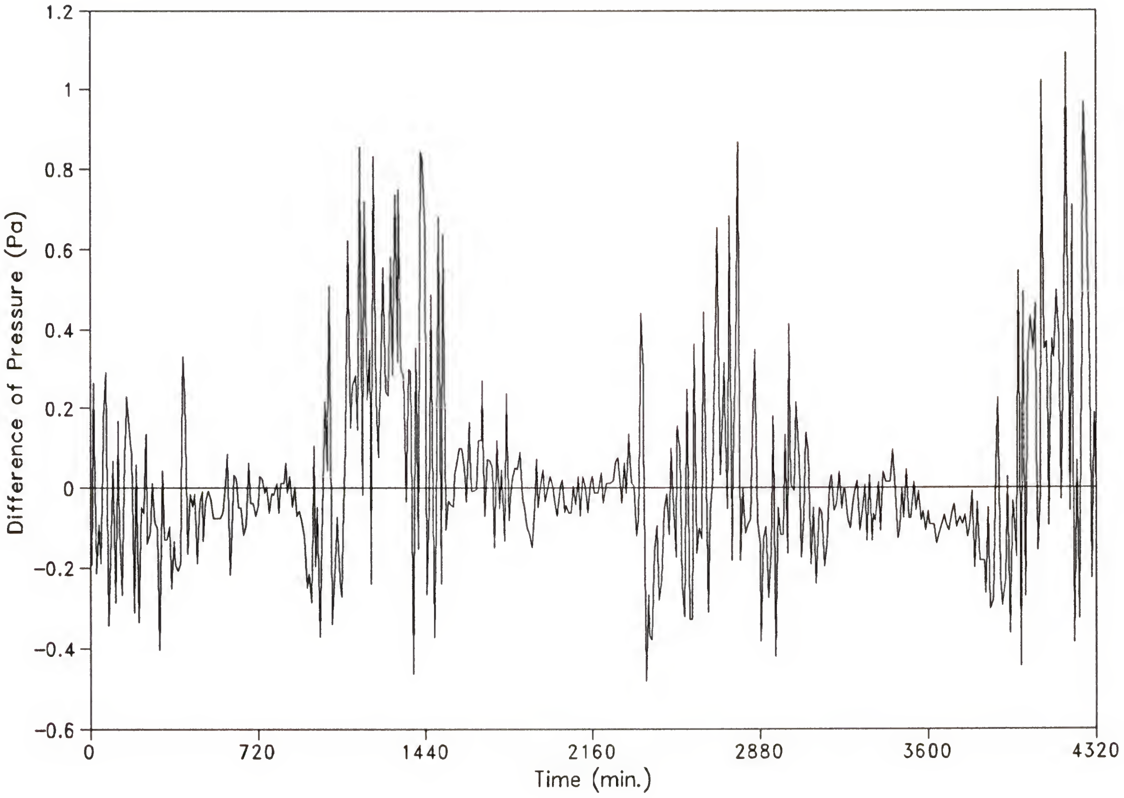

FIGURE 4-50 B: The time-variations of differences in the measured pressure differentials across the walls and the modeled temperature-induced pressure differentials for the same experimental period of Figure 4-50 A.

differences, unlike the currently developed model. The MSE values of the Furrer et. al. model are 0.012 Pa, and 0.014 Pa for the predictions in Figures 4-49 A and 4-50 A, respectively. When these values are compared with the one generated by the currently developed model, an improvement in the MSE value of prediction of approximately 15 % can be realized.

The small figure of improvement may be generated from the non-linearity built in the current model. Since the two models differ by the existence of non-linearity content, the excellent agreement between both models with the existence of such relationship between temperature and pressure supports the inclusion of non-linear term in the current model.

The temperature-induced pressure differential model can be used to predict pressure differences induced over a range of temperature differences. Figure 4-53 shows predictions of the temperature-induced pressure differences over a temperature difference range from -50 to 50 °C. As seen in the graph, the temperature-induced pressure differentials show a linear relationship with the temperature difference driving forces. Differences between the indoors and outdoors show a linear correlation to the corresponding temperature differences.

The source of non-linearity, which generates the small curvature in the plot of Figure 4-53, is generated from the term (T_1T_2) in Equation 4-17 which represents the non-linear source in the model. It is also important to note that, for the same reason, the temperature-induced pressure differential model shows that pressure differences are sensitive not only to the temperature differences, but also to the average temperature between the indoors and outdoors. Figure 4-54 illustrates the model prediction of the pressure difference dependency on the average temperature between the indoor and the outdoors.

This small non-linearity might be further reduced if corrections to the constant value, calculated based on air mass at a standard temperature and pressure, are made in the calculations based on the average temperatures rather than the standard temperature. However, such effort might not be needed when three factors are considered.

First, the pressure differences induced by the non-linearity are small (on the order of 0.2 pascal) for a wide range of average temperatures between 260 and 310 degrees. Second, the calculations of air mass ignored the existence of humidity, which might widely differ with respect to the particular location and the time of the year. This might introduce a small divergence in pressure difference predictions in a range comparable to the non-linearity factor effect.

Third, the actual differential equation (before the approximation) relates temperature to pressure (Equation 4-16) in a temperature zone under hydrostatic equilibrium, itself

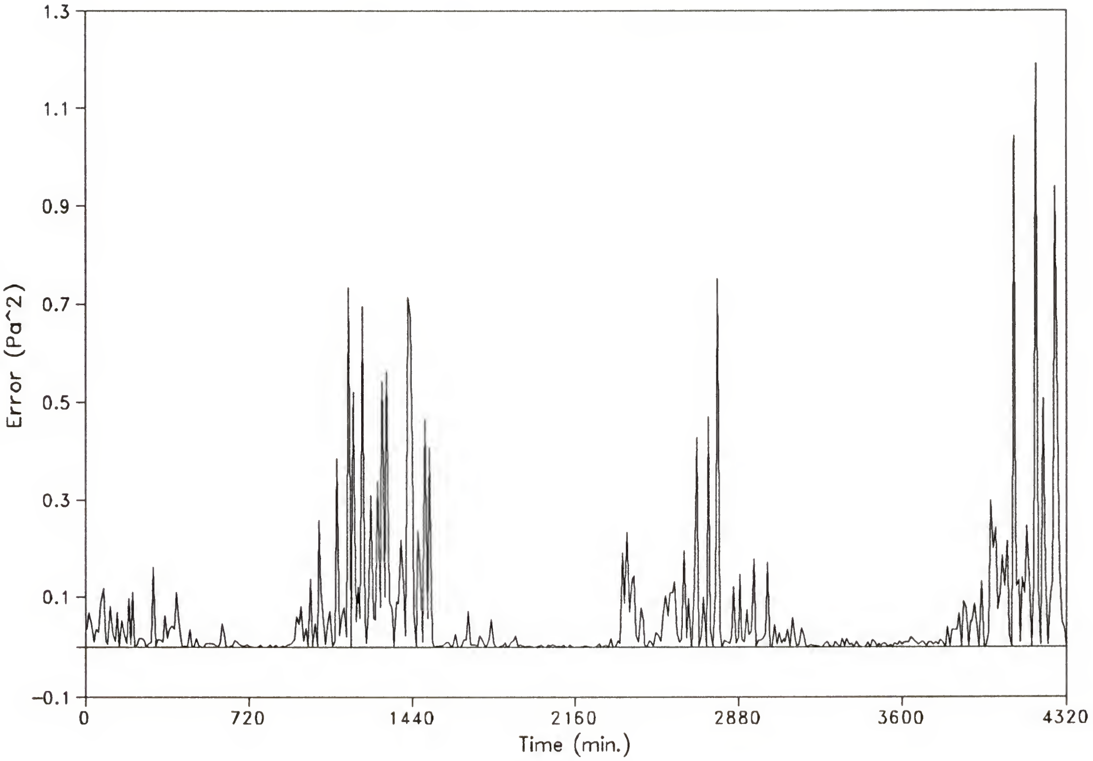

FIGURE 4-50 C: The temporal variations of the square difference (SD) values between the measured and the modeled differential pressure across the structure shell for the experimental data of Figure 4-50 A.

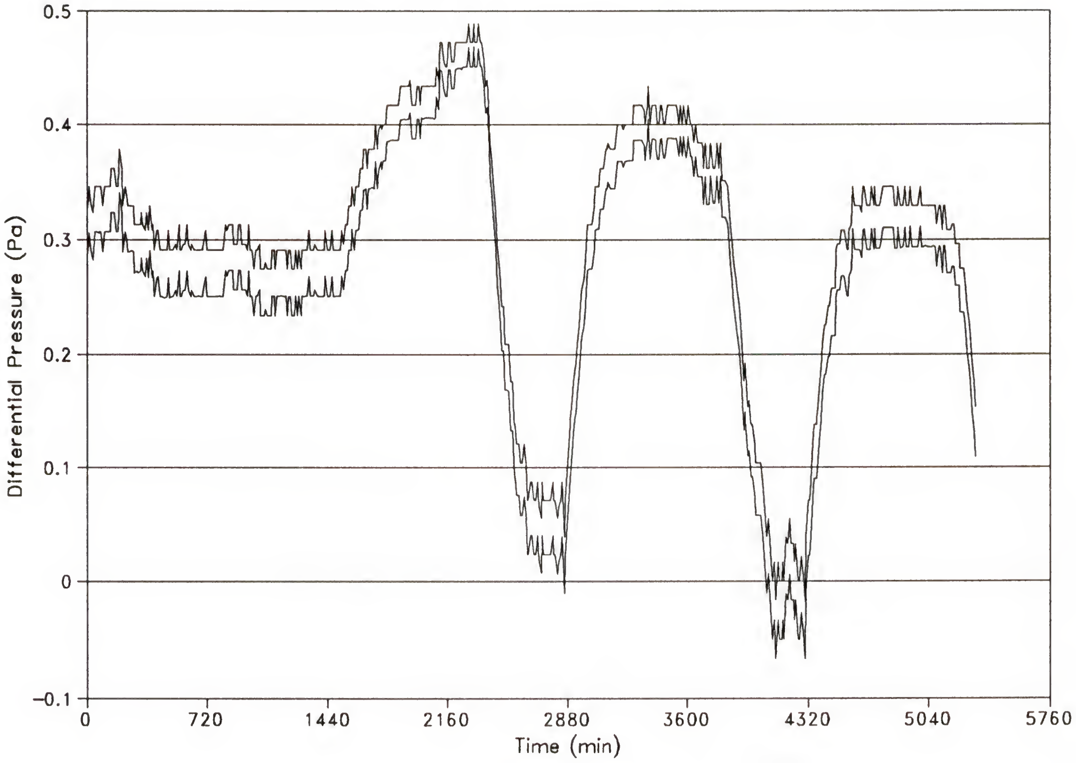

FIGURE 4-51 A: The temporal variations of temperature-induced pressure differences predicted by Furrer model (upper curve) and the current model (lower curve) for the data of Figure 4-49 A.

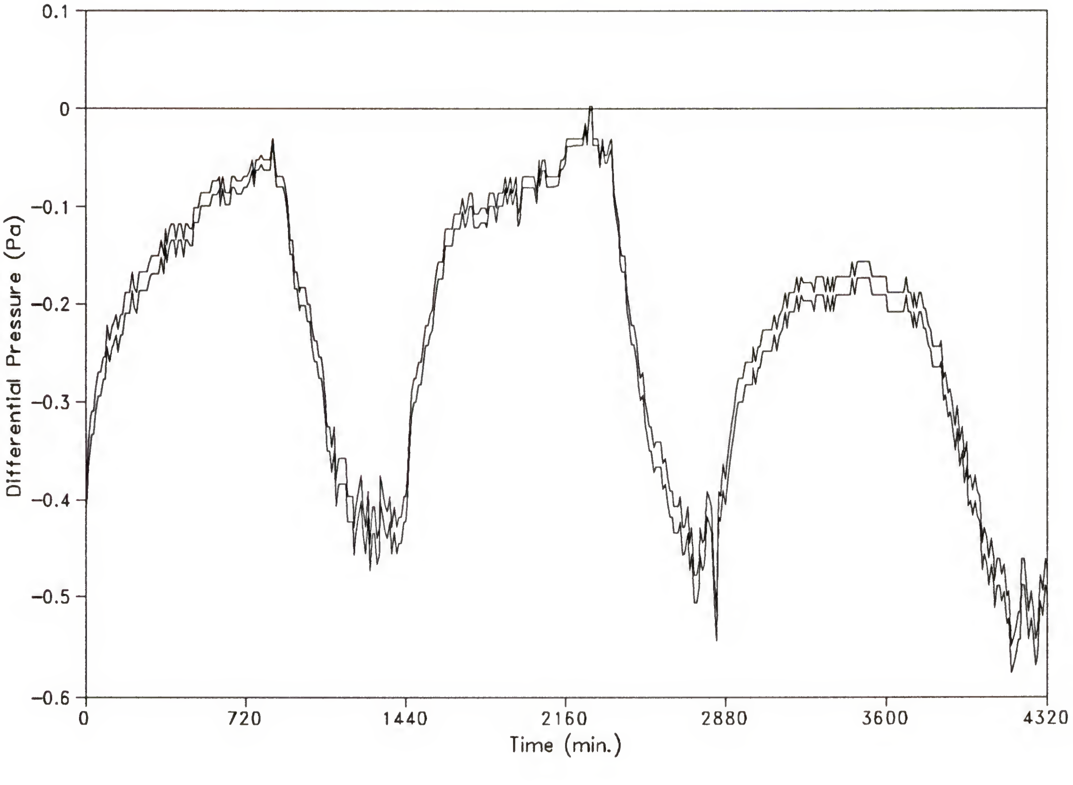

FIGURE 4-51 B: The temporal variations of temperature-induced pressure differences predicted by Furrer model (upper curve) and the current model (lower curve) for the data of Figure 4-50 A.

containing a weak source of non-linearity because of the existence of the exponential term. Finally, the overall possible error that might be introduced (a few tenths of a pascal) because of the non-linearity is comparable with the experimental uncertainty of the measurement.

For the above reasons, the temperature-induced pressure differentials model is left in its simple form to provide pressure-difference predictions when compared to the complicated form resulting from including mass corrections to the model constant and evaluation of the exponent.

The effect of the temperature on the sub-slab air volume pressure is expected to be smaller than its effect on indoor pressure, based on temperature difference measurements at the UFRRH between the indoors and the sub-slab which show maximum differences of about 2 °C. These effects may be larger for different types of soil, different types of buildings, and different overall weather behaviors.

A positive temperature difference contributes to the indoor pressure and reduces the differential pressure across the slab, thereby reducing the natural pumping radon driving force. As evidenced from the model, a minimum radon driving force is associated with the negative portions of the semi-diurnal barometric pressure cycle (the sub-slab is depressurized relative to the indoors) and with the positive temperature difference of the temperature diurnal cycle.

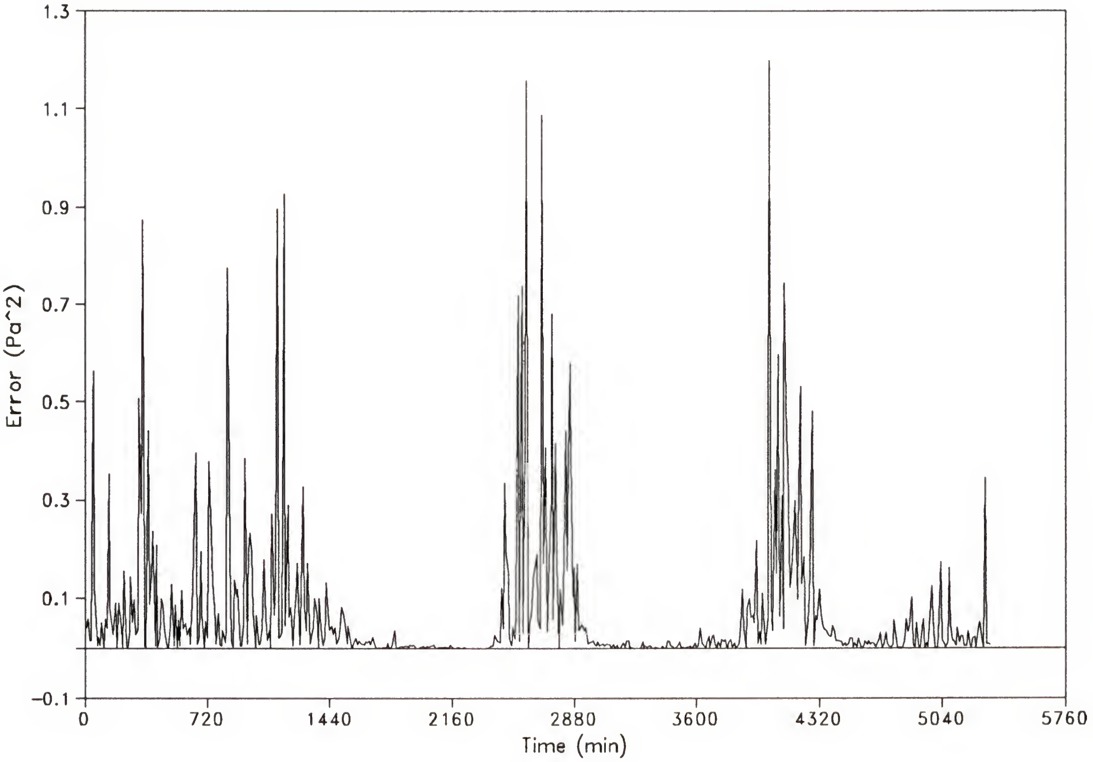

FIGURE 4-52 A: The square difference of the temporal variations of predicted pressure differences using the MSE method for the experimental measurements of Figure 4-49 A.

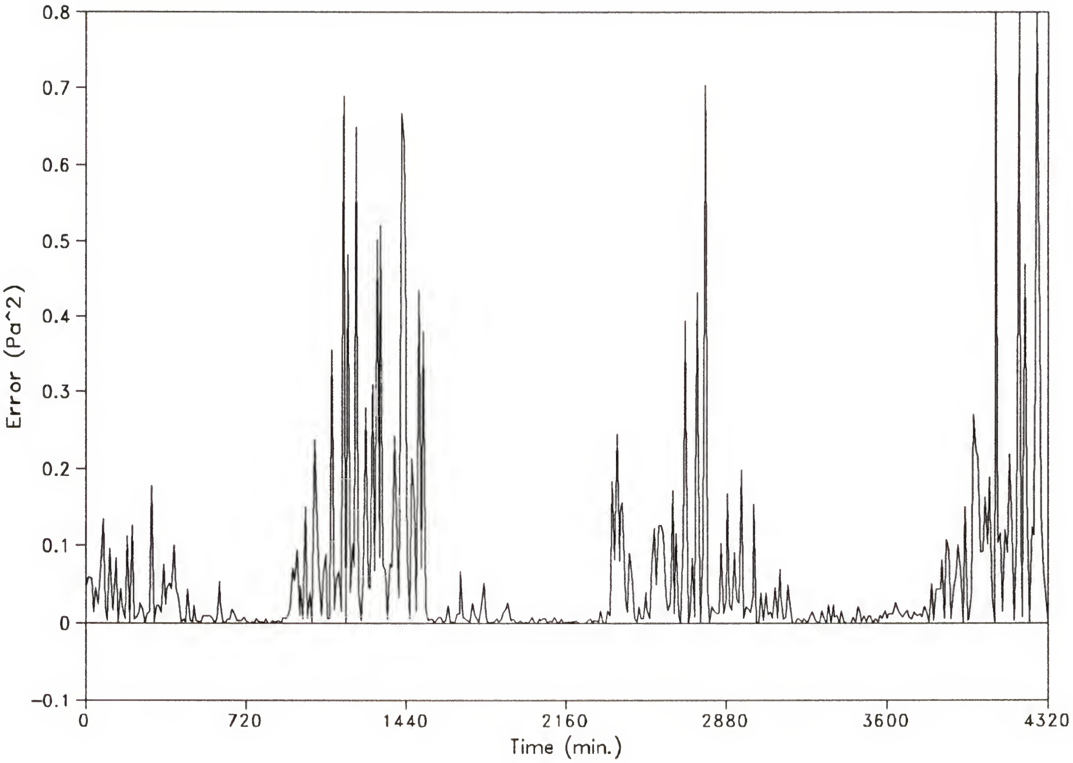

FIGURE 4-52 B: The square difference of the temporal variations of predicted pressure differences using the MSE method for the experimental measurements of Figure 4-50 A.

Estimation of the ratio between the temperature dependent pressure differential and the temperature independent pressure differential across the slab can be performed by utilizing equations 4-20 and 4-21. This ratio can be constructed such as,

$$R = -\Delta P_{i/o}/[P_{ss}(t+\Delta t)-P_b(t+\Delta t)] \qquad (4\text{-}24)$$

The absolute dimensionless value of R can be used to extend the examination of the model predictions to other configurations, for example, variations in the temperature difference, the magnitudes of barometric pressure changes, or the sub-slab geometrical equilibrium time.

The spatial dependence of the pressure differences across the slab can be examined by changing the equilibrium time response, T_R, that characterizes the location under the slab. This application is restricted to cases in which the indoor and outdoor temperatures remain constant during the time that the indoor pressure is stabilized with the barometric pressure. This assumption is associated with the model development, and further investigation is needed in order to include the effects of the observed time shifting in temperature responses between the indoors and outdoors, so that time dependent configurations may be analyzed.

Humidity measurements were simultaneously collected with temperature and other monitored parameters. However, humidity

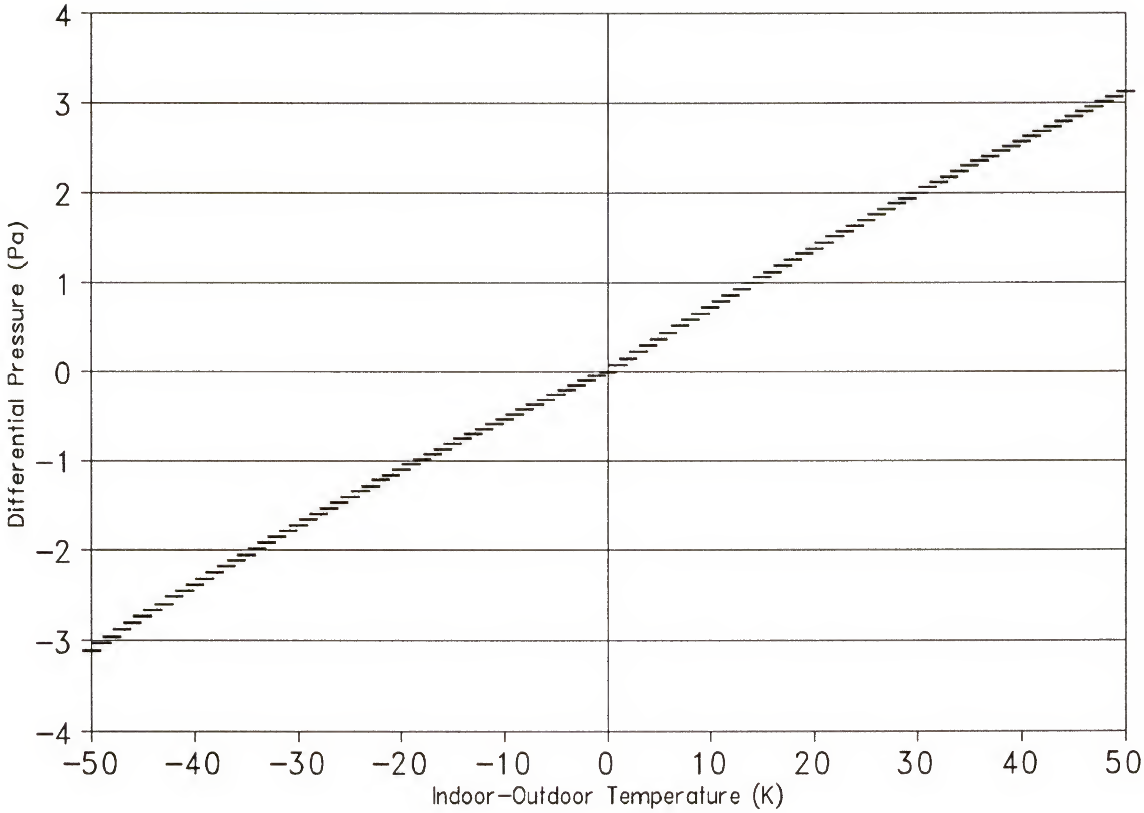

FIGURE 4-53: The model predictions of the temperature-induced pressure differential between the indoor and outdoors as a function of the indoor/outdoor temperature differences.

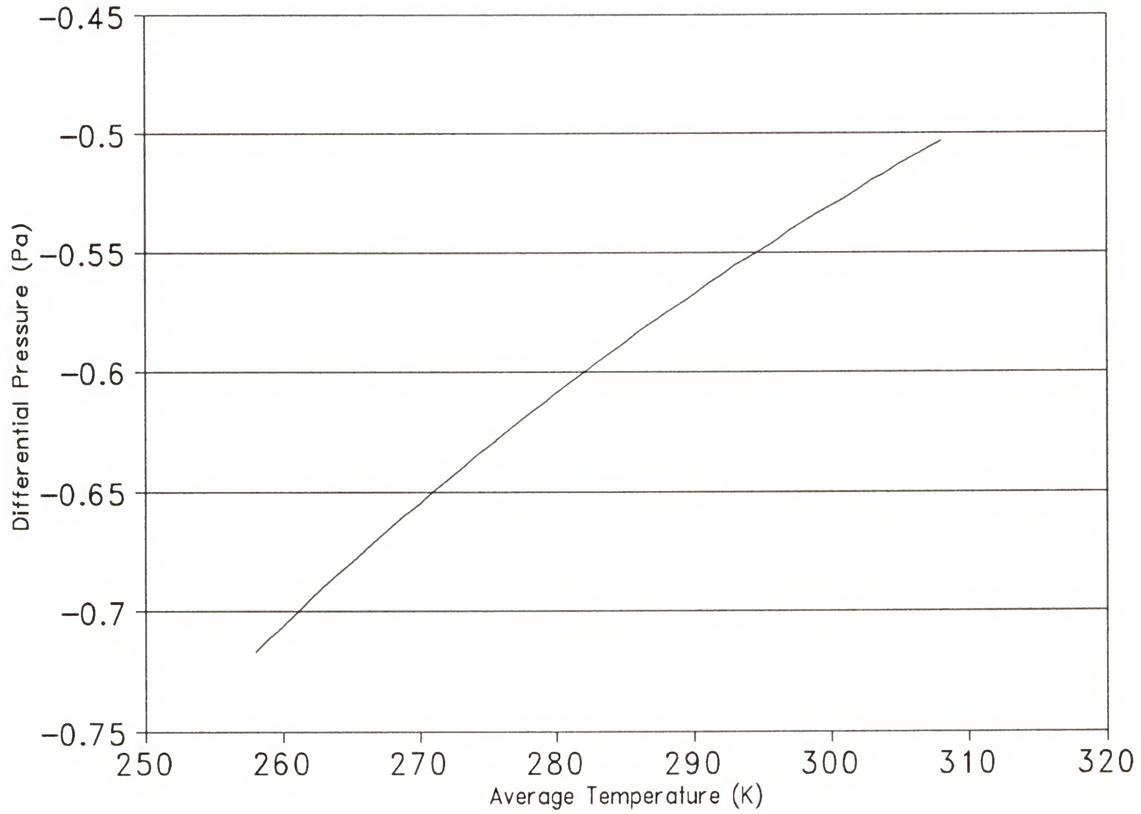

FIGURE 4-54: The model predictions for a constant temperature difference of 10 degrees that induce pressure differentials for different average temperatures.

is not considered as an influencing factor on an indoor radon-related driving force parameter. Observations at the UFRRH indicate that no significant correlation can be determined between indoor radon concentration and indoor humidity for the particular configuration at the UFRRH.

The existence of air humidity may provide a limited removal mechanism for elevated indoor radon concentrations when indoor air temperature is low and the air is moved to the outdoors and replaced with new humid air. The latter possibility is derived from the fact that radon gas has a coefficient of solubility in water that can be characterize with an exponential function. Radon solubility increases with decreasing temperature.

Relative humidity observations at the UFRRH indoor environment can be generally characterized to have a quantity change direction that is indirectly proportional to the change in indoor temperature. This observation can be explained from the derivation of the relative humidity since the heat capacity of air increases with increasing temperature and causes decreases in the relative humidity.

Figures 4-55 A and B show samples of the temporal variations of relative humidity measured at the UFRRH for two different testing periods illustrating humidity increase and fluctuation patterns, respectively.

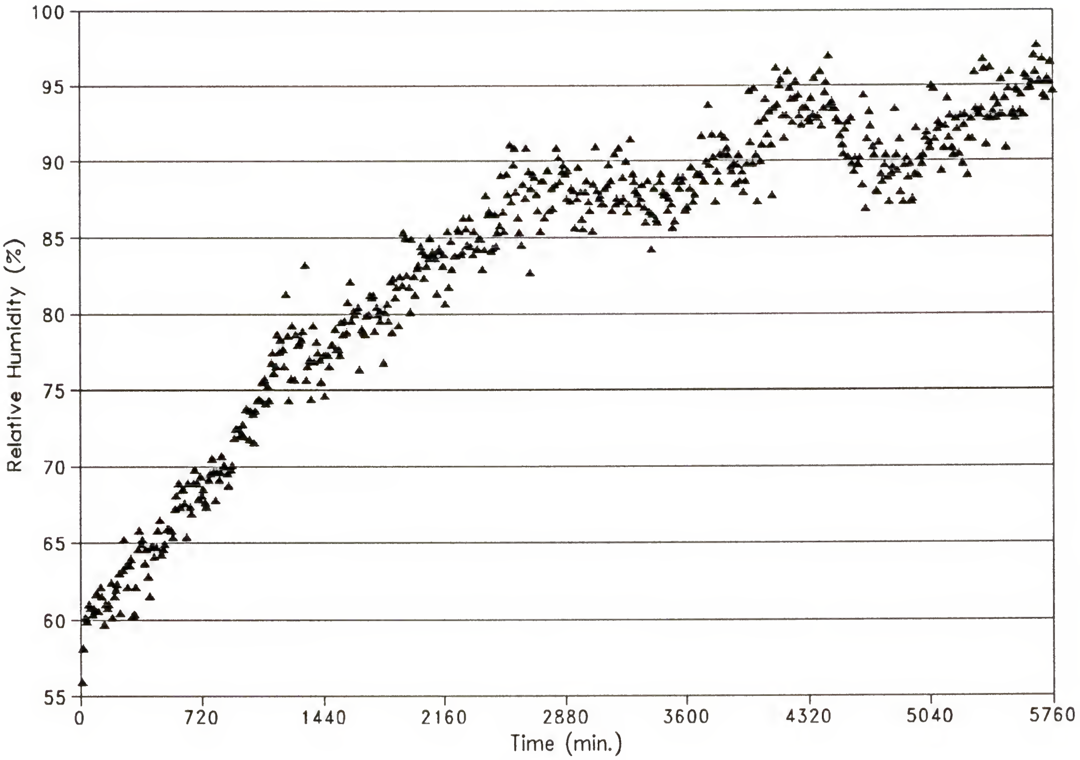

FIGURE 4-55 A: A 4-day sample of the temporal variations of relative humidity monitored at the UFRRH.

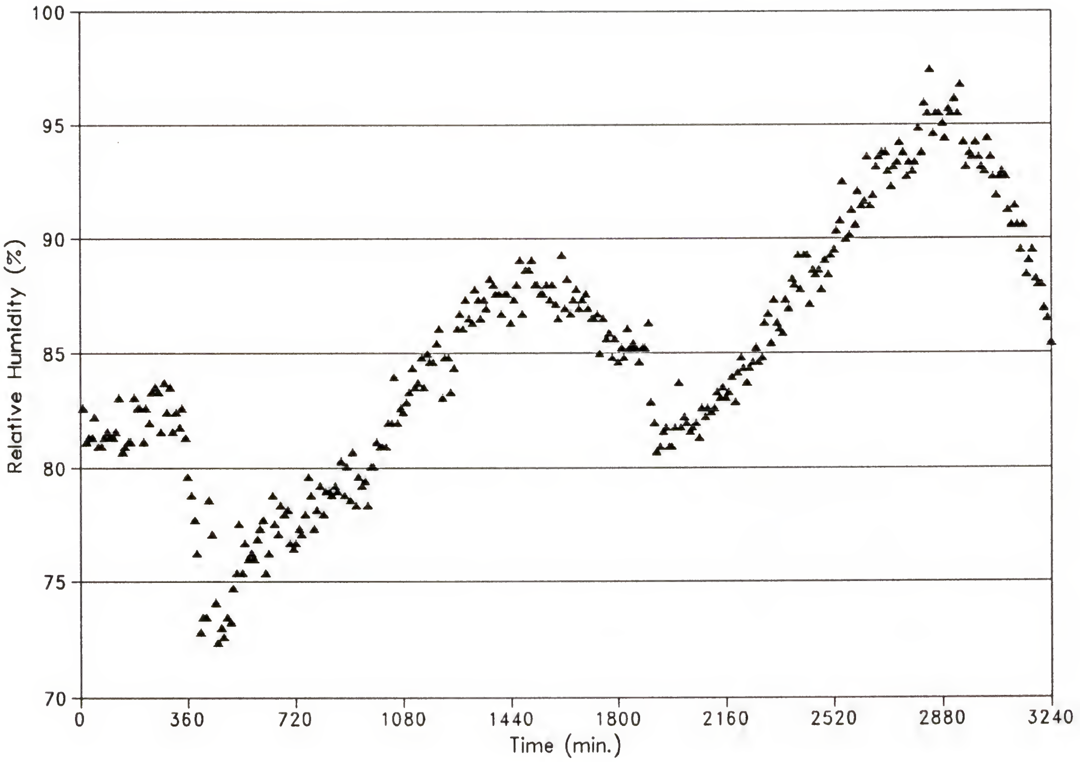

FIGURE 4-55 B: A 3-day sample of the temporal variations of relative humidity monitored at the UFRRH.

Structure Ventilation

The effects of natural and forced ventilation air on indoor radon concentrations can be generally attributed to the dilution of indoor radon through mixing with the ambient air which has a much lower radon concentration. Once the steady state radon concentration in the indoor environment reaches a high level, reduction of this concentration by ventilation is the only effective radon removal mechanism that can be employed. Ventilation forced by pressure differences between the indoor and outdoor needs to be employed to cause air change rates that dilute the elevated indoor radon concentration. Prevention of indoor radon should be approached with treatment of radon entry mechanisms, before radon concentration reaches high levels, and the structure ventilation is a fundamental component in any indoor radon prevention system.

The infiltration rate is the uncontrollable component of the structure ventilation rate. Infiltration rate has been used, or associated, with the indication of the natural ventilation in structures. However, in this research infiltration air shall refer to the uncontrollable air in the structure ventilation. Natural ventilation shall refer to the structure ventilation derived by naturally-induced (non-mechanical) forces versus the forced (mechanically-induced) ventilation; therefore, it may or may not contain an infiltration component.

As indicated in the experimental design and methodology, ventilation measurements were performed using three different techniques: Perfluorocarbon trace gases (PFTs), pulsed tracer injection, and the calibrated-fan blower door testing. PFTs were used to evaluate air exchange rates when no artificial pressurization or depressurization of the structure occurred. The PFT sources and capillary adsorption tube samplers (CATS) were obtained from the Brookhaven Nation Laboratory Tracer Technology Center and were deployed for 4 to 7 d periods, during which the house remained in the same configuration. PFT CATs were returned to, and analyzed by, Brookhaven National Laboratory.

The PFT testing involved a constant injection of perfluorocarbon tracers that were collected by the passive capillary adsorption tube samplers (CATS) in the indoor, outdoor, and sub-slab areas. Results of OFT measurements at the UFRRH were analyzed at Brookhaven National Laboratory. To model the time dependent tracer gas concentration behavior in the indoor environment, the gas mass balance equation was employed. If the concentration is assumed to be constant over geometrical location, i.e., homogenous distribution in the zone under consideration, the time rate of change of the tracer gas concentration can be written as,

$$V \frac{dC(t)}{dt} = S(t) - C(t)\, Q(t) \tag{4-25}$$

where S(t) is the tracer gas source injection rate (kq/s),
Q(t) is the structure ventilation rate in (m^3/s),
V is the structure indoor air volume in (m^3), and
C(t) is the tracer gas concentration in (kg/m^3).

Equation 4-25 is a first order linear differential equation since the source term has no dependency on the concentration itself. Solution requires an initial condition such as C(t)=C_0 at t=0. The standard solution to the equation employing the initial condition is then,

$$C(t) = C_0\, e^{-\frac{Q(t)}{V}t} + \frac{S(t)}{Q(t)}\,(1 - e^{-\frac{Q(t)}{V}t}) \tag{4-26}$$

Both ventilation rate and tracer gas injection rate in this application are constant with time; therefore the above equation can be written as,

$$C(t) = C_0\, e^{-\frac{Q\,t}{V}} + \frac{S}{Q}\,(1 - e^{-\frac{Q\,t}{V}}) \tag{4-27}$$

where all parameters are constants with time except the tracer gas concentration.

The sensitivity of Equation 4-27 with respect to time was evaluated to determine the validity of the results obtained from the PFT experiments. Figure 4-56 illustrates the time-dependant responses of the tracer gas concentration, normalized to the initial concentration C_0, for different ventilation rates (0-0.5 m^3/s) at the UFRRH as predicted by the above equation for the indoor air volume of 400 m^3. As seen from the graph, except for initial time periods, the value (Q/V) is constant. Since the PFT experiments were performed for periods of 3-7 days, the obtained results from this testing were accurate enough in representing the UFRRH ventilation rates under different testing configurations.

Figure 4-56 also indicates that the effect of the exponential terms in Equation 4-27 is negligible after a long period of time, therefore, the exponent components in the first and second terms of the R.H.S. could be eliminated,

$$C_{average} = \frac{S}{Q} \tag{4-28}$$

where $C_{average}$ is the time-averaged concentration of the tracer gas concentration. Since $C_{average}$ is measured and S is constant, the structure ventilation rate, and consequently the air change rate per hour (ACH) can be calculated. For the UFRRH (V=400 m^3), the latter quantity is then calculated by,

$$ACH = \frac{S\ (kg/s)}{9\ C_{average}\ (kg/m^3)} \tag{4-29}$$

It should be noticed that the above derivation assumes that the structure ventilation rate Q(t) is constant over the testing period (per structure configuration). All the PFT experiments performed at the UFRRH were conducted with an unchanged structure configuration. However, Q(t) can be affected by environmental factors such as temperature and

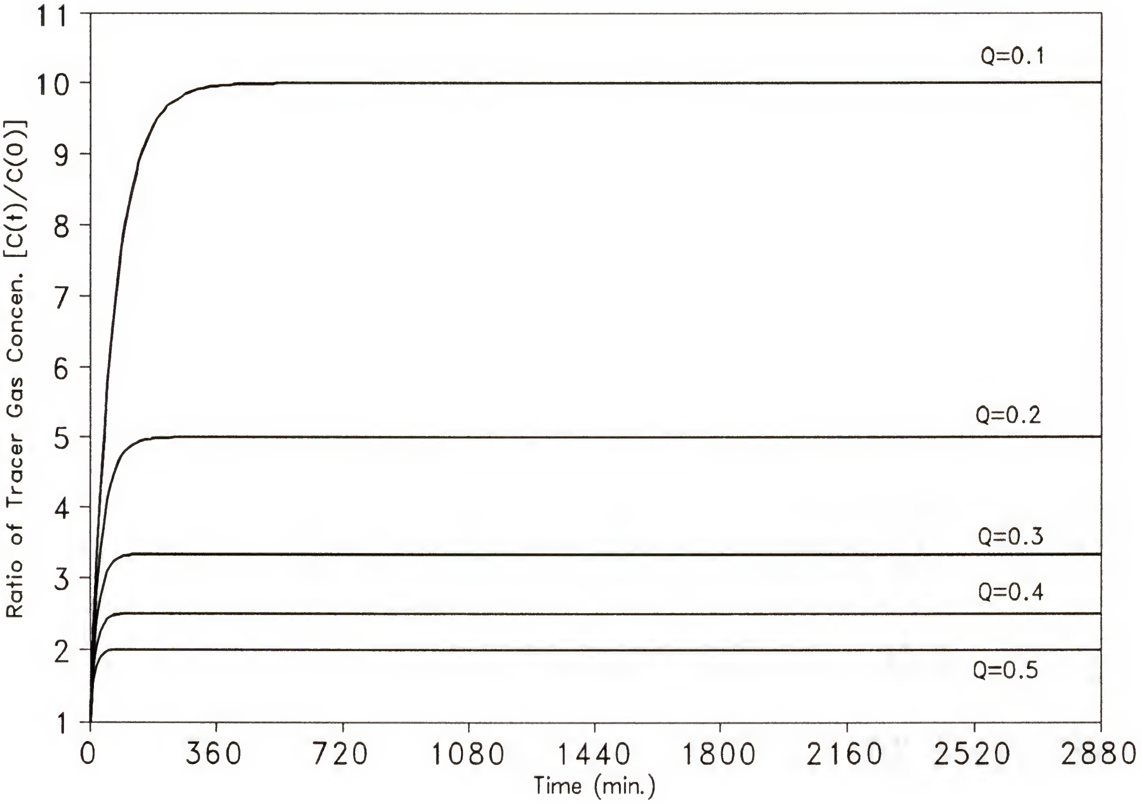

FIGURE 4-56: The time-dependent responses of the tracer gas concentration normalized to the concentration at t=0, for different ventilation rates.

weather parameters, particularly wind speed. Temperature corrections were considered in calculating the average concentration of tracer gas by the Brookhaven National Laboratory, while weather parameters have a negligible effect in the UFRRH (as discussed before). If the time dependency of the structure ventilation rate Q(t) for the same testing period does exist, Equation 4-25 can still be used to calculate this parameter. However, there is no known analytical solution to the latter case and numerical computation must be employed.

The pulse injection technique was employed using the CO_2 and SF_6 testing assemblies illustrated in the experimental design and methodology. The tracer gas was injected in the indoor volume every six hours while its concentration was continuously monitored. The mass balance approach can be utilized to model this technique and the same Equation 4-25 can be utilized to describe the time rate of change of CO_2 or SF_6. However, the gas source term is now represented by Dirac delta function as follows,

$$V\,\frac{dC(t)}{dt} = S(t)\;\delta(t-t_i) - C(t)\;Q(t) \qquad (4\text{-}30)$$

where t_i is the injection time. If t_i is selected as 0 for any segment (6 hours) of the testing period, the previous equation will reduce to Equation 4-25. Although the gas injection started at t=0 was continued for a period of 10 minutes, for all practical purposes, there was some dead time for the released gas to reach the monitoring system. This time depended on the diffusion process since most of these experiments were performed under neutral pressure conditions. Therefore for t>0 after the pulse injection, Equation 4-30 becomes,

$$V \frac{dC(t)}{dt} = - C(t)\ Q(t) \qquad t > t_i \qquad (4\text{-}31)$$

The solution to the above equation using initial condition $C=C_0$ at t=0 is,

$$C(t) = C_0\ e^{-\frac{Q\,t}{V}} \qquad t > t_i \qquad (4\text{-}31)$$

The initial CO_2/SF_6 concentration value and the measured concentrations C(t) were expressed in ppm. The structure ventilation rate can be calculated from the exponent of Equation 4-32 and, therefore, the air change rate per hour for the UFRRH is,

$$ACH = \frac{\ln(C_0)\ -\ \ln(C)}{9\ \Delta\ t} \qquad (4\text{-}33)$$

$$\Delta t = T - t_i \ , \qquad T > t_i$$

Figure 4-57 illustrates the ACH predictions at the UFRRH for different time intervals between the injection and measurement time when the measured tracer gas concentration varies between 100% to 0% of the initial pulsed injection concentration (C_0). Figure 4-58 shows samples of the pulse injection tracer gas measurement results.

Most of the preceding ventilation experiments performed at the UFRRH targeted structure configurations of neutral pressure conditions and small pressure differences between the indoor and outdoor environment. For higher pressure differences, blower door testing was utilized to calculate the structure ventilation and leakage area.

For the scope of applications in this work concerning indoor radon concentrations, the characterization of the variation in structure ventilation rate with utilization of the blower door is sufficient. The blower door was used to quantify infiltration air and air exchange rates for the house using the standard blower door testing protocol (ASTM 1987). This technique provided accurate measurements of indoor/outdoor differential pressures and the corresponding ventilation rates over the range of 2 to 50 Pa.

The other advantage of using blower door testing is to relate the structure ventilation rates directly to the pressure differences; thus incorporation into the mathematical framework of indoor radon removal and entry rate can be easily facilitated. The blower door tests generated a family of response curves of the volumetric airflow rate into and out of the structure, as a function of the differential pressure across the structure shell when the structure underwent pressurization or depressurization. These curves can be well described by the expression,

$$Q = K \, (\Delta P_{shell})^{n} \tag{4-34}$$

where Q is the volumetric ventilation (or leakage) flow rate into or out of the structure in (m^3/s),

ΔP_{shell} is the differential pressure across the structure shell in (Pa),

n is the flow exponent and has a value between 0.5 and 1, and

K is the flow coefficient for the structure in ($m^3/Pa^n.s$).

For the purpose of calculating the flow coefficient and exponent, the above equation is transformed to log format as follows,

$$\ln(Q) = \ln(K) + n \ln(\Delta P) \tag{4-35}$$

The values of K and n are then empirically determined by the best linear regression line on the transformed variables. For the UFRRH, the flow coefficient was 0.0566 ± 0.0006, and the flow exponent was found to be equal to 0.69 ± 0.04. At pressure differences of 50 Pa, the resulted air change rate (ACH_{50}) was 7.6 ± 1.3. Figure 4-59 illustrates the predictions of the UFRRH ventilation rates using the above results.

The 7-day PFT measurement under all-systems-off conditions yielded a small air exchange rate of 0.076 per hour. With the HVAC circulation fan operating continuously, more accurately simulating occupied house conditions, a 7-day PFT deployment measured air exchange rates of 0.25 air changes per hour, which correspond to an air infiltration rate of

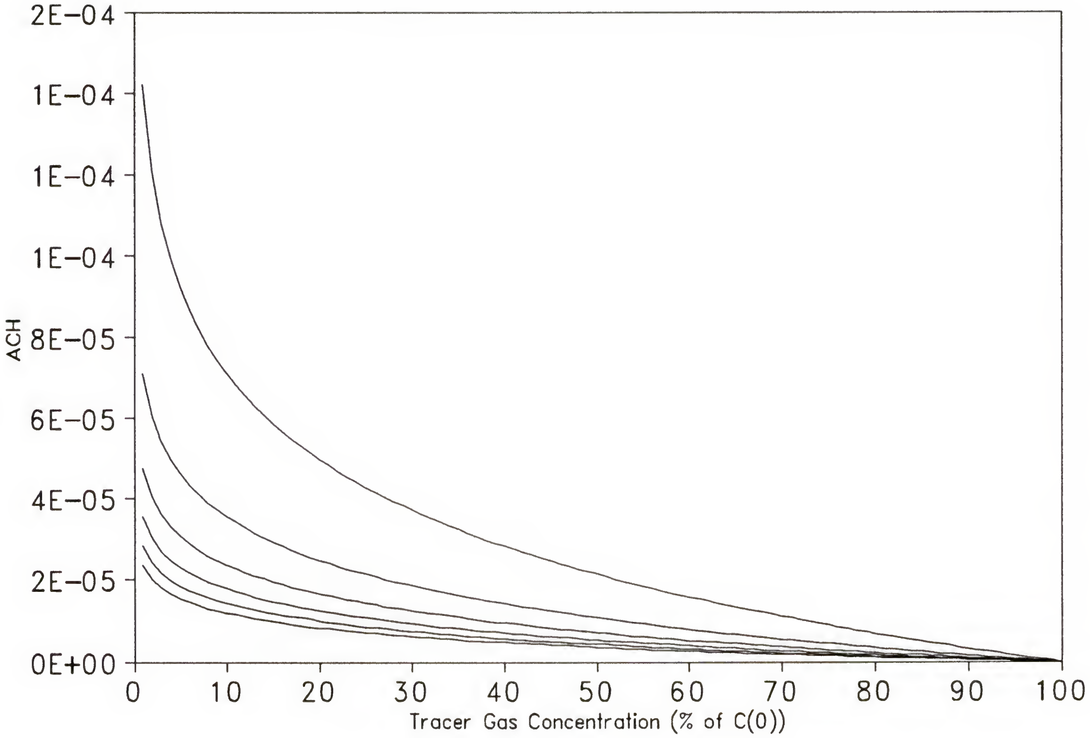

FIGURE 4-57: Predictions of the ACH at the UFRRH for various measurement intervals when the tracer gas concentration varies between 0-100% of the concentration at the pulsed injection time. Measurement intervals (top to bottom) 1h, 2h, 3h, 4h, 5h, & 6h.

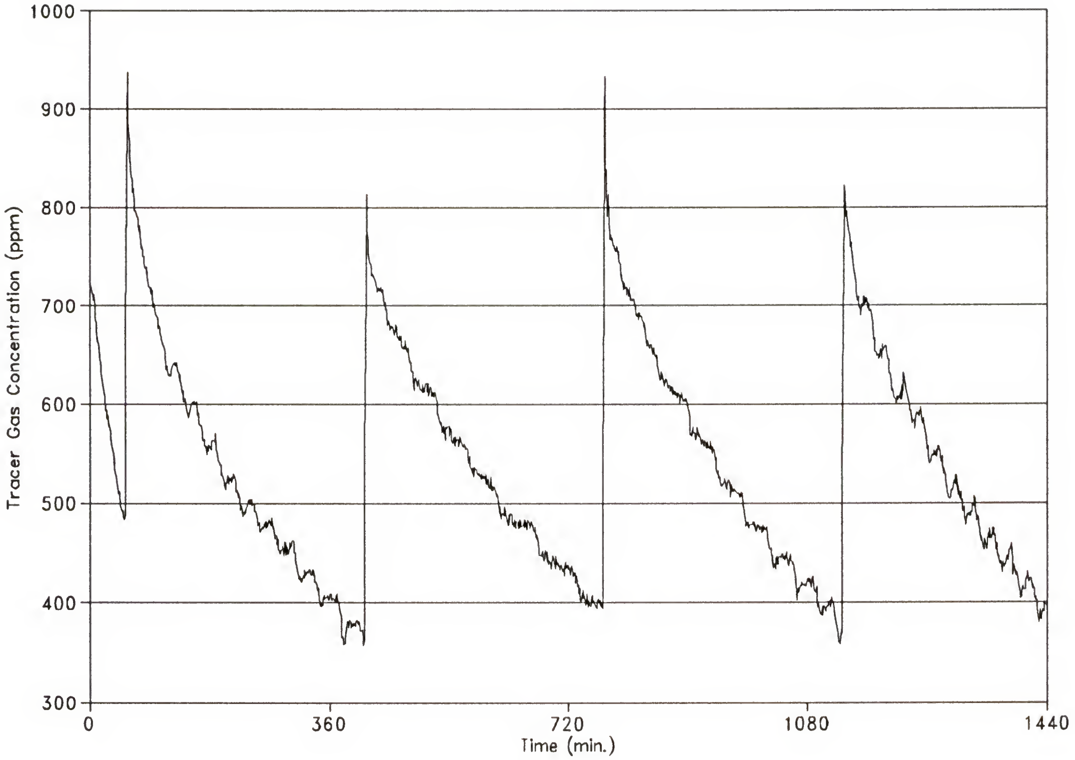

FIGURE 4-58: Samples of the time-dependent behavior of the SF_6 tracer gas concentration during measurements.

0.028 m^3/s. Continuous operation of the HVAC circulation fan produced a small change in the measured house shell differential pressures and resulted in an indoor radon concentration of 17.57 ± 2.7 pCi/l (650 ± 100 Bq/m^3).

Since Equation 4-34 utilized a direct correlation between differential pressure across the shell and the volumetric air flow rate, it can be used to study the effect of temperature and wind-induced pressure differences on the structure ventilation. Incorporation of wind-induced pressure differences into the empirical formulation of the UFRRH ventilation rate yields,

$$Q = 0.0566\ (P_{in} - P_b - 0.5\ \rho\ V^2)^{0.69} \qquad (4\text{-}36)$$

Figures 4-60 A, B, and C illustrate the effect of wind speed, previously modeled, when the wind blows on the windward, side, and leeward walls of the structure and the indoor pressure is constant and equal to the barometric pressure. Figure 4-60 D illustrates the effects of wind blowing across the structure shell for different speeds applied to the full range of wind drag coefficients. As seen in the graphs, the influence of wind-induced pressure differences on the UFRRH ventilation rates is negligible for the range of wind speed experienced at the site.

Characterization of the temperature difference effects on the UFRRH ventilation rates can be performed by incorporating the temperature-induced pressure differential model and Equation 4-34 as,

$$Q = 0.0566 \left(\frac{P_o\, C\, (T_{in} - T_{out})}{T_{in}\, T_{out}}\right)^{0.69} \qquad (4\text{-}37)$$

Figure 4-61 A illustrates the prediction of the indoor/outdoor temperature difference effect on the UFRRH ventilation rates. Figure 4-61 B illustrates the effect of the average temperature between the indoor and outdoor on the structure ventilation when the temperature difference is constant.

Indoor Radon Concentrations

Preceding sections in this chapter have shown the measurements, results, and theoretical modeling of the fundamental radon driving forces with regard to indoor radon concentrations. The overall objective of the experimental design, data analysis, and the modeling effort were to identify a parameter that is common to all radon driving forces that may contribute to the increase or the decrease of the indoor radon concentration. This parameter is the pressure difference that controls the air flow mechanism of the radon gas in these applications.

The mathematical framework for the semi-diurnal barometric pressure variations pressure differentials, the wind-induced pressure differentials, the temperature-induced pressure differentials, and the pressure differentials associated with the structure ventilation have been developed. In the following treatment, a system approach will be utilized to construct the explicit relationship between the pressure

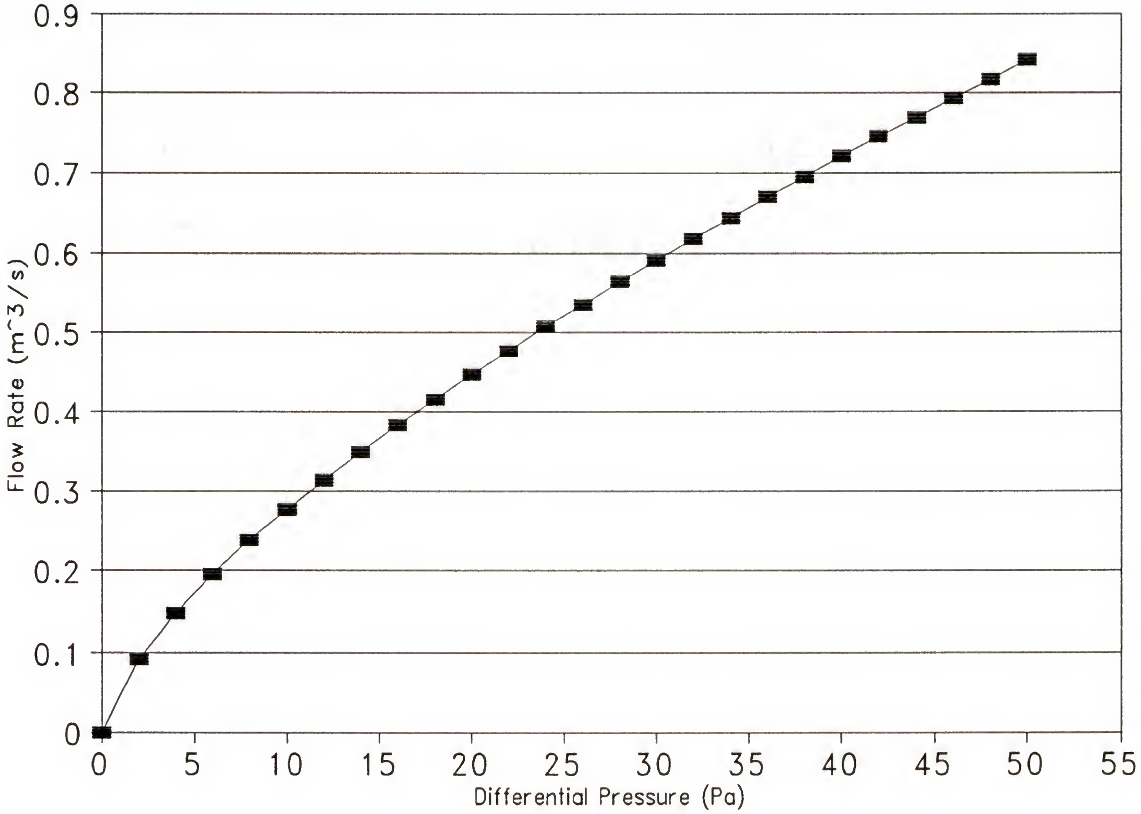

FIGURE 4-59 A: An illustration of the variation in UFRRH air volumetric flow rate experienced for various differential pressures applied across the structure shell.

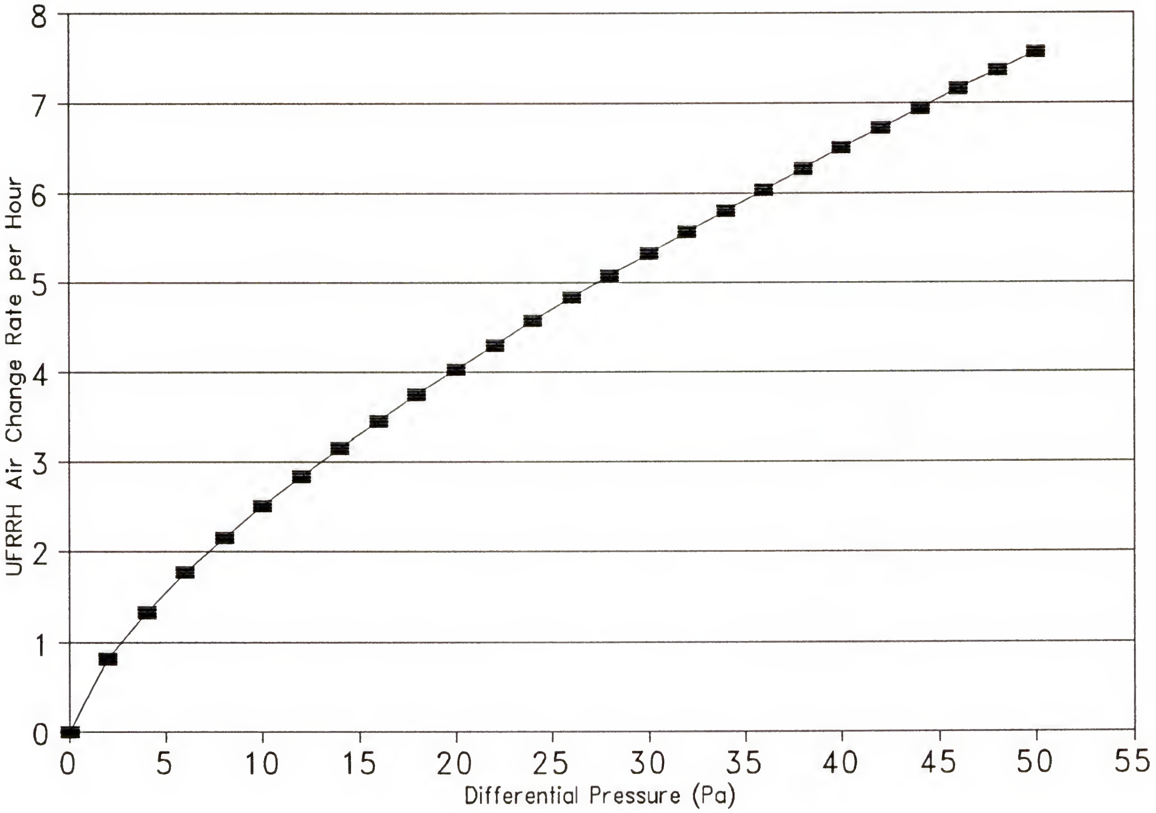

FIGURE 4-59 B: An illustration of the variation in UFRRH air change rate per hour experienced for various differential pressures applied across the structure shell.

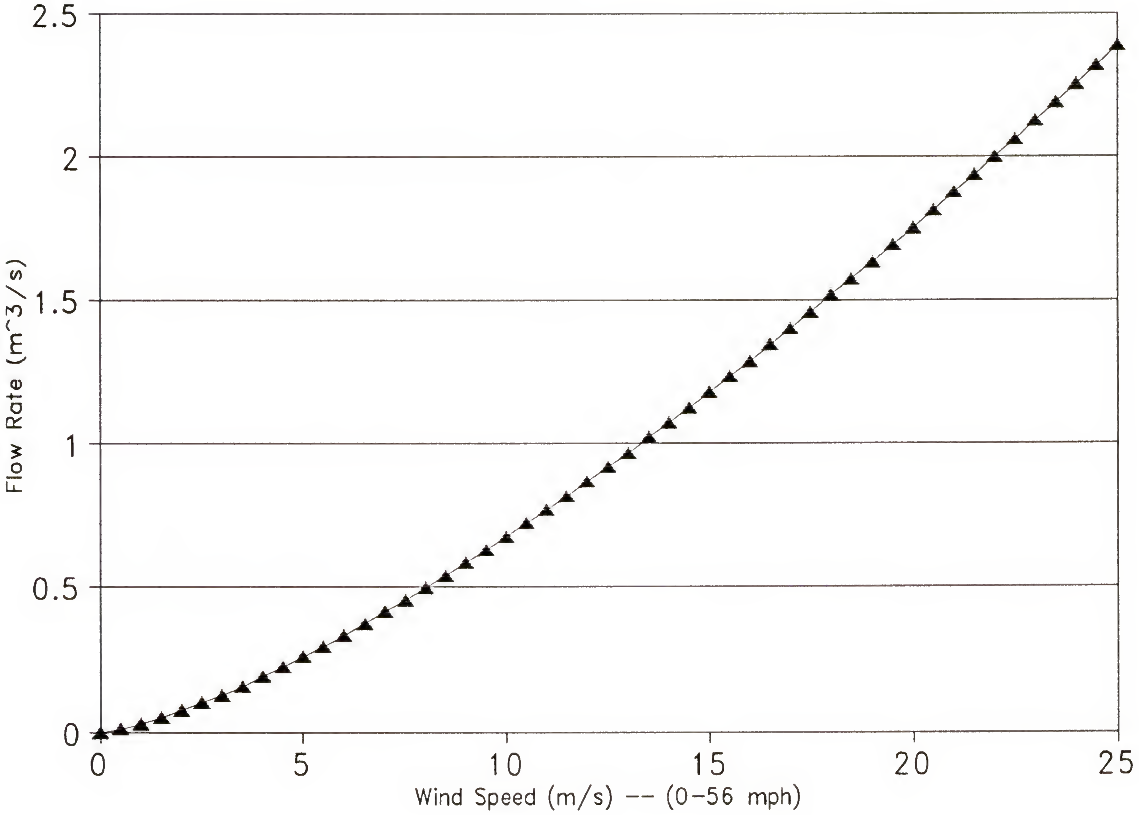

FIGURE 4-60 A: Predictions of the wind-induced pressure differentials effects on the UFRRH ventilation for a range of wind speed blowing on the windward wall of the structure.

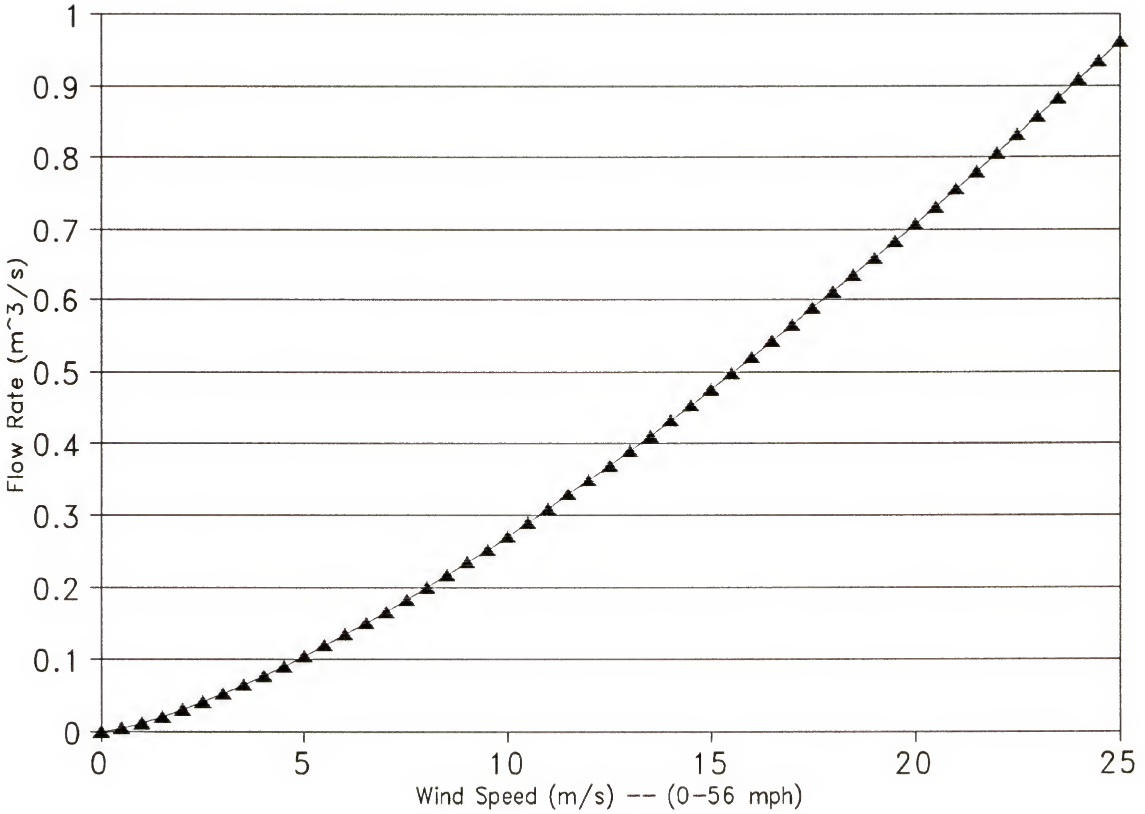

FIGURE 4-60 B: Predictions of the wind-induced pressure differentials effects on the UFRRH ventilation for a range of wind speed blowing on the leeward wall of the structure.

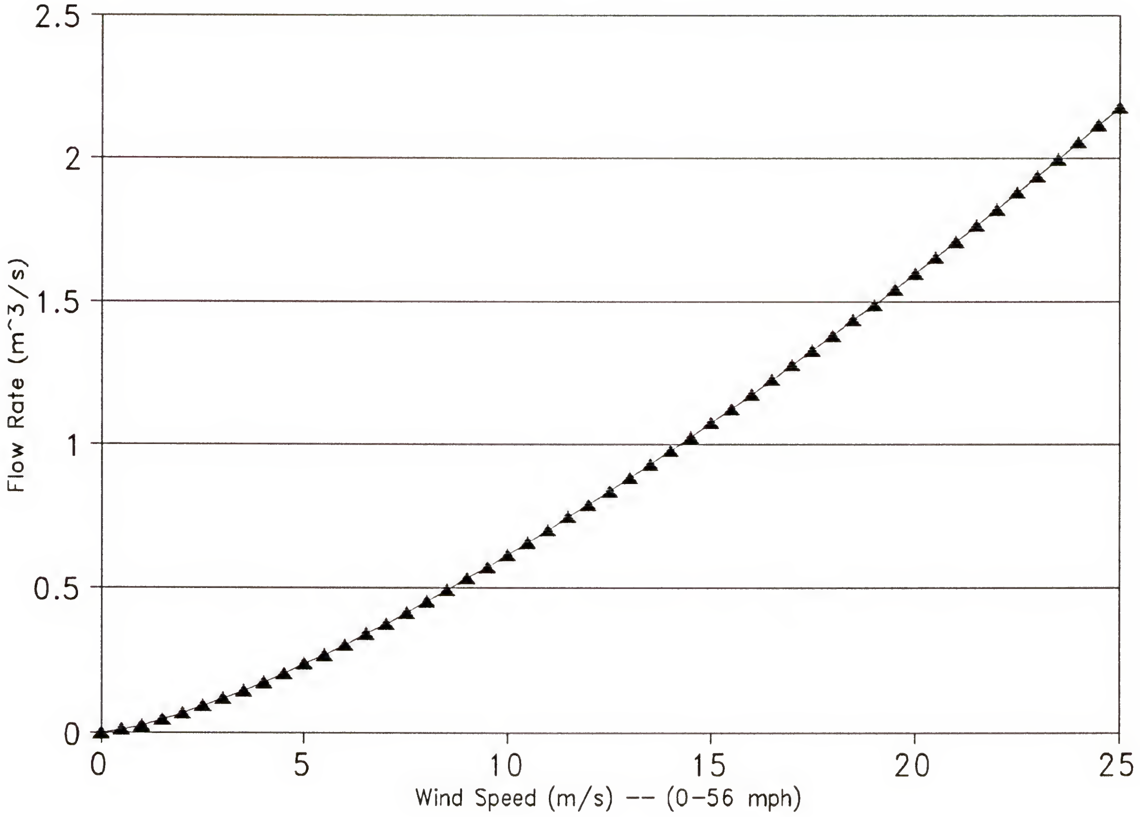

FIGURE 4-60 C: Predictions of the wind-induced pressure differentials effects on the UFRRH ventilation for a range of wind speed blowing on the side wall of the structure.

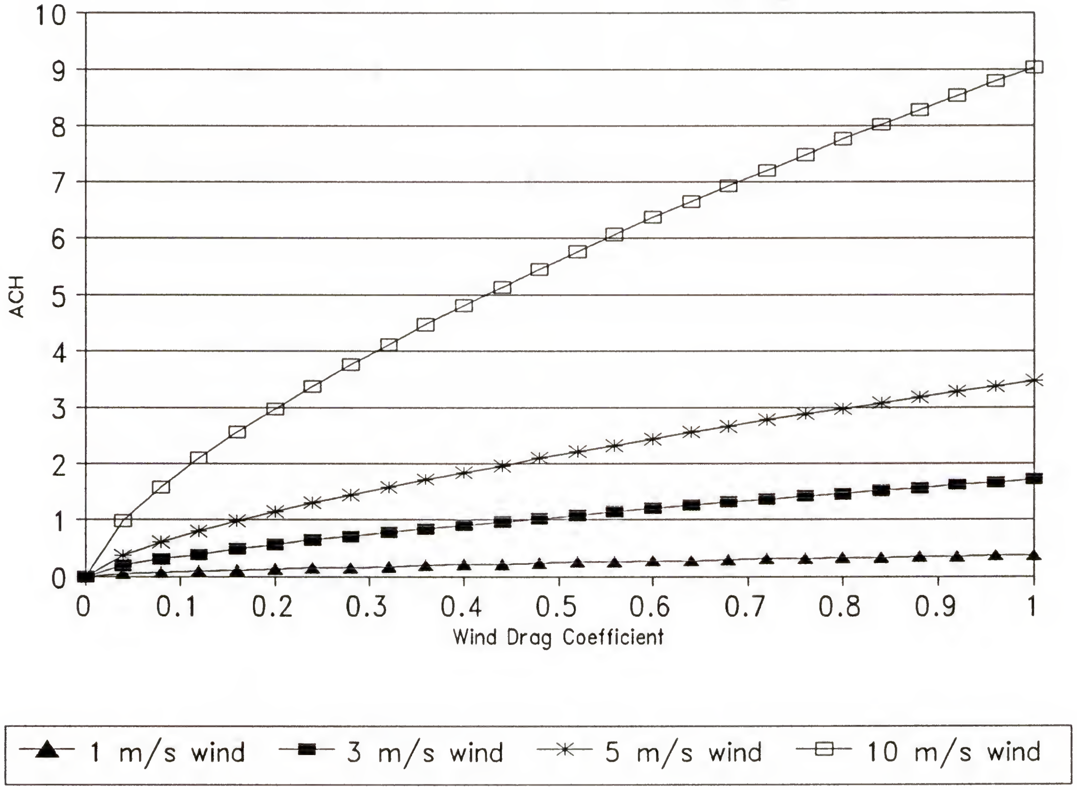

FIGURE 4-60 D: Predictions of the effect of wind speed on the UFRRH ventilation for all the possible interaction configurations developed by the wind direction and fluctuations across the structure.

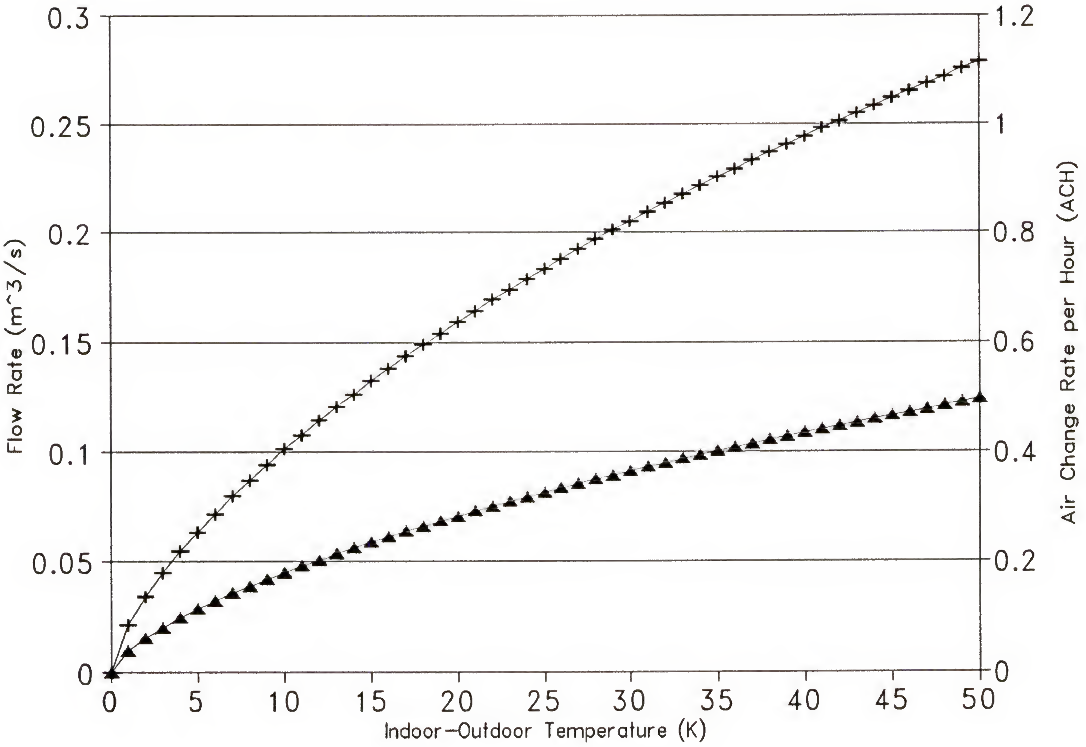

FIGURE 4-61 A: Predictions of the effects of indoor/outdoor temperature differences on the UFRRH ventilation rates. (plus sign-ACH).

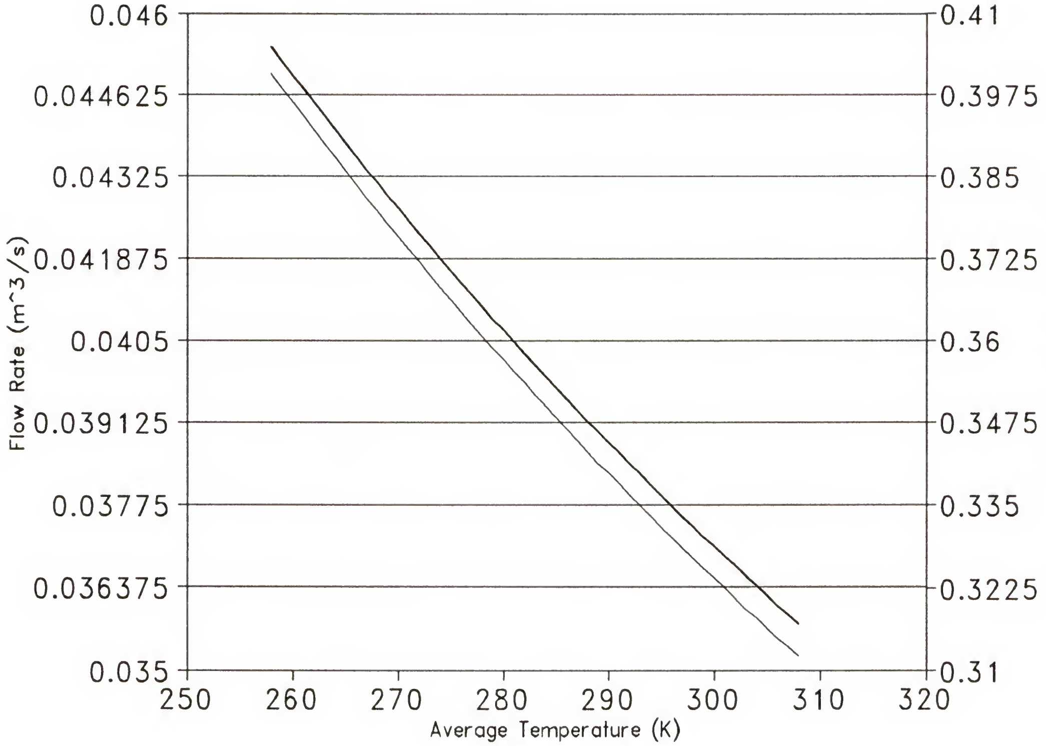

FIGURE 4-61 B: Predictions of the effects of the average temperature between the indoor and outdoors on the UFRRH ventilation rates. (heavy line- ACH).

differentials and both the indoor radon entry rate and the indoor radon removal rate.

After such a module is established, previously developed radon driving forces can be incorporated into the module structure. Finally, the structure components will be integrated using the mass balance equation along with other radon independent source and removal terms in the indoor environment to develop the relation governing indoor radon concentration.

The concentration of a substance in a volume can be calculated by solving the mass balance equation. The mass balance equation of radon gas in the indoor volume consists of two major components: radon entry and radon removal. Each major component may consist of various radon driving forces. The basic radon removal mechanisms consist of radon removal by ventilation and the decay rate.

The differential pressure across the structure envelope and duct leakage associated with the (HVAC) system basically regulate the air infiltration rates in the structure. Pressure differentials between the interior and soil gas govern radon entry into structures and are not necessarily coupled to the differential pressures across the structure shell. Each of these pressure differentials originates from an independent mechanism and must therefore be considered separately in any model of radon entry into structures.

Efforts to control indoor radon concentrations using ventilation strategies must therefore account for changes to the driving forces for radon entry and the ventilation rate, both of which are a function of the technique used to provide infiltration air (Hintenlang et. al. 1993a)

Building pressure has long been identified as an effective technique to change indoor radon concentrations. However, the pressurization applications are not always practical due to considerations such as energy cost and interfacing with comfort level. The traditional concepts linking indoor radon and building pressure arise from the recognition that pressure driven flow mechanisms dominate radon entry (Nazaroff 1988; Nazaroff & Nero 1988) from sub-structure area into interiors where the soil gas has been identified as the principle source of indoor radon (Crameri et. at. 1989; Nazaroff et. al. 1988; Nero & Nazaroff 1984).

Building depressurization increases radon entry rates and is expected to lead to higher indoor radon concentrations, while building pressurization reduces pressure driven radon entry and results in lower indoor radon concentrations. These concepts of pressure driven radon entry, however, frequently neglect the associated changes in air exchange rates when interior and outdoor pressures are different. The increased air exchange rate that occurs when a structure is depressurized tends to offset the increased radon entry rate so that indoor radon concentrations usually exhibit only a modest increase as a structure is depressurized.

Differential pressures across the house shell, ΔP_{shell}, demonstrate a diurnal cycle with peak amplitudes of only about 0.4 Pa. These are attributed to varying temperature differentials between the indoor and outdoor environments that occur throughout the 24 h day and remain small because the house is well sheltered from wind effects. These variations are partially driven by the diurnal temperature cycle.

Figure 4-20 illustrates the average indoor radon concentrations measured as a function of house shell differential pressure. As discussed previously, the highest indoor radon concentrations occur when the average differential pressure across the house shell is zero. Small changes in ΔP_{shell} result in a decrease in radon concentration. The peak near neutral pressures occurs because the ventilation rate becomes quite small in this region but the radon entry rate does not substantially decrease.

Although ΔP_{shell} may be very small, radon-containing soil gas continues to enter the structure, by convective flows (which can be generated by the periodic behavior of ΔP_{slab} and by diffusion processes (Al-Ahmady 1992a). Large indoor radon concentrations build up under these conditions because the air exchange rate, governed by ΔP_{shell}, is small as evidenced by the results of the PFT measurements. A quantitative model of this phenomenon may be developed utilizing the measurements and theoretical concepts of radon entry and transport.

Estimation of the source term of indoor radon concentration can be divided into four contributing components. Those components are entry for sub-structure area by convection and diffusion, entry from potable water, entry form ambient air, and entry from building materials. Building materials and potable waster sources of indoor radon are negligible when compared to the sub-slab radon concentration as discussed in Chapter 1. Contributions of the diffusive sub-slab radon into the indoor environment is not dependent on pressure driven processes.

The convective entries from sub-slab radon and the ambient radon into the indoor environment are controlled by pressure differences. Utilizing the system approach in this treatment, the diffusive entry is considered constant and can be determined for each particular structure but remain reasonably constant over the range of pressure differences that might normally be experienced by the structure. Assessment of the contribution from ambient air can be derived from the pressure differential dependent structure ventilation rate developed in the preceding section and the average concentration of radon in the outdoor environment.

Quantification of the generic radon convective entry from the sub-structure area into the indoor can be determined by computing the correlation between simultaneous monitoring of indoor radon concentration and pressure differentials across the slab for a period of time.

If a reasonable spatial distribution measurement of indoor radon concentration in the structure over a period of time, is made, the time-averaged radon entry rate into the indoor environment can be determined from,

$$R = \frac{1}{T}\int_0^T \int_v C(r,t)\ dt\ dv \qquad (4\text{-}38)$$

where C(r,t) is the radon activity concentration per unit volume, per unit time in the indoor environment (Bq/m^3s), and T is the time period of the measurement (s), when the spatial integration is performed over the indoor volume.

Application of the mass balance equation for the radon gas in the indoor environment can be performed by using the differential volume, dV, approach. In the differential volume, the time-rate of change (the accumulation rate) must be equal to the difference between radon generation and removal rates, therefore

$$\frac{dC(t)}{dt} = S(r,t) - RE(r,t) \qquad (4\text{-}39)$$

where C(t) is the radon activity concentration in the differential volume dV (Bq/m^3),

S(r,t) is the radon source term in (Bq/m^3s) which mostly consists of radon entry from the sub-structure area, and

RE(r,t) represents the radon activity removal term from dV in (Bq/m^3s). The latter term includes radon removal by ventilation and radon removal by radioactive decay. If the above equation is applied for the indoor volume, then

$$\int_v \frac{dC}{dt}\, dv = \int_v -\lambda\, C(r,t)\, dv + \int_v -Q(t)\, C(r,t)\, dv + \int_v R(r,t)\, dv \tag{4-40}$$

where Q(t) is the structure ventilation rate (m^3/s),
R(r,t) is the total radon entry rate (Bq/s), and
λ is the ^{222}Rn decay constant. If the spatial integration is performed over the volume, rearranging yields

$$\frac{dC(t)}{dt} + \left(\frac{Q(t)}{V} + \lambda\right) C(t) = \frac{R(t)}{V} \tag{4-41}$$

where V is the indoor volume (m^3).

The above equation is a first order linear differential equation with one independent variable (time). Utilizing the integrating factor method, the product of the integrating factor and the solution C(t) is an exact differentiation,

$$\frac{d}{dt}\left[e^{\int\left(\frac{Q(t)}{V} + \lambda\right)dt}\, C(t)\right] = \frac{R(t)}{V}\, e^{\int\left(\frac{Q(t)}{V} + \lambda\right)dt} \tag{4-42}$$

and the general solution to Equation 4-41 is,

$$C(t) = \frac{\int e^{\int\left(\frac{Q(t)}{V} + \lambda\right)dt}\, \frac{R(t)}{V}\, dt + C}{e^{\int\left(\frac{Q(t)}{V} + \lambda\right)dt}} \tag{4-43}$$

Experimental measurements at the UFRRH, and most of other similar applications, assumed that Q(t) and R(t) did not change during the experimental period for each of the experimental setups. If the time distributions of Q(t) and

R(t) are available, then time dependent solutions to Equation 4-41 could be obtained by substituting expressions into Equation 4-43. However, the system approach has been utilized in this application and a common parameter (ΔP) has been used as an input parameter to the ventilation and entry rates.

If the latter parameter is constant over the experimental execution period per each experimental configuration, which is the case for most of the testing, the dependency of ventilation and entry rates on the time inside the integration is negligible, and consequently, they can be treated as constants. Therefore, Equation 4-43 can be re-written as

$$C(t) = \frac{\int e^{(\frac{Q}{V} + \lambda)\int dt} (\frac{R}{V})\, dt + C}{e^{(\frac{Q}{V} + \lambda)\int dt}} \tag{4-44}$$

Performing the integrations in the above equation yields,

$$C(t) = \frac{(\frac{R}{V}) \dfrac{e^{(\frac{Q}{V} + \lambda)\, t}}{(\frac{Q}{V} + \lambda)} + C}{e^{(\frac{Q}{V} + \lambda)\, t}} \tag{4-45}$$

Rearranging the above equation produces,

$$C(t) = \frac{(\frac{R}{V})}{(\frac{Q}{V} + \lambda)} + C\, e^{-(\frac{Q}{V} + \lambda)\, t} \tag{4-46}$$

This equation represents the general solution to the radon concentration in the indoor environment when the radon entry rate and the structure ventilation rate stay constant during the period of the experiment.

The particular solution to Equation 4-46 can be performed by selecting an initial condition of the indoor radon concentration at the beginning of the experiment which is usually determined by the specific experimental run and testing configuration. If an initial condition of C(t)=0 at t=0 is applied to Equation 4-46, then

$$C(t) = \frac{R}{Q + \lambda\ V} \left(1 - e^{-(\frac{Q}{V} + \lambda)\ t}\right) \qquad (4\text{-}47)$$

In all the experiments performed at the UFRRH, a minimum testing period of 48 hours was utilized, which produced a stable indoor radon concentration for the testing configuration. As seen in Equation 4-47 the effect of the exponential term decreases with time. For the stable indoor radon concentration (steady state), i.e., t>>0, the above solution reduce to,

$$C = \frac{R}{Q + \lambda\ V} \qquad (4\text{-}48)$$

Equation 4-48 relates the average indoor radon concentration with the structure ventilation and radon entry rates.

Neglecting the contribution of building materials, the total radon entry in Equation 4-48 consists of three components: (1) the convective flow of soil gas into the structure (R_{conv}), (2) the ambient radon entering the structure with infiltration air (R_{amb}), and (3) the diffusive flow of radon from and through the concrete slab (R_{diff}). Therefore, the total radon entry rate can be written as,

$$R = R_{diff} + R_{amb} + R_{conv} \tag{4-49}$$

and the individual contributions to the total entry rate can be examined independently.

Convective entry of radon from the sub-structure area into the indoors can be quantified by relating the measured differential pressure across the slab to the corresponding measured indoor radon concentrations. If the structure experienced large magnitudes of depressurization, i.e, the differential pressures across the shell, $\Delta P_{in/out}$, were greater than 10 Pa, convective flow of radon containing soil gas dominated radon entry, and $\Delta P_{slab} \approx \Delta P_{in/out}$, since the differential pressure across the slab was much greater than the differential pressure between the sub-slab soil gas and the ambient atmosphere for this case.

Figure 4-20 shows the time-averaged indoor radon concentrations measured as a function of the whole house pressure. The results section shows that structure depressurization greater than 10 Pa can be employed with Equation 4-48 and the structure ventilation (Equation 4-34) for the depressurization range greater than 10 Pa. Since the term λV is constant and equal to 8.39×10^{-4} m^3/s (^{222}Rn half-life = 3.825 days), then

$$R = C\,(0.0566\,(\Delta P_{slab})^{0.69} + 8.38x10^{-4}) \qquad (4\text{-}50)$$
$$\Delta P_{in/out} \leq -10\ Pa$$

where R in Bq/s and C in Bq/m^3. Figures 4-62 A and B show the experimental results used for estimating the convective radon entry rate of Equation 4-50. The least squares fit to these experimental results produces the correlation between the pressure differences and the average convective radon entry of that has a correlation coefficient (R^2) of 0.9 as,

$$R_{conv} = 13.23\ (\Delta P_{slab}) \qquad (4\text{-}51)$$

where R_{conv} in Bq/s and ΔP_{slab} in Pa.

This convective entry expression may be extrapolated to lower magnitudes of ΔP_{slab} since convective entry is governed by Darcy's Law which remains proportional to the differential pressure to very small magnitudes (Bear 1972). Figure 4-63 shows the convective radon entry rate as a function of the differential pressure across the slab for a depressurization range 2 to 60 Pa.

For levels of depressurization where $\Delta P_{in/out} > -10$ Pa, the approximation that $\Delta P_{slab} \approx \Delta P_{in/out}$ begins to fail, as a result of the barometric pressure driven periodic variations of ΔP_{slab} previously discussed in the semi-diurnal barometric pressure variation radon driven entry (see Figures 4-6, 4-7, 4-8, 4-14, and 4-28). The total differential pressure across the slab is the sum of the indoor/outdoor differential pressure and a periodic function, $\Delta P_{sd}(t)$, describing the time variation of differential pressures measured across the slab,

$$\Delta P_{slab}(t) = \Delta P_{in/out} + \Delta P_{sd}(t) \tag{4-52}$$

Since the preceding application addressed time averaged radon concentrations, the time average of $\Delta P_{sd}(t)$, which varies approximately sinusoidally, is effectively zero as long as $\Delta P_{in/out}$ is greater than the peak-to-peak amplitude of $\Delta P_{sd}(t)$. For smaller magnitudes of $\Delta P_{in/out}$, ΔP_{slab} becomes positive for part of the pressure cycle, and therefore does not contribute to the convective entry of radon during that portion of the cycle. If $\Delta P_{sd}(t)$ is modeled by a sine function with maximum amplitude, P_a, the time averaged driving pressure across the slab can be expressed for two pressure ranges as,

$$\begin{gathered} \Delta P_{slab}(t) = \Delta P_{in/out}(t) \\ + \frac{P_a(t)}{\pi} \cos\left[\arcsin\left(\frac{\Delta P_{in/out}(t)}{P_a(t)}\right)\right] \\ -P_a(t) \le \Delta P_{in/out}(t) \le 0 \end{gathered} \tag{4-53}$$

and,

$$\begin{gathered} \Delta P_{slab}(t) = \frac{P_a(t)}{\pi} \cos\left[\arcsin\left(\frac{\Delta P_{in/out}(t)}{P_a(t)}\right)\right] \\ -P_a(t) \ge \Delta P_{in/out}(t) \ge 0 \end{gathered} \tag{4-54}$$

Determination of the value of the convective contribution to the total radon entry rate can be performed for the structure ventilation rate and the average radon concentration in ambient air. The latter quantity was measured as approximately 0.5 pCi/l 19 (Bq/m^3) outside the UFRRH. By

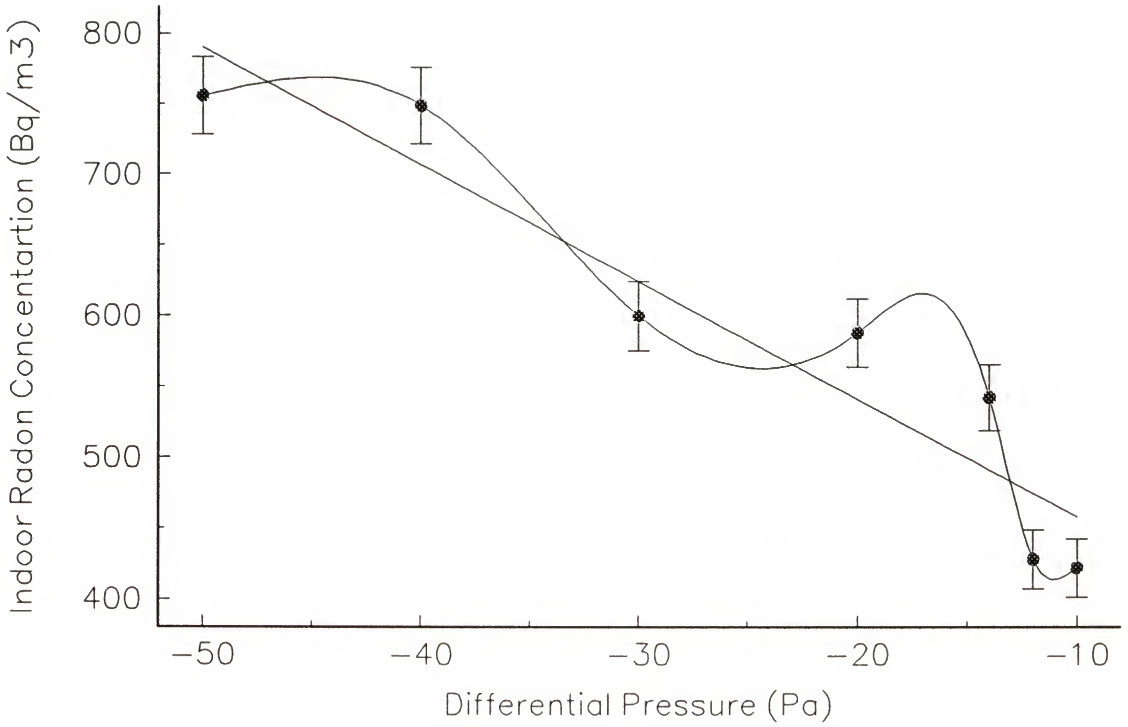

FIGURE 4-62 A: The experimental results and linear fit (R-value =0.95) of the time-averaged indoor radon concentration measurements at the UFRRH for a whole house depressurization range of 10 to 50 Pa.

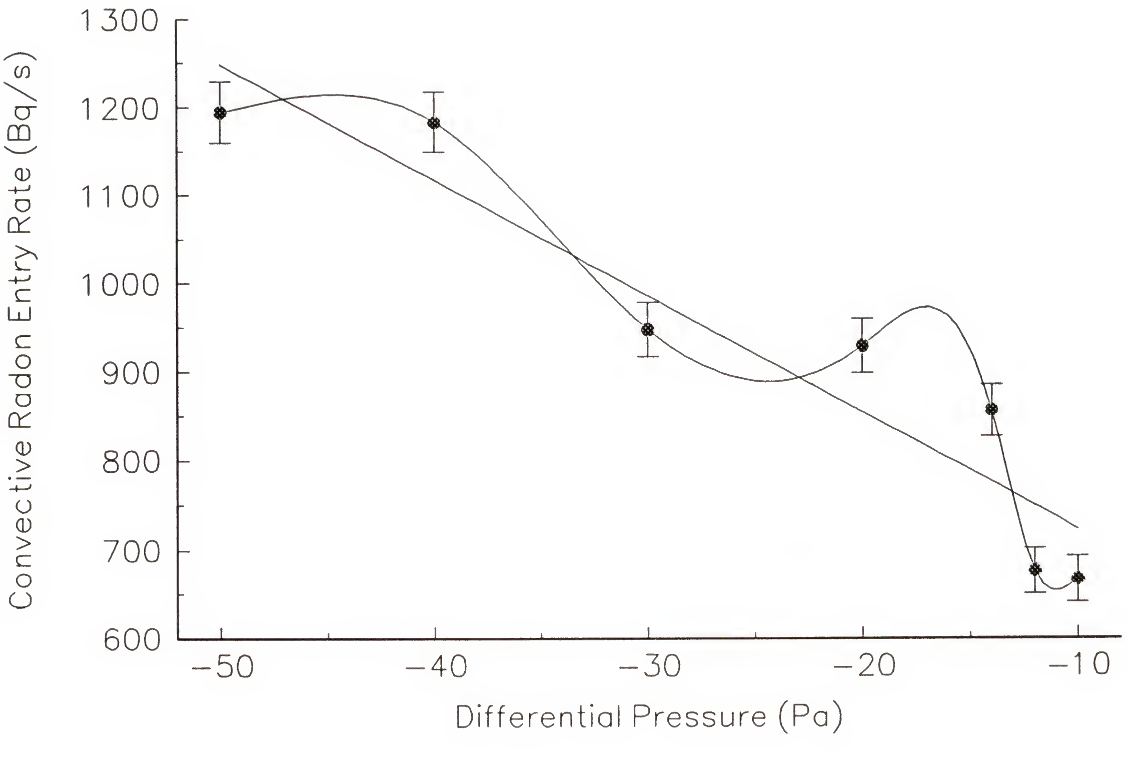

FIGURE 4-62 B: The experimental results and linear fit (R-value =0.95) of the time-averaged radon entry rate measurements at the UFRRH for a whole house depressurization range of 10 to 50 Pa.

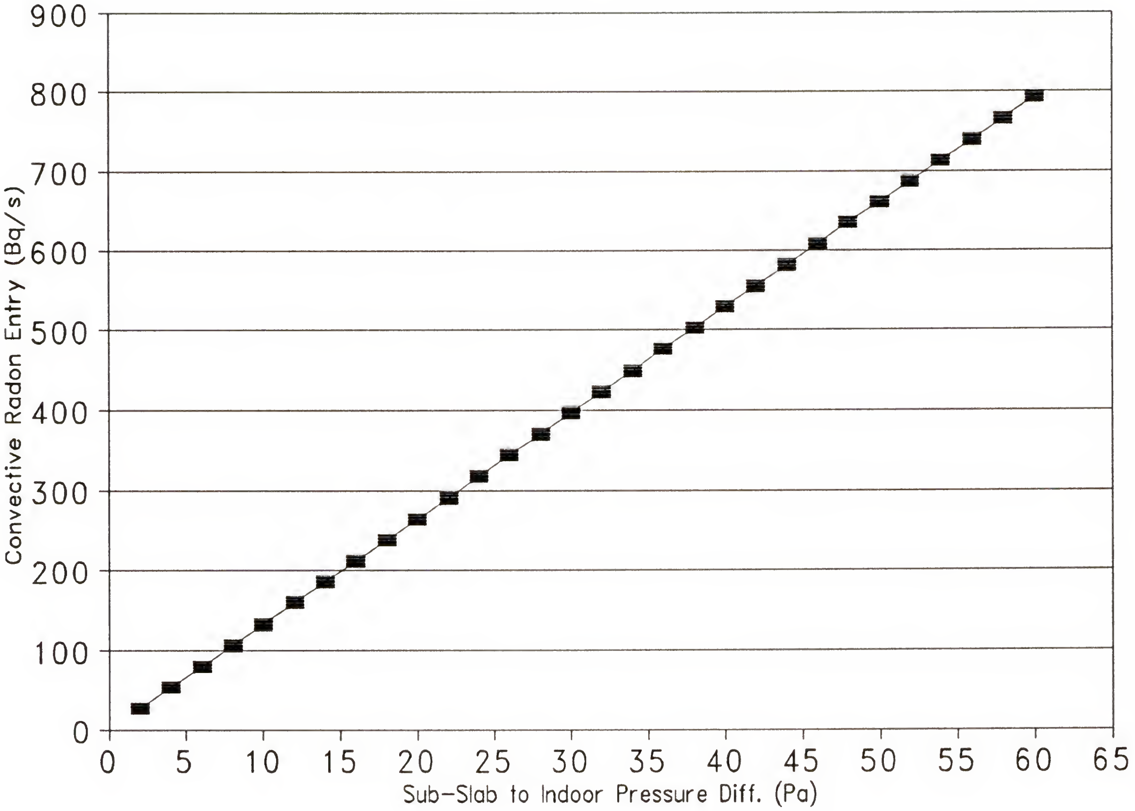

FIGURE 4-63: Predictions of the convective radon entry rate from the sub-structure area into the indoor for interior depressurization of 2 to 60 Pa.

using Equation 4-34,

$$R_{amb} = Q\ C_{amb} = 1.075\ (\Delta P_{in/out})^{0.69} \tag{4-55}$$

where R_{amb} in Bq/s and C_{amb} is the average measured ambient concentration of radon. This entry contribution and the diffusion entry are evaluated for pressure ranges where $\Delta P_{in/out} > P_o > 0$, since $R_{conv} = 0$. R_{amb} is then evaluated from

$$\begin{aligned} R_{diff} = C\ (0.0566\ (\Delta P_{in/out})^{0.69} + 2.0974x10^{-6}) \\ - 1.075\ (\Delta P_{in/out})^{0.69} \end{aligned} \tag{4-56}$$

Figure 4-64 illustrates the calculated diffusive radon entry at the UFRRH from the measured time-averaged indoor radon concentration for pressure differential testing of 2 to 60 Pa depressurization. R_{diff} is assumed to remain constant since the sub-slab radon concentrations remain constant and are much greater than the indoor concentrations.

The total radon entry can be constructed by combining each of the contributing components as,

$$R = 13.23\ \Delta P_{slab} + 1.075\ (\Delta P_{in/out})^{0.69} + R_{diff} \tag{4-57}$$

where R is in Bq/s and ΔP in Pascal. Application of this equation is limited to the pressure regime $|\Delta P_{in/out}| \geq 1$ Pa because the relationship quantifying air infiltration rate is not demonstrated for small magnitudes of $\Delta P_{in/out}$.

For smaller magnitudes of the indoor/outdoor differential pressure, the observed air infiltration rate, Q, becomes smaller than that predicted by Equation 4-34. It is experimentally very difficult to maintain constant pressures with any accuracy for pressures that are this small using the blower door. However, the PFT and CO_2/SF_6 tracer gas measurements were used to provide time averaged air exchange rates in this small pressure regime.

From Figure 4-27 it is apparent that $\Delta P_{in/out}$ naturally fluctuates slightly about zero, providing a driving force for natural indoor/outdoor air exchange (0.076 ACH), although the time average of $\Delta P_{in/out}$ is nearly zero (0.06 Pa). The PFT trace gas provides a time averaged measurement of the air exchange rate from which Q may be determined for conditions where $\Delta P_{in/out}$ fluctuates slightly about zero.

Since expressions for both radon entry and removal (by ventilation) have been developed, utilization of these expressions in Equation 4-48 can be employed in each pressure range to predict the average indoor radon concentration as a function of average indoor/outdoor differential pressure for comparison with the measured indoor radon concentration in Figure 4-20. This model generates the solid line of Figure 4-20 which is in excellent agreement with the experimental data. Using this semi-empirical approach, independent determination of the parameters that might affect the time averaged indoor radon concentration can be performed.

A parametric analysis can be performed using the total radon entry rate equation to evaluate the effect of each driving force on the radon entry rate. Temperature induced pressure differences have been shown to affect the convective

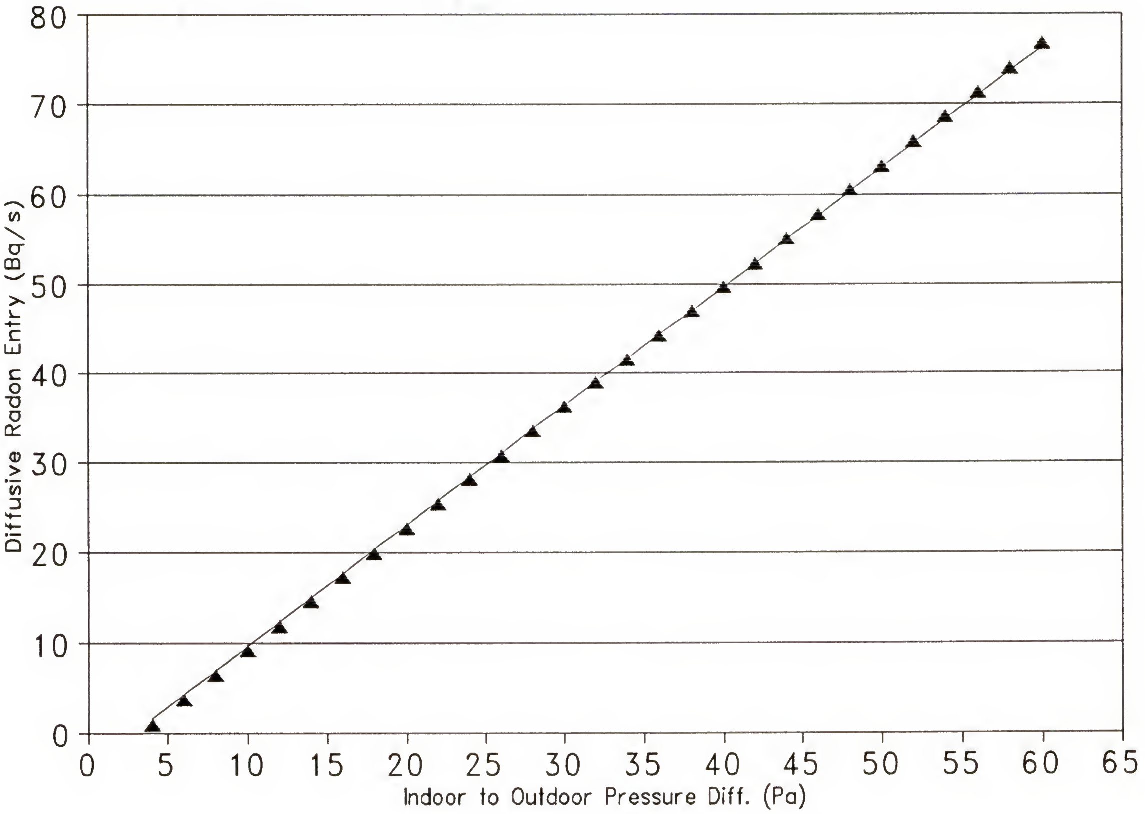

FIGURE 4-64: An illustration of the radon diffusive entry rate calculated from time-averaged indoor radon concentration measurements at the UFRRH.

flow across the structure shell for temperature ranges associated with the UFRRH. If the temperature-induced pressure differentials model (Equation 4-17) is incorporated into the total radon entry expression (Equation 4-57) when the indoor pressure is lower than the sub-slab air volume pressure and the outdoor pressure, then

$$R = 13.32 \left(P_0 \, B \, \frac{T_{ss} - T_{in}}{T_{ss} \, T_{in}}\right) + 1.07 \left(P_0 \, B \, \frac{T_{in} - T_{out}}{T_{in} \, T_{out}}\right)^{0.69} + R_{diff} \tag{4-58}$$

where T_{ss} is the sub-slab air volume temperature and T_{in} is the indoor temperature.

Figure 4-65 illustrates the effect of sub-slab air volume temperature on the total radon entry rate for a weather pattern of indoor temperature equal to the outdoor temperature and less than the sub-slab air volume temperature. Such patterns particularly examine the convective contribution expressed in the first term of the right hand side of Equation 4-58 since the convective entry from the ambient is zero.

Figure 4-66 illustrates the predictions of the indoor/outdoor temperature difference on the total radon entry for a weather pattern produced indoor temperature that is equal to the sub-slab air volume temperature and less than the outdoor temperature. This pattern examines the effect of the second term of the right hand side of Equation 4-58. Figure 4-67 A, B, and C shows the predictions of the time dependent variations of the total radon entry rate influenced by the experimental temperature difference measured between the indoors and sub-slab area. Both cycles are illustrated in Figure 4-43 B.

As seen in Figure 4-67 A only a small radon entry rate was driven by the temperature difference during this particular period of testing when the sub-slab sir volume temperature exceeded the indoor temperature between the 2160 and 2500 minutes in Figure 4-34 B.

Parametric analysis of the wind-induced pressure differences on the total radon entry is restricted to the second term of the right hand side of Equation 4-57. If the wind-induced temperature model is incorporated into Equation 4-57, the following expression results,

$$\begin{aligned} R &= 13.32\ (\Delta P_{slab}) \\ &+ 1.07\ (P_{in} - P_b - 0.5\ \rho\ v^2)^{0.69} + R_{diff} \end{aligned} \qquad (4\text{-}59)$$

where both convective and diffusive entries from the sub-structure area are considered independent of the wind speed. Such conditions exist if the interaction between the outside area and the sub-slab area through the structure wall interface is negligible.

Since the later feature is highly dependent on the particular structure and there is no general consideration that can be employed, and the wind-induced pressure differences at the UFRRH site were negligible, the parametric analysis available from the previous equation was restricted to the second term only. Figure 4-68 illustrates the predictions of the wind-speed effects on the total radon entry rate when the wind blew on the leeward of the structure since the interior will be depressurized in such a case. Figure 4-69 illustrates the predictions of contributions of all possible interaction with the structures for wind speed ranges from 1 to 10 m/s.

Parametric analysis of the temperature-induced and wind induced pressure differentials on the time-averaged indoor radon concentrations can be performed by incorporating both models into the expression in Equation 4-43. The wind-induced pressure differentials yield,

$$C = \frac{13.23\ \Delta P_{slab} + 1.075\ (P_{in} - P_B - 0.5\ \rho\ v^2)^{0.69}{}_{leeward} + R_{diff}}{0.0566\ (P_{in} - P_b - 0.5\ \rho\ v^2)^{0.69}{}_{windward/side} + 8.389x10^{-4}} \tag{4-60}$$

and the temperature-induced pressure differentials yield,

$$C = \frac{13.23\ (0.0477\ P_0\ \frac{T_{ss} - T_{in}}{T_{ss}\ T_{in}}) + 1.075\ (0.0477\ P_0\ \frac{T_{out} - T_{in}}{T_{out}\ T_{in}})^{0.}}{0.0566\ (0.0477\ P_0\ \frac{T_{in} - T_{out}}{T_{in}\ T_{out}})^{0.69} + 8.389x10^{-4}} \tag{4-61}$$

Figures 4-70 A and B illustrate the results of the time-averaged indoor radon concentration predicted by the above two equations for specific configurations.

As evidence in Figure 4-20, the results of applying Equation 4-43 to the range of whole house pressures provided excellent agreement between the model predictions and the

UFRRH experimental data. Since the model provides good agreement with the UFRRH indoor radon concentrations over a large range of air change rates, it can be extended to predictions for other configurations of the structure as well as examining the sensitivity of the predictions to variations in several physical parameters. This analysis provides insight into the performance of structures of similar construction features and radon source terms.

The relative effects of different ventilation configurations, and radon entry mechanisms on the average indoor radon concentration can be evaluated for these structures. Figure 4-71 illustrates the model prediction of average indoor radon concentrations as a function of indoor/outdoor differential pressure for diffusion radon entry rates of 2, 10, and 20 Bq/s. The indoor radon concentrations are not dramatically affected by variations of the diffusive entry contribution. As expected, the largest differences occur near zero indoor/outdoor differential pressure where the air exchange rate is small. This illustrates that changes to the diffusive entry rate of radon will not significantly alter indoor radon concentrations when imbalanced air flows produce air exchange rates greater than 0.3 ACH, the exchange rate corresponding to $\Delta P_{in/out} = \pm 0.5$ Pa.

Figure 4-72 illustrates the model predictions of average indoor radon concentrations as a function of indoor/outdoor differential pressure where the air exchange rate of the

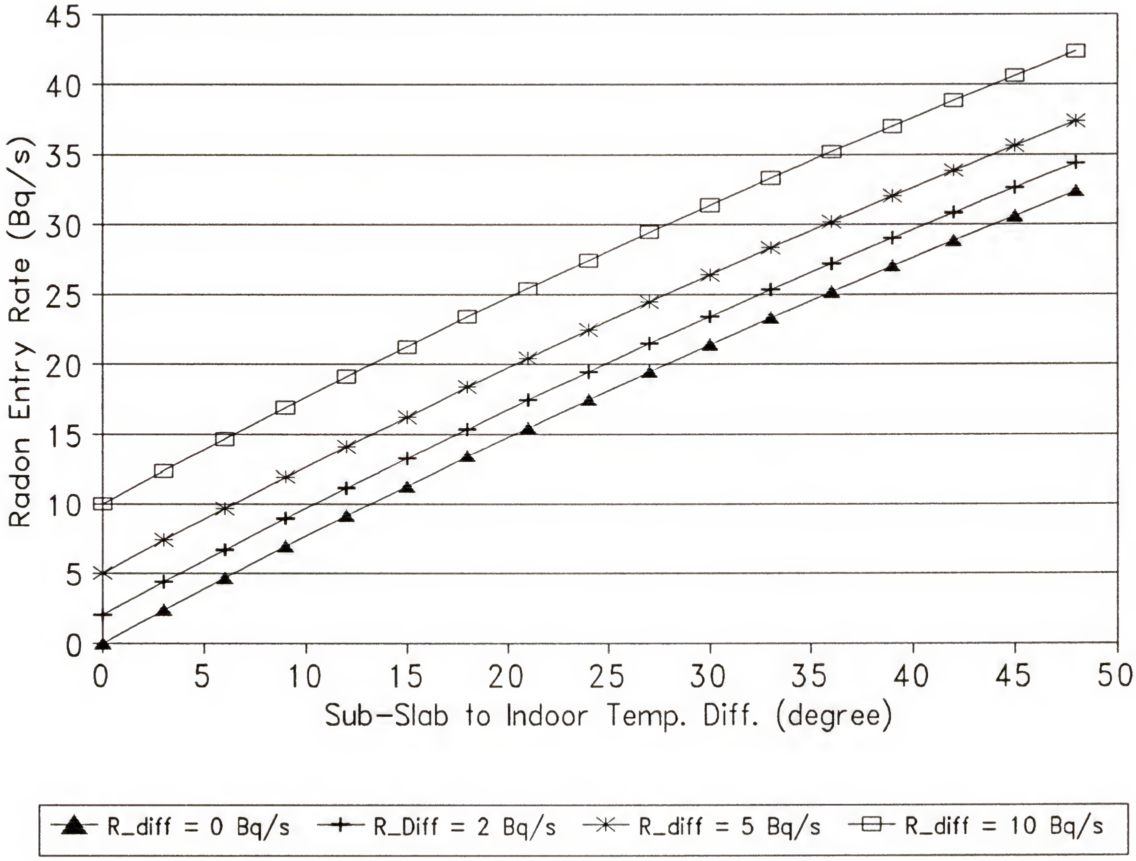

FIGURE 4-65: Predicated effects of temperature difference between the sub-slab temperature and the indoor on the total radon entry rate when the temperature of the indoor environment is less than that of sub-slab area and equals to the outdoor temperature.

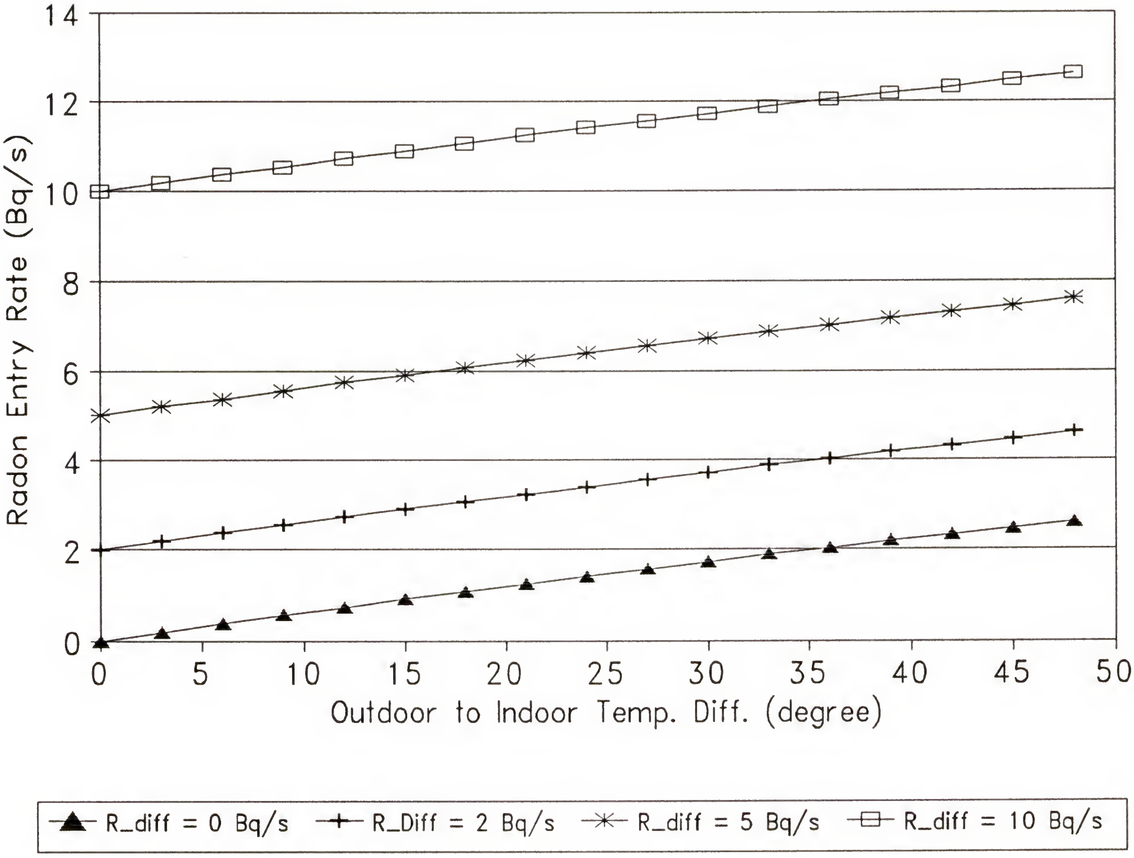

FIGURE 4-66: Predicted effect of temperature difference between the indoor and outdoors on the total radon entry rate when the temperature of the indoor environment is less than that of the outdoors and equal to the sub-slab area temperature.

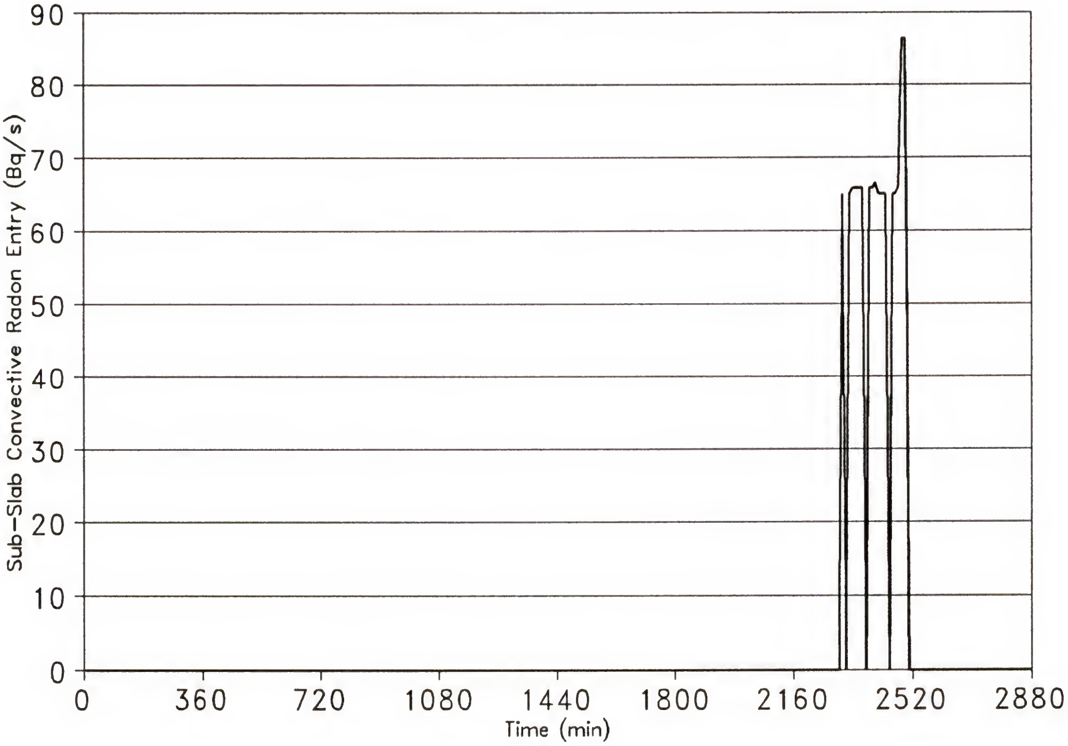

FIGURE 4-67 A: Predictions of the temporal variations of the sub-slab convective contribution at the UFRRH influenced by the temperature difference between the sub-slab and the indoor illustrated in Figure 4-43 B.

structure is manipulated by changing the effective leakage area, ELA (ASTM 1987). This manipulation is equivalent to changing the air infiltration/exfiltration characteristics of the house envelope by opening windows or sealing the house shell. The curves of Figure 4-72 exhibit changes of the ELA by factors of 2, over the range from one-half to four times the observed ELA (ELA_o) of the research structure.

The curves for different ELA's retain a similar shape and the principle features scale approximately inversely proportional to the ELA. This demonstrates how structures with larger effective leakage areas to the outdoors, providing an increased ventilation rate, will have reduced indoor radon concentrations, but that concentrations will continue to peak for neutral indoor/outdoor differential pressures as long as no internal forced air circulation exists.

The discussion thus far has been confined to natural air infiltration processes that result from the pressurization, or depressurization, of a structure. Infiltration air may also be provided while maintaining near neutral indoor/outdoor differential pressure by providing a balanced source of outdoor air to the structure interior. This can be accomplished with HVAC systems having controlled duct ventilation or with an air-to-air heat exchanger. Trace gas measurements at the research house with the HVAC circulation fan operating continuously indicate that the air change rate increases to 0.25 ACH without disturbing the natural variation

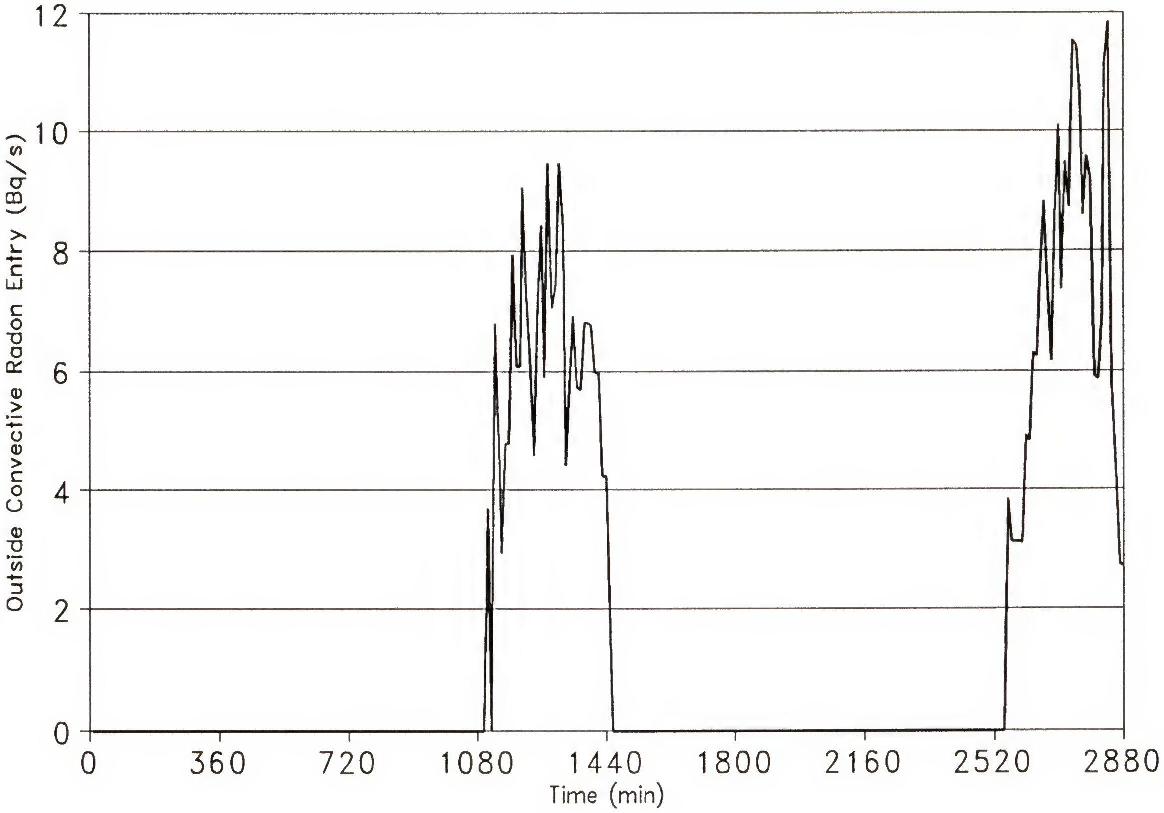

FIGURE 4-67 B: Predictions of the temporal variations of the sub-slab convective contribution at the UFRRH influenced by the temperature difference between the outdoors and the indoor illustrated in Figure 4-43 B.

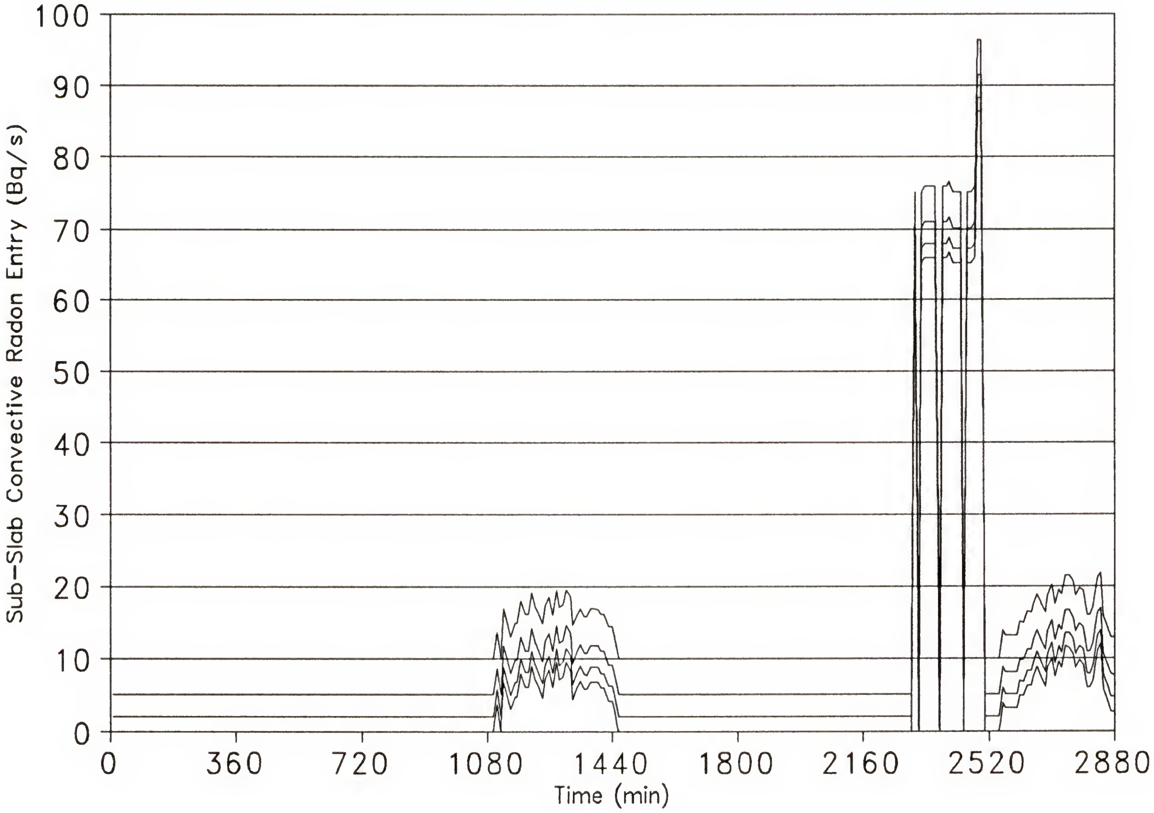

FIGURE 4-67 C: Predictions of the temporal variations of the sub-slab convective entry at the UFRRH influenced by the temperature cycles illustrated in Figure 4-43 B for diffusive entries (top to bottom): 10, 5, 2, and 0 Bq/s.

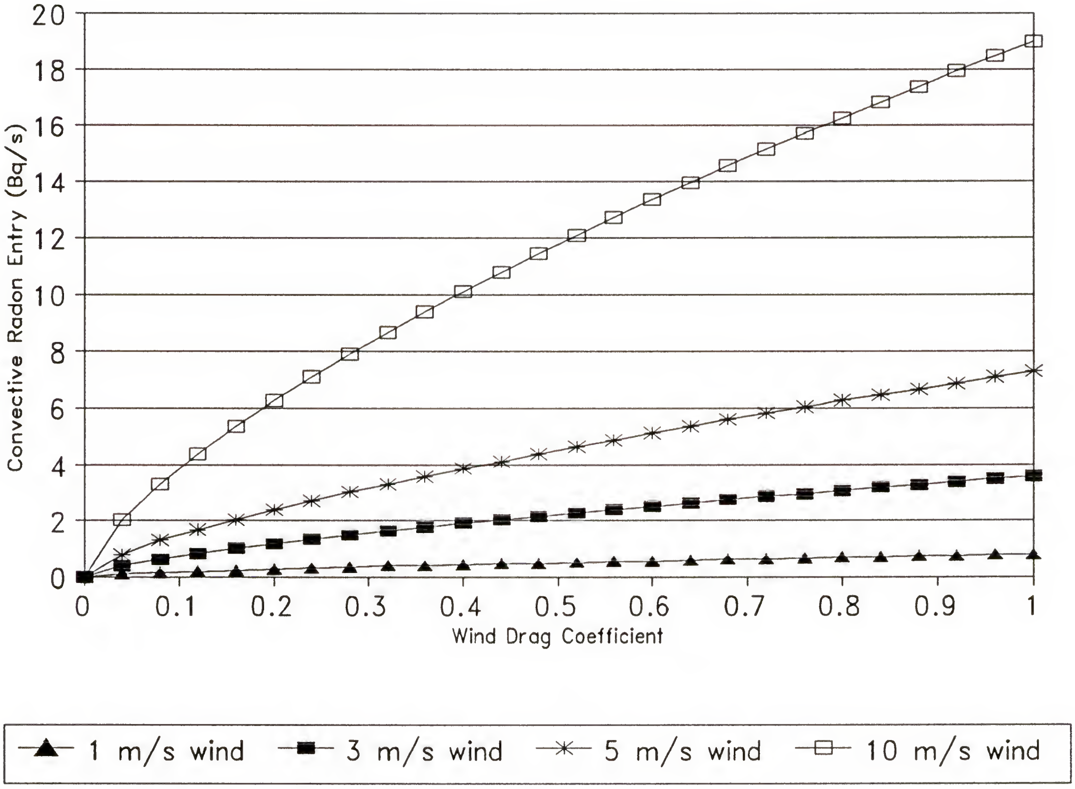

FIGURE 4-69: Predictions of the wind speed effects on the convective radon entry rate for the possible range of interaction between the wind and the structure.

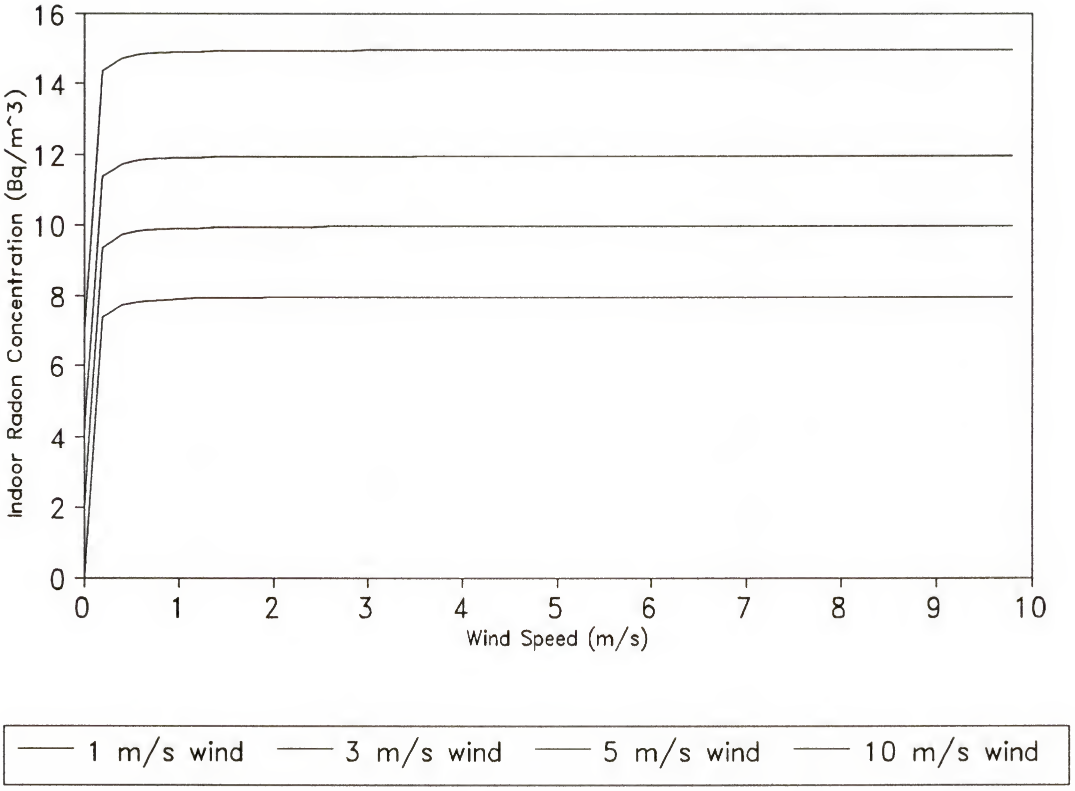

FIGURE 4-70 A: Predictions of the wind effect on the time-averaged indoor radon concentration. Non-wind induced indoor radon concentration components (top to bottom): 7, 4, 2, and 0 Bq/m^3.

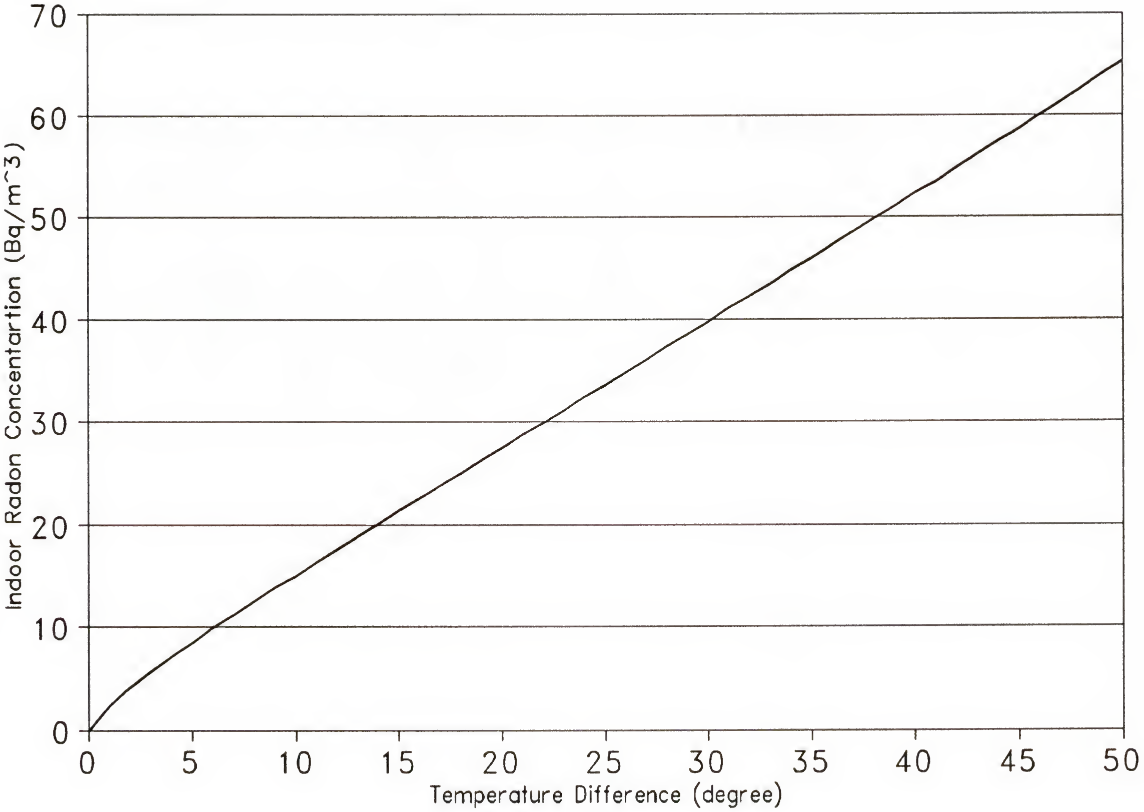

FIGURE 4-70 B: Predictions of the temperature difference effects on the time-averaged indoor radon concentration when the outdoor and sub-slab temperature is 50 °C and the indoor temperature ranges from 0 to 50 °C.

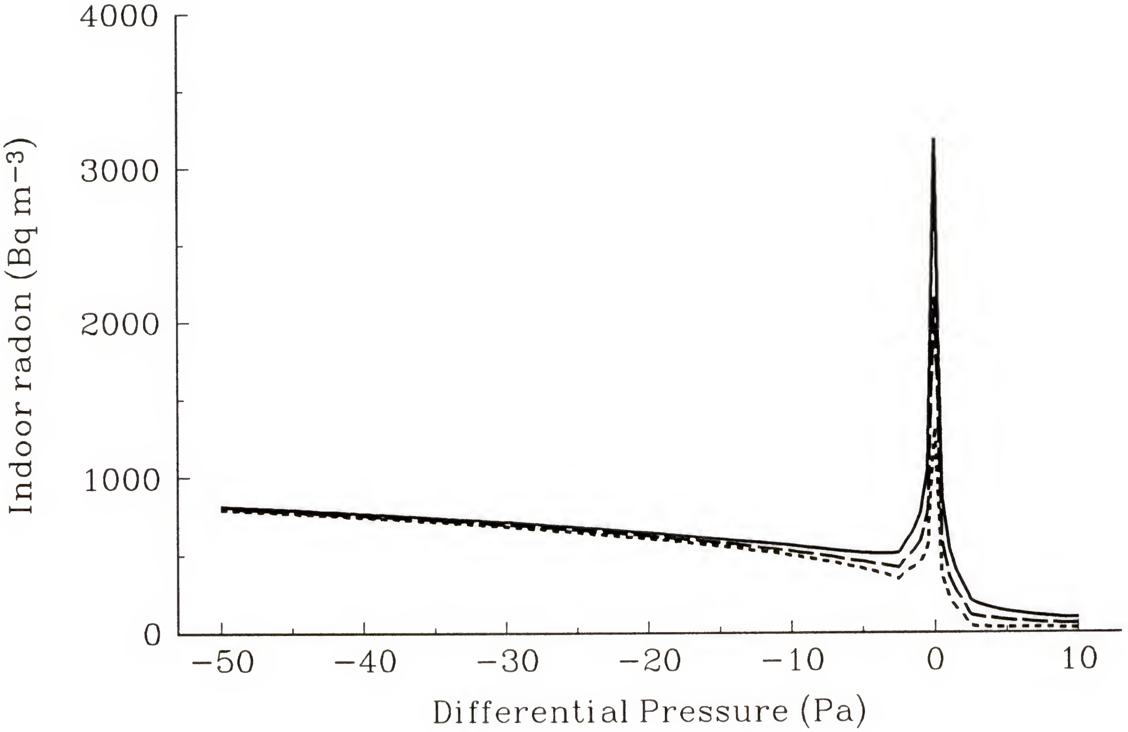

FIGURE 4-71: Predicted time-averaged indoor radon concentrations as a function of whole house pressure for diffusive entry rates (top to bottom curves): 20 Bq/s, 10 Bq/s, and 2 Bq/s.

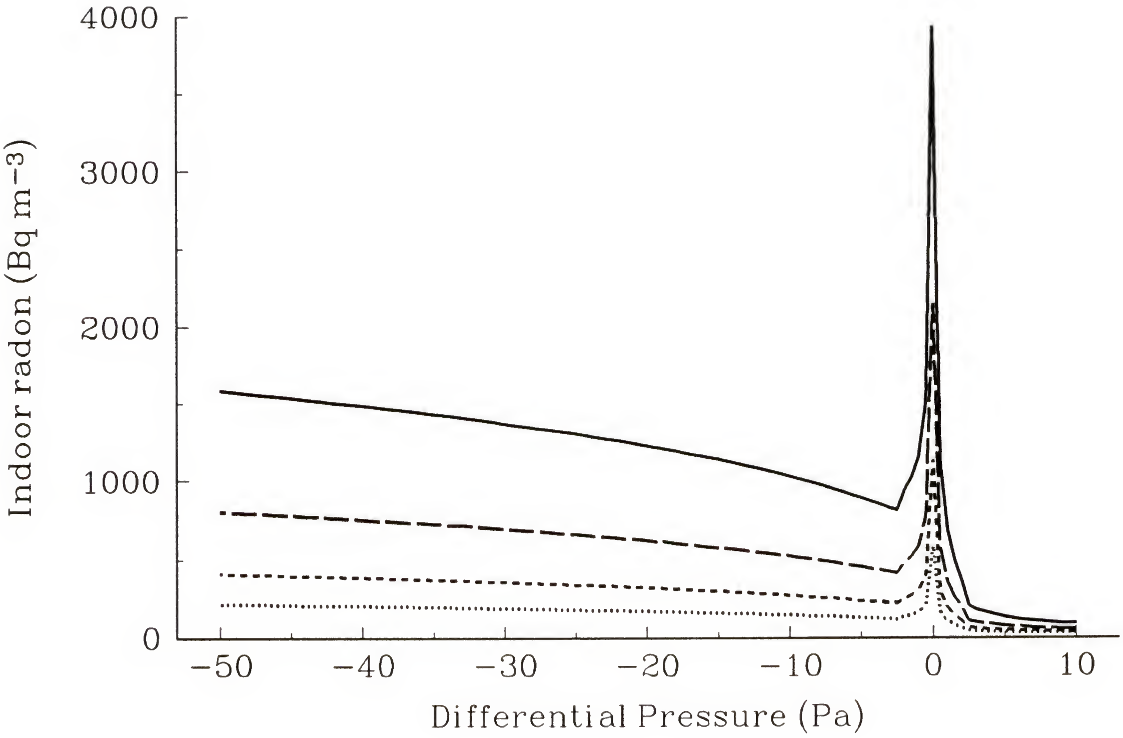

FIGURE 4-72: Predicted time-averaged indoor radon concentrations as a function of whole house pressure for structure effective leakage areas ELA_0 of (top to bottom curves): 0.5, 1, 2, and 4.

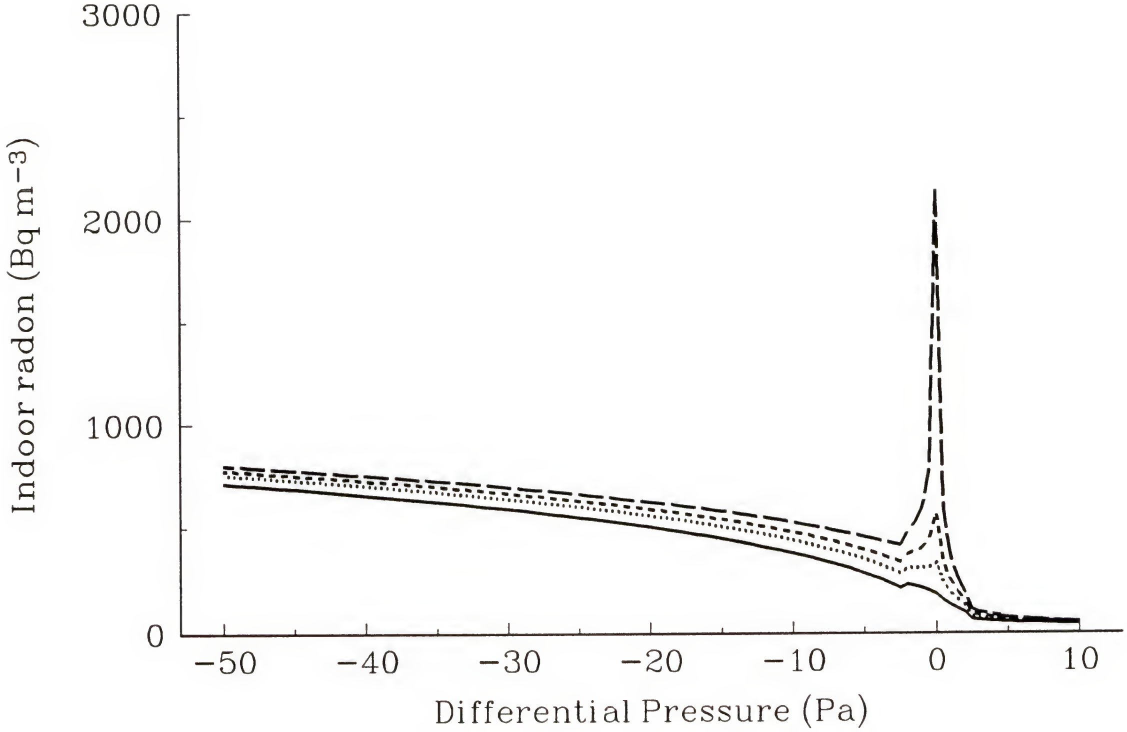

FIGURE 4-73: Predicted time-averaged indoor radon concentrations as a function of increased ventilation rates through controlled duct ventilation of the HVAC system. The system contributions (ACH) are (top to bottom curves): 0, 0.25, 0.5, and 1.

Bq/m^3 at neutral indoor/outdoor differential pressure and the HVAC circulation fan operating continuously. The measured radon concentrations did not change substantially for larger magnitudes of indoor/outdoor differential pressure which is also consistent with the model predictions.

Applications for Predicting and Controlling Long-Term Indoor Radon Concentrations

Long-Term Indoor Radon Concentrations

Prediction of long-term indoor radon concentrations has been a major source of disagreement when some issues of the indoor radon problem are considered. The conflict arises from what is considered practical for testing and the health hazards and liability issues. On one hand, obtaining a long-term measurement of the average indoor radon concentration in a structure by continuous testing for possibly several years (a minimum of one year) is not practical (although it is possible). On the other hand, health and some legal-related actions are based on the annual exposure to indoor radon concentration.

Most of the radon testing utilized commercially is performed over a very short period of time, 48 hours, following the US Environmental Protection Agency short-term testing protocols. Although such testing may be sufficient for determining the need for mitigation action for some cases, using these results to represent the annual indoor radon concentration in the structure can create major debate for marginal cases, estimation of health hazards, and liability related issues. The problem is particularly complex given the known fluctuations of indoor radon concentrations.

Several studies have addressed the issue of predicting annual indoor radon concentration from short-term testing results. Such studies utilized two basic methodologies in approaching the problem. The first methodology uses specific research structures and develops correlations between indoor radon concentrations and other environmental parameters that are simultaneously monitored for a long period of time (a minimum of one year). Then researchers experimentally fit the data and obtain the best representation of indoor radon concentration based on the particular set of data (Hull and Reddy 1990; Reddy et. al. 1990).

The second methodology analyzes large data bases (survey data) related to indoor radon measurement, although they are not particularly designed for this purpose, and tried to obtain general correlations relating indoor radon concentrations to the available parameters in the survey data set (White et. al 1994, White et. al. 1992; Cohen 1990, Roessler et. al. 1990, Steck 1990;). The second approach covers a large number of houses, but there is uncertainty in the results and a lack of experimental control parameters. However, this type of study may provide an indication of the relationship between parameters based on statistical evaluation. The first approach has the advantages of design and control of the experiments and better measurement uncertainty, however, it is restricted to the experimental fit of data of the particular structure.

Neither of these approaches provide a means to explicitly predict the average annual indoor radon concentration from the short term-testing results, but rather provide indications of the trends of annual indoor radon concentrations when other parameters are considered. An approach that provides an explicit relationship between the short-term testing and the actual annual indoor radon concentration has not been developed.

In this section, an analytical method will be utilized to relate the annual indoor radon concentration to the short-term testing results. A mathematical framework is developed, based on the mass balance equation of radon in the indoor environment which facilitates semi-analytical predictions of annual indoor radon levels. This treatment can serve as a tool to establish the general relationship, based on the actual physical processes of entry and removal, between the time-averaged annual level of indoor radon concentration and the short-term testing of the indoor radon concentration.

Starting with the general linear differential equation governing the generation and removal of radon gas in the indoor environment (Equation 4-41), the general solution to this equation was derived using the integrating factor approach as shown in Equation 4-43. This equation represents the expected value of indoor radon concentration (Bq/m^3) at a particular point of time (time stamp) that is measured from a specific time when the solution performed using a specific initial condition of indoor radon concentration. The time stamp of the initial condition is selected to be t=0 representing the start of solution application in the indoor environment. A time period of 1 year (3.1536x10^7 s) is applied from this t=0, and the total period of the solution has 3.1536x10^7 time stamps.

The integration terms in Equation 4-43 need to be evaluated based on indefinite integration and establishing an initial condition which will serve as a reference to the solution in any time stamp point that is located in the range t>0. The constant value C derived by the indefinite integration can be evaluated by using the initial condition. Such evaluation requires solving the integral, and consequently, the relationship between radon entry and ventilation rates with time need to be known. If the latter rates (Bq/s) are constant over the time period of the solution, application of the initial condition, such as $C=C_0$ at t=0 yield,

$$C = -\left[\int e^{\int \left(\frac{Q(t)}{V}+\lambda\right)dt} \frac{R(t)}{V}\, dt\,\right]_0 + C_0 \left[\, e^{\int \left(\frac{Q(t)}{V}+\lambda\right)dt}\right]_0 \qquad (4\text{-}62)$$

where the straight brackets indicate that integral expression between brackets is to be evaluated indefinitely first, then the value of t is set equal to 0.

As seen from Equation 4-62, the term C in Equation 4-43 may have an expression as opposed to a number, however, it is constant over the time period of the solution. The evaluated constant term C in Equation 4-43 is then redefined as C_e indicating that the general solution in Equation 4-43 contains a known constant that has been evaluated at t=0. The general solution to Equation 4-41 including the utilization of initial conditions can then be written as,

$$C(t) = \frac{\int e^{\int \left(\frac{Q(t)}{V} + \lambda\right)dt} \frac{R(t)}{V}\, dt + C_e}{e^{\int \left(\frac{Q(t)}{V} + \lambda\right)dt}} \qquad (4\text{-}63)$$

Equation 4-63 represents the time-dependent indoor radon concentration that can be evaluated at any point in the time spectrum $t \geq 0$. For each time stamp there is a corresponding value for C(t). For example, the indoor radon concentration in the structure, where C_e is evaluated at t=0, at 6 months, 9 months, and one year later are then equal to, $C(t=1.5552\text{x}10^7$ s) , $C(t=2.3328\text{x}10^7$ s), and $C(t=3.1536\text{x}10^7$ s), respectively.

Indoor radon measurements using any system are based on counting a parameter corresponding to the alpha particles that is converted into a concentration of Bq/m^3. The minimum collection time is 1 second. If the system is designed to provide time dependent measurements, then outputs can be reported per time interval that may vary in length or be selected by the user. If the system provides time-integrated measurements, then one value representing the average indoor radon concentration can be extracted at the conclusion of the testing. In both cases, the system accumulates values of the radon concentration in the minimum period of time based on the design.

For the time-dependent systems, the reported indoor radon concentration values collected in time periods can be used to calculate the average indoor radon concentration using a simple arithmetic average or a weighting method such as the reciprocal of the measurement variance. In all cases, the reported average indoor radon concentration is the weighting of the accumulated indoor radon measurements recorded in all the time stamps which occurred during the testing. Such a value, in fact, is the average of the integral of C(t) over the testing period,

$$C_{avg} = \langle\, C(t)\, \rangle = \frac{\int_0^t C(t)\ D(t)\ dt}{\int_0^t D(t)\ dt} \tag{4-64}$$

where D(t) is the time distribution of indoor radon concentration over the period of t=0 to t=t. In all testing purposes, D(t) is the arithmetic average of readings or the weighted average of readings by the reciprocal of the variance. If the first case is selected, Equation 4-64 then becomes,

$$C_{avg} = \frac{1}{T} \int_0^t C(t)\ D(t)\ dt \qquad (4\text{-}65)$$

where T=t-0, and equal to the total number of time stamps in the testing period. For example, if the testing system is set to calculate indoor radon concentration based on 1 second measurement intervals, and the test was performed from noon the first day to noon the third day of the seven month after t=0, then the average indoor radon concentration reported by the measurement is,

$$\begin{aligned} C_{avg} &= \frac{1}{t_2 - t_1} \int_{t_1}^{t_2} C(t)\ dt \\ &= \frac{1}{1.5768x10^7 - 1.55952x10^7} \int_{1.55952x10^7}^{1.5768x10^7} C(t)\ dt \end{aligned} \qquad (4\text{-}66)$$

where there is $1.728x10^5$-time stamps of 1 second during this 48-hour testing period.

A measurement time interval may be reported for a period greater than one second by using a simple conversion. If the measurement is reported in a one hour period, then the previous example will contain 48 readings and the averaging will be performed on the 48-hour testing period. However, conversion will need to be made during evaluation of the integral in order to maintain the correct units since the components of C(t) are the radon entry and removal rates which are reported in Bq/s.

It is important to note that the following treatment provides means not only to estimate the averaged indoor radon concentration over the testing period but also to relate the latter to the particular time of the year. To facilitate this capability, the ratio of the indoor radon concentration reported by a testing period, $(C_{avg})_{ST}$, performed during a particular time in the year (T_x, T_y) to the average indoor radon concentration over the whole year, $(C_{avg})_{LT}$, can be estimated as,

$$\frac{(C_{avg})_{ST}}{(C_{avg})_{LT}} = \frac{\frac{1}{T_y - T_x}\int_{T_x}^{T_y} C(t)\ dt}{\frac{1}{T}\int_{0}^{T} C(t)\ dt} \qquad (4\text{-}67)$$

$$T > T_y > T_x$$

where T is the long-term length of time (one year for annual estimation),

T_y is the time stamp representing the end of the short-term testing period, and

T_x is the time stamp representing the beginning of the short-term testing period.

Equation 4-67 establishes the relationship between the average indoor radon concentration measured over a short-term testing period in a random segment during the year and the time-averaged annual indoor radon concentration. It should be noted that Equation 4-67 establishes the described relationship independently from how long and when the short-term testing occurs during the year.

If the indoor radon concentration over the year is constant, then Equation 4-67 will return a value of 1 despite how long and when the short-term testing is performed. For complete evaluation of the equation, the time distribution of indoor radon concentration, particularly the entry and removal rates, needs to be known. If those expressions (Equations 4-44, 4-45) are incorporated into Equation 4-67 then,

$$\frac{(C_{avg})_{ST}}{(C_{avg})_{LT}} = \frac{\frac{1}{T_y - T_x}\int_{T_x}^{T_y}\left[\frac{\int e^{\int(\frac{Q(t)}{V}+\lambda)\,dt}\,\frac{R(t)}{V}\,dt + C_e}{e^{\int(\frac{Q(t)}{V}+\lambda)\,dt}}\right]_{T_x}^{T_y} dt}{\frac{1}{T}\int_{0}^{T}\left[\frac{\int e^{\int(\frac{Q(t)}{V}+\lambda)\,dt}\,\frac{R(t)}{V}\,dt + C_e}{e^{\int(\frac{Q(t)}{V}+\lambda)\,dt}}\right]_{0}^{T} dt}$$

(4-68)

The general approach to applying the relationship above between the short-term testing result and annual indoor radon concentration is to estimate the right hand side of Equation 4-68 using the previously developed expressions for radon removal and entry rates. After the right hand side of Equation 4-68 is evaluated, the long-term annual indoor radon concentration can be calculated from,

$$(C_{avg})_{LT} = \frac{(C_{avg})_{ST}}{RHS} \qquad (4\text{-}69)$$

where RHS is the numerical value of the right hand side of Equation 4-68.

The best results of estimating this ratio are obtained by performing the integration when the time distribution functions of R(t) and Q(t) are available. The latter case corresponds to time interval that asymptotically approaches zero. Actual measurement must have a time interval greater than zero and the minimum known interval is 1 second. Therefore, estimations of the integral of Equation 4-68 can be accurately performed using the actual value of the variable (R and Q) at each of the time step. The time step is therefore the actual time interval used during the measurement. Smaller time intervals will produce better results.

The discrete nature of the variables in the above mathematical framework allow an estimation of the integral of indoor radon concentration such as,

$$\int_{T_x}^{T_y} C(t)\; dt \equiv \sum_{i=T_x}^{T_y} C_i \qquad (4\text{-}70)$$

where i is an incremental index representing the time stamp where a measurement value is reported. Incorporating the integral equivalent in Equation 4-70 into Equation 4-67 yields,

$$\frac{(C_{avg})_{ST}}{(C_{avg})_{LT}} = \frac{\dfrac{T}{T_y - T_x}\left[\sum_{i=T_x}^{T_y} C_i\right]}{\left[\sum_{i=0}^{T} C_i\right]} \qquad (4\text{-}71)$$

The time term of the above equation is known. Components which drive the indoor radon concentration (C) need to be known (measured) during the long-term period to be estimated in a time interval equal to the time interval of the short-term measurement performed during a particular time of the year in that year.

Components of indoor radon concentration were modeled and discussed in the previous section. The total radon entry rate of Equation 4-57 for the above application during the short-term testing can be evaluated as,

$$R = (\frac{1}{n\delta t}\ [13.23 \sum_i^n \Delta P_{slab} + 1.075\ (\sum_i^n \Delta P_{in/out})^{0.69}) + R_{diff} \qquad (4\text{-}72)$$

where δt is the measurement time interval, and n is the number of measurements during the testing period. The same treatment is utilized for the long-term period (1 year) but n is replaced by m which represents the number of measurements during the year.

Pressure differentials that may contribute to Equation 4-72 are the pressure differences that drive the convective radon entry from the sub-structure area into the indoor and from the ambient into the outdoors. Expressions and analysis for such driving forces have been developed in previous sections of this work. Convective entry from the sub-structure area into the indoor may be derived from the semi-diurnal barometric pressure variations (Equation 4-6), the temperature difference between the sub-slab area and the building interior (Equation 4-17) and wind blowing that causes interior depressurization (Equation 4-12). Radon convective entry from the sub-slab area is then,

$$R_{conc}^{ss} = 13.23\sum_i [([P_b(i+\Delta i)-P_b(i)]e^{(-\frac{\Delta i}{T_R})} + C_w(P_{in}(i)-P_b(i) + 0.5\rho v(i)^2) + 0.0477P_0(\frac{T_{ss}(i)-T_{in}(i)}{T_{ss}(i)T_{in}(i)})] \qquad (4\text{-}73)$$

Radon convective entry from the ambient may be driven by the temperature difference between the outdoor and the indoor and the wind blowing that causes interior depressurization. Therefore this entry is calculated by,

$$R_{conc}^{amb} = 1.075 \sum_i [C_w(P_{in}(i)-P_b(i)+0.5\rho v(i)^2) + 0.0477P_0(\frac{T_{out}(i)-T_{in}(i)}{T_{out}(i)T_{in}(i)})]^{0.69} \qquad (4\text{-}74)$$

Radon removal rate contributes to the reduction of indoor radon concentrations and is derived from the temperature difference between the indoor and the outdoor and wind blowing on the structure which pressurizes the interior. The radon removal rate for this application can be calculated by the same manner as the radon entry rate as,

$$Q = 0.0566 \sum_i [C_w(P_{in}(i)-P_b(i)+0.5\rho v(i)^2) + 0.0477P_0(\frac{T_{in}(i)-T_{out}(i)}{T_{in}(i)T_{out}(i)})]^{0.69} \qquad (4\text{-}75)$$

Radon diffusive entry is independent from the above driving forces and needs to be estimated for this application. If Equations 4-73, 4-74, and 4-75 are integrated into Equation 4-71, the fundamental expression relating the short-term time-integrated measurement of indoor radon concentration and the long-term annual time-averaged indoor radon concentration is produced. A year's worth of temperature, wind speed, and barometric pressure measurements are needed for this application. Application of the above mathematical framework was performed to estimate the annual indoor radon level during one year period May 1991 to May 1992 at the UFRRH and compare it with the short-term testing performed under neutral pressure conditions. The predicted time-averaged indoor radon concentration is 1539.2 Bq/m^3 (41.6 pCi/l), while six short-term tests produced results that differ from the estimated annual value by a maximum factor of approximately 1.6.

Data required to perform estimation of the time-averaged annual indoor radon concentration are available from the National Weather Information Center operated by the Federal Aviation Administration. All the above data are collected on an hourly bases in most of the cities at the airport locations. The diffusive component of radon from the sub-structure area into the indoor can be estimated or ignored if the convective flow is dominant, depending on the soil properties and structure features. Indoor and sub-slab temperature can also be estimated if they are not available, depending on the general weather pattern in the area. This application provides a significant tool to predict the time-averaged annual indoor radon concentration used for health hazard estimations and legal issues from the wide spread practice of short-term (48-hour) testing of indoor radon concentration.

A System Design for Controlling Indoor Radon Concentrations

Previous results have shown that highest time-averaged indoor radon concentrations for a slab-on-grade structure occur when the structure experiences neutral pressure conditions. Experimental evidence has been provided through the utilization of the University of Florida Radon Research House (UFRRH) showing that semi-diurnal atmospheric pressure variations are responsible for continuous pumping of radon-rich soil gas into the structure which elevates indoor radon concentrations.

The application of the basic time-averaged indoor radon concentration model has shown that manipulation of the house air change rate per hour may provide significant reduction in the indoor radon concentration. Increased building pressure has long been identified as an effective technique to change indoor radon concentrations. However, this technique is not always practical. House depressurization contributes to increased radon entry rates by increasing the pressure-driven flow of radon-containing soil gases into the interiors.

Typical sources of house depressurization that have previously been investigated include wind and temperature effects, stack effects, and mechanical depressurization of a structure by household appliances including heating, ventilating and air-conditioning (HVAC) systems (Nazaroff et. al. 1988, Nero 1988, Nazaroff et. al. 1987).

The temperature-driven differential pressure model suggests that temperature-induced pressure differences can be a significant influence on radon driving forces and consequently the indoor radon concentrations under particular configurations associated with the utilization of the HVAC system. The effects of air infiltration rates, that are governed by the differential pressure across the structure shell, on indoor radon concentrations can be attributed to the exchange and dilution of indoor radon with ambient air having much lower radon concentrations.

For the development of the house dynamic interaction system design, integration of the previously developed radon driving force model into the temperature-induced pressure difference model needs to be performed to calculate indoor radon driving forces associated with the HVAC system operation under different environmental conditions and heating and cooling loads.

Mathematical treatments are also needed to reduce the expressions into a single control design equation associated with the ventilation of the HVAC system. The control design equation then will be employed in the process of developing the two designs, mechanical and electronic control, that can reduce indoor radon concentrations.

Indoor/outdoor pressure differences are produced by a calibrated-fan, Minneapolis blower door, over a range of 2-50 Pa; and the HVAC positive ventilation system over a range of 0-3 Pa. These operations are also utilized to quantify infiltration air and air exchange rate for the house using the ASTM standard blower door protocol (ASTM 1987). Supply and return duct flow rates are performed using a flow hood in addition to the air flow transducers that are integrated into the Metrabyte system for each experimental configuration.

All the exterior pressure ports (for barometric pressure and those penetrating the walls) are covered by a perforated, hollow sphere to dampen rapid pressure variations caused by wind gusts. The measurements between the outdoor and the sub-slab are carried out utilizing a T-type connector to one of the sub-slab points. The transmitters are connected to the Metrabyte system using an Omega switch board to provide flexibility during calibrations or to run the measurements at specific slab points as needed.

The experimental period of 96 hours and a measurement interval of 60 seconds, averaged every 600 seconds was used to perform the measurements. These test periods provided suitable time to monitor the transient response in the house system as well as after the house system had stabilized. The same experimental protocol was followed for each experimental period. Experiments typically consisted of performing zero checks on all instrumentation, setting the desired differential pressure using the blower door/HVAC system, and monitoring the device outputs over the duration of the experiments.

Pressure differentials between the indoor and outdoors, $\Delta P_{i/o}$, of values less than 1 Pa are usually associated with neutral pressure conditions when the other sources of mechanical pressurization or depressurization do not exist. Semi-diurnal atmospheric tidal barometric pressure variations are responsible for driving radon-rich soil gas from the sub-structure area into the interior and consequently causing elevated indoor radon concentrations under neutral pressure conditions.

The sub-slab soil system below the foundation limits soil gas velocities and causes the sub-slab air volume pressure to experience a delayed response to changes in atmospheric pressure. These transient effects of barometric pressure changes on radon entry and concentrations are being increasingly recognized as an important driving force of radon into residential structures.

Careful examination of Figure 4-20 suggests that slightly pressurized or depressurized conditions could provide significant a reduction in indoor radon concentrations. A particular pressure range, between -10 to 10 Pa, seems to minimize indoor radon concentrations, with more reduction being observed on the pressurized side. This critical range of indoor pressure conditions is usually associated with the utilization of HVAC systems and some other household appliances.

Hintenlang and Al-Ahmady have shown how the naturally occurring semi-diurnal radon entry can be reduced by HVAC operation (Hintenlang & Al-Ahmady 1993). They have developed radon entry and concentration models to simulate the operation of the HVAC system in residential structures. A previous radon concentration model that successfully predicted the average indoor radon concentrations was being used to study the effects of several parameters on radon entry.

Simulations were performed for different diffusion entry rates, different air exchange rates that were developed utilizing the HVAC system ventilation and changing the structure's effective leakage area. It has been demonstrated that increasing the house ventilation rate by increasing the effective leakage area of the house shell does not reduce indoor radon concentrations as effectively as increasing house ventilation rates by controlling duct ventilation associated with the HVAC system (Hintenlang & Al-Ahmady 1994).

Further investigations revel that controlled duct ventilation applications that provide positive ventilation, in which the indoors is slightly pressurized relative to the outdoors, provides a better reduction of indoor radon concentrations compared with balanced ventilation (Hintenlang et. al. 1993). Figure 4-73 illustrates the reduction of indoor radon concentration associated with controlled duct ventilation for several air exchange rates.

In order to utilize these findings, several considerations were taken into account to develop a design control equation that can be used in controlling the positive ventilation in the HVAC system. The system required to provide and perform this control must be a pressure sensitive device that un-balances the HVAC system according to pressure considerations.

Temperature effects, differential pressure across the slab, barometric pressure and the differential pressure between the indoor and outdoor have to be considered in the design of a pressure sensitive HVAC Unbalanced Pressurization Controller (HUPC) system for minimizing indoor radon concentrations.

It is important to note that the temperature differences between the indoor and outdoor could seriously disturb the indoor pressure patterns over a small pressure span around zero Pa. Figure 4-27 shows the time variance of differential pressures between indoors and outdoors and between the indoor and sub-slab area. The two differential pressure responses do not appear to be coupled to each other.

The pressure differential response between the indoors and outdoors demonstrates a diurnal cycle with a peak amplitude of about 0.4 Pa. This cycle is attributed to the varying temperature differences between indoor and outdoor environments that occur throughout the day. Under neutral pressure conditions these responses are small in magnitude because temperature differences between the indoor and outdoor remain small during the time when these experiments were performed. The house is also well sheltered from the wind.

Pressure differences induced by winds across the structure could have a profound influence for the critical indoor pressure span around zero. However, the minimal contribution of wind effects during the performance of these experiments are verified by the weather station mounted on the structure and the indoor/outdoor differential pressure monitors mounted on two opposite sides of the house.

The anemometer indicated wind speeds less than 0.18 m/s greater than 90% of the time and the indoor/outdoor pressure responses measured across the different walls were observed to be nearly identical in phase throughout the experimental periods. This demonstrates that the influence of wind-induced imbalances during these experiments is negligible.

Al-Ahmady and Hintenlang have linearly combined the pressure differences between the indoor and outdoor that are induced by indoor/outdoor temperature differences. Their studies provide experimental evidence and theoretical modeling that lends support to the diurnal temperature induced pressure differentials between the indoor and outdoor under neutral pressure conditions and other conditions associated with the operation of the HVAC systems.

Figures 4-49 A and 4-50 A illustrate the temporal variation of pressure differences induced by the temperature differences between the indoor and outdoors over different time periods at the UFRRH under moderate temperature and low wind weather conditions. It has been demonstrated that the pressure differences induced by temperature differences, between indoor and outdoors, are directly proportional to both the magnitude of the temperature difference and the average temperature between the indoor and outdoor (Al-Ahmady & Hintenlang 1993a).

The blower door measurements are utilized to characterize the required volumetric flow rate that must be induced to maintain the interior at a given pressure measured relative to outdoors. These measurements are performed at selected time intervals when the indoor and outdoor temperatures are approximately equal and constant.

These measurements provide indoor/outdoor pressure differences that are only developed by the induced air and are isolated from the temperature induced pressure differences. The measurement procedure follows the standard ASTM blower door testing protocol (ASTM 1987) and the empirical fit to the collected data provides,

$$\Delta P_{i/o,I} = \exp[1.44 \ln(Q/79.76)] \qquad (4\text{-}76)$$

where $\Delta P_{i/o,I}$ is the pressure differential generated between the indoor and outdoor generated by the induced fresh air (Pa), and Q is the induced fresh air volumetric flow rate (m^3/s). Figure 4-74 shows a small portion of Figure 4-59 A illustrating the relation between the pressure differences and the flow rate over a small range of the house pressure conditions. The relationship can be approximated as a straight line and can be extrapolated to smaller pressure differences that simulate the HVAC operation.

Experimental verifications using the pressure transducers that are distributed over the slab indicate similar values of induced indoor pressure. Equation 4-76 is also independent of the position where the induced fresh air originate, this permits the utilization of Equation 4-76 for the induced fresh air developed by the HVAC system.

The pressure differences between indoor and outdoors that are induced by temperature differences, $\Delta P_{i/o,T}$, are previously modeled based on a linear approximation of the weakly exponentially dependent pressures between two different temperatures under hydrostatic equilibrium and given in Equation 4-17 as,

$$\Delta P_{i/o,T} = P_o\ C\ [(T_i - T_o)/T_i T_o] \qquad (4\text{-}17a)$$

where P_o is the atmospheric pressure at sea level (10^5 Pa). C is a constant which has been previously calculated as 0.0477 K (Al-Ahmady & Hintenlang 1993a), and T_i and T_o are the indoor and outdoor temperatures (K), respectively.

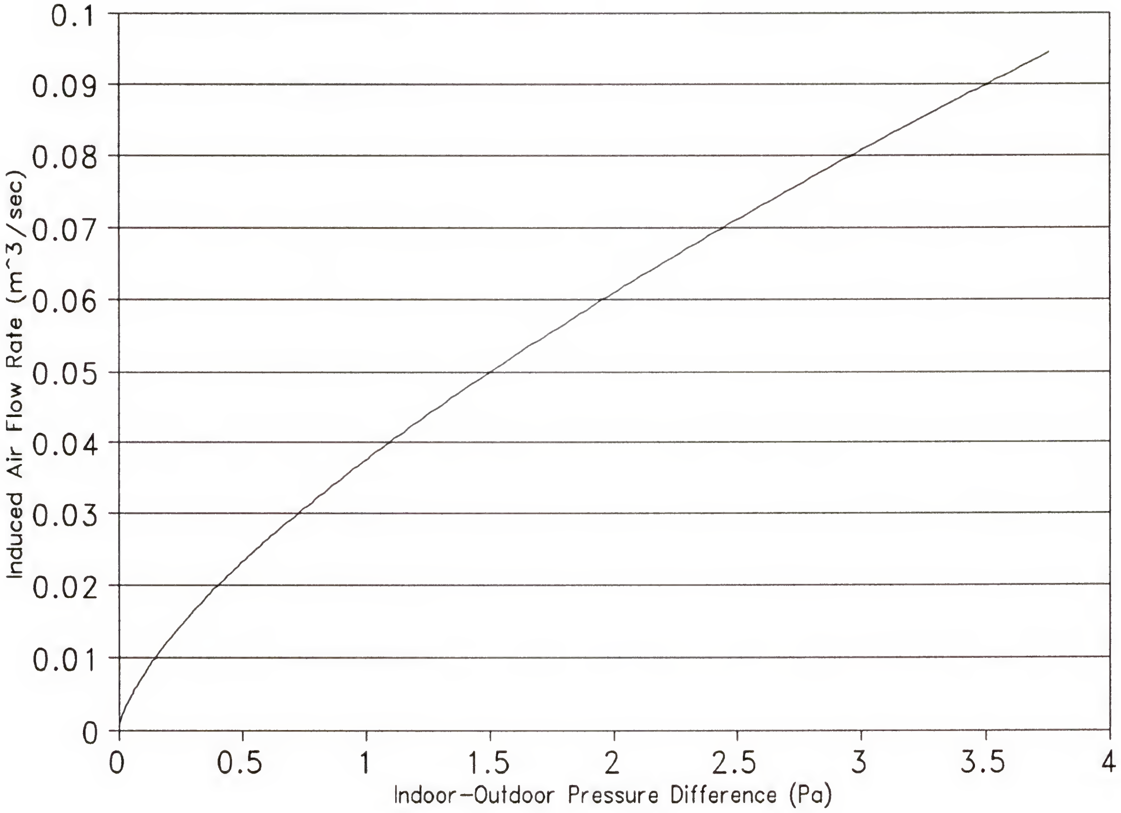

FIGURE 4-74: Induced fresh air flow rate as a function of the UFRRH indoor/outdoor pressure differentials.

If pressure differences due to the induced fresh air and temperature are linearly combined with their partial weights normalized to one, the indoor/outdoor pressure differential is then,

$$\Delta P_{i/o} = \Delta P_{i/o,I} + \Delta P_{i/o,T} + B\ \Delta P_{i/a} \tag{4-77}$$

where $\Delta P_{i/a}$ is the pressure difference between the indoor and attic zones. B is a constant that characterizes the partial contribution of pressure differences that might exist between the attic and indoor zone due to leakage in the HVAC duct system and different temperature zones. Leakage in the supply duct system in the attic area can depressurize the house interior compared to the situation when no leakage exists.

The attic area may be pressurized if the leakage rate exceeds the rate of exfiltrated air into the outdoors through the attic vents. A portion of this air may return to the interior in proportion to the constant B. The value of the constant B is therefore dependent on the characterization of the attic area interface with the interior and the ceiling integrity for an individual structure.

This contribution can be large especially for cases when duct leaks are not sealed or large gaps exist between the ducts and registers. This contribution is highly dependent on duct system installation practices as well as different attic zone temperatures. The UFRRH duct system, including supply and return, are well sealed to minimize the leakage into and from the attic area.

Differential pressure transducers monitoring the pressure difference between the indoor and attic area indicate a minimal difference that is attributed to temperature differences between the zones. Visual inspection of the house/ceiling integrity indicates that B should be very small. Therefore, the third term of Equation 4-77 is assumed to be approximately zero for this application.

Pressure differentials across the structure slab can be estimated as $\Delta P_{slab}=P_{ss}-P_{in}$, and pressure differences between the indoor and outdoors can be written as $\Delta P_{i/o}=P_{in}-P_{out}$. The outdoor pressure is the barometric pressure, P_b, and therefore the indoor pressure becomes,

$$P_{in}=\Delta P_{i/o}+P_b \tag{4-78}$$

The sub-slab air volume pressure, P_{ss}, was modeled as an exponentially damped response to the changes in barometric pressure. The delay in the sub-structure soil volume is a function of the geometric location under the slab.

For the current application, a geometric location that produces the maximum differential pressure across the slab is chosen, which is usually located near the center of the slab. The sub-slab air volume pressure can be calculated by,

$$P_{ss}=P_b-[P_b-P_{ssp}]\exp(-\Delta t/t_m) \tag{4-78}$$

where P_{ssp} is the sub-slab air volume pressure at the previous time interval, Δt, that depends on the barometric pressure changes, and t_m is the maximum delay time of the sub-structure soil system pressure to equalize with the barometric pressure. Utilizing Equations 4-77 and 4-78, the pressure differential across the slab can be calculated as,

$$\Delta P_{slab}=(P_{ssp}-P_b)\exp(-\Delta t/t_m)-\Delta P_{i/o} \tag{4-79}$$

This pressure differential is the major contributor of pressure driven radon entry, the convective component of radon transport into structures. Other radon entries components can be represented by the diffusion and convection from ambient into indoor. The latter two components are small compared with the convective transport from the sub-structure area into the interior. The minimal contributions of these two components are offset by the utilization of a safety design factor in the HUPC system.

Implementing Equation 4-79 as the design control parameter in the process of developing the required quantity of induced fresh air under positive ventilation. The design requires that,

$$\Delta P_{i/o} >= \Delta P_{slab} \tag{4-80}$$

and therefore,

$$\Delta P_{i/o} = D_c >= 0.5\ f_s\ (P_{ssp} - P_b) \exp\ (-\Delta t/t_m) \qquad (4\text{-}81)$$

where f_s is the safety design factor and has a value ≥ 1.0, and D_c is the design control parameter.

It is important to note that P_{ssp} is the previous sub-slab air volume pressure prior to the current change in barometric pressure. The value of this pressure is the same as barometric pressure P_b after the sub-slab air volume pressure reaches equilibrium. Therefore the quantities P_{ssp} and P_b are referenced to the same parameter (barometric pressure) with time interval of Δt.

The barometric pressure observations at the research structure indicate that temporal variations are significantly slower than the time interval required for stabilization of the sub-slab air volume pressure following barometric pressure changes. This results from the fact that the value of Δt exhibited by the barometric pressure behavior is significantly larger than the maximum equilibrium time of the sub-structure soil system near the center of the slab, $\Delta t >> t_m$.

An analysis of the design control parameter equation indicates that D_c is equal to zero when no change in the barometric pressure occurs after Δt, and has a negative value when the barometric pressure exhibits an increase in its value over the consecutive time interval. Neither case requires the HUPC system to modify the operation of the HVAC system. These cases match the experimental observations and the theoretical predictions when the sub-slab soil system exhibits a slower response to the increasing changes in barometric pressure. At the same time the indoor pressure responds much faster, leaving the indoors pressurized compared to the sub-slab area.

The value of the exponent in the design control Equation 4-81, can then be treated as a constant. A minimum Δt is chosen that is limited by the mechanical system's time response to generate the required Q following changes in barometric pressure. The t_m value could range from less than one to about 20 minutes depending upon the soil system, slab geometry, slab size, and the position under the slab. In this application a value of 12 min. is chosen based on observations at the UFRRH, and a value of Δt=2 min. is applied.

It is important to note that this practice introduces a more conservative safety factor into the required indoor/outdoor pressure difference that must be developed by the system to minimize indoor radon concentrations. The design equation becomes,

$$D_c = F_s \ (P_{ssp} - P_b) \qquad (4\text{-}82)$$

where $F_s = 0.4\ f_s$, is the overall design factor.

Figure 4-75 illustrates an application of the HUPC system design. A simple modification to the duct system can be made to accommodate this feature. A barometric pressure port can be installed and connected to a damper on the return duct in line with the HVAC blower which is open to the atmosphere at the outer end. The return duct damper is designed to be a mechanically balanced enclosure that can be moved by a rod connected to a barometric pressure piston.

Piston movements are allowed only in the direction that corresponds to a decrease in barometric pressure. The damper enclosure position is calibrated with the range of the required flow rate to the interior. The damper position creates access to the ambient environment and the fresh air is induced into the system by the depressurization on the blower intake side. This configuration provides a calibrated quantity of fresh air to pressurize the interior providing positive ventilation.

The control rod between the damper and the barometric pressure piston has a double-sided electromagnetic (EM) relay switch that supplies power to the HVAC blower when the thermostat is in the OFF position. The relay is activated once the damper moves from the full closed position. This switch started the HVAC system ventilation without influence from the cooling or heating load. For some particular cases when the barometric pressure is not sufficient to produce enough force to move the damper, the piston assembly can be replaced with a servo-system to move the damper.

The servo-system is controlled by a pressure transducer. The application of the controlled induced fresh air positive pressure ventilation implemented by the HUPC concept and design is expected to be remarkably successful in minimizing indoor radon concentrations. Continuous positive ventilation of a rate of about 0.047 m^3/sec, supplied by the UFRRH 2.5 ton HVAC circulation fan, was able to reduce indoor radon concentrations from about 54 pCi/l (2000 Bq/m^3) to less than 3.2 pCi/l (120 Bq/m^3).

A more complicated system could be applied to the HUPC design and operation. This would include the installation of an auxiliary fan on a barometric pressure access duct to the utilization of electronic controls and microprocessors. In the case of auxiliary fan installation, a parallel connection is made from the EM triggering switch to provide power to the auxiliary fan motor. Two EM switches can be employed to provide different trigger timing to the auxiliary fan and the main HVAC blower if needed.

This installation gives the flexibility to trigger the auxiliary fan at a specific volumetric flow rate when the flow rate provided by the HVAC blower is no longer sufficient. Partial level combinations between these two blowers, or among more than two infiltration ducts, could be utilized based on designated ranges of the volumetric flow rates to provide better system performance and/or energy efficiency for more complicated structures and indoor radon problems.

The system could also use a heat exchanger unit that might utilize a built-in supplementary fan for increased efficiency. Figure 4-76 illustrates a schematic diagram that employs a more sophisticated utilization of the design control equation with feedback applications. A barometric pressure and differential pressure transducer provide continuous analog signals to the microprocessor control device.

The microprocessor calculates the time interval Δt by scanning the barometric pressure channel signal at some selected scan rate. The differential pressure transducer that mounts between the indoors and outdoors provides a signal that feeds back in to the program to adjust the amplitude of the control signal to the return duct damper. The duct damper position is moved by a stepping motor controlled by the microprocessor.

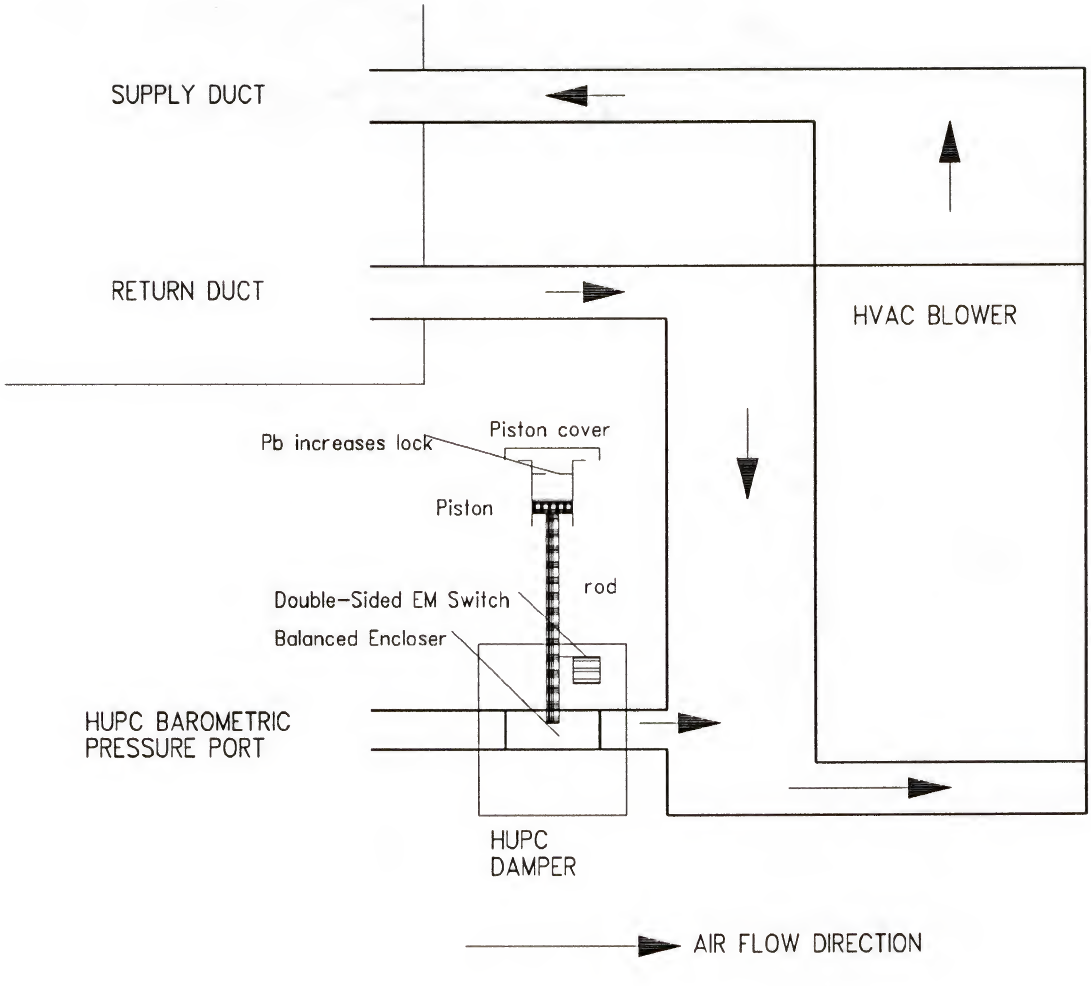
SUPPLY DUCT
RETURN DUCT
HVAC BLOWER
Piston cover
Pb increases lock
Piston
rod
Double-Sided EM Switch
Balanced Encloser
HUPC BAROMETRIC PRESSURE PORT
HUPC DAMPER
AIR FLOW DIRECTION

FIGURE 4-75: A schematic diagram for a simple mechanical application of the HUPC system design concept.

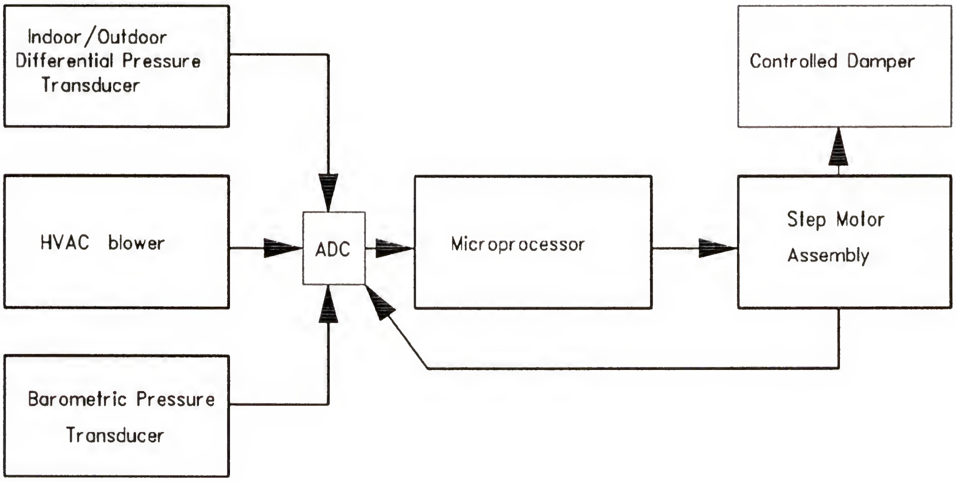
Indoor/Outdoor Differential Pressure Transducer
HVAC blower
Barometric Pressure Transducer
ADC
Microprocessor
Controlled Damper
Step Motor Assembly

FIGURE 4-76: A block diagram of a microprocessor controlled HUPC system.

CHAPTER 5
CONCLUSIONS

Indoor radon concentration can be derived from radon gas moving from the sub-structure area and the ambient into the indoor environment. Major driving forces responsible for air flow from the sub-structure area into the indoor through structure openings are the semi-diurnal barometric pressure variations, temperature-induced pressure differences generated between the sub-structure area and the indoor, wind effects on the structure, occupant activities that may cause interior depressurization, and some configurations for the utilization of the HVAC system.

The main driving forces responsible for pressure differences across the structure shell, and increased consequently structure ventilation, that contribute to the radon removal from the indoor environment are temperature-induced pressure differences due to the temperature differences between the outdoor and indoor zones, HVAC system, and occupant activities.

The average over time and space of the indoor radon concentration is strongly dependent on the whole-house pressure conditions. When the whole house undergoes depressurization, enhancement of both the radon entry rate and the radon removal rate occurs. The rate of increase in the radon entry rate with depressurization is higher than the rate of increase in the removal rate, causing an increase in the radon accumulation inside the structure. The rate of radon accumulation is proportional to the amount of depressurization. The radon accumulation increases to a saturated level and becomes almost independent of the interior pressure at high depressurization levels.

The indoor radon concentration reaches its minimum possible level on the depressurization side at a critical point and then starts to increase very rapidly as the depressurization level decreases. The mirror point on the pressurization side, which is almost equivalent in magnitude to the critical point, represents the pressurization turning point that causes a dramatic change in the indoor radon concentration from very high to lower concentrations. The mirror point does not necessarily represent the minimum possible radon concentration on the pressurization side.

The indoor radon concentration is also directly proportional to the pressurization beyond the mirror point, but the slope is lower when compared to the depressurization side and tends to become constant, especially if the overall slab penetrating probability is not a function of the pressurization level. The sub-slab and indoor radon concentrations respond quickly to changes in pressurization and depressurization levels.

The maximum possible indoor radon concentrations exist at neutral pressure conditions, when the pressure difference between the indoors and the outdoors is on the order of one Pascal. The cycle in the indoor radon concentration is currently difficult to observe because of the whole-house damping effect and also the time limitations of the radon monitors, as well as the monitor damping effects.

The semi-diurnal atmospheric tidal barometric pressure variations can provide the dominant airflow driving force for the convective component of the radon transport from low permeability soils and fill materials when the other pressure difference mechanisms are quickly stabilized.

The atmospheric tidal barometric pressure variation airflow driving force causes a pressure differential across the structure slab. This initiates a natural pumping of the radon-rich soil gas from the sub-slab area into the building interior. The other sources of building pressurization and depressurization and, consequently, the radon removal and prevention rates are small when this happens.

The elevated indoor radon concentration under neutral pressure conditions can dramatically change in the pressure range between the critical and mirror points. This pressure range, in fact, characterizes the operational pressures of several household appliances, including the air conditioning HVAC system. Therefore, the new observations and modeling provided in this research can significantly influence the design and operation of HVAC and other household appliances for the purpose of minimizing the indoor radon concentrations.

Wind-induced pressure differences are the most frequently changing environmental driven parameter affecting indoor radon concentrations. These differences develop as the wind stream loses its velocity across the structure walls and consequently develops pressure differences with the wind pressure in the main stream. These differences can be predicted by a model that is based on the application of the conservation of energy principle based on the difference in wind speed at the structure walls and the main stream. These predictions can then be adjusted by a factor accounting for the fluctuations in wind magnitude and wind direction with respect to the structure.

Indoor, outdoor and sub-slab temperature measurements at the UFRRH have shown periodic time variations with a diurnal cycle. The diurnal temperature differences between the indoors and outdoors are strongly correlated to diurnal pressure differences induced between the indoors and outdoors. The induced pressure differences are linearly proportional to the magnitude of the temperature differences and to the average temperature between the indoors and outdoors. These pressure differences are linearly combined with the semi-diurnal radon driving forces between the indoors and the sub-structure area. The minimum indoor radon concentration exists in the house when the structure undergoes positive temperature differences in the temperature diurnal cycle, when the indoor area is pressurized relative to the outdoors, and during the negative portions of the radon natural pumping semi-diurnal cycle when the sub-slab is depressurized relative to the indoors.

This scenario is limited to situations in which the indoor and outdoor temperatures stay constant during the transient indoor pressure response to changes in barometric pressure. The temperature effects on radon driving forces can significantly influence the natural pumping mechanism, particularly when larger temperature differences are present due to the utilization of heating and cooling systems. Temperature-driven pressure difference predictions can be performed by the use of a linear approximation to the weakly dependent pressures of two temperature zones under hydrostatic equilibrium.

An analytical model can be constructed to determine pressure differences (output) in response to temperature inputs. Since such a model results in pressure difference outputs, integrations into radon entry, radon removal, and indoor radon concentration models are systematic. The temperature-driven pressure differences model can be incorporated into models which input pressure differences and therefore can access the temperature effects on radon entry rate from the sub-structure area and from the ambient into the interior. Assessment of the radon removal rate can be characterized by calculating the temperature effects on the natural and mechanical ventilation rates of the structure. Consequently, the combination of the radon removal and entry rates can be used to determine the indoor radon concentration. Temperature differences encountered with the use of the HVAC system may produce pressure differences of the size as radon entry driving forces observed in slab-on-grade residential structures built over low permeability soil and fill materials. Such differences, therefore, could profoundly influence radon entry rates and indoor radon concentration.

The manner in which ventilation air is introduced into a structure significantly influences indoor radon concentrations through several mechanisms, providing direct air exchange and associated dilution of indoor radon, and also influences radon entry rates by changing differential pressures. Measurements from a well-characterized experimental facility provide the framework for a semi-empirical model based on physical relationships. The model is capable of predicting indoor radon concentrations as a function of indoor/outdoor differential pressures.

Parametric studies with the model illustrate the inadequacy of radon reduction strategies that require HVAC systems to be designed and installed to minimize house depressurization and duct leakage without concern for ventilation rate. While this strategy reduces the radon entry rate, air infiltration rates are also significantly reduced causing indoor radon concentrations to become elevated. This is particularly critical for energy efficient structures having tight shells that limit exterior air infiltration. Small levels of house depressurization permit increased infiltration air through the house shell and may therefore be preferable to extremely tight HVAC systems that maintain the house shell at neutral pressure. In order to minimize indoor radon concentrations for slab-on-grade residential structures, it is advantageous for HVAC systems to be designed to provide minimal air exchange rates, of at least 0.3 ACH, when the circulation fan is operating.

Remarkable reduction of indoor radon concentrations can be achieved through design utilization of the HVAC. Induced fresh air from the outdoors into the indoors by the HVAC blowers and/or auxiliary fans can be utilized to provide slight pressurization of the indoors compared to the outdoors and increase the air exchange rates through the structure. HVAC system operations that provide positive pressure ventilation throughout the structure significantly reduce indoor radon concentrations by increasing the air exchange rate from the entire structure.

The air exchange rate increases developed by increasing the structure’s effective leakage areas are not as effective as increases developed by positive ventilation. The HVAC positive pressure ventilation provided through the design concept and application of the pressure sensitive HVAC Unbalanced Pressurization Controller (HUPC) System are capable of providing designated control over the HVAC operation. Such control includes adjustable induction of fresh air into the depressurized side of the HVAC blower which creates positive structure ventilation that increases the air exchange rate and slightly pressurizes the structure. The HUCP design concept can be implemented through simple mechanical system alternations, which can control the fresh air supply damper corresponding to transient changes in barometric pressure. More complicated systems can provide sophisticated control over the ventilation system for more complex structures and/or indoor radon problems.

The mass balance approach can be used to establish the relationship between the short-term indoor radon concentration measurement and the time-averaged annual indoor radon concentration measurement. This approach developed the first mathematical framework needed for such an application and needed to support an explicit semi-analytical treatment that accounts for all radon entry and removal driving forces in the indoor environment. A semi-analytical framework can be developed by integrating the semi-diurnal barometric pressure variation driven pressure differences across the slab, temperature-induced pressure differences across the structure slab and shell, and wind-induced pressure differences across the slab and the structure walls into the differential pressure formulation of the total radon convective entry from the sub-structure area into the building interior.

Radon removal driving forces consisting of the models of structure ventilation and accounted for in the decay of radon in the indoor environment are also integrated into the time-dependent indoor radon concentration derived from the mass balance principle. The latter mathematical structure can then be applied to the short- and long-term averaged indoor radon concentration estimation in two different time periods when a common reference time is established. The ratio of the short-term indoor radon concentration to the long-term time averaged indoor radon concentration can be evaluated for all configurations of testing periods and the relative occurrence of the short-term test with respect to the long-term period.

Utilization of such applications to predict the annual averaged indoor radon concentration requires the possession of a year's (or more) worth of environmental data such as temperature, barometric pressure, and wind speed. These data are integrated into the calculation process using the concept of time indexing to facilitate the solution. Such data are available from the National Cimate Data Center which reporte the Federal Aviation Administration weather measurements. Most of the above data are collected on an hourly basis in most large cities at airport locations. The diffusive component of radon from the sub-structure area into the indoor can be estimated or ignored if the convective flow is dominant, depending on the soil properties and structure features. Indoor and sub-slab temperatures can also be estimated if not available, depending on the general weather pattern in the area. This application provides a significant tool to predict the time-averaged annual indoor radon concentration used for health hazard estimations and legal considerations from the wide spread practice of short-term (48-hour) testing of indoor radon concentration.

Recommendations for Future Work

During the course of this research several areas of future development can be realized. These areas correspond to the general structure of developments in this research from radon driving forces models to the applications of the integrated indoor radon concentrations model. These areas have not been addressed since they are out of the scope of this work, however, they represent excellent opportunities for future work. Future works related to the current research are recommended as the following:

1. Analytical modeling of the sub-slab equilibrium time response T_R and comparison with experimental data. This modeling can be developed from the consideration of pressure wave propagation in soil porous media. The modeling will permit analyses for the soil parameters, such as soil moisture, effects on the T_R;

2. Investigation of the interactions between the sub-slab and outdoor environments through the wall/foundation interface and its effects on the wind-induced pressure differentials. Analyses of these effects could provide better predictions to the steady state and transient indoor and sub-slab air volume pressures.
3. Investigation of the effects of indoor humidity on the radon entry and indoor radon concentrations including characterization of contributing factors such as the operation of house appliances and HVAC systems.
4. Investigation of the temperature-induced pressure differential dependence on the average of the driving temperatures. This analysis is particularly important for the characterization of the average temperature between the indoor and outdoors, and the consequent effect on indoor radon concentrations.
5. Extension of the short-term/long-term indoor radon concentration approach and procedure in two directions: (A) comparisons with currently available statistical studies and results, and (B) developing specific predictions for the short-term to long-term indoor radon concentration ratios for specific cities or geographical areas.
6. Extension of the HUPC design concept from a single-zone single-air handler configuration into a multi-zone/multi-handler configuration to support applications in large

buildings. This would include analyses of the system interactions with building support systems, and other radon prevention and mitigation and indoor air quality systems.

REFERENCES

Al-Ahmady, K.K., "Measurements and Theoretical Modeling of A Naturally Occurring ^{222}Rn Entry Cycle For Structures Built Over Low Permeability Soils", Master of Engineering Thesis, University of Florida, Gainesville, FL; 1992a.

Al-Ahmady, K.K., "Semi-Passive Pressurized Forbidden Space (PFS) For Radon Prevention and Mitigation", Summary of Awards Winners, the 1992 Innovative Radon Mitigation Design Competition, The Association of Energy Engineers and The U.S. Environmental Protection Agency, 14-16; 1992b.

Al-Ahmady, K.K.; Hintenlang D.E., "Measurements and Theoretical Modeling of Diurnal Temperature Effects on The Natural Periodic Atmospheric Pressure Variations Driven Radon Entry into Structures Built Over Low Permeability Soils", Accepted for Presentation, The 16th World Energy Engineering Congress, The Association of Energy Engineers; 1993a.

Al-Ahmady, K.K.; Hintenlang, D.E. "Application of The Semi-Passive Pressurized Forbidden Space (PFS) Method For Radon Prevention and Mitigation Technology", Health Physics, 64: S43; 1993b.

Al-Ahmady, K.K. "Semi-Passive Pressurized Forbidden Space (PFS) Method, System and Apparatus For Radon Prevention and Mitigation Technology", The BFGoodrich Collegiate Inventor Program, National Invention Center, Ohio; 1993.

Al-Ahmady, K.K.; Hintenlang, D.E.; Kozik, A; Oppenheim, P. "Design and Development of A Pressure Sensitive HVAC Unbalanced Pressurization Controller System (HUPCS) for Minimizing Indoor Radon Concentrations in Slab-on-Grade Structures", Proceedings of The International Conference on Radon and Radon Reduction Technology, Denver, Colorado, VI23-VI40; 1993.

Al-Ahmady, K.K.; Hintenlang, D.E.; Tulenko, J.S. "Development of Indoor Radon Related Laboratory Exercises for Undergraduate Studies", Proceedings of the 1994 Annual Conference of The American Society for Engineering Education (ASEE), Alberta, Canada, Vol. 2, 1906-1915; 1994.

Al-Ahmady, K.K.; Hintenlang, D.E. "Characterization of the Temperature Effects on Radon Driving Forces and Radon Entry for Slab-on-Grade Residential Structures", Health Physics, 66: S59; 1994a.

Al-Ahmady, K.K "The HVAC Unbalanced Pressurization Controller (HUPC) Radon Reduction System: A Semi-Analytical Approach for The Design and Operation in Large Structures", Proceedings of the 1994 International Radon Symposium, Atlantic City, New Jersey, V5; 1994.

Al-Ahmady, K.K.; Hintenlang, D.E. "Assessment of Temperature-Driven Pressure Differences With Regard to Radon Entry and Indoor Radon Concentration", Proceedings of the 1994 International Radon Symposium, Atlantic City, New Jersey, III6.1-III6.11; 1994b.

Al-Ahmady, K.K.; Hintenlang, D.E. "Modeling of Sub-Slab Depressurization (SSD) Radon Mitigation Systems for Large Structures", Proceedings of the 1994 International Radon Symposium, Atlantic City, New Jersey, VP1.1-VP1.9; 1994c.

ASTM (American Society for Testing and Materials). "Standard Test Method for Determining Air Leakage Rate by Fan Pressurization", Philadelphia: ASTM; ASTM E779-87; 1987.

Beer, T. "The Aerospace Environment", Springer-Verlag, New York, 52-55; 1976.

Bird, R.B.; Stewart, W.E.; Lightfoot, E.N. "Transport Phenomena", John Wiley and Sons, New York; 1960.

Blair, T.A.; Fite, R.C. "Weather Elements", Prentice Hall, Englewood Cliffs, New Jersey, 122-123; 1965.

Brookins, D.G. "The Indoor Radon Problem", Columbia University Press, New York; 1990.

Browne, E.; Firestone, R.B. "Table of Radioactive Isotopes", Shirley, V.S. (eds.), Wiley-Interscience, New York; 1986.

Bossus, D.A.W. "Emanating Power and Specific Surface Area", Radiation Protection Dosimetry, 7: 73; 1984.

Clements, W.E.; Wilkening, M.H. "Atmospheric Pressure Effects on ^{222}Rn Transport Across the Earth-Air Interface", Journal of Geophysical Research, 79, 33: 5025-5029; 1974.

Cohen, B.L. "Surveys of Radon Levels in Homes by University of Pittsburgh Radon Project", Proceedings of the 1990 International Symposium on Radon and Radon Reduction Technology, Atlanta, Georgia, EPA: EPA-600/9-91-026a; 1990.

Cothern, C.R.; Rebers, P.A. Radon eds. "Radium and Uranium in Drinking Water", Lewis Publication, Michigan; 1990.

Cothern, C.R.; Smith, J.E. eds. "Environmental Radon", Plenum Press, New York; 1987.

Crameri, R.; Brunner, H.H.; Buchli, R.; Wernli, C.; Burkart, W. "Indoor Rn Levels in Different Geological Areas in Switzerland", Health Physics, 57: 29; 1989.

Cummings, J.B.; Tooley, J.J.; Moyer, N. "Investigation of Air Distribution System Leakage and its Impact on Central Florida Houses", Florida Solar Energy Center Report FSEC-CR-397-91, Cocoa Beach, Florida; 1991.

DOE. "Understanding Radiation", U.S. Dept. of Energy, Energy Booklet DOE/NE-0074, 97-105; 1986.

Dyess T.M., Brennan T., Clarkin M. "Designs for New Residential HAC Systems to Achieve Radon and Other Soil Gas Reduction" Proceedings of the 1993 International Radon Conference, AARST, Denver, Co., 1993.

EPA "A Citizen's Guide To Radon, What It Is And What To Do About It", United States Environmental Protection Agency and Department of Health and Human Services, OPA-86-004; 1986.

EPA "A Citizen's Guide to Radon", second editions, United States Environmental Protection Agency, Air and Radiation (ANR-464), 402-k92-001; 1992.

EPA "Application of Radon Reduction Methods", Air and Energy Engineering Research Laboratory, North Carolina, EPA/625/5-88/024; 1988.

Fejer, J.A. "The Encyclopedia of Atmospheric Sciences and Astrogeology", R.W. Fairbridge, ed., New York, Reinhold; 1967.

Fukuda, H. "Air and Vapor Movement in Soil Due to Wind Gustiness", Soil Sciences, 79: 249; 1955.

Furrer, D.; Crameri, R.; Burkart, W. "Dynamics of Rn Transport From the Cellar to The Living Area in an Unheated House", Health Physics, 60: 393; 1991.

Garzon, L.; Juanco, J.M.; Perez, J.M.; Fernandez, J.M.; Arganaz, B. "The Universal Rn Wave: An Approach", Health Physics, 51: 185; 1986.

Gumming, C.; Scott, A.G. "Radon and Thoron Daughters in Housing", Health Physics, 42: 527; 1982.

Hems, G. "Acceptable Concentration of Radon in Drinking Water", International Journal of Air and Water Pollution, 10: 769; 1966.

Hintenlang, D.E.; Al-Ahmady, K.K., "Pressure Differentials For Radon Entry Coupled to Periodic Atmospheric Pressure Variations", Indoor Air, 2: 208; 1992a.

Hintenlang, D.E.; Al-Ahmady, K.K., "Effects of Natural Mechanically Induced Pressurization on Indoor Radon Concentration", Health Physics, 62: S-144; 1992.

Hintenlang, D.E.; Al-Ahmady, K.K., "Building Dynamics and HVAC System Effects on Radon Transport in Florida Houses", The 1992 International Symposium on Radon and Radon Reduction Technology, Vol. 1:VI:93-106, EPA-600/R-93-083a, Springfield, VA. NTIS PB93-196194, 1993.

Hintenlang D.E.; Al-Ahmady, K.K., "Influence of Ventilation Strategies on Indoor Radon Concentrations Based on a Semi-Empirical Model for Florida-Style Houses", Health Physics, 66: 427, 1994.

Hintenlang, D.E.; Al-Ahmady, K.K.; Kozic, A. "Optimized HVAC Induced Ventilation For The Reduction of Indoor Radon in Slab-on-Grade Structures", Health Physics, 64: S22; 1993.

Hintenlang, D.E; Al-Ahmady, K.K.; Oppenheim, P.; Kozik, A.; Roessler, C. "Evaluation of House Envelope and HVAC System Design and Operation on Radon Entry", University of Florida Final Report, EPA Cooperative Agreement CR-817367-01, Gainesville, FL; 1993a.

Hintenlang, D.E.; Shanker, A.; Al-Ahmady, K.K. "Evaluation of Radon Resistant Residential Construction", Health Physics, 66: S30; 1994.

Hintenlang, D.E.; Ward, D.B.; Al-Ahmady, K.K. "Field Evaluations of a Radon Resistant Construction Standard Proposed for Residential Structures in Florida", Proceedings of the 1994 International Radon Symposium, Atlantic City, New Jersey, II7.1-II7.11; 1994a.

Hintenlang, D.E. "Reference Manual for RASSMIT Version 2.1: Sub-Slab Depressurization Design Performance Simulation Program", EPA-600/R-93-027; 1993.

Hintenlang, D.E.; Barber, J.M. "Practical Engineering Analysis for Indoor Radon Mitigation Using Sub-Slab Depressurization Techniques", Radiation Protection Management, 8: 63; 1991.

Hintenlang, D.E.; Furman, R.A. "Sub-Slab Suction System Design for Low Permeability Soils", Proceedings of the Symposium on Radon And Radon Reduction Technology", EPA/600/9-90/005, III: V.1-V.4; 1990.

Hubbard L.M., Bolker B., Socolow R.A., Dickerboff D., Mosley R.B. "Radon Dynamics in a House Heated Alternatively By Forced Air and By Electric Resistance" Proceedings of the 1988 Symposium on Radon and Radon Reduction Technology, Vol.1, EPA-600/9-89-006a (NTIS PB89-167480), 1989.

Hull, D.A.; Reddy, T.A. "Study on the Reliability of Short-Term Measurements to Predict Long-Term Basement Radon Levels in a Resident", Proceedings of the 1990 International Symposium on Radon and Radon Reduction Technology, Atlanta, Georgia, EPA: EPA-600/9-91-026a; 1990.

James, A.C. "Dosimetric Approaches for Risk Assessment for Indoor Exposure to Radon Daughters", Radiation Protection Dosimetry, 7: 353; 1984.

Kahlos, H.; Asikainen, M. "Internal Radiation Doses from Radioactivity of Drinking Water in Finland", Health Physics, 39: 108; 1980.

Kozik, A.C.; Oppenheim, P.; Schneider, D. The effect of interior door position and methods of handling return air on differential pressures in a Florida house. The 1992 International Symposium on Radon and Radon Reduction Technology, Vol. 1:VI: 79-92, EPA-600/R-93-083a, Springfield, VA. NTIS PB93-196194, 1993.

Landman, K.A. "Diffusion of Radon Through Cracks in a Concrete Slab", Health Physics, 30: 65; 1982.

Makofske, W.J.; Edelstein, M.R. eds. "Radon and the Environment", Noyes Publications, New Jersey; 1988.

NAS. "Health Risks of Radon and Other Internally Deposited Alpha-Emitters", BEIR IV, National Academy of Science Press, Washington, D.C.; 1988.

Nazaroff, W.W.; Feustal, A.; Nero, A.; Revzan, K.L.; Grimsrud, D.T.; Essling, M.A.; Toohey, R.E. "Radon Transport into a Detached One-Story House with a Basement", Atmospheric Environment, 19: 31; 1988.

Nazaroff, W.W.; Lewis, S.R.; Doyle, S.M.; Moed, B.A.; Nero, A.V. "Experiments on Pollutant Transport from Soil into Residential Basements by Pressure-Driven Airflow", Environmental Science and Technology, 21: 459; 1987.

Nazaroff, W.W.; Moed, B.A.; Sextro, R.G. "Soil as a Source of Indoor Radon: Generation, Mitigation and Entry, In: Radon and its Decay Products in Indoor Air", Nazaroff, W.W.; Nero, A.V., eds., John Wiley & Sons, New York, 57-112; 1988a.

Nero, A.V. "Radon and Its Decay Product in Indoor Air: An Overview, In: Radon and its Decay Products in Indoor Air", Nazaroff; W.W., Nero, A.V., eds., John Wiley & Sons, New York, 1-52; 1988.

Nero, A.V.; Nazaroff, W.W. "Characterizing The Source of Radon Indoors", Radiation Protection Dosimetry, 4: 23; 1984.

Nielson, K.K.; Rogers, V. C. "Modeling Indoor Radon Entry from Soil Radon Emanation and Transport, Proceedings of the Radon Modeling Workshop of the Florida Radon Research Program", Hintenlang, D.E. ed., US EPA - AEERL, Research Triangle Park, N.C.; 1991.

Owczarski, P.C.; Holford, D.J.; Freeman, H.D.; Gee, G.W. "Effects of Changing Water Content and Atmospheric Pressure on Radon Flux From Surfaces of Five Soil Types", Geophysical Research Letters, 17, 6: 817; 1990.

Prichard, H.M.; Gesell, T.F. "An Estimate of Population Exposure Due to Radon in Public Water Supplies in the Area of Houston, Texas", Health Physics, 41: 599; 1981.

Reddy, T.A.; Molineaux, F.B.; Gadsby, K.J.; Scocolow, R.H. "Statistical Analyses of Radon Levels in Residences Using Weakly and Daily Averaged Data", PU/CEES Report No. 249; 1990.

Rigby J.G., Daphne D.L. "Wind and Barometric Pressure Effects on Radon in Two Mitigated Houses", Proceedings of the 1993 International Radon Conference, AARST, Denver, Colorado, 1993.

Rogers, V.C.; Nielson, K.K.; Kalkwarf, D.R. "Radon Attenuation Handbook for Uranium Mill Tailings Cover Design, Report NUREG/CR-3533, United States Nuclear Regulatory Commission; 1984.

Rogers, V.C.; Nielson K.K. "Multiphase Radon Generation and Transport in Porous Materials", Health Physics, 60: 807; 1991.

Roessler, C.E.; Revel, J.W.; Wen, M.J. "Temporal Patterns of Indoor Radon in North Central Florida and Comparison of Short-Term Monitoring to Long-Term Average", Proceedings of the 1990 International Symposium on Radon and Radon Reduction Technology, Atlanta, Georgia, EPA: EPA-600/9-91-026a; 1990.

Scheidegger, A.E. "The Physics of Flow Through Porous Media", 2nd ed., John Wiley and Sons, New York; 1960.

Schery, S.D. "Measurements of Airborne ^{212}Pb and ^{220}Rn Concentrations at Varied Indoor Locations Within the United State", Health Physics, 49: 1061; 1985

Smith, B.M.; Grune, W.N.; Higgins, F.B.; Terrill, J.G. "Natural Radiology in Ground Water Supplies in Maine and New Hampshire", Journal of American Water Workers Association, 53: 75; 1961.

Steck, D.J. "A Comparison of EPA Screening Measurements and Annual ^{222}Rn Concentrations in Statewide Surveys", Health Physics, 60: 523; 1990.

Stranden, E. "Building Materials as A Source of Indoor Radon, In: Radon and its Decay Products", Nazaroff, W.W.; Nero, A.V. eds., John Wiley and Sons, New York, 113-130; 1988.

Strong, K.P.; Levins, D.M. "Effect of Moisture Content on Radon Emanation from Uranium Ore and Tailings", Health Physics, 42: 27; 1982.

Suomela, M.; Kahlos, H. "Studies on The Elimination Rate and Radiation Exposure Following Ingestion of ^{222}Rn rich water", Health Physics, 23: 641; 1972.

Tanner, A.B. "Radon Mitigation in the Ground: A review, In: Natural Radiation Environment", Adams, J.A.; Lowder, W.M. eds., University of Chicago Press, Chicago, 161; 1964.

Tanner, A.B. "Radon Migration in the ground: a supplementary review, In: Proc. Natural Radiation Environment III", Gesell, F.; Lowder, W.M. eds., Conf 780422, U.S. Dept. of Commerce, National Technical Information Service, Springfield, VA; 1980.

Toohey, R.E. "Radon vs. Lung Cancer: New Study Weight the Risks", logos, Argonne National Lab., 5: 7 1987.

Toth, A. "Simple Field Method for Determining of ^{220}Rn and ^{222}Rn Daughter Energy Concentrations in Room Air", Radiation Protection Dosimetry, 7: 247; 1984.

Turner, R.C.; Radley, J.M.; Mayneord, W.V. "Naturally Occurring Alpha-Activity of Drinking Waters", Nature, 189: 348; 1961.

Tsang, Y.W.; Narasimhan, T.N. "Effects of Periodic Atmospheric Pressure Variation on Radon Entry into Buildings", Journal of Geophysical Research, 97: 9161; 1991.

United Nations Scientific Committee on The Effect of Atomic Radiation "Ionizing Radiation: Sources and Biological Effects, United Nations Press", New York; 1982.

USDOI "The Geology of Radon", United States Department of Interior/U.S. Geological Survey, U.S. Government Printing Office, 0-326-248; 1992.

Van der Hoven, I. "Power Spectrum of Horizontal Wind Speed in the Frequency Range from 0.0007 to 900 cycles per hour", Journal of Meteorology, 14, 160, 1957.

White, S.B.; Alexander, B.V.; Rodman, N.F."Predicting the Annual Concentration of ^{222}Rn From One or More Short-Term Measurements", Health Physics, 66: 55; 1994.

White, S.B.; Bergsten, J.W.; Alexander, B.V.; Rodman, N.F.; Phillips, J.L. "Indoor ^{222}Rn Concentrations in a Probability Sample of 43,000 Houses Across 30 States", Health Physics, 62: 41; 1992.

Wilkening, M.H.; Clements, W.E.; Stanley, D. "Radon-222 flux measurements in widely separated regions, In: Proceeding of Natural Radiation Environment II", Adams, J.A.; Lower, W.M.; Gesell eds., Conf-720805, U.S. Dept. of Commerce, National Technical Information Service, Springfield, VA, 717; 1972.

BIOGRAPHICAL SKETCH

Kaiss K. Al-Ahmady was born in Mosul, Iraq, in 1965. He started his undergraduate education in electrical engineering at the University of Mosul in 1983. In 1986 Kaiss ranked first among the class of 177 students at the Department of Electrical Engineering. He then admitted to a concentrated two-year program in nuclear engineering at the University of Baghdad and received his B.Sc. (with honors) in 1988. Kaiss was admitted to the graduate program of the Department of Nuclear Engineering Sciences (NES) at the University of Florida in the Fall of 1990. However, his fellowship was discontinued due to the conflict of the Gulf War. During and after the war he faced great difficulties but he managed to continue his education. He was awarded a departmental graduate research assistantship in the radon field, initiated his master's research and completed the degree requirements. In the Spring of 1992 he received his Master of Engineering degree with a thesis that highlighted the discovery, modeling, and first experimental observation of a natural pumping mechanism of radon-rich soil gas from the sub-structure area into the interior of buildings.

In October 1992, Kaiss won the Grand Prize in the international Innovative Radon Mitigation Design Competition sponsored by the U.S. Environmental Protection Agency (EPA), the Association of Energy Engineers (AEE), and the Environmental and Energy Managers Institute (EEMI). He was the first and only student to receive this award. In April 1993 he was recognized as one of the top twenty five in the nation at the national BFGoodrich Collegiate Invention Competition administered by a national judging panel in all fields at the National Invention Center in Ohio. In July 1993 he received a best scientific paper presentation award at the 1993 Annual Meeting of the Health Physics Society (HPS) in Atlanta, Georgia.

In February 1994 he was honored with the James E. Swander Memorial Scholarship award in recognition for outstanding graduate students at the Department of Nuclear Engineering Sciences during the joint meeting between the Department of Nuclear Engineering Sciences and the American Nuclear Society (ANS) Florida chapter. In April 1994 he was selected as a recipient of the 1994 Health Physics Society Graduate Student Fellowship Award. In June 1994 he won, for the second time in a row, a best scientific paper presentation award during his participation at the 1994 Annual Meeting of the HPS in San Francisco, California. With this achievement, Kaiss marked the first time in HPS history for anyone to receive this award two times. In April 1995 Kaiss received the President's Outstanding Student Recognition Award for his achievement and contribution to the University of Florida.

He is a member of the Association of Energy Engineers, the American Nuclear Society, the Health Physics Society, the American Society for Engineering Education, the American Association of Radon Scientists and Technologists, the American Physical Society, the American Society of Safety Engineers, the Phi Kappa Phi international honor society, and the Alpha Nu Sigma nuclear engineering honor society. He is a reviewer for the Health Physics Journal. Since 1992, Kaiss has authored and coauthored more than thirty papers published in research journals and in national and international conference proceedings covering subjects such as radon, radioactive waste, computer simulation, and education.

Kaiss K. Al-Ahmady has been married to Zahrah S. Al-Noory since September, 1989. They have two children; Ahmed, their four and a half year old son, and Farrah, their three year old daughter.

I certify that I have read this study and that in my opinion it conforms to acceptable standards of scholarly presentation and is fully adequate, in scope and quality, as a dissertation for the degree of Doctor of Philosophy.

David E. Hintenlang, Chair
Associate Professor of
Nuclear Engineering Sciences

I certify that I have read this study and that in my opinion it conforms to acceptable standards of scholarly presentation and is fully adequate, in scope and quality, as a dissertation for the degree of Doctor of Philosophy.

G. Ronald Dalton

George R. Dalton
Professor of Nuclear
Engineering Sciences

I certify that I have read this study and that in my opinion it conforms to acceptable standards of scholarly presentation and is fully adequate, in scope and quality, as a dissertation for the degree of Doctor of Philosophy.

William G. Vernetson
Associate Engineer of
Nuclear Engineering Sciences

I certify that I have read this study and that in my opinion it conforms to acceptable standards of scholarly presentation and is fully adequate, in scope and quality, as a dissertation for the degree of Doctor of Philosophy.

Paul Oppenheim

Paul Oppenheim
Associate Professor of
Building Construction

I certify that I have read this study and that in my opinion it conforms to acceptable standards of scholarly presentation and is fully adequate, in scope and quality, as a dissertation for the degree of Doctor of Philosophy.

Fazil T Najafi

Fazil T. Najafi
Associate Professor of
Civil Engineering

This dissertation was submitted to the Graduate Faculty of the College of Engineering and to the Graduate School and was accepted as partial fulfillment of the requirements for the degree of Doctor of Philosophy.

May 1995

Winfred M. Phillips
Dean, College of Engineering

Karen A. Holbrook
Dean, Graduate School